Electrochemical Activation of Ni-based Electrodes for the Alkaline Oxygen Evolution Reaction

Elektrochemische Aktivierung von Ni-basierten Elektroden für die alkalische Sauerstoffentwicklungsreaktion

Von der Fakultät für Maschinenwesen der Rheinisch-Westfälischen Technischen Hochschule Aachen zur Erlangung des akademischen Grades einer Doktorin der Naturwissenschaften genehmigte Dissertation

vorgelegt von

Clara Gohlke

Berichter/in: Univ.-Prof. Dr. rer. nat. Anna Mechler
Prof. Dr.-Ing. Bastian J. M. Etzold

Tag der mündlichen Prüfung: 08.04.2025

Diese Dissertation ist auf den Internetseiten der Universitätsbibliothek online verfügbar.

Et es wie et es,

Et kütt wie et kütt,

Et hätt noch immer jot jejange!

Acknowledgments

An dieser Stelle möchte ich herzlich den Menschen danken, die durch ihre fachliche und persönliche Unterstützung zum Gelingen dieser Dissertation beigetragen haben.

Zuerst möchte ich mich bei Prof. **Anna K. Mechler** bedanken für die Möglichkeit meine Promotion in ihrer Arbeitsgruppe zu machen und für ihre Betreuung. Anna, vielen Dank für dein Vertrauen in mich und die Möglichkeit die ERT gemeinsam aufzubauen. Es war eine sehr spannende und schöne Zeit für mich und hat mich sehr viel gelehrt. Danke auch für die angenehme Arbeitsatmosphäre, die du geschaffen hast, und dass du immer ein offenes Ohr für all meine Herausforderungen hattest. Vor allem aber danke ich dir, dass du mir während meiner Zeit hier immer mir Rat und Tat unterstützt hast und gleichzeitig mir die Freiräume gegeben hast mich selbst zu finden und zu verwirklichen.

Vielen Dank an Prof. **Bastian Etzold** für die unkomplizierte Übernahme des Zweitprüfers. Auch Danke für den regen wissenschaftlichen Austausch und gute Hinweise zu meiner Arbeit während der vielen PrometH_2eus Treffen.

Für die finanzielle Unterstützung möchte ich mich bei dem deutschen **Bundesministerium für Forschung, Technologie und Raumfahrt** (BMFTR-Projekt „PrometH2eus“,FKZ 03HY105A) bedanken.

Ein riesengroßes Dankeschön geht an den gesamten **ERT-Arbeitskreis** für die entspannte und angenehme Arbeitsatmosphäre mit all unseren netten Gesprächen im Büro, wo jeder immer ein offenes Ohr für wissenschaftliche Diskussionen hatte. Als Alternative stand die spontane Tanzparty oder einen Ball von der Deckenabtrennung zu holen auf dem Plan. Vielen Dank auch für die vielen schönen gemeinsamen Momente bei Chill-den-Studi, Koch- oder Kneipenabenden, beim Feierabendbier oder einfach beim alltäglichen Kaffee. *A huge thank you goes to my **ERT working group** for the relaxed, nice working atmosphere with all our chats in the office, where everyone is always open for scientific discussions. The alternatives on the agenda were a spontaneous dance party or getting a ball from the ceiling partition. Thank you also for the many wonderful moments together at chill-outs, cooking evenings, pub evenings, after-work beers or just everyday coffees.* Ganz besonders möchte ich **Florian Schwarz, Christian Marcks, Yashwardhan Deo** danken. Flo, was hätte ich ohne dich gemacht? Du warst mein Partner-in-crime von Tag eins an und zusammen haben wir alle Hürden gemeinsam genommen. Vielen Dank, dass du dir immer meine Sorgen angehört hast, egal welcher Natur, mich aufgemuntert, mir neue Hoffnung gegeben hast, und mich unterstützt hast, wo es ging! Danke auch für all die wissenschaftlichen und nicht wissenschaftlichen Diskussionen, die gute Laune, die Musik, und all die Abenteuer neben der Arbeit! Christian, von der Masterarbeit bis hin zu unserer gemeinsamen Arbeit an der kleinen Diva-Flusszelle oder an der Konditionierung von pulverbasierten Elektroden, die Arbeit mit dir hat mir immer sehr viel Spaß gemacht. Danke für wunderbare Zusammenarbeit, insbesondere all die Konstruktionen (+Nachhilfe)! Yash, es ist so einfach mit dir sich zu verquatschen, ob 10 oder 60 min und egal ob über die Konditionierung meiner/deiner Elektroden oder über das letzte Wochenende. Danke dir für all die wertvollen Gespräche und wissenschaftlichen Ideen. Sie haben mir nicht nur in meiner Forschung geholfen, sondern auch meinen Arbeitsalltag ein bisschen schöner, lustiger, und bunter gemacht! Danke auch an **Vera Seidl**, **Florian Schwarz, Christian Marcks, Janis Schmitt, und Niklas Thissen** fürs Korrekturlesen meiner Arbeit. Außerdem möchte ich **Malgorzata Kwiatkowska** danken für ihre Unterstützung der ERT-Labore, Laborverantwortlichen, und vor allem, danke fürs ICP-OES messen und fürs Kümmern um die ICP-OES!

Mein herzlichster Dank geht an die Studierende, die ich über die Jahre betreut habe und auf deren Arbeit diese Dissertation beruht: Danke an **Christian Marcks, Wilson Turner, Fabian Edwin, Victor Schulte, Nico Niederprüm, Johann Kautz, Xuehuai Hou, Hannah Ingendae**, **Janis Schmitt, und Raphael Diebold.** Die Arbeit mit euch hat mir am meisten Spaß gemacht und ihr habt alle großartige Arbeit geleistet, die in unterschiedlichster Form hier mit eingeflossen ist! Dafür bin ich euch sehr dankbar! Ganz besonders möchte ich Nico Niederprüm danken, der mir am allerlängsten zur Seite stand. Nico, danke, dass ich mich immer 100% auf dich verlassen konnte und du mir das Leben so viel einfacher gemacht hast!

Auch beim Programmieren der Skripte zur Datenauswertung hatte ich etwas Hilfe und dafür möchte ich **Ramona Bendias**, **Daniel Van Zeil**, and **Rifael Z. Snitkoff-Sol** ganz herzlich danken. *Thanks to Ramona Bendias, Daniel Van Zeil, and Rifael Z. Snitkoff-Sol for their help with the programming.*

Mit meiner Promotion an der AVT bin ich Teil der **AVT-Community** geworden und ich möchte allen danken für den einzigartigen Zusammenhalt, die Hilfsbereitschaft, und all die schönen Erinnerungen! Ich habe die Zeit hier sehr genossen und einige wunderbare Menschen beim Kaffee, Beach-Volleyball, Feierabendbier, Konferenzen, oder diverser AVT-Veranstaltungen kennenlernen dürfen. Danke für die schöne gemeinsame Zeit! Danke auch an die technischen und administrativen Mitarbeiter der AVT für ihre Unterstützung im Hintergrund.

Meine Arbeit wäre außerdem nicht möglich gewesen ohne externe Kollaborationen. Danke an Prof. **Jan Philip Hofmann** und **Julia Gallenberger** (Surface Science Laboratory, Department of Materials and Earth Sciences, Technical University of Darmstadt). Sie haben meine Elektroden ex-situ charakterisiert, ausgewertet, meine vielen Fragen beantwortet und unser gemeinsames Manuskript Korrektur gelesen. Während meiner Promotion hatte ich außerdem die Möglichkeit für zwei Monate die Arbeitsgruppe von Assoc. Prof. **Alexandr Simonov** an der Monash University in Australien zu besuchen und hier die Methode FTacV zu erlernen. Dafür bin ich sehr dankbar! ***Sasha**, thank you very much for the opportunity to visit your research group and for your supervision. I was very thankful for your valuable input and that you were always open for a quick talk or email chat. Many thanks also to the entire working group, who warmly welcomed me and always helped me out. Thank you for all the lunches, great laughs and evenings out! Especially I want to thank **Darcy Simondson and Sam Johnston**, who taught me the FTacV technique and helped me with all the difficulties that arose during that time. Thank you both so much for making time, being patient, and turning this short research period into such a valuable time! I also had the privilege to share my flat with a wonderful group of girls, who I spent the most time with during these weeks, exploring Melbourne and the area and even Tasmania. Thank you, you really turned these two months into a wonderful time!* Für die finanziellen Unterstützung, die diesen Aufenthalt möglich gemacht hat, möchte ich dem **DAAD** danken.

Das Leben besteht selbstverständlich nicht nur aus Arbeit, und ohne meine Familie, Freunde, und meinen Partner hätte ich die Herausforderungen der letzten Jahre wohl kaum bewältigen können. Danke an **meine allerliebste Familie**, ihr gebt mir den Halt, den ich für all die Herausforderungen des Lebens brauche. Danke an meine **Olga-, Aloha- & Krabben-Mädels** für all die wundervollen Momente zusammen, die mir ein grandioser Ausgleich in dieser Zeit waren, und für all die Krisenbewältigung in so vielen Situationen. Vielen Dank vor allem an **Alisa** als beste Schreibpartnerin! Und das Beste kommt zum Schluss: Vielen lieben Dank **Max** für dein Verständnis, deine Unterstützung und, dass du einfach für mich da warst, und natürlich für all die wunderbar geplanten Rennradtouren, bei denen ich den Kopf frei kriegen konnte!

Contributions

In the following, the contributions to the *Results and Discussion*-chapters are explained in detail:

Chapter 5.1: The electrochemical flow cell was designed in equal contribution with C. Marcks. My lead was in project conceptualization, design development, data interpretation, methodology, and manuscript drafting. The simulations, data processing, data curation, and data visualization in subchapter 5.1.1 were performed by C. Marcks. The access to COMSOL Multiphysics was granted by the Department of Chemical Process Engineering from RWTH Aachen University (M. Wessling and M. Padligur). The experimental validation of the simulation results was done by C. Marcks and me in equal contribution. V. Schulte conducted the experimental investigation and data analysis of the relative-electrode-positioning study (subchapter 5.1.2) as part of his bachelor thesis. The experimental investigation, data processing, data curation, and data visualization in subchapters 5.1.3-5.1.5 were performed primarily by me and supported by C. Marcks. R. Diebold and N. Niederprüm supported with experimental investigation, data analysis, and data curation. N. Rüttcher (AG K. Mayrhofer) contributed with samples of 3D-printing material. A. K. Mechler and C. Marcks supported the project conceptualization and corrected the manuscript. Parts of chapter 5.1. and of the respective chapters in the State-of-the-Art and Experimental-Section are published in the article titled *Simulation-assisted Design of an Electrochemical Flow Cell for Performance Studies of Electrocatalytic Reactions* (J. Electrochem. Soc.).

Chapter 5.2: Parts of the published articles titled *Boosting the Oxygen Evolution Reaction Performance of Ni-Fe-Electrodes by Tailored Conditioning* (ChemElectroChem) and *Electrochemical Modification of Nickel-based Electrodes for the Oxygen Evolution Reaction (OER)* (EFCF Conference Proceeding) are incorporated in this chapter (contributions are listed below the article, see next page). N. Niederprüm supported the experimental investigation, data analysis, and data curation also beyond this publication as a student assistant. W. Turner contributed by experimentally investigating the methodology for the electrochemical measurements in the iEFC. Further, *ex-situ* ICP-OES measurements were conducted by M. Kwiatkowska. X. Hou supported experimentally the definition of the ICP-OES methodology. FTIR was performed and analyzed by J. Gallenberger (AG J. P. Hofmann). FTacV was conducted in collaboration with A. Simonov's group at Monash University. A. Simonov, D. Simondson, and S. Johnston provided intellectual contributions, supervision, and supported with project conceptualization. A. Simonov further edited and reviewed the parts of this chapter regarding FTacV (+ chapter 4.4.6.). A. K. Mechler contributed by support in project conceptualization and reviewing.

Chapter 5.3: The data presented in this chapter is based on the master thesis from J. Schmitt. Hence, he contributed with setting up the experimental methodology for the flex-E-cell experiments, experimental investigation, data analysis, data curation, and data visualization. My lead was in project conceptualization, data interpretation, supervision, and manuscript writing. C. Marcks equally contributed to the project conceptualization, data interpretation, and supervision. Further, I supported data analysis, curation, and visualization. A. K. Mechler contributed by support in project conceptualization and reviewing.

Throughout this work, **analytics** were performed by

- M. Kwiatkowska (*ex-situ* ICP-OES measurements of samples)

- J. Gallenberger (XPS, FTIR incl. data analysis, experimental description, and proof-reading of the manuscript)

The following **software** assisted this work

- ChatGPT3.5-4.o for literature research, rephrasing, shortening of self-written text, coding assistance
- GrammarlyPRO for spell and grammar checking, rephrasing/sentence untangling
- DeepL for translation

Python codes were generated with the help of R. Bendias (ICP-OES), D. Van Zeil (FTacV), and R. Z. Snitkoff-Sol (FTacV).

Parts of this thesis are published as

1. C. Gohlke, J. Kautz, N. Niederprüm, A. K. Mechler*, Electrochemical Modification of Nickel-based Electrodes for the Oxygen Evolution Reaction (OER)*, Conference Proceeding, EFCF, Luzern, Switzerland, 04-07.07.**2023**
    - Contributions: Clara Gohlke (lead in conceptualization, data curation, data analysis, experimental investigation, methodology, validation, visualization, writing; support in supervision), J. Kautz/N. Niederprüm (support in data curation, investigation, methodology, validation, review & editing), A. K. Mechler (support in conceptualization, lead in funding acquisition, project administration, supervision, review & editing)
2. C. Gohlke, J. Gallenberger, N. Niederprüm, H. Ingendae, J. Kautz, J. P. Hofmann, A. K. Mechler, Boosting the Oxygen Evolution Reaction Performance of Ni-Fe-Electrodes by Tailored Conditioning, *ChemElectroChem* **2024**, *11*, e202400318, DOI 10.1002/celc.202400318.
    - Contributions: Clara Gohlke (lead in conceptualization, data curation, data analysis, experimental investigation, methodology, validation, visualization, writing; support in supervision), J. Gallenberger (support in data analysis, experimental investigation [XPS measurements], review & editing), N. Niederprüm/J. Kautz (support in data curation, experimental investigation, methodology, validation, review & editing), H. Ingendae (support in data curation, experimental investigation, validation, review & editing), J.P. Hofmann (support in funding acquisition, project administration, supervision, review & editing), A. K. Mechler (support in conceptualization, lead in funding acquisition, project administration, supervision, review & editing)
3. C. Gohlke, C. Marcks, V. Seidl, M. Padligur, A. K. Mechler, *J. Electrochem. Soc.* **2025,** *172,* 126501, DOI 10.1149/1945-7111/ae215e
    - Contributions: Clara Gohlke (lead in conceptualization, design development, data interpretation, methodology, experimental investigation, manuscript drafting), C. Marcks (lead in simulations, data processing, data curation, and data visualization, support in conceptualization, experimental investigation), M. Padigur (support in simulation, review & editing), V. Seidl (review & editing), A. K. Mechler (support in conceptualization, lead in funding acquisition, project administration, supervision, review & editing)

In association with this thesis, the following articles were published:

- J. Gallenberger, C. Gohlke, M. Neumann, A. Mechler, J. P. Hofmann, Water Dissociation on NiOOH in Alkaline Water Electrolysis Improves with Increasing Alkali Metal Cation Size, *ChemSusChem* **2025**, 2402596.

- R. J. Seidenberg, C. Gohlke, R. Diebold, V. Seidl, A. K. Mechler, A. Mitsos, D. Bongartz, *ChemElectroChem* **2025**, *12*, e202500284.

In association with this thesis, the following article is in preparation:

1. C. Marcks, M. Chatwani, C. Gohlke, R. Diebold, A. Jain, T. Wagner, V. Seidl, N. Wöhrl, V. Vinayakumar, D. Segets, A. K. Mechler, Activation of Powder-Coated Electrodes for the Alkaline Oxygen Evolution Reaction

During the PhD, the following student theses were supervised, whose contributions are part of this work:

1. C. Marcks, Simulation and validation of an Electrochemical Flow Cell for in-situ activity studies of electrocatalytic reactions, 12/2021, Master thesis.
2. W. Turner, Methodology & Evaluation of the Oxygen Evolution Reaction in a 3D-Printed Electrochemical Flow Cell, 09/2021, Project thesis.
3. V. Schulte, Optimization of an Electrochemical Flow Cell for Activity Measurements of Electrocatalytic Reactions, 04/2022, Bachelor thesis.
4. N. Niederprüm, Method Development for an Electrochemical Flow Cell with Online Analytics, 09/2022, Bachelor thesis.
5. J. Kautz, Electrochemical Modification of Nickel-Iron Electrodes for Alkaline Water Electrolysis, 01/2023, Bachelor thesis
6. X. Hou, Development of methods for online ICP-OES measurement and purification of alkaline electrolytes, 07/2023, Project thesis.
7. H. Ingendae, Influence of Operating Conditions on Electrochemical Activation of NiFe based Electrodes for Alkaline Oxygen Evolution, 07/2023, Master thesis.
8. J. Schmitt, Scale-up of water electrolysis: electrode activation under industrial conditions, 01/2024, Master thesis.
9. R. Diebold, Powder based electrode activation for OER, 04/2024, Project thesis.

Abstract

The transition to renewable energy sources requires efficient and sustainable energy storage systems, such as green hydrogen produced by alkaline water electrolysis (AWE). To meet the rising demands, reducing cell potential and lowering manufacturing costs are crucial. The sluggish kinetics of the oxygen evolution reaction at the anode offers optimization potential by efficient electrocatalyst design. Here, electrochemical conditioning is a promising tool as it is easily applicable and versatile. Previously, electrochemical conditioning has already been used to study the oxide growth on Ni and Fe and to find a low-cost and highly active electrocatalyst from steel. However, the interplay of the conditioning and the Ni:Fe-ratio of the electrode, which is often stated as oxygen evolution reaction activity descriptor, is not fully understood yet. This raises the question of how activation, surface changes, and electrochemical conditioning parameters are correlated for a model electrode with a Ni:Fe ratio in the optimum regime, considering the influence of Fe from the electrolyte. Investigating this requires a suitable testing system. While reported analytical electrochemical flow cells with online downstream analysis (iEFCs) are valuable for studying activity and stability, their designs differ significantly from industrial setups, complicating knowledge transfer.

This work addresses these challenges by designing an iEFC with 1 cm^2 parallel electrodes to study the activity and stability of electrocatalysts simultaneously under industrially more relevant conditions. Simulation and experimental validation showed that the herein-designed iEFC enables a precise activity determination (Koutecký-Levich slope of >0.95) over a wide potential range and minimal dilution of reaction products with a restricted volume flow. The stability determination was proven by online monitoring of the electrode dissolution with peak smearing comparable to reported values. This advanced iEFC was used to study the electrochemical conditioning of Ni-(Fe)-based electrodes to enhance the oxygen evolution reaction performance. Systematic parameter variation revealed consistent activation trends across the tested materials, promising universal activation guidelines and suggesting a similar activation mechanism. These activation trends are suggested to result primarily from surface oxidation and enlargement, with Fe dissolution from Ni-Fe-based electrodes or rather Fe incorporation into Ni-based electrodes being linearly linked with the (hydr)oxide formation. This increased understanding of conditioning parameters, activation, and surface changes offers a framework for tailoring any (pre-)catalyst's conditioning to maximize performance or induce a certain surface change. Finally, the enduring activation efficacy during long-term electrolysis at 100 mA cm^{-2} and relevance to industrially more relevant conditions was demonstrated, *i.e.* 12 cm^2 electrodes, application of a separator, 30 wt% KOH, 80 °C, and higher loads. This makes the technology, including *in-situ* (re)activation of electrodes, more viable for large-scale applications, helping to reduce cell potential and optimize the anode manufacturing.

Overall, this work stresses the importance of conditioning in enhancing the OER performance and demonstrates how to improve the catalysts' effectiveness by tailoring oxides.

Zusammenfassung

Der Übergang zu erneuerbaren Energiequellen erfordert effiziente und nachhaltige Energiespeichersysteme, wie z. B. durch alkalische Wasserelektrolyse (AWE) erzeugten grünen Wasserstoff. Um der steigenden Nachfrage gerecht zu werden, sind die Reduzierung des Zellpotenzials und die Senkung der Herstellungskosten von entscheidender Bedeutung. Die träge Kinetik der Sauerstoffentwicklungsreaktion (OER) an der Anode bietet Potenzial für eine Optimierung durch ein effizientes Elektrokatalysatordesign. Hier ist die elektrochemische Konditionierung ein vielversprechendes Werkzeug, da sie leicht anwendbar und vielseitig ist. In der Vergangenheit wurde die elektrochemische Konditionierung bereits eingesetzt, um das Oxidwachstum auf Ni und Fe zu untersuchen und um einen kostengünstigen und hochaktiven Elektrokatalysator aus Stahl herzustellen. Das Zusammenspiel zwischen der Konditionierung und dem Ni:Fe-Verhältnis der Elektrode, das häufig als Aktivitätsdeskriptor für die Sauerstoffentwicklungsreaktion angegeben wird, ist jedoch noch nicht vollständig verstanden. Dies wirft die Frage auf, wie Aktivierung, Oberflächenveränderungen und elektrochemische Kondi-tionierungsparameter für eine Modellelektrode mit einem Ni:Fe-Verhältnis im optimalen Bereich korreliert sind. Dabei soll der Einfluss von Fe aus dem Elektrolyten berücksichtigt werden. Um dies zu untersuchen, ist ein geeignetes Testsystem erforderlich. Zwar sind analytische elektrochemische Durchflusszellen (EFCs) mit Online-Downstream-Analyse (iEFCs) für die Untersuchung von Aktivität und Stabilität wertvoll, doch unterscheiden sie sich erheblich von industriellen Anlagen, was den Wissenstransfer erschwert.

Die vorliegende Arbeit befasst sich mit diesen Herausforderungen, indem sie eine iEFC mit parallelen 1 cm^2-Elektroden entwickelt, um gleichzeitig die Aktivität und Stabilität von Elektrokatalysatoren unter industriell relevanteren Bedingungen zu untersuchen. Simulation und experimentelle Validierung haben gezeigt, dass die hier entworfene iEFC eine präzise Aktivitätsbestimmung (Koutecký-Levich Steigung von >0.95) über einen breiten Potenzialbereich und eine minimale Verdünnung der Reaktionsprodukte bei einem begrenzten Volumenstrom ermöglicht. Die Stabilitätsbestimmung wurde durch die Online-Überwachung der Elektrodenauflösung mit einer Spitzenverschmierung nachgewiesen, die mit Literaturwerten vergleichbar ist. Diese fortschrittliche iEFC wurde zur Untersuchung der elektrochemischen Konditionierung von Elektroden auf Ni-(Fe)-Basis verwendet, um die Leistung der Sauerstoffentwicklungsreaktion zu verbessern. Eine systematische Parametervariation ergab konsistente Aktivierungstrends bei allen getesteten Materialien, was universelle Aktivierungsrichtlinien verspricht und auf einen ähnlichen Aktivierungsmechanismus hindeutet. Es wird angenommen, dass diese Aktivierungstrends in erster Linie aus der Oberflächenoxidation und -vergrößerung resultieren, wobei die Fe-Auflösung aus Ni-Fe-basierten Elektroden bzw. der Fe-Einbau in Ni-basierte Elektroden linear mit der (Hydr)oxidbildung verbunden ist. Dieses bessere Verständnis der Konditionierungsparameter, der Aktivierung und der Oberflächenveränderungen bietet einen Rahmen für eine maßgeschneiderte Konditionierung eines beliebigen (Vor-)Katalysators, um dessen Leistung zu maximieren oder um eine bestimmte Oberflächenveränderung zu bewirken. Schließlich wurde die dauerhafte Wirksamkeit der Aktivierung während der Langzeitelektrolyse bei 100 mA cm^{-2} und die Relevanz für industriell relevantere Bedingungen nachgewiesen, d. h. 12 cm^2 Elektroden, Verwendung eines Separators, 30 Gew.-% KOH, 80 °C und höhere Belastungen. Dies macht die Technologie, einschließlich der *in-situ* (Re-) Aktivierung von Elektroden, für großtechnische Anwendungen praktikabler. Die elektrochemische Konditionierung hat so das Potential, das Zellpotenzial der alkalischen Wasserelektrolyse zu verringern und die Anodenherstellung zu optimieren.

Insgesamt unterstreicht diese Arbeit die Bedeutung der Konditionierung für die Verbesserung der OER-Leistung und zeigt, wie die Wirksamkeit der Katalysatoren durch maßgeschneiderte Oxide verbessert werden kann.

Glossary

Abbreviations

ac	Alternating current
ads	Adsorbed
aq	Aqueous
AWE	Alkaline water electrolysis
BW	Bandwidth
CE	Counter electrode
CF	Circular flow
CP	Chronopotentiometry
CV	Cyclic voltammetry
dc	Direct current
EDX	Energy Dispersive X-ray Spectroscopy
EFC	Electrochemical flow cell
EIS	Electrochemical impedance spectroscopy
EPDM	Ethylene propylene diene monomer rubber
eq.	Equation
FTacV	Fourier Transform alternating current Voltammetry
FT	Fourier Transform
FTIR	Fourier Transform Infrared Spectroscopy
GC	Glassy carbon
HER	Hydrogen evolution reaction
ICP-OES	Inductively Coupled Optical Emission Spectroscopy
iEFC	*In-situ* electrochemical flow cell for online electrolyte monitoring (by *e.g.* ICP-OES)
IFT	Inverse Fourier Transform
IL	Integration limit
KL	Koutecký-Levich
LSV	Linear sweep voltammetry
M	Metal

n.a.	Not applicable
O(*)	(Adsorbed) oxidized species
OER	Oxygen evolution reaction
OCP	Open circuit potential
PEEK	Polyether ether ketone
PP	Polypropylene
PTFE	Polytetrafluoroethylene
PVC	Polyvinylchloride
R(*)	(Adsorbed) reduced species
RE	Reference electrode
redox	Reduction-oxidation
ref.	Reference
RHE	Reversible hydrogen electrode
RT	Room temperature
SFC	Scanning flow cell
SEM	Scanning Electron Microscopy
SHE	Standard hydrogen electrode
SP	Single-pass
Temp.	Temperature
WE	Working electrode
XPS	X-ray photoelectron spectroscopy

Symbols

Symbol	Meaning	Unit
α	Charge transfer coefficient	-
a	1st Empirical parameter (saturation of oxide charge with number of cycles)	C
A	Electrode surface area	m^2
b	2nd Empirical parameter (saturation of oxide charge with number of cycles)	$cycle^{-1}$
B	Number of sine waves in FTacV (J in Python Code)	-
c	Concentration	$mol\ L^{-1} = M$
C_{dl}	Double layer capacitance	F
d	Diameter	m
D	Diffusion coefficient	$m^2\ s^{-1}$
E_F	Fermi energy	eV
E	Potential	V
$-\Delta E$	Electrochemical activation	V
η	Overpotential	V
f	Frequency	$s^{-1} = Hz$
F	Faraday constant	$A\ s\ mol^{-1}$
$\boldsymbol{F}$	Volume force of the system (**vector**)	N
f_s	Sampling frequency	$s^{-1} = Hz$
G	Quality parameter for the deviation of $i_{kin,sim}$ from $i_{kin,input}$	-
h	Planck constant	J s
$\boldsymbol{I}$	Unity matrix (**vector**)	-
I	Current	A
I_0	Exchange current	A
i	Current density	$A\ m^{-2}$
J	Species flux	$mol\ m^{-2}\ s^{-1}$
K	Volumetric homogeneous reaction rate	-

Symbol	Meaning	Unit
k_0	Reaction rate constant	s^{-1} (1^{st} order)
L	Length (of electrode/middle section in EFC)	m
μ_{dyn}	Dynamic fluid viscosity	Pa s
N_{CV}	Number of CV cycles	-
N	2^N = Data points in FTacV (N in Python code)	-
p	Pressure	Pa
Q	Oxide charge capacity	C
ρ	Fluid density	kg m^{-3}
R	Universal gas constant	J mol^{-1} K^{-1}
R_u	Uncompensated resistance	Ohm
S	Number of atoms (FTIR)	-
T	Temperature	K
t	Time	s
$\boldsymbol{u}$	Flow velocity field (**vector**)	m s^{-1}
u_0	Flow velocity (0: in the center of the channel)	m s^{-1}
v	Scan rate	V s^{-1}
z	Number of electrons exchanged in the reaction	-

Content

1. Introduction

Global warming urgently calls for a transition from fossil to renewable energy sources like wind, water, and solar power.[1,2] One of the biggest challenges is the time gap between the supply and demand of these renewable energy resources.[2,3] Thus, efficient energy conversion and storage systems are absolutely essential. One promising energy carrier is hydrogen, which can be sustainably produced by electrochemical water splitting into hydrogen and oxygen (see Figure 1.1).[4–6] The most mature electrochemical water splitting technology is the alkaline water electrolysis (AWE), which has been implemented for decades.[7] Compared to other electrochemical water splitting technologies, the advantage of the AWE is the possibility of using non-noble, earth-abundant electrode materials, enabling a more cost-effective and sustainable process.[6,8–10]

Nevertheless, large-scale hydrogen production is still hindered by the sluggish kinetics of the anodic oxygen evolution reaction (OER).[2,5] Currently, coated Ni electrodes according to the dimensionally stable anode approach are the state-of-the-art electrodes for the alkaline OER.[11,12] Further improvements in the reduction of the cell potential, enabling high performance and stability at high current densities, and cost reduction in the manufacturing process are, however, of great interest.[13–15] By achieving a realistic target of 50 mV cell potential reduction at 10 kA m^{-2}, the power consumption would drop by 2.5-3%, assuming a cell potential of 1.85 V.[16] Considering that power consumption is the largest cost contributor of the overall plant system with about 27%[14] and that immense amounts of electricity are required, this can have a significant impact. The potential of optimizing the electrode manufacturing becomes clear when considering that 50% of the overall AWE plant costs are due to the electrolyzer stack, from which the largest portion of 25% is due to the anode plus 8% for the pre-electrodes.[13,14] This makes it crucial to develop a highly efficient, stable, and cost-effective electrode for the OER.

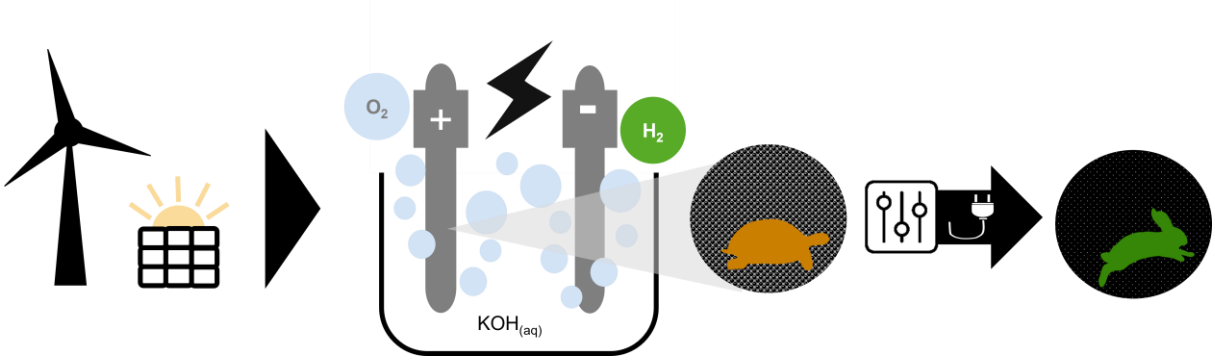

Figure 1.1. Schematic illustration of this thesis' approach to address one of the challenges of sustainable hydrogen production by AWE. The intermittency of renewable resources requires energy storage systems, such as green hydrogen production by AWE with aqueous (aq) KOH electrolyte. Electrochemical conditioning is one promising and cost-efficient design method for active OER catalysts to improve the limiting OER kinetics.

The research community has explored many different catalyst compositions, and among those, $NiFeO_xH_y$ is reported to be one of the most active alkaline OER catalysts.[17–22] Earlier, NiO_xH_y electrocatalysts were regarded as benchmark non-noble metal OER catalysts. Nowadays, it is, however, known that the high activity of these NiO_xH_y electrocatalysts is due to the incorporation of Fe from the electrolyte.[17–22] The optimum Fe content and active site are, however, still discussed. The optimum Fe content is reported to be between 15-60 wt%.[17–22]

These $NiFeO_xH_y$ can be synthesized by many different methods. For example, Ni-Fe layered double hydroxides can be produced by hydrothermal treatment,[23] precipitation method,[24] alcohothermal method,[25] and Ni-Fe-based oxides by evaporation induced self-assembly, hard templating, and dip-coating.[26] While promising activities have been reported for most of these syntheses, they often involve multiple steps, unfavorable process conditions such as high temperatures, complex ink-preparation, difficulty of scalability, and are resource intensive.

Irrespective of the synthesis method, the surface structure is the critical factor affecting catalytic activity. This surface cannot only be tuned by the synthesis but also by conditioning a (pre-)catalyst electrochemically (see Figure 1.1). Often untailored electrochemical conditioning is already used in addition to the existing synthesis procedure.[23–26] However, tailored conditioning of (pre-)catalysts or bulk metals could save cost- and labor-intensive catalyst synthesis steps. It can be simply added to existing preparation procedures to exploit the electrocatalyst's full potential or tailor a certain surface change. Further, it can substitute a certain preparation step, or it can be performed as a stand-alone technique with bulk metal electrodes. Since electrochemically conditioned electrodes do not require any post-treatment, this technique can be applied to activate and reactivate electrodes. This way the electrode lifetime could be prolonged. Further, electrochemical conditioning is a very versatile technique as process parameters such as conditioning parameters, electrolyte concentration, temperature, and additives can be adjusted. Going one step further, electrochemical conditioning might even be applicable *in-situ* in the electrolyzer as part of the ramp-up procedure, making the electrode manufacturing even simpler.

Previous works by primarily one research group have already systematically studied the effect of conditioning by cyclic voltammetry (CV) on the oxide growth of Ni and Fe. It was suggested that the oxide growth improves the electrode activity by enlarging the active surface area for the OER. These studies, however, only showed little spectroscopic evidence and did not consider the effect of Fe incorporation from the electrolyte or Fe dissolution at the electrodes.[12,27–29] As a different application of electrochemical conditioning, conditioned steel electrodes were recently explored as cost-efficient and highly active electrocatalysts. In this context, primarily constituent dissolution was suggested to cause the activation.[30–33] This dissolution behavior was proposed to be assessable by the Ni:Fe ratio. The lower the Ni:Fe ratio, the higher is supposedly the dissolution.[34,35] Summarizing, the studies presented on electrode conditioning concentrated on understanding the oxide growth on Ni and Fe and designing a steel-based electrocatalyst with high activity. Nonetheless, there is yet the need for a systematic correlation between electrode activation, analytically characterized surface changes, and electrochemical conditioning parameters for a model electrode with an optimal Ni:Fe ratio under consideration of Fe incorporation and dissolution.

To do so, a suitable system to analyze the activity and stability of the electrocatalysts is required. In the past few years, the combination of electrochemical flow cells (EFCs) with online downstream electrolyte analysis has become increasingly important in electrocatalysis, enabling simultaneous assessment of electrocatalytic activity and stability.[36–39] However, the reported EFCs, which have been used for this so far, are far from the conditions in industrial electrolyzers regarding channel and flow geometries, electrode size, and current distribution at the electrodes. Consequently, the knowledge obtained from these analytical EFCs requires careful reconsideration when translating it to industrial-scale processes. This stresses the need to develop an EFC, which can be linked to online electrolyte monitoring and with which the

activity of electrocatalysts can be precisely determined under industrially more relevant conditions.

These challenges are tackled in this work in three steps. First, an EFC is designed for online electrolyte monitoring and simultaneous precise activity determination at industrially more relevant conditions compared to previously reported EFCs in this field (*i.e.* 1 cm^2 planar parallel electrodes). With this EFC, the conditioning of Ni- and Ni-Fe-based electrodes with Ni:Fe ratios in the optimum regime (10-30 wt%) is systematically investigated by correlating the electrochemical conditioning parameters, surface changes, and activation. Lastly, electrochemical conditioning as an anode preparation technique is scaled up from 1 cm^2 to 12 cm^2 and tested as a proof-of-concept under industrially more relevant conditions (*i.e.* 12 cm^2, separator, 30 wt%, 80 °C) to get one step closer to industrial application. Overall, this work assesses the potential of electrochemical conditioning as an anode manufacturing technique for the AWE.

2. State of the Art

For the production of green hydrogen by AWE, electrocatalysts are required to maximize the OER performance. Therefore, the following chapter 2.1 explores how the activity of an electrocatalyst can be determined. In chapter 2.2, promising OER catalysts, such as Ni-, Fe-, Ni-Fe-, and steel-oxides, are evaluated.

2.1. Determining Electrocatalytic Activity

For many decades now, the rotating disk electrode (RDE) has been one of the standard tools to study electrocatalytic activity. Its major advantage is the highly controllable and homogeneous mass transport over the electrode. This results in a uniformly accessible electrode, where the reactant flux is the same at any point on the electrode. This is not only essential for controlled and homogenous mass transport of products and educts, but also of other additives and impurities, which might influence the reaction. It is, however, especially important when studying reactions, which become mass-transport-limited with increasing potential. This occurs *e.g.* when the reactant concentration is limited. On the contrary, the limitation by the reactants' mass transport is neglected for the alkaline OER since that is minimal due to the high availability of hydroxide ions. In the case of a mass-transport-limited reaction, the defined mass transport and the uniform accessibility of the RDE allow experimental determination as well as analytical estimation of the reaction kinetics in the mixed-kinetic-mass-transport-dominated regime.[38,40] For this, the Koutecký-Levich (KL) equation can be applied:[41]

$$\frac{1}{I} = \frac{1}{I_{\mathrm{kin}}} + \frac{1}{I_{\mathrm{lim}}} \tag{2.1}$$

with the overall current I, kinetic current I_{kin}, and mass-transport-limited current I_{lim}.

Apart from the controllable and uniform mass transport and the precise determination of the reduction-oxidation (redox) reaction kinetics, the RDE, however, shows certain disadvantages. Besides the complex and error-prone sample and cell preparation, the limitation to small electrode sizes, and incompatibility with industrially relevant conditions, a major drawback is its batch nature, which prevents integration with downstream online analysis.[6,38,40]

Online downstream analysis of the electrolyte becomes significantly essential when studying the electrode stability as it allows the monitoring of electrode dissolution. Thus, coupling EFCs with online downstream analysis of the electrolyte has been established as a tool in electrocatalysis to study simultaneously electrocatalytic activity and stability.[36–39] However, analyzing the reaction kinetics in EFCs according to the KL relation is more difficult due to the complex mass transport. There are many different approaches to describe convective mass transport problems in electrochemical reactors depending on the reactor and electrode design and the flow conditions. Detailed descriptions and derivations for classical convective mass transport problems can be found in the work from Pickett.[42] For a fully developed laminar flow with steady-state conditions, the average mass-transport-limited current I_{lim} over the electrode in an EFC with planar, parallel, short electrodes of finite width can be approximated for first-order reaction kinetics by equation (2.2):[42]

$$\bar{I}_{\mathrm{lim}} = w \cdot z \cdot F \cdot \mathrm{c_{el}} \cdot A \cdot D^{\frac{2}{3}} \cdot u_0^{\frac{1}{3}} \tag{2.2}$$

with electrons exchanged in the reaction *z*, the Faraday constant *F*, concentration of active species in electrolyte *c*, electrode surface area *A*, diffusion coefficient *D* of the reactive species, geometry-dependent constant *w*, and the fluid velocity u_0. Short electrodes refer to a small ratio of the electrode length in the flow direction to the distance between the electrodes. As a point of reference, a ratio of 10 is considered comparatively small.[42] The geometry constant for channel electrodes has been reported differently throughout literature.[43–45]

Plotting l_{lim} *vs.* $u_0^{1/3}$ for different fluid velocities will result in a linear correlation, from which *e.g.* the diffusion coefficient of the reactive species can be determined. This is in analogy to the Levich analysis for the RDE, where l_{lim} is plotted *vs*. the square root of the rotation speed. Thus, plotting l_{lim} *vs.* $u_0^{1/3}$ for different fluid velocities will herein be referred to as Levich analysis for EFCs. Note that equation (2.2) is only valid under the assumption of negligible axial mass transport in the direction of the flow, meaning l_{lim} is averaged over the electrode length. When considering the axial mass transport of the reactive species, a boundary layer forms, indicating a decreased reactant concentration compared to the electrolyte bulk due to axial mass transport. Due to the characteristic concentration gradient, this boundary layer will be referred to as the diffusion layer in the following. Imaging a small volume unit of reactants, the reactant concentration in this volume unit will deplete due to the consumption by the electrochemical reaction at the electrode while being transported along the electrode by convection. Thus, the boundary layer progressively grows along the electrode, approaching saturation, as can be seen in Figure 2.1. According to Fick's law, the species flux is antiproportional to the diffusion layer thickness. Hence, the corresponding limiting current density decreases first rapidly and then more slowly over the length of the electrode.[46]

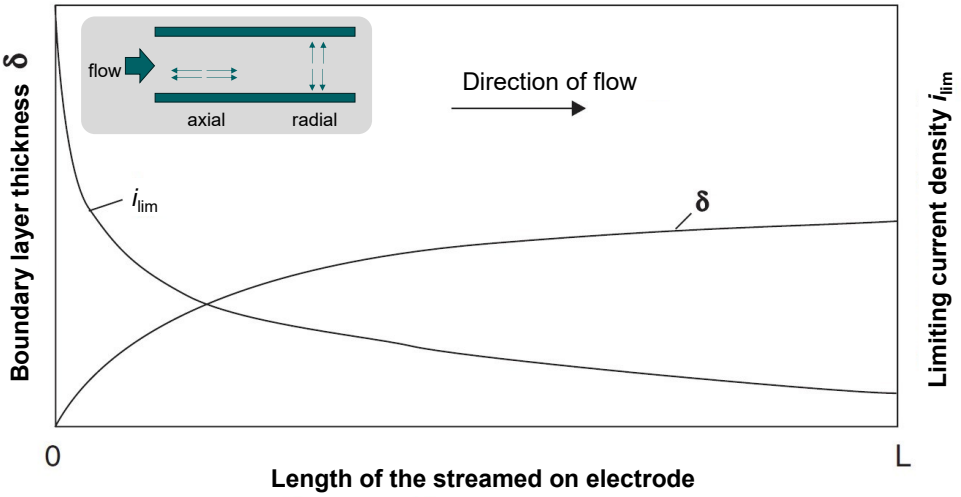

Figure 2.1. Dependence of the limiting current density and the boundary layer on the electrode geometry in the presence of laminar flow. [adapted from [46] with permission from John Wiley and Sons]

Even though an EFC does not feature a uniformly accessible electrode, Watanabe's group was the first to use the KL equation for an EFC.[47] In 2007, Engelhardt *et al*. also applied the KL equation to a tubular EFC with the working electrode (WE) mounted on the inner radius of the flow channel. They showed that the relation between the average current density and the limiting current precisely aligns with the KL relation for a one-step reaction of arbitrary order. This correlation was stated to be independent of the electrode length.[48] Later, Scherson *et al*. validated theoretically that the KL relation can be used with high precision for channel electrodes under certain conditions. They assumed a first-order heterogeneous electron

transfer, fixed cell geometry, electrolyte composition, and temperature. Under these conditions, the KL relation was demonstrated to be highly accurate, provided that the ratio of the first-order reaction rate constant k to the central fluid velocity u_0 is low (very small values of $k/u_0^{1/3}$). This corresponds to a slow redox reaction and a fast electrolyte flow. In Scherson's study, the precision of the KL relationship was defined as the slope of the KL plot ($1/I$ *vs*. $1/I_{lim}$), which equals one for uniformly accessible electrodes (see equation (eq.) (2.1)). Scherson *et al*. suggested introducing a multiplication factor of 0.93 (= 7% deviation from one) for channel electrodes with very small values of $k/u_0^{1/3}$. With higher values of $k/u_0^{1/3}$, the deviation from one is anticipated to rise. Such a higher ratio of $k/u_0^{1/3}$, due to *e.g.* a larger reaction rate, indicates that the diffusion limitation sets in earlier.[43]

As a different approach for combining the advantages of continuous flow and uniform accessibility of the electrode, other groups designed flow cells with a nearly uniform limiting current across the electrode. Examples are the wall-jet flow cell,[49] the flow-type scanning droplet cell microscope,[50] the scanning flow cell (SFC),[40] and a specialized V-shaped EFC.[37] Overall, these analytical EFCs feature very small electrodes (0.08-0.5 cm^2) and cell-specific electrolyte flow and positioning of the counter electrode (CE), which is typically not parallel to the WE.[40,50] These characteristics are in contrast to industrial electrolyzers for prominent electrosyntheses like the Chlor-Alkali[51] and water electrolysis.[52] Such electrolyzers consist of planar, parallel electrodes with a separator between the anode and cathode chamber and an electrolyte flow parallel to the electrode. The differences in electrolyte flow and cell geometry between the analytical EFCs and industrial electrolyzers can result in different mass transport to the electrode and dead zones. Thus, gas removal and accumulations of products, educts, or other additives might vary. This can not only influence product distribution but also electrode performance and stability. The cell-specific arrangement of CE and WE within analytical EFCs introduces an inhomogeneous current distribution at the WE, which changes the electrochemically active surface area and could induce inhomogeneous catalyst use and degradation. It becomes even more challenging when scaling up the electrodes. The larger the electrodes, the more pressure gradients, bubble curtains, or an increasing diffusion layer thickness along the electrode length become important.[46] Thus, when transferring knowledge gained in the analytical EFCs to an industrial scale, these analytical EFCs need to be questioned.

To sum up, while attempts to analytically describe the mass transport in different EFCs have been made, these EFCs were not combined with online downstream analysis. Alternatively, the flow cells that can be both analytically described and used with online downstream analysis are not representative of industrial conditions.

2.2. OER Catalysis

For the alkaline OER, a common activity descriptor is the (over-)potential at a given current density or *vice versa*. In order to enhance the OER activity, a highly active electrocatalyst is required. The state-of-the-art electrode for the alkaline OER is a coated Ni electrode based on the dimensionally stable anode concept.[2,5] It is usually prepared by thermal decomposition of precursor metal salts. A predetermined mix of metal salts in the desired stoichiometry is dissolved with a solvent. This paste is painted on a metal substrate, the solvent evaporates, and finally, the electrode is annealed at a given temperature. This procedure can be repeated until a sufficiently thick coating of 1-5 mg oxide per cm^2 is achieved. The annealing temperature

is very decisive for the electrocatalytic properties. The Tafel slope was reported to increase with increasing compactness of oxide, corresponding to a decreased OER performance.[12,27]

Despite this being an established process, there is significant interest in further decreasing the cell potential, ensuring durable performance at high current densities, and optimizing manufacturing costs.[13–15] The optimization potential becomes apparent when considering that enormous electricity amounts are required to meet the global H_2 demand by AWE, 27%[14] of the overall plant costs is due to the power consumption, and 12.5%[13,14] due to the anode incl. manufacturing.

Thus, a lot of research has been conducted in the field of electrocatalyst design. One of the most efficient catalysts for the alkaline OER is reported to be $NiFeO_xH_y$, achieving optimal performance with an Fe content between 15 and 60 wt%.[8,10,17–22] Among the various techniques to synthesize this highly active $NiFeO_xH_y$, electrochemical conditioning of (pre-)catalysts or bulk metals is a promising tool due to its easy applicability and versatility, as discussed in detail in the introduction (chapter 1). Hence, electrochemical conditioning could significantly reduce the complexity and expense of catalyst production for the OER anode.

As a first step toward understanding the electrochemical conditioning of Ni-Fe-based electrodes, the electrochemical surface processes of Ni and Fe in alkaline electrolytes and the interplay of Ni and Fe as OER catalysts are discussed in chapters 2.2.1-2.2.3. Chapter 2.2.4 elucidates the oxide formation during electrochemical conditioning of Ni and Fe and the behavior of the formed oxides in the OER. Lastly, chapter 2.2.5 summarizes the developments in the electrochemical conditioning of steel electrodes, giving a first perspective on how electrochemical conditioning can be used as an efficient and cost-effective synthesis method.

2.2.1. Electrochemical Processes on Ni

In this chapter, the surface electrochemistry of Ni in alkaline electrolytes is elucidated by examining the redox transformations that occur at different potentials. Figure 2.2 shows three CVs of a bulk Ni electrode in 0.5 M KOH, identifying the redox processes of Ni between –0.15-1.55 V *vs*. the reversible hydrogen electrode (RHE), recorded by Alsabet *et al*.[53] Scheme 2.1 presents the associated redox reactions according to Lyons *et al*.[29]

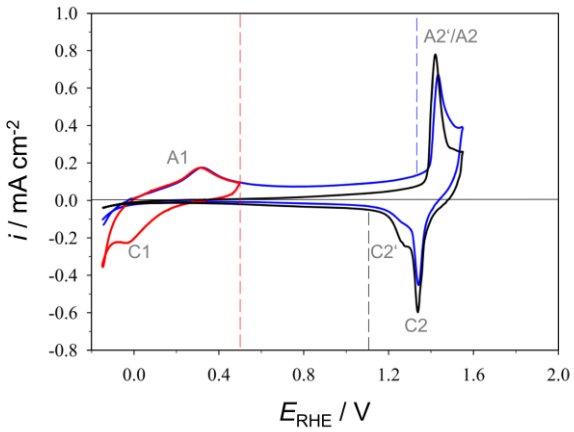

Figure 2.2. CV profiles (current density *i vs*. potential *E*) at 100 mV s^{-1} for Ni in 0.5 M KOH at 20 °C. The red (–0.15-0.50 V), blue (–0.15-1.55 V, 1st CV), and black (–0.15-1.55 V, 10th CV) profile corresponds to the region of reversible formation of α-$Ni(OH)_2$ (A1/C1), irreversible formation of β-$Ni(OH)_2$+NiO, and reversible formation of β-NiOOH (A2'/C2' or A2/C2), respectively. [adapted from ref. [53] with permission from Springer Nature]

In Figure 2.2, the red CV in the low potential regime between –0.15-0.5 V identifies the redox peaks A1 and C1, which can be attributed to the Ni(0)/Ni(II) redox couple. Lyons *et al*. suggested that a layer of adsorbed (ads) hydroxy is formed on Ni (reaction-eq. 1.1), which is oxidized to $Ni(OH)_2$ (reaction-eq. 1.2) and NiO (reaction-eq. 1.3), as seen in Scheme 2.1.[29] In contrast to this peak interpretation in Scheme 2.1 by Lyons *et al*., Alsabet *et al*. proposed that NiO forms irreversibly from $Ni(OH)_2$ at intermediate potentials between 0.5-1-3 V *vs*. RHE.[53] At higher potentials between 1.2-1.5 V, the black and the blue CV in Figure 2.2 show the peaks A2/A2' and C2/C2', representing the redox transition Ni(II)/Ni(III) from $Ni(OH)_2$ to NiOOH (reaction-eq. 2.1) according to Scheme 2.1.

A1/C1	$Ni + OH^-$	$Ni\text{-}OH_{(ads)} + e^-$	(1.1)
	$Ni\text{-}OH_{(ads)} + OH^-$	$Ni(OH)_2 + e^-$	(1.2)
	$Ni\text{-}OH_{(ads)} + OH^-$	$Ni\text{-}O + H_2O + e^-$	(1.3)
A2/C2 A2'/C2'	$Ni(OH)_2 + OH^-$	$NiOOH + H_2O + e^-$	(2.1)

Scheme 2.1. Ni redox reactions, showing the oxidation of Ni(0) to Ni(II), present as $Ni(OH)_2$ and NiO, and to Ni(III), present as NiOOH. Peak A1/C1: A layer of adsorbed (ads) hydroxy is formed on Ni, which is oxidized to $Ni(OH)_2$ and NiO. Peak A2/C2 or A2'/C2': $Ni(OH)_2$ is reversibly converted to NiOOH.[29]

The real interfacial (oxyhydr)oxide layer formation on Ni is, however, more complex as already indicated by the two redox peaks A2/C2 and A2'/C2'. $Ni(OH)_2$ and NiOOH can be present in different phases, α-$Ni(OH)_2$/γ-NiOOH or β-$Ni(OH)_2$/β-NiOOH. One prominent model for the changes between the different Ni phases was developed by Bode, which can be seen in Scheme 2.2.[19,54]

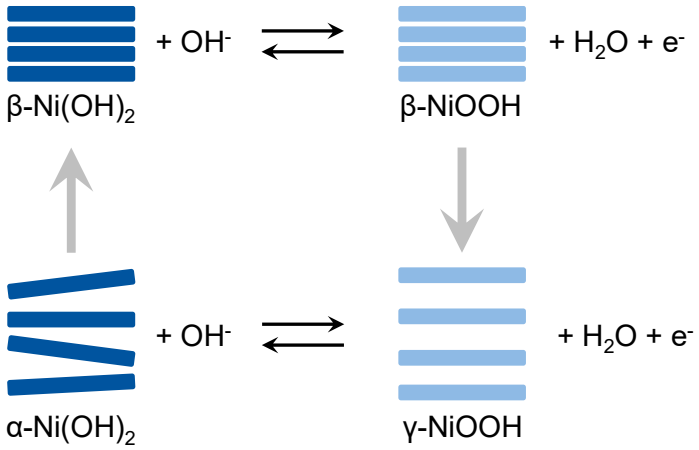

Scheme 2.2. Schematic Bode model for the phase changes of $Ni(OH)_2$ and NiOOH. α-$Ni(OH)_2$ converts irreversibly to β-$Ni(OH)_2$ by aging. α-$Ni(OH)_2$ is oxidized reversibly to γ-NiOOH and β-$Ni(OH)_2$ to β-NiOOH at the Ni(II)/Ni(III) redox transition. By overcharging, β-NiOOH can be converted to γ-NiOOH.[53,54]

Starting from Ni, α-$Ni(OH)_2$ is formed when oxidizing Ni mildly and β-$Ni(OH)_2$ at moderate anodization, according to Alsabet *et al*.[55] The Bode model in Scheme 2.2 illustrates that the amorphous, hydrous α-$Ni(OH)_2$ can convert irreversibly to crystalline, anhydrous β-$Ni(OH)_2$, *e.g*. by aging. α-$Ni(OH)_2$ is oxidized reversibly to γ-NiOOH and β-$Ni(OH)_2$ to β-NiOOH at the Ni(II)/Ni(III) redox transition. Lyons *et al*. suggested that the peaks A2/C2 correspond to the α-$Ni(OH)_2$/γ-NiOOH transition and A2'/C2' to β-$Ni(OH)_2$/β-NiOOH.[29] β-NiOOH can be converted to γ-NiOOH by overcharging. While this model is widely accepted, the questions of how γ-

NiOOH forms and whether it serves as the active phase are still heavily discussed.[19,54,56] For example, Steimecke *et al*.[17] and Zhou *et al*.[57] proposed β-NiOOH as the active phase during the alkaline OER, while Angeles-Olvera *et al*.[56] suggested γ-NiOOH.

Based on this, Figure 2.2 can now be explained in detail according to Alsabet *et al*.[53] The red (–0.15-0.50 V) CV corresponds supposedly to the reversible formation of α-$Ni(OH)_2$. During the first CV between –0.15-1.55 V (blue CV), α-$Ni(OH)_2$ is irreversibly converted to NiO and β-$Ni(OH)_2$, resulting in a layered structure of Ni, NiO, and β-$Ni(OH)_2$. The black CV (–0.15-1.55 V, 10th CV) indicates the reversible transformation between β-$Ni(OH)_2$ and β-NiOOH.[53,55] When analyzing CVs of Ni, it needs to be considered that the A1/C1 redox features can be superimposed on a background current associated with a combination of adsorbed hydrogen oxidation and the formation of a layer of adsorbed hydroxyl species.[29,58]

These redox features change under potential cycling depending on the potential window, scan rate, temperature, and KOH concentration. Different groups have reported systematic variations of one or multiple parameter(s).[29,53,55,58] An overview of the redox features of Ni and their dependencies on repetitive cycling, scan rate, pH, and temperature variation can be seen in Table 2.1.

Alsabet *et al*. reported that upon cycling Ni between –0.15-1.55 V, the α-$Ni(OH)_2$ formation A1 and reduction C1 disappear with increasing transformation of α- to β-$Ni(OH)_2$.[53] In contrast to this, Lyons *et al*. showed that the α-$Ni(OH)_2$ formation is still visible in CV for a hydrous NiOOH thin film electrode on Ni (grown in 1 M NaOH, –0.53-1.6 V, 40 mV s^{-1}), while the reduction is not.[29] Both stated that the $Ni(OH)_2$ reduction peak C1 is only visible if the potential is reversed well below the OER onset potential (< 0.7 V *vs*. RHE), which restricts the phase transition of α-$Ni(OH)_2$.[29,55] Lyons *et al*. suggested that the A1/C1 redox features could also be superimposed on a background current associated with a combination of adsorbed hydrogen oxidation and the formation of a layer of adsorbed hydroxyl species, making a distinct peak detection difficult.[29] Regarding the Ni(II)/Ni(III) transition at higher potentials, the two oxidation peaks A2’ and A2 are reported to merge with an increasing number of cycles.[29] When increasing the scan rate, the peak currents of the Ni(II)/Ni(III) redox reaction increase, and the anodic peak shifts to higher and the cathodic to lower potentials.[53] Different peak splitting and merging behavior was reported for the Ni(II)/Ni(III) transition depending on the scan rate. While Alsabet *et al*.[53] reported one Ni(II)/Ni(III) oxidation peak for scan rates between 2-500 mV s^{-1}, Burke *et al*.[58] stated two peaks to be observable at a scan rate of 2-10 mV s^{-1}, which merge for higher scan rates (>10 mV s^{-1}). Both identified two reduction peaks for scan rates between 2-50 mV s^{-1}.[53,58] According to Alsabet *et al*.,[53] these reduction peaks merge for scan rates larger than 100 mV s^{-1}. The influence of an increasing temperature on the Ni(II)/Ni(III) redox peaks was also studied by Alsabet *et al*. For these investigations, a RHE was placed in the same electrolyte. With increasing temperature between 8 to 40 °C, the anodic and cathodic peaks shift toward lower potentials *vs*. RHE, and the magnitude of both peaks increases. The increase in peak intensity and peak shift of the anodic peak is reported to be more intense. It needs to be noted that these observations probably partly result from the Ni(II)/Ni(III) oxidation being superimposed with the OER.[53] The redox reactions of Ni also show a pH dependence. The $Ni(OH)_2$ formation A1 peak shifts with -13 mV pH^{-1} at 80 mV s^{-1} *vs*. RHE, with the shift being scan rate dependent.[58] The $Ni(OH)_2$ reduction C1 peak does not vary with the pH *vs*. RHE.[29,58] The anhydrous A2’/C2’ redox peaks exhibit a potential shift of –59 mV pH^{-1} and the

hydrous A2/C2 of –88 mV pH^{-1} at 25 °C *vs*. a pH-independent reference electrode (RE), such as the standard hydrogen electrode (SHE).[29]

Concluding, the redox couple Ni(0)/α-$Ni(OH)_2$ is reported between –0.15-0.5 V, and $Ni(OH)_2$/NiOOH between 1.2-1.5 V *vs*. RHE. For the $Ni(OH)_2$/NiOOH redox couple, it needs to be differentiated between the α-$Ni(OH)_2$/γ-NiOOH and β-$Ni(OH)_2$/β-NiOOH transition. According to the Bode model, α-$Ni(OH)_2$ ages to β-$Ni(OH)_2$, and γ-NiOOH can convert to β-NiOOH by overcharging. These redox features change with the number of performed CVs, the applied scan rate, pH, and temperature. However, the results from the different groups are partly contradictory, suggesting that the Ni redox peaks depend strongly on the interplay of the process conditions. Despite these partly contradictory results, they still contribute to a better understanding of the Ni redox behavior, based on which CVs of Ni or Ni-containing electrocatalysts can be interpreted.

Table 2.1. Redox reactions of Ni and their dependencies on repetitive cycling, scan rate, pH, and temperature (Temp.) variation.

Identified peaks	**A1**	**C1**	**A2'**	**A2**	**C2'**	**C2**
E_{RHE} **/ V**	–0.15-0.5	–0.15-0.5	1.2-1.5	1.2-1.5	1.2-1.5	1.2-1.5
Reaction	Ni/$Ni(OH)_2$[29,55]	$Ni(OH)_2$/Ni[29, 55]	β-$Ni(OH)_2$/ β -NiOOH[29]	α-$Ni(OH)_2$/ γ-NiOOH[29]	β-NiOOH/ β-$Ni(OH)_2$[29]	γ-NiOOH/ α-$Ni(OH)_2$[29]
Cycling	visible[29] disappears[55]	Only visible if E is reversed < 0.7 V [29,55]	A2' and A2 merge[29]		n/a	n/a
Scan rate	Scan rate increases: shift to higher potentials[58]	Constant potential[58]	Scan rate increases: Magnitude increases, shifts to higher potentials[53] Merge at >10 mV s^{-1}[58]		Scan rate increases: Magnitude increases, shifts to lower potentials[53] Merge at > 100 mV s^{-1}[53,58]	
pH	–13 mV pH^{-1} at 80 mV s^{-1} *vs*. RHE [58]	Constant *vs*. RHE [29,58]	–59 mV pH^{-1} *vs*. SHE[29]	–88 mV pH^{-1} *vs*. SHE[29]	–59 mV pH^{-1} *vs*. SHE[29]	–88 mV pH^{-1} *vs*. SHE[29]
Temp.	n/a	n/a	Temp. increases: shift to lower potentials and increase in magnitude (*vs*. RHE in the same electrolyte)[53]		Temp. increases: shift to lower potentials and increase in magnitude (*vs*. RHE in the same electrolyte)[53]	

2.2.2. Electrochemical Processes on Fe

The following section explores the surface electrochemistry of Fe in alkaline electrolytes by examining the redox transformations occurring at different potentials. Figure 2.3 shows a series of CVs (–1.42-0.68 V *vs*. Hg/HgO [–0.5-1.6 V *vs*. RHE], 40 mV s^{-1}) forming a hydrous Fe (oxyhydr)oxide film in 1 M NaOH.[59] Various groups have reported and assigned the redox features in Figure 2.3. Scheme 2.3 indicates the peak assignment to the respective redox reactions, according to Lyons *et al*.[28,59,60]

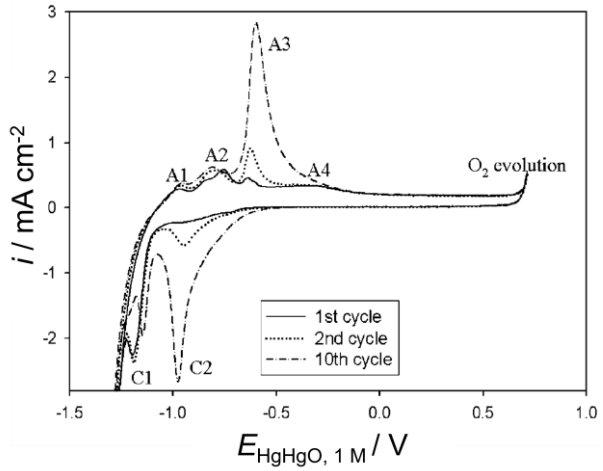

Figure 2.3. 1st, 2nd, and 10th CV (–1.42-0.68 V *vs*. Hg/HgO, 40 mV s^{-1}) of Fe in 1 M NaOH at 25 °C, showing the redox transitions from Fe(0) to Fe(II) and from Fe(II) to Fe(III). [adapted from ref. [59] with permission from Royal Society of Chemistry]

Figure 2.3 shows that the initially seen peak fine structure during the first CV changes drastically within the first 10 CVs. Peak A1 is reported to arise from the deposition of a layer of adsorbed hydroxy species (reaction-eq. 1.2) along with the electrochemical displacement of adsorbed hydrogen (reaction-eq. 1.1), as seen in Scheme 2.3. The oxidation to $Fe(OH)_2$ (reaction-eq. 2.1) or FeO (reaction-eq. 2.2) may be attributed to peak A2. In simplified terms, the redox peaks A3/C2 corresponds to the Fe(II)/Fe(III) transformation (reaction-eq. 3.1). More specifically, the peak couple A3/C2 exhibits a potential-pH shift of –88 mV pH^{-1} at 25 °C, which deviates from the SHE's potential-pH shift of -59 mV pH^{-1}. Hence, the Fe(II)/Fe(III) transition is suggested to occur in a polymeric micro-dispersed hydrous oxide layer. This hydrous oxide layer possibly forms by hydration of the outer layers of FeO and $Fe(OH)_2$. Peak A4 is suggested to relate to the oxidation of Fe(II) to Fe(III) in the inner oxide layer region closer to the metal surface. The resulting oxidation products might be the anhydrous phases of Fe_2O_3, Fe_3O_4, or FeOOH. The reduction of the compact, anhydrous inner oxide layer might correspond to the reductive peak C1 (reaction-eq. 4.1), as indicated in Scheme 2.3.[59]

A1	$Fe\text{-}H_{(ads)}$	$\longrightarrow$	$Fe + H^+ + e^-$	(1.1)
	$Fe + OH^-$	$\longrightarrow$	$Fe\text{-}OH_{(ads)} + e^-$	(1.2)
A2	$Fe\text{-}OH_{(ads)} + OH^-$	$\longrightarrow$	$Fe(OH)_2 + e^-$	(2.1)
	$Fe\text{-}OH_{(ads)} + OH^-$	$\longrightarrow$	$FeO + H_2O + e^-$	(2.2)
A3/C2	$Fe(OH)_2 + OH^-$	$\rightleftharpoons$	$FeOOH + H_2O + e^-$	(3.1)
C1	$FeO \cdot FeOOH + H_2O + 3\ e^-$	$\longrightarrow$	$Fe + FeO_2^{2-} + H_2O + OH^-$	(4.1)

Scheme 2.3. Fe redox reactions, showing the oxidation of Fe(0) to Fe(II), present as $Fe(OH)_2$ and FeO, and Fe(III), present as FeOOH. Peak A1: Hydroxy layer formation on Fe ($Fe\text{-}OH_{(ads)}$) and electrochemical displacement of adsorbed hydrogen. Peak A2: Oxidation of $Fe\text{-}OH_{(ads)}$ to $Fe(OH)_2$ or FeO. Peak A3/C2: Reversible conversion of $Fe(OH)_2$ to FeOOH. Peak C1: Reduction of the compact, anhydrous inner oxide layer.[28,59,60]

For a multicycled Fe electrode (–0.5 to 1.25 V *vs*. RHE, 0.35 V s^{-1}, 30 cycles, 1 M NaOH, 25 °C), these redox features change depending on the cycling conditions. The magnitude of the anodic and cathodic peak potentials and currents increases linearly with the scan rate.

With increasing temperature, the peak potentials decrease linearly except for peak C1. With increasing pH, the peak potentials of A3 and C2 decrease linearly, the peak potential of C1 increases, and the others remain constant. As RE, a RHE in the same electrolyte and compartment was applied for these studies. The effect of scan rate, temperature, and pH on peak position and current can be read in detail in the works by Lyons *et al*.[59,60] After cycling in an alkaline electrolyte, the grown Fe (oxy)hydroxide films feature different colors depending on their thickness. Thin films are transparent in their reduced and green-yellow in their oxidized form. Color changes from the reduced to the oxidized form are visible when scanning the potential up and down with a scan rate of up to 4 V s^{-1}. Thick films show a yellow-brown color in their oxidized state, and a color change can only be seen at a very low scan rate of 3 mV s^{-1}.[60]

In conclusion, the Fe redox reactions from Fe(0) to Fe(II) and *vice versa* occur between –0.5-0.9 V *vs*. RHE in 1 M NaOH, with a peak fine structure visible in the 1st CV, but disappearing within the first 10 CVs. The redox features of a multicycled Fe electrode are sensitive to the cycling conditions, such as scan rate, temperature, and pH. Based on this, CVs of Fe or Fe-containing electrocatalysts can be assessed.

2.2.3. Ni-Fe Catalysts

The highly OER-active $NiFeO_xH_y$ catalysts trace their development back to NiO_xH_y electrocatalysts, which were previously regarded as the benchmark non-noble metal catalyst for the OER. Today, it is recognized that the incorporation of Fe from the alkaline electrolyte into the NiO_xH_y electrocatalysts leads to the formation of $NiFeO_xH_y$, which is responsible for the superior activity.[8,10,17–22,61–67]

Fe is incorporated into Ni-based materials during aging with and without applied current or potential but is significantly enhanced during electrochemical conditioning.[19,61] Klaus *et al*. reported that aging of $Ni(OH)_2$ films without electrochemical conditioning in unpurified 1 M KOH (≤0.66 ppm Fe) results in a logarithmic Fe incorporation from the electrolyte with time. After 38 days, a maximum Fe content of 26% at the surface was measured by X-ray photoelectron spectroscopy. The optimum activity was reached after five days of aging with an Fe content of 15% and a potential reduction of about 50-70 mV at 10 mA cm^{-2} (overpotential of 280 mV). The authors compared this aging process in an Fe-containing electrolyte to aging in an Fe-free electrolyte. In the Fe-free electrolyte, they observed a degradation of the $Ni(OH)_2$ films' catalytic OER performance over time (initial overpotential of 529 mV at 10 mA cm^{-2}). Comparing the aging in Fe-containing and Fe-free electrolyte, it must be noted that the much more significant activity gap of about 150 mV between $Ni(OH)_2$ in Fe-free and Fe-containing electrolyte already existed before aging.[19] This indicates that the OER activity is defined by the presence of Fe in the electrolyte and is only slightly influenced by the aging process. In supplement to this, Trotochaud *et al*. observed that the $Ni(OH)_2$ phase in Fe-containing and Fe-free electrolytes ages similarly, *i.e*. transforms from α-$Ni(OH)_2$ to β-$Ni(OH)_2$.[61]

Regarding Fe incorporation from the electrolyte by electrochemical conditioning, Kuai *et al*. reported that the Fe incorporation during chronoamperometry is much greater at OER potentials than at lower potentials (1.6 *vs*. 1.3 V).[62] Son *et al*. further showed that Fe incorporation into NiO_xH_y layers is higher by CV (1.1-1.63 V *vs*. RHE for more than 1000 cycles until constant OER activity) compared to chronopotentiometry (CP) (5 mA cm^{-2} for 24 h).[63]

Combining the results from Son *et al*. and Kuai *et al*. indicates that while Fe incorporation is superior at OER potentials compared to lower potentials, cycling to lower potentials seems essential for an efficient Fe incorporation. When cycling different Ni-based pre-catalysts in Fe-containing electrolyte, Mattinen *et al.* stated that the amount of Fe uptake in the catalyst film is strongly correlated with the catalysts' amount of $Ni(OH)_2$.[68]

This *in-situ* Fe incorporation into NiO_xH_y catalysts during aging or electrochemical conditioning in alkaline electrolytes produces $NiFeO_xH_y$, which represents an alternative synthesis route to *ex-situ* techniques. Regardless of the specific synthesis methods used, the activities of these $NiFeO_xH_y$ catalysts were reported to be consistent when compared at the same Fe content.[20,64] However, a broad range for the optimum Fe content is reported, covering 15 wt%,[17] 20-25 wt%,[18–20] ≤33 at%,[22] 20-40%,[65] 25-50%,[66] 25-50 at%,[67] and 40-60 at%.[21] In contrast to the activities of $NiFeO_xH_y$ being consistent regardless of the synthesis method, the electrochemical behavior, particularly the Ni(II)/Ni(III) redox peaks, varies depending on the synthesis method.[64] Still, it was repeatedly demonstrated that increasing the Fe content in the electrode results in a shift of the Ni(II)/Ni(III) redox peaks to higher potentials. This was often interpreted as a suppressed Ni oxidation or dissolution.[61,67,69]

The Ni(II)/Ni(III) redox peak behavior during *in-situ* Fe incorporation in $Ni(OH)_2$ films is illustrated in Figure 2.4 for the study from Stevens *et al*. They reported CV cycling of an electrolyte permeable $Ni(OH)_2$ film (cycles 0-4: 0-0.85 V *vs*. Hg/HgO [0.924-1.774 V *vs*. RHE], 10 mV s^{-1}, Fe-free 1 M KOH; cycles > 4: 0.2-0.7 V *vs*. Hg/HgO [1.124-1.624 V *vs*. RHE], 10 mV s^{-1}) in an Fe-free (Figure 2.4a) and Fe-containing (Figure 2.4b) electrolyte.[64]

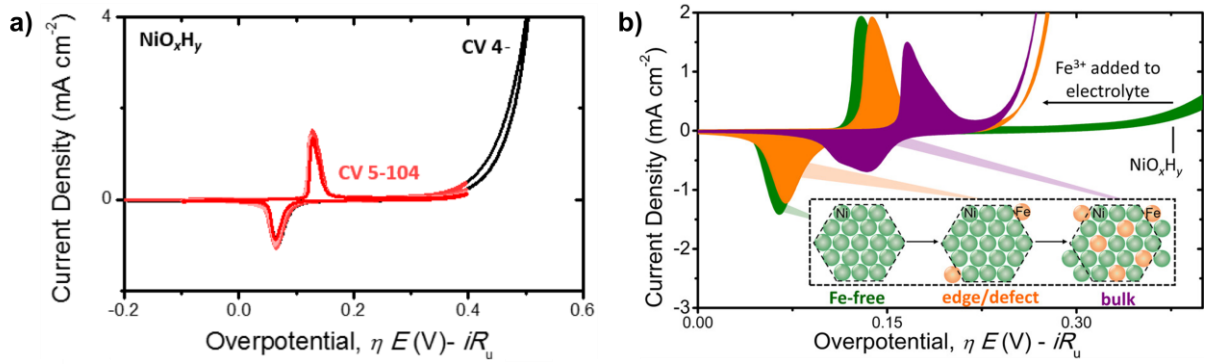

Figure 2.4. CV illustrating the influence of Fe incorporation from the electrolyte into NiO_xH_y on the Ni(II)/Ni(III) redox peak and the OER activity. a) CV (10 mV s^{-1}) of NiO_xH_y in Fe-free 1 M KOH. b) NiO_xH_y cycled first in Fe-free 1 M KOH (green), which is then spiked with 1 mM $Fe(NO_3)_3$ (orange, purple). The inset shows how Fe could potentially be incorporated during cycling. [reprinted from ref. [64] with permission from American Chemical Society]

Cycling NiO_xH_y in Fe-free 1 M KOH, the anodic peak potential shifted within the first four CVs to higher potentials by 12-15 mV and the peak area decreased by 2-5%. Figure 2.4a shows that for cycles 5-104, the oxidative Ni(II)/Ni(III) peak did not significantly shift in potential or change in peak area anymore. The OER activity decreased significantly. In Figure 2.4b, one can see that $Ni(OH)_2$ was first cycled in Fe-free electrolyte (green CV), which was then spiked with 1 mM Fe(III) (orange, purple CV). The comparison of the green and orange CV demonstrates that spiking the electrolyte with 1 mM Fe(III) resulted in an immediate 130-150 mV decrease in the OER potential but no significant change of the Ni(II)/Ni(III) peaks. After two cycles in the spiked electrolyte, the Fe content of the $Ni(OH)_2$ film increased to 11%. Upon cycling in the Fe-containing electrolyte, the oxidative and reductive Ni(II)/Ni(III) peaks shifted to higher potentials and decreased in intensity, as indicated by the comparison of the orange

and purple CV. After 100 cycles, the oxidative peak potential was shifted to higher potentials by 30 mV, the oxidative peak area was decreased by 30%, a second reduction peak was visible, and the Fe content was increased to 24%. These changes in the Ni(II)/Ni(III) peak behavior were not reflected in the activity increase, which was minimal compared to the initial potential drop after Fe(III)-spiking of the electrolyte. Stevens *et al*. explained this by an initial Fe incorporation at easily accessible edge/defect sites, enhancing the activity, as illustrated in the inset in Figure 2.4. The subsequent rearrangement and Fe incorporation into the NiO_xH_y bulk were suggested to have only a minor influence on the activity.[64]

Similar results were reported by Klaus *et al*. and Trotochaud *et al*., who investigated the aging of $Ni(OH)_2$[19,61] and Ni-(Fe)-O_xH_y[61] films in purified and unpurified 1 M KOH without applying electrochemical conditioning. Aging a $Ni(OH)_2$ film in an Fe-free electrolyte resulted in a decline in OER activity, a shift of the oxidative Ni(II)/Ni(III) peak potential to higher values (by 40 mV,[19] 5 mV[61]), and a reduction in the oxidative Ni(II)/Ni(III) peak intensity. For an Fe-containing electrolyte, the OER activity increased with aging, and the oxidative Ni(II)/Ni(III) peak potential was shifted to higher potentials (by 70 mV,[19] 27 mV[61]) and its intensity first decreased and then increased. These studies support the hypothesis from Stevens *et al*. that the differentiation between the activation and deactivation of NiO_xH_y in an Fe-containing and Fe-free electrolyte is not distinctly represented in the Ni(II)/Ni(III) redox peak behavior.

While it is agreed that Fe incorporation into NiO_xH_y structures enhances the OER activity, the active site of these $NiFeO_xH_y$ catalysts is still heavily discussed. Burke *et al*. were among the first to examine the role of Fe in NiOOH structures, and they proposed that Fe is the active site and $Ni(OH)_2$ serves as a stabilizing conductive support. The NiOOH phase supposedly shows a high surface area and allows nearly every Ni cation to be accessible. The Fe sites are suggested to be activated and stabilized from dissolution due to the electronic interaction between Ni and Fe.[10] Louie and coworkers identified Ni as the active site, with Fe lowering the oxidation state of Ni to a more favorable one (from Ni^{3+} to Ni^{2+},[57] from the average oxidation state $Ni^{\sim+3.5}$ to $Ni^{\sim+2.5}$).[67] A synergetic effect of Ni and Fe *via* the Mars-van-Krevelen mechanism for the OER at O-bridges Fe-Ni moieties was hypothesized by Dionigi *et al*.[70]

Regarding the stability of the $NiFeO_xH_y$ catalysts, a few groups stated that those are not stable in Fe-free 1 M KOH,[71–73] while others reported the opposite.[61] Kuai *et al*. suggested that a dynamic Fe exchange between catalyst and electrolyte is required for an active and stable OER performance.[62] Recently, dynamically stable Fe active sites, which result from dissolution and redeposition at the host/electrolyte interface, were proposed as a descriptor for OER activity and stability.[72] The authors suggested that Fe from the electrolyte is deposited and redissolved over a MO_xH_y host. In their study, the OER activity increased linearly with Fe coverage until maximum surface coverage was reached for Fe-Ni-O_xH_y and Fe-Co-O_xH_y. For each surface, there is supposedly a unique Fe saturation coverage. Fe surface coverage was adjusted and sustained by varying the initial Fe(III) concentration of the KOH electrolyte.[72] Feng *et al*. found that this dynamically stable Fe equilibrium could not be maintained for Ni-Fe layer double hydroxides during long-term OER operation by only initially adjusting the electrolyte's Fe(III) concentration. They postulated that the Fe redeposition is too ineffective at the OER operating potentials (< 1.6 V to obtain 10 mA cm^{-2}) compared to the Fe dissolution. Thus, they introduced Co(II) into the Ni-Fe layer double hydroxide lattice and intercalated borate to promote the stability of the Fe-dissolution-redeposition-equilibrium.[73]

To sum up, all these findings demonstrate that a lot is already known about $NiFeO_xH_y$ as an electrocatalyst for the OER and about Fe incorporation into NiO_xH_y materials from the alkaline electrolyte. Still, many of these topics are heavily discussed, and open questions remain. For example, the interplay of Fe incorporation and the Ni (hydr)oxide formation has not been fully evaluated yet.

2.2.4. Oxide Formation on Ni and Fe during Electrochemical Conditioning

In the class of oxides as OER catalysts, anhydrous and hydrous oxides can be differentiated. Anhydrous oxides typically refer to compact metal-oxygen materials with a rigid network of polar covalent bonds, where oxygen is present as a bridging species between metal cations (see Figure 2.5). Examples are $NiCo_2O_4$, Co_3O_4, and RuO_2 as rutile, perovskite, or spinel structures. Ionic transport is difficult, but electronic conductivity is comparably high. As a coating on a support, these are state-of-the-art alkaline OER catalysts.[12] During the AWE operation, these anhydrous oxides turn into hydrous oxides at the surface.

Hydrous oxides refer to a hydrated, dispersed material with a polymeric character, where oxygen is present not just as bridging species but also as O^-, OH^-, and H_2O (see Figure 2.5). It contains trapped and loosely bound water and electrolyte species. The boundary between solid and aqueous phases is poorly defined, and ionic charge percolation proceeds comparatively quickly. The hydrous oxide layer is reportedly amorphous and prone to rearrangement. One of the most straightforward preparation techniques is the direct anodization of a metal in an aqueous electrolyte by constant polarization or potential cycling.[12,27]

In 1981, Burke and O'Sullivan introduced the duplex layer model to describe oxide films formed on metal surfaces during anodization, as illustrated in Figure 2.5.[27]

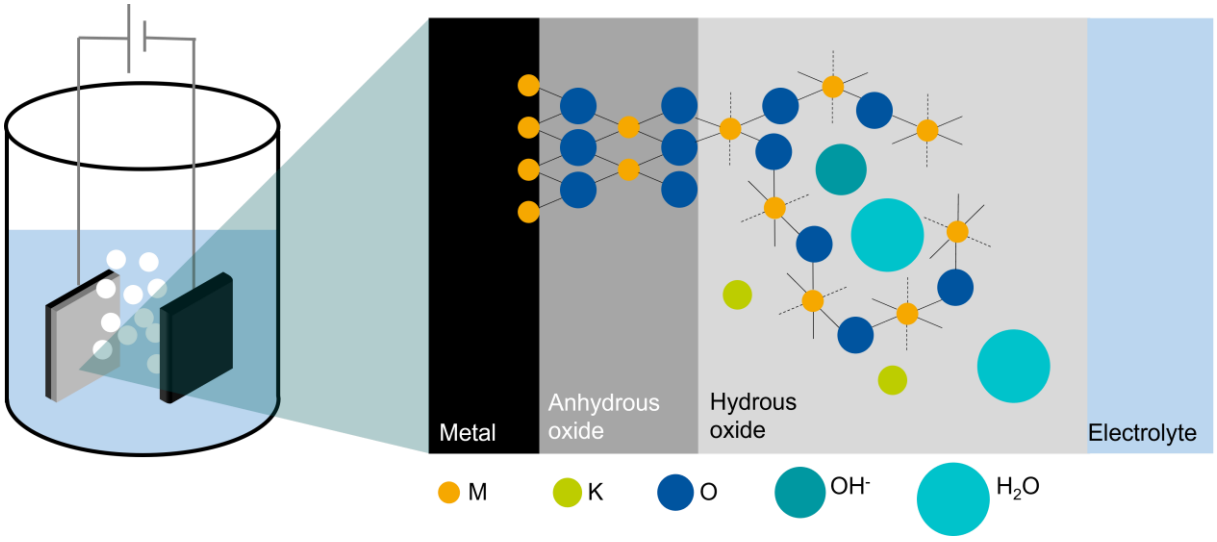

Figure 2.5. Schematic representation of the metal(oxide)/electrolyte interface on metals (M) according to the duplex layer model from Burke and O'Sullivan.[27]

Here, the metal is covered by a thin (1-5 layers), anhydrous, inner oxide layer and an outer hydrous oxide layer, which is extensively hydrated with both bound and trapped water.[27] The capacity of the electrochemical double layer remains relatively unchanged during the growth of the hydrous film due to the absence of a well-defined double layer in the hydrous phase as

the aqueous phase permeates it at the molecular level. Therefore, the major potential drop is also assumed to occur at the outer surface of the compact film.[27,28]

Regarding synthesizing this hydrous oxide layer by anodization, Son *et al*. compared the anodization of Ni by constant polarization and potential cycling. The authors demonstrated that CV conditioning results in a higher degree of oxidation and, thus, in thicker NiO_xH_y layers, which show an increased OER activity.[63] This was attributed to the fact that at constant current conditions, further oxidation is limited by restricted ion movement through the anhydrous oxide layer. For CV, the reductive sweep is suggested to partially reduce the anhydrous layers and facilitate the rearrangement of the oxycation species to be more susceptible to oxidation and incorporation into the hydrous layer. [12,29,63,74]

Lyons and coworkers built upon the duplex layer model and investigated the formation of hydrous oxide films on Fe and Ni under potential cycling by varying the number of cycles, scan rate, potential window, temperature, and hydroxide concentration.[12,28,29,60,74] One key evaluation parameter was the oxide charge capacity *Q*, which was determined by integrating the M(II)/M(III) redox peak. The correlation between the oxide charge capacity of the grown Ni and Fe oxides and the number of cycles, potential limits, scan rate, KOH concentration, and temperature during CV conditioning and the OER performance of the produced hydrous oxide films are summarized in Table 2.2. The hydroxide concentration and temperature were 1 M and room temperature (RT), if not subject to variation. To put it in perspective, it needs to be noted that while these extensive investigations suggest this topic to be widely researched, these studies were primarily conducted by Lyons *et al*.

Influence of the number of cycles on the oxide charge capacity

When growing an oxide film on a metal, the resulting oxide charge capacity depends on the number of performed CV cycles. With a larger number of cycles, the oxide charge capacity *Q* is reported to increase and saturate with increasing number of cycles N_{CV} according to equation (2.3),

$$Q = a\left(1 - e^{-bN_{CV}}\right) \tag{2.3}$$

with *a* and *b* being empirical parameters, which depend on the applied CV parameters.

For example, the oxide charge capacity of a hydrous oxide film on Ni was reported to saturate after approx. 250 cycles (–0.526-1.574 V *vs*. RHE, 40 mV s^{-1}) in 1 M NaOH. The reduced oxide growth rate with increasing film thickness was attributed to an increasing limitation of water and hydroxide ion transfer to the inner region of the oxide layer.[28,29]

Influence of upper and lower potential limit on the oxide charge capacity

The works on hydrous Fe oxide films further indicate that the oxide growth rate depends strongly on the upper and lower potential limit of the CV. The lower potential limit plays a crucial role in the extent of the partial reduction of the anhydrous oxide layer. Regarding the upper potential limit, different effects were reported. Increasing the upper potential of the CV could lead to a deeper oxygen penetration into the outer regions of the metal lattice, thickening the compact anhydrous layer.[12,74] It may also help to induce expansion and stress at the metal oxide interface, facilitating the uptake of excess oxygen. Plus, reducing the compact anhydrous oxide layer might become more challenging for more oxidative upper potentials.[12,28] Consequently, Lyons and coworkers saw that the oxide charge capacity is increased with increasing the upper potential of the CV and that the optimal lower potential limit depends on

the upper limit.[12,28] For Fe, the oxide charge is maximized when the potential is reversed at the peak potential of the reduction of the compact anhydrous Fe-oxide layer (approx. –0.2 V *vs*. RHE).[12,28,60] The higher the upper potential limit between 1.25-1.65 V *vs*. RHE, the larger the oxide charge capacity.[12,28] For Ni, the oxide charge capacity is maximized if the lower limit is below –0.4 V *vs*. RHE.[58,75] For the upper potential limit, an increasing oxide charge capacity with increasing potential until 1.6 V *vs*. RHE[58,75] with saturation[58] and as optimum[75] was reported.

Influence of scan rate on the oxide charge capacity

When discussing the influence of the scan rate *v* on the oxide charge capacity, a distinction needs to be made between the scan rate used for the oxide growth and analysis. The oxide charge capacity in dependence on the analytical scan rate for different oxide film thicknesses on Ni and Fe is shown in Figure 2.6.

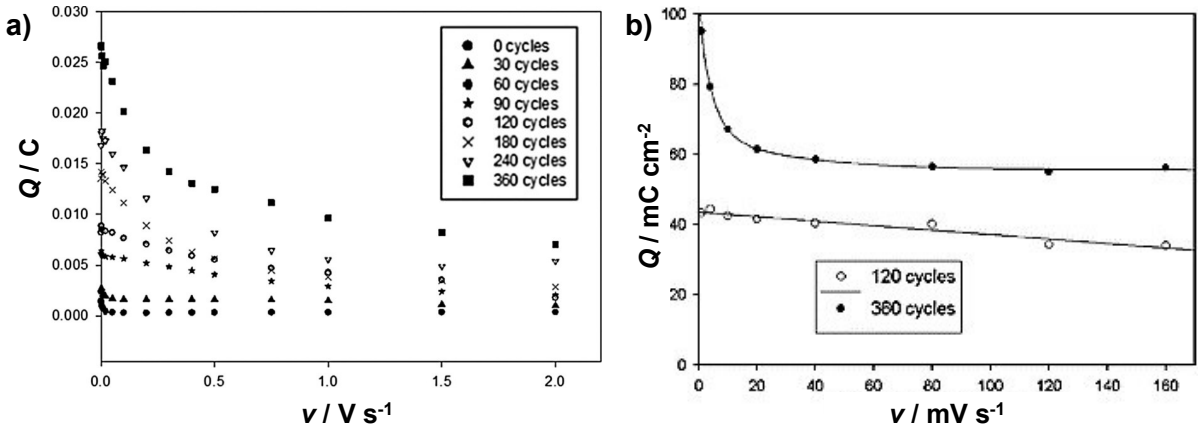

Figure 2.6. Effect of the analytical scan rate on the oxide charge capacity of the M(II)/M(III) redox peak for a) Ni oxides grown under CV cycling (–0.526-1.574 V *vs*. RHE, 150 mV s^{-1}, 1 M NaOH, RT) and b) Fe oxides grown under CV cycling (–0.5-1.25 V *vs*. RHE, 350 mV s^{-1}, 1 M NaOH, 25 °C). [a) adapted from ref. [29] with permission from IOP Publishing, Ltd, b) adapted from ref. [60] with permission from Elsevier]

In Figure 2.6a, the oxide charge capacity is independent of the analytical scan rate between 10 and 2000 mV s^{-1} for thin oxide films on Ni (< 60 cycles, −0.526-1.574 V *vs*. RHE, 150 mV s^{-1}, < 2 mC). Here, the redox reaction has sufficient time to extend throughout the entire dispersed hydrous oxide layer. For thicker Ni-oxide films (> 60 cycles, −0.526-1.574 V *vs*. RHE, 150 mV s^{-1}, > 2 mC), the oxide charge capacity decreases drastically from low scan rates to 50 mV s^{-1}. From 50 to 2000 mV s^{-1}, this decrease of the oxide charge capacity with increasing scan rate is reduced to a linear trend. This suggests that for the thicker oxide films, there is not enough time for the redox reaction to extend throughout the hydrous oxide layer.[29] The same relation was found for Fe-oxide films, as seen in Figure 2.6b.[60]

In Figure 2.7, the effect of the oxide growth scan rate on the oxide charge capacity for oxides grown on Ni and Fe can be seen. The oxide charge capacity shows maxima depending on the applied oxide growth scan rate. Figure 2.7a indicates two local maxima and a minimum at 100 mV s^{-1} for the oxide charge capacity of Ni oxides. Although the maxima could not be determined consistently, the overall trend was reproducible.[58] The development of these maxima has not yet been fully explained. One possible explanation is that the oxide growth rate decreases below or above an optimum due to excessive or insufficient reduction or rupture

of the anhydrous oxide layer, respectively.[60] For Fe, Figure 2.7b identifies an optimum oxide growth scan rate of 350 mV s^{-1} to obtain the largest possible oxide layer.[60]

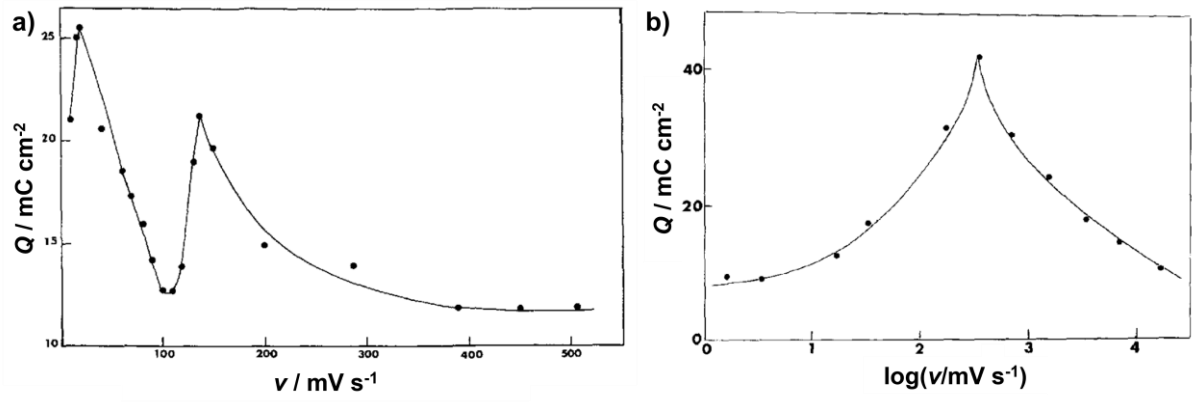

Figure 2.7. Effect of the oxide growth scan rate on the oxide charge capacity of the M(II)/M(III) redox peak for a) Ni oxides grown under CV cycling (1 M NaOH, 25 °C, oxide growth: –0.5-1.55 V *vs*. RHE, 35 cycles, analytical conditions: 0-1.55 V *vs*. RHE, 31 mV s^{-1})[58] and b) Fe oxides grown under CV cycling (in N_2-stirred 1 M NaOH at 25 °C, oxide growth: –0.5-1.25 V *vs*. RHE, 30 cycles, analytical conditions: –0.35-1.65 V *vs*. RHE, 40 mV s^{-1}).[60] [a) adapted from ref. [58] with permission from Elsevier, b) adapted from ref. [60] with permission from Elsevier]

Influence of hydroxide concentration on the oxide charge capacity

The oxide charge capacity of a metal oxide produced by CV in alkaline electrolytes also varies with the applied hydroxide concentration. This is because varying the hydroxide concentration of the electrolyte affects the thermodynamic equilibrium potential of a redox surface reaction, its redox kinetics, and the electrolyte conductivity.

For oxide films on Ni, the oxide charge capacity of the reductive peak of the Ni(II)/Ni(III) redox reaction increases with increasing electrolyte concentration and saturates at 4 M NaOH (–0.5-1.6 V *vs*. RHE, 164 mV s^{-1}, 50 cycles).[58] The Tafel slope at low potentials of deposited $Ni(OH)_2$ on Au is reported to decrease steadily from 65 to 45 mV dec^{-1} with increasing NaOH concentration. This is proposed to occur due to dehydration of the hydrous α-$Ni(OH)_2$ to β-$Ni(OH)_2$, which is, in this case, suggested to be the electrocatalytic more active form. The Tafel slope at high potentials is invariant at approx. 120 mV dec^{-1}, irrespective of the applied base concentration during conditioning.[12,76]

Burke and Lyons reported in 1986 that for thin oxide films on Fe (30 cycles, Q < 30 mC cm^{-2}, –1.425-0.325 V *vs*. Hg/HgO [–0.5-1.25 V *vs*. RHE], 350 mV s^{-1}), the oxide charge capacity of the oxidative Fe(II)/Fe(III) peak shows an optimum for a NaOH concentration of 1 M, as seen in Figure 2.8a. Figure 2.8a indicates that for thicker oxide films (120 cycles, Q < 120 mC cm^{-2}, –1.425-0.325 V *vs*. Hg/HgO [–0.5-1.25 V *vs*. RHE], 350 mV s^{-1}), the largest oxide charge capacity is obtained for the most diluted solutions with a fast initial and then slow decay with increasing NaOH concentration.[60] Partly contradicting the results from Burke and Lyons in 1986, Doyle and Lyons reported in 2013 that for a small number of CV cycles, the oxide growth rate is higher in more concentrated hydroxide solutions (5 M *vs*. 0.1 M), as shown in Figure 2.8b. The growth rate, however, decreases faster in 5 M concentrated electrolyte, and saturation of the oxide charge capacity with the number of cycles can already be seen after 20-30 cycles at approx. 10 mC cm^{-2}. Thus, significantly larger oxide charge capacities can be generated at lower concentrations. In Figure 2.8b, the saturated oxide charge capacities follow the order 1 M = 0.5 M > 0.1 M >> 5 M. Further, Doyle and Lyons observed that the Tafel slope of the Fe oxides generated in high hydroxide concentration is larger than at low concentrations

(<1 M) with approx. 60 mV dec^{-1} compared to 40 mV dec^{-1}. This is suggested to result from stronger dehydration of the hydrous oxide layers in highly concentrated bases, with the hydrous phase being more active for the OER.[12,28]

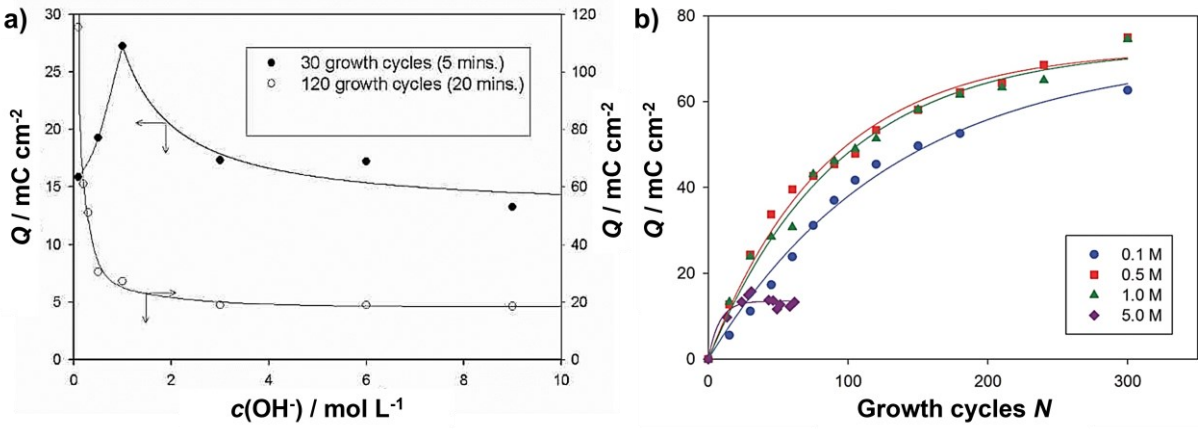

Figure 2.8. Effect of the hydroxide concentration on the oxide charge capacity of the Fe(II)/Fe(III) redox peak. a) Oxide charge capacity of an Fe oxide electrode, grown by CV cycling (–1.425-0.325 V *vs*. Hg/HgO [–0.5-1.25 V *vs*. RHE], 350 mV s^{-1} at 25 °C) for 30 and 120 cycles, in dependence on the hydroxide concentration.[60,74] b) Oxide charge capacity of an Fe oxide electrode in dependence on the number of cycles. Oxide films were prepared in 0.1, 0.5, 1.0, and 5.0 M NaOH. The cycling parameters were optimized for the respective base concentration.[12,28] [a) adapted from ref. [74] with permission from Elsevier, b) adapted from ref. [28] with permission from IOP Publishing, Ltd]

Influence of temperature on the oxide charge capacity

Lastly, the oxide charge capacity of a metal oxide layer grown by CV in an alkaline electrolyte depends on the applied temperature. Regarding the M(II)/M(III) oxide charge capacity of Ni and Fe, the oxide charge capacity of Ni oxides increases with increasing temperature up to 60°C, potentially because of an enhanced oxide formation rate.[53,58] For Fe, the hydrous oxide structures produced by potential cycling are not stable at elevated temperatures larger than 40 °C.[60]

OER on hydrous oxide films with different oxide charge capacity

The OER activity, measured by the current response at a certain overpotential, was studied for hydrous oxide films of different thicknesses, corresponding to different oxide charge capacities. The OER activity increases with the oxide charge capacity and saturates at approx. 0.01 C cm^{-2} for Ni[29] and at 0.07 C cm^{-2} for Fe.[28] This enhancement of the electrocatalytic activity with increasing oxide charge capacity supposedly results from increased contact between oxycations and the aqueous phase in the outer hydrous oxide layer.[27,28] Regarding the intrinsic catalytic OER activity measured by the Tafel slope, different trends for the correlation with the oxide charge capacity have been reported. For Ni, a Tafel slope of approx. 60 mV dec^{-1} at low and 120 mV dec^{-1} at high potentials for thin and thick oxide films was reported by Lyons *et al*.[29] In contrast, Son *et al*. presented an increase in the Tafel slope with higher surface oxidation.[63] For FE, the Tafel slope decreases from 75 to 47 mV dec^{-1} with an increasing oxide charge capacity at low potentials, and at higher potentials, it is invariant at 120 mV dec^{-1}.[77]

When applying these hydrous oxides in prolonged electrolysis, it was reported that hydrous Fe oxides are unstable and that half of the oxide charge capacity is lost after applying 1.7 V *vs*. RHE for 30 min. This was explained by the formation of ferrate during polarization.[60] For Ni,

Vuković *et al*. showed that the oxide charge capacity remains stable during polarization at 0.1 A cm^{-2} for 14 days. However, the performance could not be maintained.[78]

Table 2.2. Correlation between oxide charge capacity Q of Ni and Fe oxides and the number of cycles, potential limits, scan rate, KOH concentration, temperature during CV conditioning, and OER performance of the produced hydrous oxide films.

		Fe		Ni	
Number of cycles		Q saturates with an increasing number of cycles N_{CV} according to $Q = a(1-e^{-bN_{CV}})$			
Potential limits *vs*. RHE	**Upper limit**	Q increases the higher E_{high} is[28]		Increased Q if E_{high} ≥1.6 V,[58] =1.6 V[75]	
	Lower limit	Increased Q if E_{low} equals C1 peak potential (approx. –0.2 V)[28]		Increased Q if E_{low} <–0.4 V[58,75]	
Scan rate	**Oxide growth**	Increased Q at 350 mV s^{-1}[60]		Two maxima of Q, one minimum of Q at 100 mV s^{-1}[58]	
	Analytical	Thin layers: slightly linear decrease of Q/invariant with increasing scan rate[60]	Thick layers: exponential decay of Q with increasing scan rate [60]	Thin layers: slightly linear decrease of Q/invariant with increasing scan rate [29]	Thick layers: exponential decay of Q with increasing scan rate[29]
KOH concentration		Thin films: maximum of Q at 1 M[60]	Thick films: exponential decay of Q with increasing c(KOH),[60] maximum of Q at 1 M[12,28]	Q increases with $c(OH^-)$ (saturation at 4 M)[58]	
Temperature		Hydrous oxide structures not stable at >40°C[60]		Linear increase of Q up to 60°C[58]	
OER performance	**Tafel slope**	Tafel slope decreases with increasing Q for low potential regime, invariant for high potentials [77]		Tafel slope is invariant with increasing Q,[29] increases[63]	
	Stability	Not stable during constant potential operation (1.7 V)[60]		Chemically stable during CP (0.1 A cm^{-2}) , but performance degradation[78]	

Concluding, intensive research has been conducted, investigating systematically the behavior of the oxide charge capacity of Ni and Fe when cycling in alkaline electrolyte under varying process conditions. This knowledge can be used to apply potential cycling as an alternative synthesis route to obtain highly active OER electrodes.

2.2.5. Electrochemical Conditioning of Steel Electrodes as Alternative Synthesis Route

Recently, many studies have explored the electrochemical metal anodization of steel electrodes as a synthesis technique. The goal was to find an efficient and cost-effective synthesis method for a highly active OER catalyst based on the abundant and low-cost raw material steel.[22,30–35,79–86]

One of the earlier works by Schäfer *et al*. reported an electrochemical activation of Ni42 steel by CP at 2 A cm^{-2} for 300 min in 7.2 M NaOH.[83] Later, Moureaux *et al*. compared the activity enhancement of 316L steel electrodes during constant current operation with the addition of a preceding activation protocol (12x [(1) E = 1.53 V *vs*. RHE, 10 min; (2) E = 0.93 V *vs*. RHE, 5 min; (3) 2x CV (0.93-1.93 V *vs*. RHE, 5 mV s^{-1})]). The purpose of the activation protocol was to favor dissolution and redeposition to restructure the electrode. The preceding activation protocol accelerated the catalytic performance enhancement by approx. 190 h.[82] This shows that the conditioning of steel with an alternation between higher and lower potentials outperforms constant current conditioning, which is consistent with reports on the conditioning of Ni by CV and CP.[63]

To identify well-suited potential limits, scan rate, and electrolyte concentration for the CV conditioning of steel electrodes, systematic parameter variation was performed by Zhu *et al*.[31] and Zuo *et al*.[33] Zuo *et al*. identified that the CV conditioning with a larger potential window between –0.074-1.924 V *vs*. RHE compared to 0.924-1.924 V is more beneficial for activating SSM316 steel. This was attributed to an increased Fe leaching at the lower potentials, which enlarges the surface area and results in an accumulation of OER-active Fe-incorporated NiOOH species.[33] Zhu *et al*. systematically studied the activation of 316L stainless steel felt by CV conditioning, focusing on the variation of potential limits, scan rate, and KOH concentration. Like Zuo *et al*., they found that out of the three tested potential windows, 0.3-0.7 V, 0.7-1.7 V, and 0.3-1.7 V *vs*. RHE, the largest potential window resulted in the most significant activation.[31] This is in line with the reports from Lyons *et al*. on oxide formation by CV cycling of Ni and Fe (see chapter 2.2.4).[28,58] Regarding the scan rate, Zhu *et al*. showed that its variation between 5 mV s^{-1} and 50 mV s^{-1} influenced the catalytic performance only minimally. Therefore, a scan rate of 50 mV s^{-1} was suggested to save time. The variation of KOH concentration between 1-6 M KOH revealed that 3D porous structures form in 1-3 M KOH. The authors stated that if the concentration is further increased, some nanosheets will agglomerate. In 6 M KOH, the 3D porous structure was lost entirely, and irregular structures appeared. Zhu *et al*. identified 3 M KOH as the optimal KOH concentration with the smallest overpotential, charge transfer resistance, and Tafel slope.[31] To summarize, a large potential window, an arbitrary scan rate between 5-50 mV s^{-1}, and 3 M KOH are reported as optimum conditioning parameters for 316L stainless steel felt.

The reasons for the activation of steel electrodes have also been discussed intensively by many groups. For example, Todoroki *et al*. used constant current operation (10 h, 30 mA cm^{-2} in 1 M KOH at 75 °C) to form Ni-Fe (hydr)oxide nanofibers on 316 stainless steel electrodes.[32] They suggested that the hetero-structured nanofibers are produced from a selective dissolution of Fe and Cr accompanied by nanoscale gaps forming from O_2 gas bubbles and a precipitation of Ni-Fe (hydr)oxides.[32] Zhang *et al*.[30] and Zhu *et al*.[31] reported independently from one another that the activation of 316L steel by CV cycling was supposedly caused by an enrichment of Ni and O species on the surface. Simultaneously, the Fe- and Cr-contents decreased.[31] According to Ferriday *et al*., the oxide layer produced by CV cycling of 316L stainless steel felt corresponds to $M(OH)_2$. Further, the Ni content can supposedly be increased when cycling the Ni redox couple, and Cr can be enriched when cycling around the Fe redox couple.[85] These studies show that stainless steel activation is suggested to result primarily from the dissolution of constituent elements.

Todoroki *et al*. had a closer look into the dissolution behavior of constituent elements of various stainless steel electrodes during CV cycling. Regardless of the stainless steel grade, constituents were dissolved in decreasing amounts in the order of Fe, Cr, Mn, and Ni. They suggested the Ni:Fe ratio as a key parameter to estimate the dissolution behavior of constituent elements. The higher the ratio, the more the dissolution is suppressed.[34] Magnier *et al*. reported that by aging or conditioning Ni-Fe-based alloys or oxides with initial Ni:Fe ratios between 0.14 to 250, the OER activity increases due to an optimized Ni:Fe ratio, which tends toward 2.5 to 5.[35]

To summarize, OER-active electrodes were synthesized by different CP and CV conditioning, which all achieved activation by dissolution of constituent elements. For industrial application, these conditioned steel electrodes, however, need to be reconsidered since the industry is limited to a defined electrolyte quality, and metal leaching might pose additional challenges.[86,87] The substantial Fe dissolution indicated by Todoroki *et al*. and the toxic hexavalent Cr ions (CrO_4^{2-}) generated in the strong alkaline electrolyte are especially troublesome.[34] Additionally, stable OER performance for over 300 h was reported to be only possible when re-activating by conditioning.[33]

3. Research Questions & Approach

Developing cost-effective, active, and stable electrodes for the alkaline OER in large-scale AWE is a complex challenge. This work tackles this challenge in three steps.

First, an EFC is designed to assess the activity and stability of electrocatalysts. Second, the electrochemical conditioning of Ni-(Fe)-based electrodes is examined by correlating electrode activation, surface modifications, and electrochemical conditioning parameters. Finally, the electrochemical conditioning is scaled up and tested under industrially more relevant conditions. The schematic objectives of this thesis are illustrated in Figure 3.1.

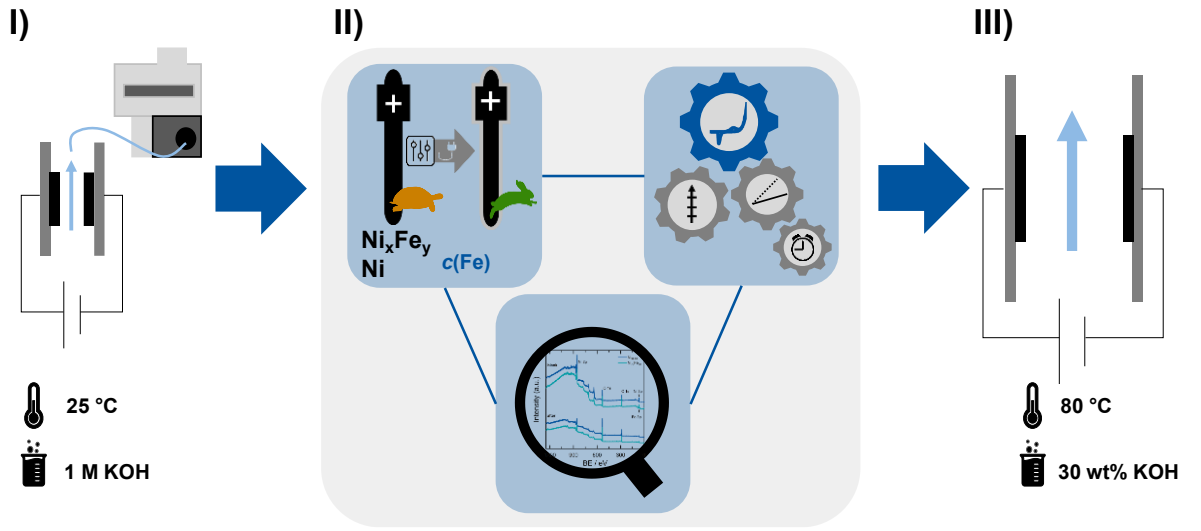

Figure 3.1. Schematic representation of the objectives of this thesis to address the challenge of designing cost-effective, active, and stable electrodes for the alkaline OER. I) An EFC for 1 cm^2 electrodes is designed. II) The correlations between electrochemical conditioning of Ni-(Fe)-based electrodes, surface changes, and electrode activation for the alkaline OER are investigated. III) The electrode activation by conditioning is scaled up and tested under industrially more relevant conditions.

To study simultaneously the electrocatalytic activity and stability of an electrocatalyst, coupling of EFCs with online electrolyte monitoring can be applied. The reported designs are, however, far from industrial conditions. Thus, in this work, an EFC with parallel 1 cm^2 electrodes is designed for this purpose. This design aims to enable experiments under more industrially relevant conditions than the previously reported specialized EFCs for online electrolyte monitoring while maintaining high precision in activity determination. For the design, the following questions need to be considered:

1.1. How can a precise activity determination over a wide potential range and minimal dilution of reaction products be ensured with a restricted volume flow?
1.2. To what extent does the mass transport of reactive species to the electrode influence the precision of the activity determination?
1.3. How can a precise definition of the WE's and CE's surface area and potential control be ensured?
1.4. What needs to be considered and adjusted for the EFC design, especially regarding a stable potential measurement, when studying AWE electrocatalysts at industrially relevant conditions (up to 100 mA cm^{-2}, 80 °C, 30 wt% KOH)?
1.5. Can metal dissolution and incorporation at the electrodes be monitored with this design?

Regarding the electrochemical conditioning of Ni-(Fe)-based electrodes, the conditioning of single- and multi-element electrodes has already been presented in the literature, focusing on oxide growth on Ni and Fe and finding a low-cost and highly active electrocatalyst from steel. However, no study has systematically correlated activation, surface changes, and electrochemical conditioning parameters for a model electrode with a Ni:Fe ratio in the optimum regime. Herein, a systematic investigation of the electrochemical conditioning for such a Ni-Fe alloy electrode with 30 wt% Fe (31 at% Fe) and other Ni:Fe ratios is performed to explore the following questions:

2.1. What are the correlations between the electrochemical conditioning protocol parameters and electrode activation of a Ni-Fe alloy electrode with 30 wt% Fe at lab conditions (1 cm^2, 1 M KOH, room temperature)? What protocol parameters result in the most extensive activation?

2.2. How do the correlations between protocol parameters and electrode activation depend on the Ni:Fe ratio of the WE and the Fe content in the electrolyte?

2.3. What influence does the conditioning with and without the hydrogen evolution reaction (HER) regime have on the WE's surface, regarding the occurring electrochemical processes, visual changes, phase changes, oxide character, and Fe content?

Based on this, the correlations derived between conditioning protocol parameters and electrode activation can be transferred to new WE materials to determine their optimized protocol and exploit their full potential. New materials can also be tailored for a specific material change and activation.

Lastly, the electrochemical conditioning is performed at industrially more relevant conditions to address the question:

3.1. Is the electrode activation by electrochemical conditioning transferable to industrially more relevant conditions (12 cm^2 mesh electrode, separator, 30 wt% KOH, 80 °C)?

Considering a successful transfer of the electrochemical conditioning to industrially more relevant conditions, applying this technology and possibly also *in-situ* (re)activation of electrodes in large-scale electrolyzers becomes more conceivable. Through its application to the right pre-catalysts, the cell potential is aimed to be reduced. Considering that a 2.5-3% reduction in power consumption might be achievable by the implementation of electrochemical conditioning and that enormous amounts of electricity are required, electrochemical conditioning as an anode manufacturing technique could make a significant difference. Reactivation of the anodes can prolong their lifetime, which would not only save investment costs but also resources. Further, the toolkit for anode manufacturing is enlarged by a very simple and versatile technique, which can be added to an existing manufacturing process, substitute a certain step, or it can be performed as a stand-alone process. Thus, electrochemical conditioning might be able to simplify and reduce costs in the anode manufacturing, which is responsible for the largest share of the electrolyzer cost.

4. Experimental Section

4.1. Materials and Methods

In this work, the experiments were conducted at RT (typically ranging between 20-24 °C) and ambient pressure, if not stated otherwise. The potentials obtained from the electrochemical experiments are reported 100% iR_u corrected and *vs*. RHE (see appendix for potential conversion into RHE scale) and all data was plotted by OriginPro, if applicable.

All materials and chemicals utilized for the experiments and the materials required for the assembly of the iEFC and the flex-E-cell are listed in Table S1-Table S3 in the appendix. Table S4 and Table S5 show an overview of the devices and software used in this work for data generation and analysis. Table 4.1 summarizes the applied electrode configurations and potentiostats for the respective electrochemical procedure.

Table 4.1. Electrode configuration and potentiostat assignment to the respective electrochemical procedure.

Electrochemical procedure	Electrode configuration	Potentiostat
Experimental validation of the iEFC Simulations in iEFC	RE: $Hg/HgSO_4$, WE: glassy carbon, CE: glassy carbon	Gamry Interface 1010E
EIS Measurements for the Investigation of the Electrode Positioning in iEFCs	RE: Hg/HgO, WE: $Ni_{99.0}$, CE: glassy carbon	Gamry Interface 1010E
Determination of the Active Surface Area with Ta in iEFC	RE: $Hg/HgSO_4$, WE: Ta, CE: glassy carbon	Gamry Interface 1010E
Investigation of Electrochemical Conditioning	iEFC: RE: Hg/HgO, WE: Ni-(Fe)-plates/rods, CE: glassy carbon, Ni flex-E-cell: RE: Hg/HgO, WE: Ni-(Fe)-plates, CE: $Ni_{99.2}$	iEFC: Gamry Interface 1010E, Gamry Reference 3000 FTacV in iEFC: Biologic VSP-300 flex-E-cell: Gamry Reference 3000 + Booster

The chemicals and materials were used as is without any purification. The electrodes and electrolyte were prepared as follows:

Electrode Preparation

Throughout this work, different WEs and CEs were tested in multiple procedures. Here, the electrode materials' compositions are in wt% and noted as subscript ($Ni_{70}Fe_{30}$ = 70 wt% Ni, 30 wt% Fe), if not stated otherwise. For electrode preparation, the electrode was ground (7000 grit size), polished with an alumina-water-slurry (either with a polishing machine or manually with polishing pads) with decreasing grain size (1 µm, 0.3 µm, 0.05 µm), ultrasonicated in ultrapure water for 5 min, and dried.

Electrolyte Preparation

1 M KOH was prepared from ultrapure water and KOH pellets. Depending on the KOH pellets batch, the amount of Fe varied. For the experiments with a low Fe content, a batch with an Fe concentration of approx. 10±5 ppb was chosen. For the standard experiments and those with higher Fe concentration, the Fe concentration was adjusted to 110±10 ppb or 950±10 ppb, respectively. This was done by adding Fe in diluted HNO_3 in the form of an ICP-OES calibration

standard. The Fe concentration in the electrolyte was determined by Inductively Coupled Plasma Optical Emission Spectroscopy (ICP-OES).

0.1 M $HClO_4$ was prepared from ultrapure water and 70% $HClO_4$.

4.2. Setups

4.2.1. *In-situ* Electrochemical Flow Cell

In this work, the *in-situ* electrochemical flow cell (iEFC) with 1 cm^2 parallel electrodes for online downstream analysis of the electrolyte was designed. It was used to validate the simulations of the iEFC and to investigate the electrochemical conditioning of electrodes. Different versions of the iEFC were employed throughout this work, which are shown in Figure 4.1. The materials used in the iEFC are listed in Table S2 in the appendix.

Figure 4.1 shows that in the iEFC, the CE and WE are placed parallel in a rectangular channel between the inlet and outlet with an electrode spacing of a) 1 mm and b-d) 3 mm. This results in a) a 10 x 1 mm and b-d) a 10 x 3 mm channel cross-section over the WE. The in- and outlet channels enclose an angle of a) 60° and b-d) 120°. The rectangular-shaped channels merge into round channels with a diameter *d* of 2 mm toward the tube connections. The CE is electrically contacted by a brass rod (*d* = 4 mm) and Ag-containing conductive adhesive. A 1 x 1 x 0.1 cm glassy carbon electrode was used as CE, if not stated otherwise. For design A, the CE is seamlessly inserted by adhesive, and for B-D, the CE is embedded in a 3D-printed holder (see detailed description below). The WE is electrically contacted by a 0.5 mm thick Cu sheet and Ag-containing conductive adhesive. To define its surface area and positioning, the WE is embedded in epoxy (CaldoFix-2 for 1 M KOH, RT and EpoHeat CLR for 30 wt% KOH, 80 °C) into a 3D-printed form (a) 20 x 25 x 10 mm, b-d) 20 x 30 x 10 mm). A detailed description of the preparation is explained below. A RE with a 6 mm diameter can be placed in the inlet channel for d). For a) and c), the RE sits in a reservoir connected to the inlet channel *via* a) a 1 mm and c) a 1.5 mm wide capillary. In the iEFC design B, a miniRHE from Gaskatel (*d* = 1.6 mm, length: 3 or 4 cm) is placed in the inlet. The advantages and disadvantages of the respective RE positioning are discussed in chapter 5.1.4. The EFC is 3D-printed. For 1 M KOH and RT, all parts can be printed in VeroClear, which has material properties similar to polymethyl methacrylate.[88] For 30 wt% KOH and 80 °C, the top-part of the EFC, the CE-holder, and the CE-screw are 3D-printed in AR-H1 or AR-M2. Due to the performed material tempering for AR-H1, the threads must be recut after printing.

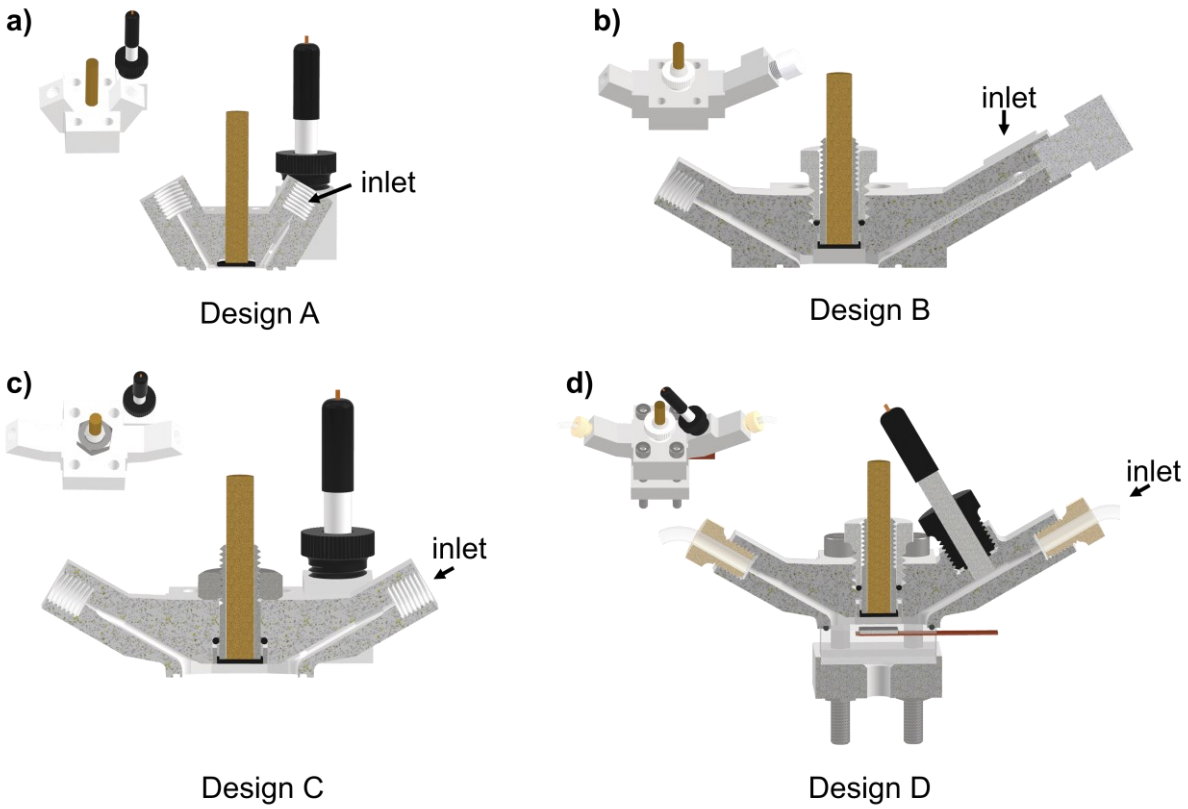

Figure 4.1. Versions of the herein-designed iEFC with parallel 1 cm^2 WE and CE. Design A: 60° between channels, electrode spacing of 1 mm, introduction of RE with a 6 mm diameter in a reservoir, seamless insertion of CE by adhesive. Design B: 120° between channels, electrode spacing of 3 mm, prolonged connecting middle section, introduction of miniRHE in the channel, introduction of exchangeable CE by screw. Design C: 120° between channels, electrode spacing of 3 mm, prolonged connecting middle section, introduction of RE with a 6 mm diameter in a reservoir, introduction of exchangeable CE by a nut. Design D: 120° between channels, electrode spacing of 3 mm, prolonged connecting middle section, introduction of RE with a 6 mm diameter in channel, introduction of exchangeable CE by screw. As an example, the cell in d) is fully assembled with tube connections, the embedded WE, and the bottom part of the EFC, which is attached to the top with screws. All cells feature a channel diameter of 2 mm. WEs are embedded in epoxy. For b-d), the CEs are embedded as well.

Figure 4.2 shows exemplarily the integration of the iEFC into the experimental setup for investigating the electrochemical conditioning of electrodes. The iEFC is assembled and sealed with 0.8 Nm. The electrolyte can run in a single-pass into an electrolyte waste or can be circulated from a PTFE electrolyte reservoir. It is important to note that a pump with little pulsation needs to be chosen and placed behind the iEFC to minimize the influence of pump pulsation on the electrochemical measurement. Herein, a peristaltic pump with 12 rolls (Ismatec Reglo Digital Pump or Masterflex L/S + 12-rolls-4-channel-pump-head) was used. The electrolyte reservoir can be purged with Ar or N_2 to increase reproducibility.

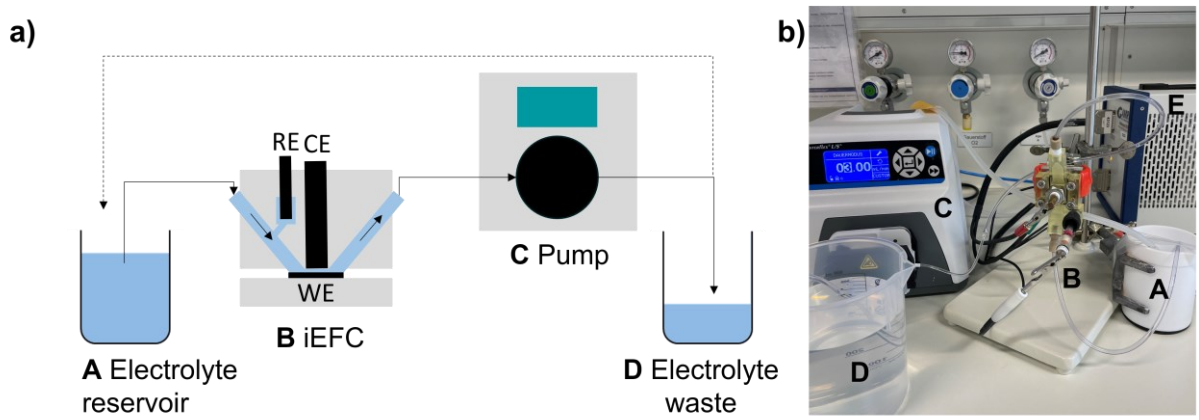

Figure 4.2. a) Schematic experimental setup for the investigation of electrode conditioning of 1 cm^2 electrodes for the alkaline OER. Electrolyte can either flow in a single-pass or be circulated from an electrolyte reservoir. b) Picture of the experimental setup. A: Electrolyte reservoir, B: iEFC, C: Peristaltic pump, D: Electrolyte waste, E: Potentiostat. [b) is adapted from H. Ingendae's master thesis][89]

Fabrication of embedded WEs

WEs are embedded into a 3D-printed holder, as illustrated in Figure 4.3. Here, the implemented structures aid in the central positioning of the WE. The holder is placed on adhesive tape with the 1 cm^2 WE in the middle. Ag-containing adhesive is attached to the WE, the Cu sheet is introduced through the cut-out in the holder, and this combination is annealed at 60 °C for 2 h. The cut-out is covered by epoxy adhesive (UHU 2-component epoxy adhesive or CaldoFix-2 or EpoHeat CLR). The embedding material is filled into the form with a syringe. In order to ensure that epoxy covers the entire bottom, epoxy is filled in on one side and, by tilting, is distributed evenly. After annealing the epoxy, the adhesive tape is removed when still warm to minimize adhesive remains.

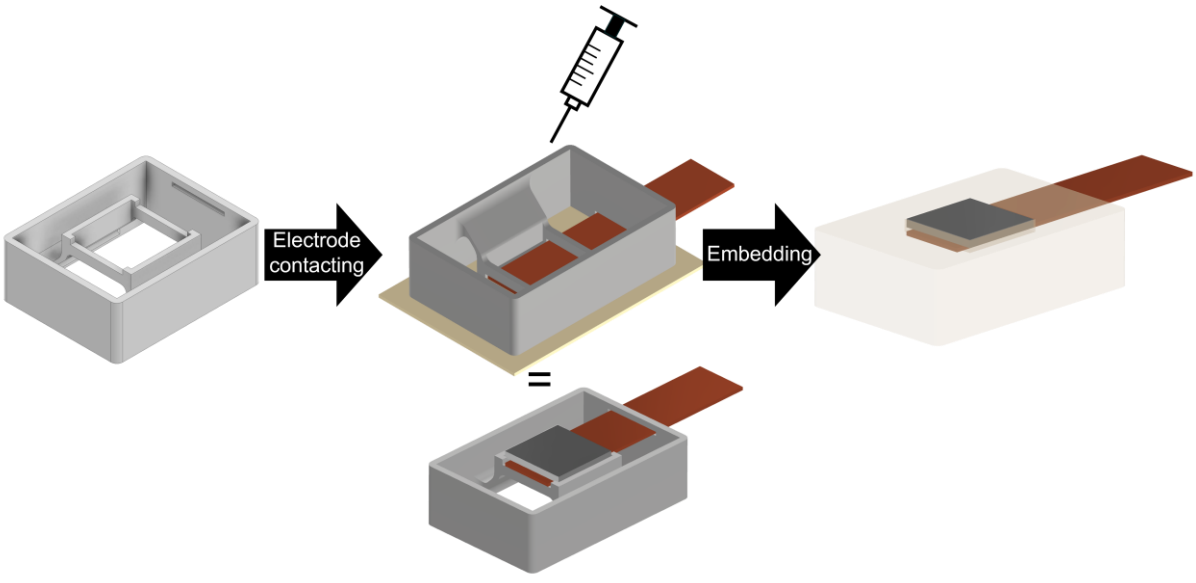

Figure 4.3. Schematic procedure to fabricate embedded WEs. The structure of the 3D-printed WE-holder ensures the central position of WE. The WE is electrically contacted by a Cu sheet and Ag-containing conductive adhesive. Embedding material is filled into the WE-holder, which is sealed at the bottom by adhesive tape.

Fabrication of exchangeable CEs

To fabricate the exchangeable CE, the CE is first electrically contacted by a metal rod (d = 4 mm) and Ag-containing conductive adhesive, as illustrated in Figure 4.4. The depicted tool ensures the central position of the WE. After annealing at 60 °C for 2 h, the contacted CE is placed on adhesive tape with the 3D-printed CE-holder surrounding it. This assembly is fixed by embedding. Deformation from embedding material leakage during annealing can occur for the CE as well as WE preparation, which can be corrected by grinding after annealing.

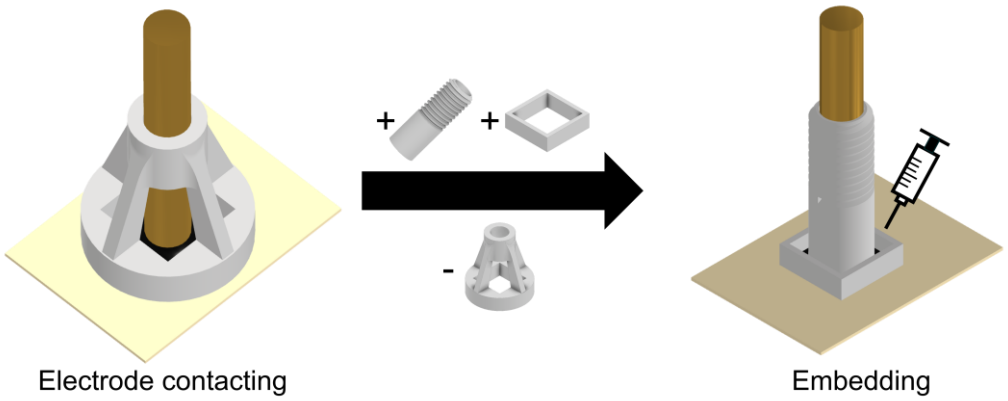

Figure 4.4. Schematic procedure to fabricate an exchangeable CE. First, the CE is electrically contacted by a metal rod and Ag-containing conductive adhesive, and afterward, the CE-holder-assembly is fixed by embedding.

4.2.2. flex-E-cell

For the investigation of electrode conditioning at industrially more relevant conditions, the flex-E-cell was used and adjusted for studying AWE electrocatalysts. Figure 4.5 shows the design of the flex-E-cell for AWE studies on plate (Design PLATE) and mesh electrodes (Design MESH). Here, only half-cells are shown, and the full cell is obtained when mirroring at component G or B/F depending on whether a separator is used. Zirfon 500 UTP with a thickness of 0.5 mm was herein used as a separator and can be introduced by placing it in a gasket of the same thickness. In the flex-E-cell, the 12 cm^2 WE and CE are parallel to one another and contacted by a 0.1 mm thick Ni foil. The electrode surface area of the built-in plates (60 x 40 x 1 mm) and meshes (60 x 40 x 0.5 mm) is defined to 12 cm^2 by the gaskets B (Design PLATE) or F (Design MESH). The currents are normalized to this projected area of 12 cm^2, which corresponds to a geometric surface area of 18.5 cm^2 for the mesh electrodes when considering both electrode sites. The geometric area of the mesh electrodes was determined by graphically measuring the dimensions from a microscope image. This was done for three different 1 cm^2 mesh electrodes and the obtained values were averaged, resulting in 0.77 cm^2. In the flex-E-cell, the electrolyte flow is defined for each half-cell as indicated by the blue arrows. If a separator is introduced and two half-cells are operated, the total flow rate for the full cell doubles compared to the undivided cell. The electrolyte flows through the flow frame, which consists of 5 Santoprene gaskets with a thickness of 0.5 mm, two bridges, and an in-/outlet spacer with a strut distance of 2.5 mm. For mesh electrodes, the flow frames are placed behind the electrode, and instead, a 0.5 mm gasket is added between the electrode and separator. This results in a gap between the mesh electrodes of 1.5 mm with a separator. For plate electrodes, the spacing between the WE and CE is 2.5 mm for an undivided cell and

5.5 mm with a separator. To ensure cell tightness, a 1 mm thick housing gasket A is introduced to avoid electrolyte contact with the housing, PTFE (hard component) and Santoprene (soft component) gaskets are applied alternately in the cell, and a tightening force of 10 Nm is applied. The utilized materials in the flex-E-cell are listed in Table S3 in the appendix.

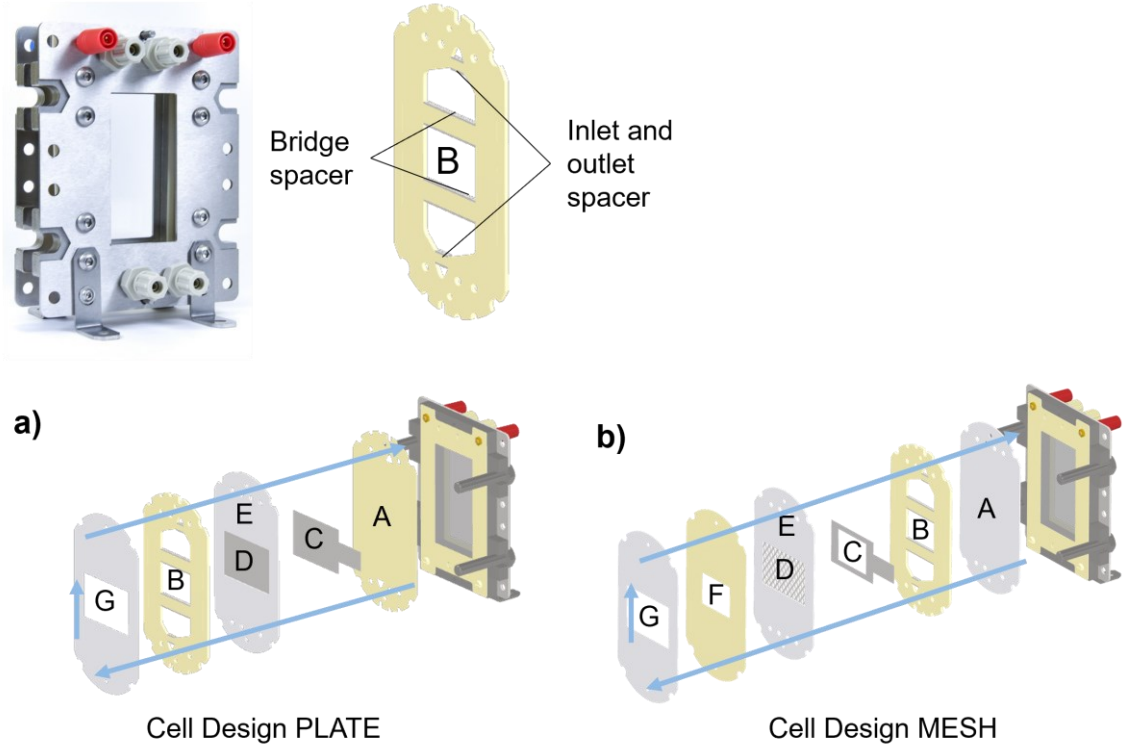

Figure 4.5. Cell design of the flex-E-cell for studying AWE electrocatalysts with a) plate (Design PLATE) and b) mesh (Design MESH) electrodes. A: Housing gasket, B: Flow frame, C: Nickel foil contacting, D: Mesh/Plate electrode, E: Electrode gasket, F: Spacer gasket, G: Separator gasket. Yellow: Santoprene gaskets, Grey: PTFE gaskets. [adapted from J. Schmitt's master thesis][90]

Figure 4.6 shows the integration of the flex-E-cell into the experimental setup. The electrolyte is circulated from a PTFE electrolyte reservoir, where the RE is positioned. Due to the high flow rates, that were required, a peristaltic with 4 rolls was chosen (Masterflex + EasyloadII) for this work. To minimize the influence of pulsation on the electrochemical measurement, the electrolyte needs to be pulled through the flex-E-cell. The electrolyte reservoir is purged with N_2 to increase reproducibility. For precise temperature control, thermocouples are positioned at the inlet and outlet of the cell, and the tubing is insulated to prevent heat loss.

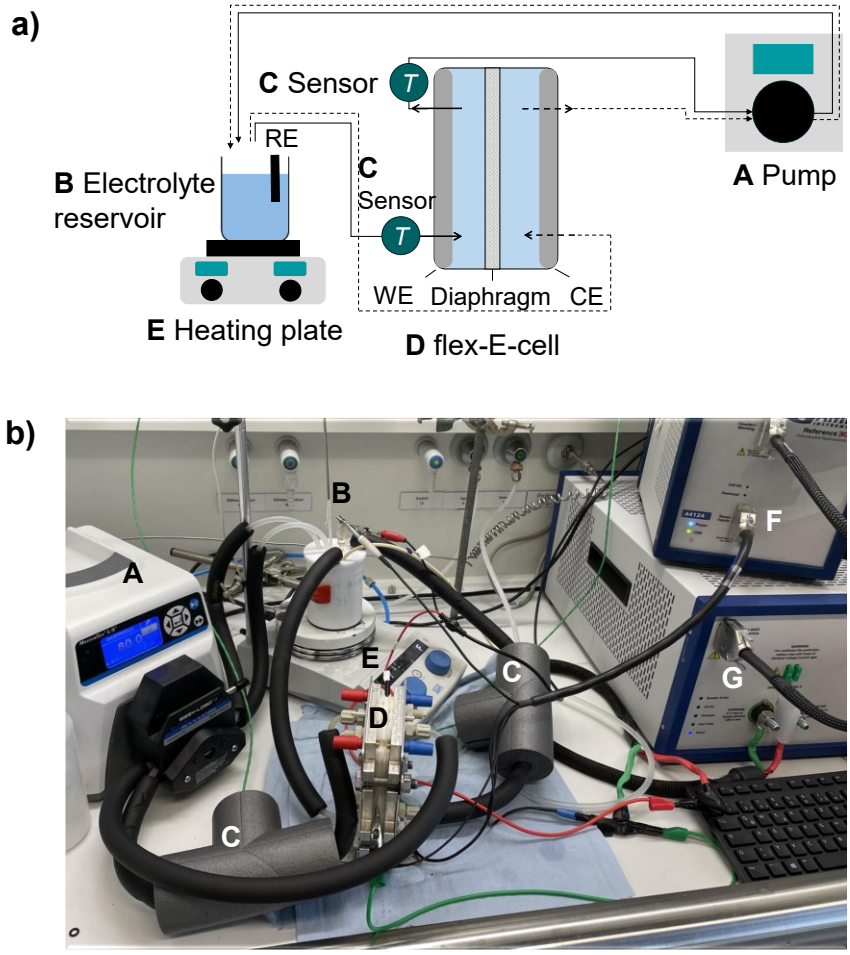

Figure 4.6. a) Schematic experimental setup for the investigation of electrode conditioning of 12 cm^2 electrodes for the alkaline OER at industrially more relevant conditions. A cell configuration with separator and plate electrodes is shown. If operated in the undivided mode, the dashed lines are omitted. The electrolyte is circulated from an electrolyte reservoir through the flex-E-cell. Thermocouples are implemented at the in- and outlet. b) Picture of the experimental setup. A: Peristaltic pump, B: Electrolyte reservoir, C: Thermocouples, D: flex-E-cell, E: Heating plate, F: Potentiostat, G: Booster. [b) is reprinted from J. Schmitt's master thesis][90]

4.3. Procedures

4.3.1. Simulative

In order to design the iEFC, the distribution of fluid flow velocity, reactant concentration, and species flux were simulated with COMSOL Multiphysics for different cell geometries. The simulations and data analysis were performed by C. Marcks, partly during his master thesis.[91]

The approach for modeling the fluid flow velocity, reactant concentration, and species flux at the electrode in an EFC is based on previous works on the KL analysis for the oxygen reduction reaction in the SFC.[38] All relevant model parameters are summarized in Table S6 in the appendix.

The simulation modeled a laminar aqueous flow, which was coupled to the transport of diluted species. The electrolyte flow was modeled by incompressible ($\nabla \boldsymbol{u} = 0$) Navier-Stokes equations and solved for fluid flow velocity and pressure:

$$\rho \frac{\partial \boldsymbol{u}}{\partial t} + \rho(\boldsymbol{u} \cdot \nabla)\boldsymbol{u} = \nabla\left[-p\boldsymbol{I} + \mu_{\mathrm{dyn}}\left(\nabla\boldsymbol{u} + (\nabla\boldsymbol{u})^{\mathrm{T}}\right)\right] + \boldsymbol{F}. \quad (4.1)$$

with the density of the fluid ρ, the flow velocity field $\boldsymbol{u}$, the time t, the Nabla Operator ∇, the pressure p, the unity matrix $\boldsymbol{I}$, the dynamic fluid viscosity μ_{dyn}, and a volume force on the system $\boldsymbol{F}$.

Here, a negligible external force on the system ($\boldsymbol{F} = 0$) and a stationary state ($\partial\boldsymbol{u}/\partial t = 0$) were assumed.

The concentration field of reactive species was calculated by the Nernst-Planck equation, neglecting the migration of ions in the electrical field:

$$\nabla \cdot (-D\nabla c) + \boldsymbol{u} \cdot \nabla c = \frac{\partial c}{\partial t} + K. \quad (4.2)$$

where K is a volumetric homogeneous reaction rate.

To solve equation (4.2), a steady-state regime ($\partial c/\partial t = 0$) and that no homogeneous reactions occur ($K = 0$) is assumed.

To solve these equations, boundary conditions were introduced. For the hydrodynamic flow equations, the flow velocity at the fluid-wall interface was set to zero (no-slip condition). The laminar flow boundary condition was defined with an average flow velocity at the inlet and atmospheric pressure at the outlet. For the species transport equations, no flux was assumed at the walls including in- and outlet. A constant inflow concentration of active species c_{inlet} was defined as an inlet boundary condition, while the backflow of the species at the outlet was suppressed. At the electrode surface, the flux of reactive species was modeled according to a first-order, Butler-Volmer-like reaction kinetic:

$$J_{\mathrm{BV}} = -\frac{i_0 c}{F z c_{\mathrm{inlet}}} \exp\left(-\frac{\alpha F}{RT}\eta\right) \quad (4.3)$$

with the species flux J, exchange current density i_0, charge transfer coefficient α, universal gas constant R, temperature T, and overpotential η.

The kinetic and electrolyte parameters were set comparable to those found in the oxygen reduction reaction, resembling an irreversible and slow first-order electrochemical reaction. Thus, the species flux is defined as negative since the simulated reaction is a reduction reaction of first order. Normalizing the concentration is necessary to account for mass transport effects at large overpotentials.

All simulations were performed using Finite Element software COMSOL Multiphysics 5.6, with the model geometry constructed in Autodesk Inventor 2021. For meshing the flow cell model, two different sets of finite elements were used. Since high concentration gradients were expected at the electrolyte-electrode interface, a set of two-dimensional triangular elements was chosen for the electrode. For the remaining geometry, tetrahedral elements with a pre-defined size were used. The transition zones between high-resolution triangular elements and lower-resolution tetrahedra were optimized by using the COMSOL Multiphysics integrated meshing script. To exclude the influence of the mesh on the simulation results, the maximum element size was gradually reduced until the current became independent of the mesh refinement. For more details regarding the simulation model and the mesh independence study please see chapter 9.2.1 in the appendix.

The model was solved for the velocity field ***u***, the concentration *c*, and pressure *p* using the default steady-state solver for flow and concentration and a segregated solution sequence. The flow rate at the inlet was varied in the simulation between 0.03 mL min^{-1} and 9.18 mL min^{-1} for the flow geometry of the SFC, V-EFC, and final herein-designed iEFC. For the simulation of the iEFC's preliminary flow geometry with a reduced cell width of 0.25 cm (see Figure 5.3), the volume flow was varied between 0.007 mL min^{-1} and 1.829 mL min^{-1}. Please note that the model geometry was divided in half by a symmetry plane and only half of the model geometry was simulated to save calculation time. The specified flow rates are, hence, defined for half of the inlet's cross-section. The overpotential was swept from 0.3 V to 1.5 V in 0.05 V potential steps, and ohmic losses were not considered in the simulation. To evaluate the Levich analysis for EFCs and the KL relation for the different EFC designs, the resulting average flux at the electrode was translated into the respective current by multiplication with *z* and *F*.

All data processing was performed with custom MATLAB scripts. Exemplary polarization curves and the respective KL plot can be seen in Figure 4.7. $I_{kin,sim}$ can be read as the inverse of the y-axis intercept of the fitted KL plot and converted into the respective current density $i_{kin,sim.}$ For the Levich analysis, i_{lim} was plotted against $u_0^{1/3}$ to verify the linear relation. Here, it needs to be noted that while the simulated limiting currents all follow the expected Levich relation ($I_{lim} \propto u_0^{1/3}$), their absolute values deviate from the analytical solutions, which can be calculated with the equations from Scherson *et al.*,[43] Compton *et al.*,[45] and O'Neil *et al.*[44] This discrepancy likely arises from simplifications in the numerical model and residual mesh dependency, leading to an overestimation of mass transport. However, since the expected proportionality ($I_{lim} \propto u_0^{1/3}$) was reproduced, the main conclusions regarding the mass-transport behavior remain valid.

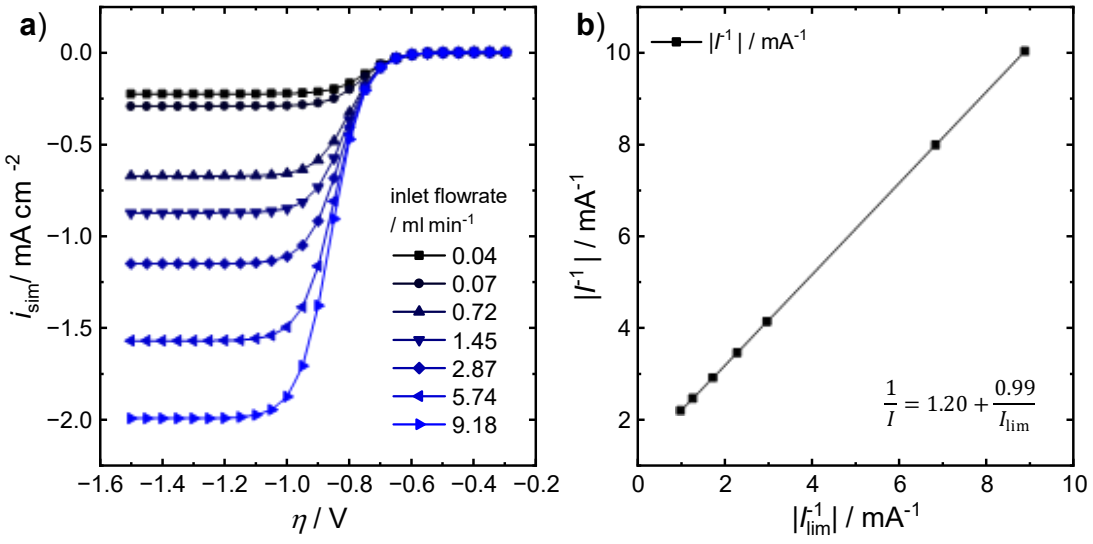

Figure 4.7. a) Simulated polarization curves for the final iEFC design at an inlet volume flow between 0.04-9.18 mL min^{-1} (for half of the inlet's cross-section), obtained from the species flux at the electrode area by multiplication with *z* and *F*. Overpotentials range from 0.3 V to 1.5 V and are plotted as negative values. b) KL plot for the final iEFC design at η = 0.85 V. The black line indicates the linear fit of the simulated data points. The KL slope amounts to 0.99 and the y-axis intercept ($1/I_{kin}$) to 1.20 mA^{-1}.

4.3.2. Electrochemical

Experimental Validation of the iEFC Simulations

To experimentally validate the applicability of the Levich analysis for EFCs and the KL equation for the herein-designed iEFC, shown in Figure 4.1a, the kinetics of the ferricyanide reduction was investigated at different flow rates. Before the experiment, the embedded WE was polished and cleaned according to the above-described standard procedure without the grinding step. A $Hg/HgSO_4$ RE and 10 mM $K_3[Fe(CN)_6]$ in 0.1 M $HClO_4$ as electrolyte were used. From the Ar-purged reservoir with a volume of 200 mL, the electrolyte ran through the flow cell and into an electrolyte waste at different flow rates (0.5, 1, 1.2, 1.3, 1.4, 1.5, 2 mL min^{-1}). The electrolyte volume in this reservoir was kept constant over the course of the experiment by redosing with the same flow rate. For each flow rate, the electrolyte resistance was determined by electrochemical impedance spectroscopy (EIS) (10 Hz – 300 kHz, 10 mV rms) at open circuit potential (OCP), and three linear sweep voltammograms (LSV) from 0.8 to 0 V *vs*. RHE at 2 mV s^{-1} were performed. All data was processed with a custom MATLAB script.

EIS Measurements for the Investigation of the Electrode Positioning in iEFCs

To investigate the applicability of EIS depending on the relative electrode positioning in different iEFC designs (see Figure 5.8 in chapter 5.1.2), EIS measurements were performed in 1 M KOH with a Ni WE (99.0%, Goodfellow). First, the Ni plate WE was ground with 7000 grit size, sonicated in ethanol and ultrapure water for five minutes each, dried, and assembled into the iEFC. A glassy carbon CE as rod (d = 1 mm) or 1x1 cm plate, a Hg/HgO RE, and a flow rate of 1 mL min^{-1} were applied. The WE was conditioned by CV (1-1.45 V *vs*. RHE, 10 mV s^{-1}, 50 cycles). Following, EIS was performed between 300 kHz and 10 Hz at OCP with an amplitude of 10 mV_{rms} and 10 points per decade.

Determination of the Active Surface Area with Ta in the iEFC

The active surface area of the WE was determined by irreversibly oxidizing a Ta WE. The standard WE (Ta, 18 x 24.4 x 0.5 mm) preparation was extended by a preceding grinding step with increasing grit size (2500, 5000) and ultrasonication in ethanol prior to the one in ultrapure water. The active surface area was then defined with a) insulating spray or b) adhesive PTFE with a 1 x 1 cm cutout. To apply the insulating spray, the active surface area was taped. The PTFE foil was cut with a cutting machine and pressed onto the electrode with a hot press (3-4 Nm, T = 21 °C). The electrodes were assembled into the iEFC, incl. a $Hg/HgSO_4$ as RE. The electrolyte $HClO_4$ (75 mL, c = 0.1 mol L^{-1}) was circulated at a flow rate of ≈ 5 mL min^{-1}. The applied electrochemical protocol consisted of applying an OCP (30 s, ± 1mV) followed by LSV (0-12 V *vs*. RHE, 100 mV s^{-1}, step size 1 mV) and two chronoamperometries at 12 V for 3 min. As a result, Ta oxidized irreversibly to form a brown oxide layer. The dimensions of the discolored surface were measured manually with a digital caliper.

Investigation of Electrochemical Conditioning

The experiments to investigate the electrochemical conditioning at lab-scale were conducted in one of the herein-designed iEFCs, shown in Figure 4.1. A Hg/HgO RE and different 1 x 1 cm

Ni-(Fe)-plate WEs were used. The WE was prepared according to the standard procedure described in chapter 4.1. For the experiment, the flow cell was aligned vertically for efficient gas removal from the electrodes. From the Ar- or N_2-purged PTFE reservoir, the electrolyte, 1 M KOH with the desired Fe content, ran through the flow cell in a single-pass with a volume flow of 1 mL min^{-1} (Design A, 1 mm electrode spacing, Figure 4.1a) or 3 mL min^{-1} (Designs B-D, 3 mm electrode spacing, Figure 4.1b-d). For conditioning times longer than 30 min, the electrolyte was circulated and not purged with inert gas to save resources. No significant increase in irreproducibility was observed, as discussed in chapter 5.1.5. A schematic overview of the applied electrochemical protocol can be seen in Figure 4.8a.

The electrochemical protocol consisted of the conditioning and an activity measurement before and after. This activity was determined by first performing EIS at OCP (100 kHz-10 Hz, 10 mV_{rms}), followed by CV (1.0-1.6 V, 3 cycles) at 5 or 10 and 100 mV s^{-1}, and a CP at 10 mA cm^{-2} for 10 min and at 100 mA cm^{-2} for 1 or 5 min. During the electrochemical conditioning, constant polarization (OCP and CP at 100 mA cm^{-2}) and potential cycling were tested as conditioning modes. For the CV conditioning, the upper and lower potential limit, scan rate, hold time at the upper or lower potential limit, and total time or rather number of CV cycles were varied. A schematic illustration of the varied parameters is shown in Figure 4.8b. For a greater understanding of the hold times at the upper and lower potential limit, Figure 4.8c schematically visualizes the potential profiles when CV conditioning is performed with a hold time of 4.4 s at the upper (1.6 V) and lower (0.5 V) potential limit. After the experiment, the iEFC was cleaned by rinsing first with ethanol and then with ultrapure water followed by ultrasonication in ultrapure water for 5 min. The cell was dried in N_2 and stored in a plastic container. Note that different cleaning procedures were tested, such as variations of rinsing and sonicating in diluted HNO_3, ethanol, and ultrapure water. However, the 3D-printing and embedding materials were very sensitive toward sonication in diluted HNO_3 and ethanol. Further, AR-H1 cannot be rinsed with ethanol as it becomes cloudy, which hinders the identification of trapped gas bubbles.

For the investigation of the electrochemical conditioning at an industrially more relevant scale in the flex-E-cell, the same procedure was applied with few differences. Here, the potentiostat booster attached to the Gamry Reference 3000 was required to achieve the high current densities. Regarding electrode preparation, the plate WEs (60 x 40 x 1 mm) were polished with decreasing grain size only down to 0.3 µm. The Ni mesh electrodes were not polished. As CE $Ni_{99.2}$ was used, and before each experiment, it was ground (2000 grit size), rinsed with ethanol and ultrapure water, ultrasonicated in ultrapure water for 5 min, and dried. Before each experiment, the flow was calibrated with water. A flow rate of 80 mL min^{-1} was applied per half-cell (undivided cell: 80 mL min^{-1} total flow rate, divided cell: 160 mL min^{-1} total flow rate). Afterward, the cell was run with electrolyte (1 M KOH at RT; 30 wt% KOH at 80 °C) for 5 min. Regarding the electrochemical protocol, the activity measurement was slightly adjusted to CP at 10 mA cm^{-2} for 10 min, 100 mA cm^{-2} for 5 min, and optionally 500 mA cm^{-2} for 5 min. The CP at 500 mA cm^{-2} was only carried out in the case of a divided cell (Design PLATE) at industrial KOH concentration and temperature.

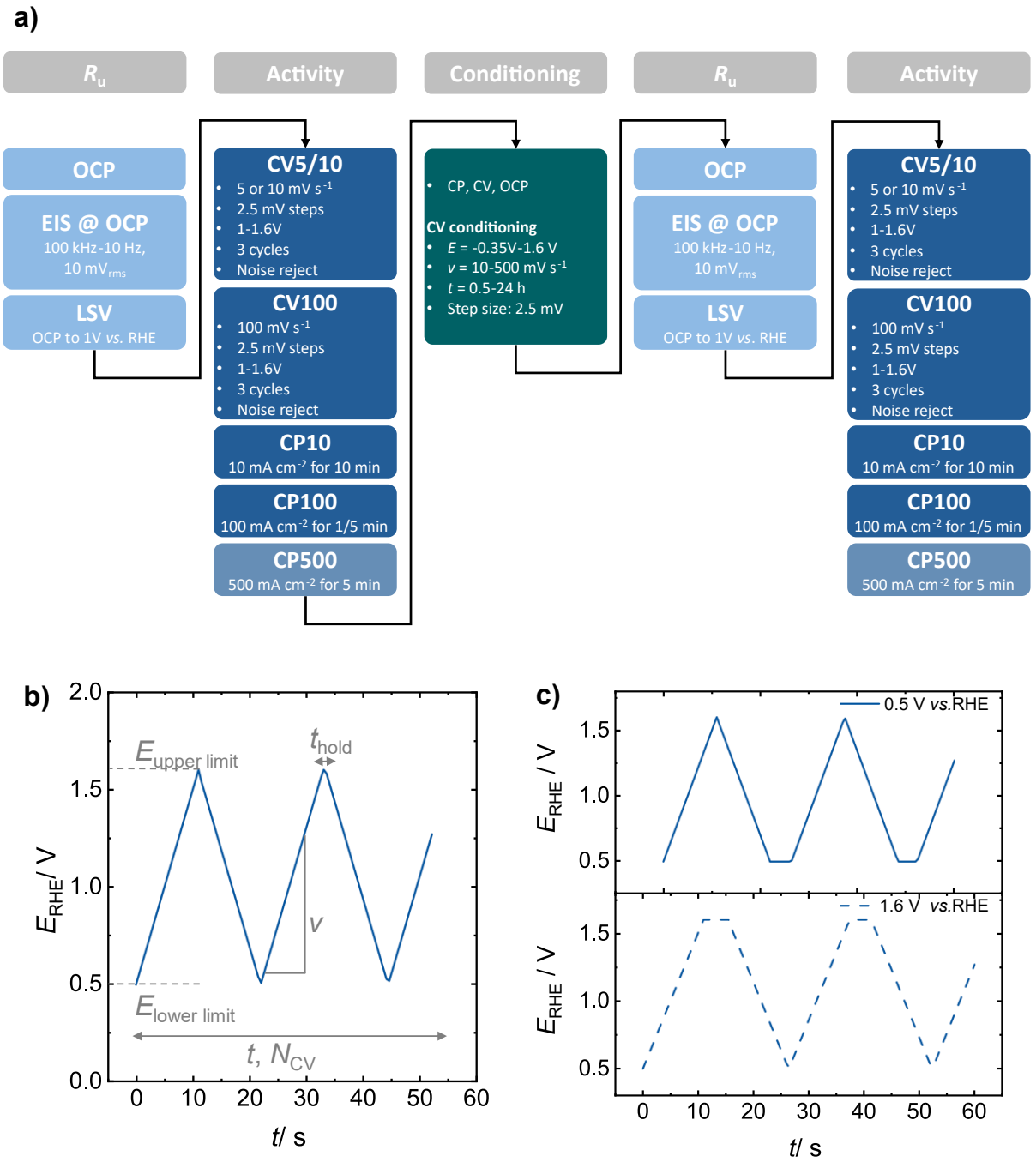

Figure 4.8. a) Schematic overview of the applied electrochemical protocol. The protocol consists of five blocks. First, the electrolyte resistance is determined by applying OCP followed by EIS (100 kHz-10 Hz, 10 mV_{rms}) at OCP. LSV ramps up the potential to 1 V *vs.* RHE. In the second block, the activity of the electrode is determined by three repeating CVs at 5/10mV s^{-1} and 100 mV s^{-1} (1-1.6 V, 2.5 mV step size, noise reject), and a CP at 10 mA cm^{-2} for 10 min, 100 mA cm^{-2} for 1/5 min, and optionally 500 mA cm^{-2} for 5 min. Conditioning by OCP, CP, and CV (E = –0.35-1.6 V, v = 10-500 mV s^{-1}, t = 0.5-12 h, step size = 2.5 mV) is performed in the third block. After that, blocks 1 and 2 are repeated. b) Schematic illustration of the parameterization of the electrochemical CV conditioning. The upper $E_{upper\ limit}$ and lower $E_{lower\ limit}$ potential limit, the scan rate v, the hold time t_{hold} at the upper and lower limit, and the overall time t or rather number of cycles N_{CV} were varied. c) Schematic potential profile of the CV conditioning with a hold time of 4.4 s at the upper (1.6 V) and lower (0.5 V) potential limit, respectively.

Data analysis was done with Echem Analyst and Microsoft Excel. For the experiments in the iEFC, potentials are 100% iR_u-corrected with the resistance from the respective EIS measurement before or after the conditioning. For the experiments in the flex-E-cell, the

reported potentials are not corrected for the iR_u-drop because reliable EIS could not be obtained. As an evaluation parameter of the conditioning efficiency, the activation by conditioning was defined as the difference between the potentials at 10, 100, and 500 mA cm^{-2} before and after conditioning, as seen in equation (4.4):

$$\Delta E_{10/100/500} = \bar{E}_{10/100/500,\text{after}} - \bar{E}_{10/100/500,\text{before}} \tag{4.4}$$

The potentials, measured before and after conditioning, were averaged over the measurement of at least 100 s, resulting in $\bar{E}$. An increase in activation results in a negative $\Delta E_{10/100/500}$ ($E_{10/100/500,\text{after}} < E_{10/100/500,\text{before}}$). For better readability, $-\Delta E_{10/100/500}$ is plotted. Each experiment was performed at least three times, from which the average and the standard deviation were calculated. For the standard deviation, the data set was assumed to be a random sample.

To gain a deeper understanding of the occurring surface processes and their correlation to the activation, the Ni(II)/Ni(III) redox peak of the conditioning and activity CVs at 100 mV s^{-1} was evaluated. The peak areas of the oxidative and reductive peak were integrated using the Echem Analyst. Integration was often difficult as the redox peaks partly overlayed with the OER current and the baseline definition was not always clear. Figure 4.9 shows exemplary how integration was done. The baseline was defined as an extension of the oxidative or rather reductive capacitive current. The integration limits (IL) were set close to the cross-section of the baseline with the CV but were adjusted to account for overlaying processes or when no stable capacitive current could be determined. When the oxidative or reductive peak overlayed strongly with the OER, as seen in Figure 4.9 for the oxidative peak, only half of the peak was integrated, and the obtained area was doubled afterward. As this integration method is very error-prone, the resulting peak areas need to be considered with great care.

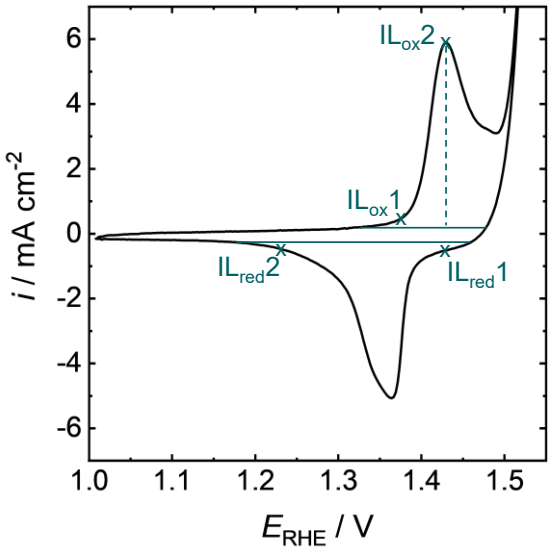

Figure 4.9. Schematic illustration of how the Ni(II)/Ni(III) redox peak was integrated. The baseline was defined as an extension of the oxidative or rather reductive capacitive current. Between the integration limits (IL) the peak was integrated. In case of an overlap of the redox peak with the OER, only half of the redox peak was integrated and the obtained area was doubled afterward.

4.4. Analytics

In the following, the conducted *in-situ* and *ex-situ* characterization techniques will be introduced. For the *ex-situ* electrode characterization after the electrochemical experiment, the electrodes were rinsed with ultrapure water, dried, and covered with Kapton tape for storage or transport. For the inhouse analytic characterization (Scanning Electron Microscopy, Energy Dispersive X-ray Spectroscopy, optical microscopy), the samples were either directly measured or stored under vacuum for a maximum of five days. For characterization by project partners (Fourier Transform Infrared Spectroscopy, X-ray photoelectron spectroscopy), 1 cm^2 $Ni_{99.99}$ and $Ni_{70}Fe_{30}$ plate electrodes were glued onto the embedded WE of the same composition by Ag-containing conductive adhesive for the experiment. After the electrochemical experiment, they were removed, cleaned, packed, shipped, and measured also up to five days after the electrochemical experiment.

4.4.1. Scanning Electron Microscopy and Energy Dispersive X-ray Spectroscopy

In Scanning Electron Microscopy (SEM), the sample is scanned with a focused electron beam to generate a high-resolution image of the sample's surface with up to 500,000x magnification. Thus, surface structures between a few nm to mm can be analyzed. When the electron beam hits the sample, part of the incident electrons is backscattered and another removes electrons, which leave the sample as so-called secondary electrons. The number of detected secondary electrons depends on the surface morphology. For example, if the electron beam hits the sample at a 90° angle the impact area is circular. At a sloped surface, the impact area is enlarged and, thus, more secondary electrons are detected. This relation is used to create a topographical image of the sample's surface.[92]

Energy Dispersive X-ray Spectroscopy (EDX) is often coupled with SEM as it also uses a focused electron beam for sample excitation. In scanning EDX, the elemental composition of the sample is spatially resolved. The removal of core electrons by the electron beam creates vacancies, which are filled by electrons from higher energy levels. If an electron transitions from a higher to a lower energy level, a photon (X-ray) with the respective energy difference will be released. As these electron transitions are element-specific, the element composition can be determined by detecting the wavelengths of the emitted photons.[93]

In this work, microstructural analysis of the electrodes was conducted by SEM using a Hitachi Schottky SU5000 FESEM. 3,000x magnification and an accelerating voltage of 15 kV was used. Elemental compositions were determined using a Bruker EDX, coupled to the SEM, with the accelerating voltage set to 15 kV.

4.4.2. Optical Microscopy

Optical microscopic images of the electrodes were taken by the Keyence VHX7000 microscope with a VHX-7100 head at a 20x magnification (VHX-E20, X20), using a 4K-CMOS camera. The head of the microscope was tilted to capture the reflecting properties of the electrodes. The illumination could be varied between ring (full, partial from four different directions), coaxial, and mixed illumination. Two illumination modes were used: full-ring illumination measured at an angle of 12° and coaxial illumination measured at a 0° angle.

4.4.3. X-ray Photoelectron Spectroscopy

X-ray photoelectron spectroscopy (XPS) measures the elemental composition and the chemical and electronic state of the elements at a material's surface with a measurement depth of approx. 10 nm.[94] Excitation of the sample occurs by X-rays at high vacuum conditions, which results in the ejection of core electrons if the photon energy exceeds the electron's binding energy (photoelectric effect). The kinetic energy of each ejected electron is measured, and the binding energy is calculated from that. The binding energy is characteristic of each element and its chemical state, such as oxidation state and chemical environment. The intensity of the signal at each binding energy corresponds to the number of ejected electrons from that element in the respective state. Thus, the various surface species such as NiO, $Ni(OH)_2$, *etc*. can be quantified.[95]

XPS measurements were performed in collaboration with Julia Gallenberger (AG Hofmann) from TU Darmstadt with a hemispherical energy analyzer from SPECS (PHOIBOS 150) as part of the DAISY-FUN ultra-high vacuum cluster tool. The spectra were acquired using monochromatic Al K_α radiation (hf = 1486.74 eV, with the Planck constant h and frequency f) in fixed analyzer transmission mode. The binding energy calibration of the system has an accuracy of 0.1 eV and was done using sputter-cleaned Ag. The pass energy was 20 eV for the survey scan and 10 eV for the core level spectra and the step size was 0.3 eV and 0.05 eV, respectively. Data analysis was performed with CasaXPS, version 2.3.22.22.[96] For the samples, where Ni metal was present, the calibration was done with the valence band spectrum to the Fermi edge E_F = 0 eV. All spectra that were used for quantitative analysis were fitted with a Shirley background. Peaks in the O 1s were fitted with a GL(30) line shape. The fitting of the O 1s spectra includes carbon and silicon compounds, the area of which was derived from the C 1s and Si 2p, respectively. For all intensity calculations, the relative sensitivity factors published by Scofield were taken.[97]

4.4.4. Fourier Transform Infrared Spectroscopy

In Fourier Transform Infrared Spectroscopy (FTIR), functional groups of (in)organic compounds and their molecular structure are identified by analyzing their absorption of infrared radiation. The chemical bonds within the material vibrate in their natural vibration modes. Vibrational modes can be differentiated into stretching and bending. Depending on whether the molecule is linear or not, 3S-5 (linear) or 3S-6 (nonlinear) vibrational modes are possible, with S being the number of atoms. For a vibrational mode to be IR active, it must induce a change in the molecular dipole moment. If a vibrational mode is IR-active, the molecule absorbs radiation at a specific wavenumber, resulting in a transition to a higher vibrational energy state. The wavenumber depends on the bond strength (single, double, triple) and the average mass of the participating atoms. The different IR-active vibrational modes of the molecule's chemical bonds result in a characteristic fingerprint. Based on the Beer-Lambert law, the absorbance is directly proportional to the concentration of the molecule in the liquid or on the surface. Experimentally, the sample is irradiated and the reflectance or the transmittance of the sample is measured and the negative of it corresponds to the absorbance. In IR, monochromatic radiation is generated by a diffraction grating, which disperses the different wavelengths in space, and beam selection occurs by a slit. Wavelength variation is performed by changing the angle of the diffraction grating. In FTIR, irradiation occurs by

broadband radiation with simultaneous multi-wavelength measurement. An interferometer is used to vary the wavelengths of the radiation. The interferometer splits the initial broadband infrared beam into two by a beam splitter, which are directed to two mirrors. At the mirrors, they are reflected and recombined again at the beam splitter. One of the mirrors is moveable. Depending on the ratio of the mirrors' distances to the beam splitter, different interference patterns result, with different wavelengths present. By the application of this interferometer, the data collection can be significantly enhanced. The resulting interferogram is converted into a spectrum by Fourier Transform (FT).[98,99]

Herein, FTIR spectroscopy was done in collaboration with Julia Gallenberger (AG Hofmann) from TU Darmstadt with a VERTEX 80v FTIR spectrometer (Bruker) using a LN-MCT detector. Samples were measured on a monolayer/grazing angle specular reflectance accessory (Specac), at an incidence angle of 70 ° from 4000 to 400 cm^{-1}. This monolayer/grazing angle reflectance accessory is a device to study thin films, monolayers, or coatings by reflection. The background scan was the polished $Ni_{99.99}$ or $Ni_{70}Fe_{30}$ surface, respectively. Both sample and background scans (1000 scans each) were acquired with a scanner velocity of 40 kHz and a resolution of 4 cm^{-1}.

4.4.5. Inductively Coupled Plasma Optical Emission Spectroscopy

Inductively Coupled Plasma Optical Emission Spectroscopy (ICP-OES) quantifies (semi)metals in liquids from a few ppb to 30 wt%. However, the lower detection limit depends on the element and measurement conditions.[100,101]

The working principle of ICP-OES is based on the excitation of the sample in a high-temperature Ar plasma and the emittance of radiation at element-characteristic wavelengths. How the spectrometer is operated can be seen schematically in Figure 4.10. The Ar plasma is generated by an Ar gas streaming through an induction coil, which operates at radio frequencies and creates a high-frequency electromagnetic field. The Ar atoms are ionized and a plasma with temperatures exceeding 10,000 K is obtained. The temperature of the plasma decreases from the flame's core toward the edges, where temperatures can fall to as low as 6,000 K. In order to introduce the liquid sample into the plasma, the sample is first nebulized into an aerosol using a stream of Ar gas, and larger droplets are removed in the spray chamber. The aerosol is carried into the plasma by another Ar stream. By the heat of the plasma, the sample is desolvated, atomized, excited, and ionized. More specifically, the excitation of an atom or ion elevates an electron from its energy level to a higher energy level or even removes it (ionization). As the excited atoms or ions return to their ground state, they emit photons at characteristic wavelengths, corresponding to the energy required for the respective transitions. The larger the distance between the energy levels, the higher the required energy and the shorter the wavelength of the emitted light. The intensity of light emitted at each wavelength is directly proportional to the number of atoms or ions undergoing the transition. For one element, different transitions are possible depending on the energy uptake. Due to the temperature distribution in the plasma flame, the various excitation processes occur in different regions of the flame. To selectively investigate certain excitations, the light emittance can be viewed radially and the viewing position can be adjusted along the vertical axis of the flame. If very small quantities are to be determined, the signal intensity needs to be maximized by applying axial viewing. The emitted light is dispersed by a diffraction grating in the spectrometer, enabling either simultaneous or sequential detection of multiple emission lines, depending on

the optical configuration and detector type. The relation between light intensity and element concentration is proportional and is quantified by calibration. It needs to be considered that the atom or ion excitation requires energy and decreases the temperature of the plasma. This stresses that the calibration is always required to be performed with the same sample matrix as the measurement. Potential sources for erroneous results in ICP-OES are (non-)spectral interferences. Spectral interferences refer to an overlap of the signal of the element (analyte), which is to be analyzed, with other elements in the sample. If possible interferences are known, they can be circumvented by considerate wavelength selection and post-background correction. Non-spectral interferences can occur due to a change in the sample transport, sample properties, nebulizer properties, nebulizer chamber aerodynamics, or excitation conditions of the plasma. The reason for this is the plasma temperature, which is sensitive to changes in these parameters. Introducing excessive sample quantities into the plasma can cause it to extinguish, as the energy is insufficient to support the processes of vaporization, atomization, and excitation. Working just below the extinguishing limit destabilizes the plasma and leads to poor reproducibility. It is, therefore, important to optimize the sample supply to ensure that the signal sensitivity is high enough and the plasma is not destabilized. For example, the standard sample introduction rate for a concentric nebulizer is around 1 ml min^{-1}.[102] To avoid or correct non-spectral interferences, using the same sample matrix for measuring and calibration, usage of an internal standard, and calibration by standard addition can help. When using an internal standard, it needs to be considered that a correction works only successfully if the interference affects all elements' analytical lines in the same way. This is, however, not given for changes in the excitation temperature of the plasma as each line reacts differently. Thus, it is vital that the wavelength of the element of interest and the internal standard have comparable excitation energies.[102]

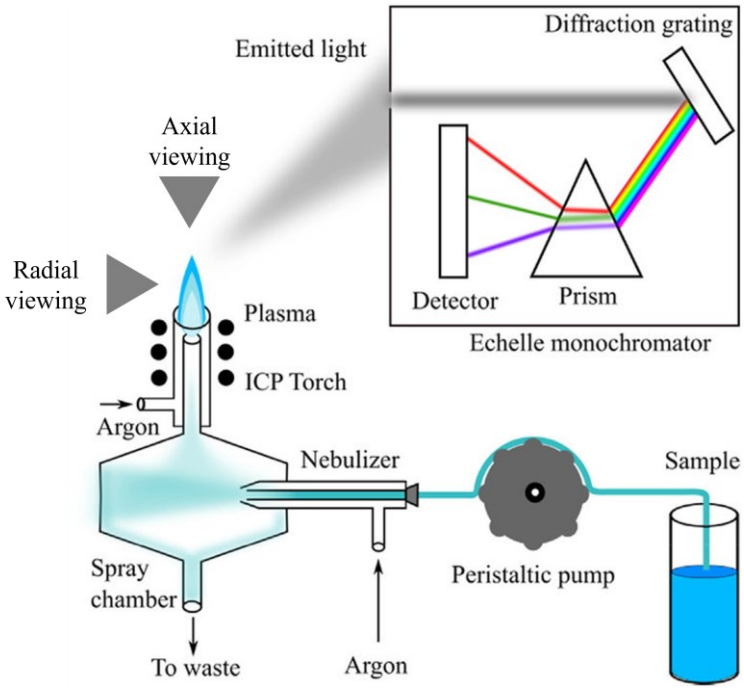

Figure 4.10. Schematic illustration of the basic operating principles of an ICP-OES. [adapted from ref. [103] with permission from Elsevier]

In this work, ICP-OES was performed with an Agilent 5800 VDV ICP-OES system with a concentric standard SeaSpray nebulizer, standard quartz torch, and humified Ar. Axial viewing was applied since concentrations in the ppb-ppm range were of interest. No extra

configurations were selected, such as O_2 injection, drift correction, autosampler, *etc*. Table 4.2 summarizes the operating parameters used for online and *ex-situ* characterization. It needs to be noted that the pump rate of 10 turns per minute corresponds to 1 mL min^{-1} for the white-white coded tubing without plasma. Online ICP-OES was performed with the so-called time scan option. With the time scan option data is continuously recorded without the shutter of the detector being closed. The time resolution corresponds to the measuring time of a single data point since no repeats are done. The minimum measuring time is limited to 3 s. The data can be exported at every point of the measurement as csv-file, but it needs to be done manually.

Table 4.2. Operating parameters for *ex-situ* and online ICP-OES.

Parameter	***Ex-situ***	**online**
Repeats x measuring time / s	3 x 30	1 (time scan) x 3
Stabilizing time / s	25	0
HF-Power / kW	1.2	1.2
View	Axial	Axial
Nebulizer gas flow / L min^{-1}	0.65	0.65
Plasma gas flow / L min^{-1}	12	12
Auxiliary gas flow / L min^{-1}	1	1
Background correction	Automatic	Automatic
Pump rate / U min^{-1}	10	10

The element-characteristic wavelengths measured in different experiments of this work are listed in Table 4.3. When choosing the wavelength, at which the element is quantified, a high intensity and little interference with other elements are essential. Based on this, the elements' wavelengths are ranked in the Agilent software. The wavelength with the highest intensity is usually ranked highest. Two to three wavelengths were measured for each element to be able to check the trends against each other. The wavelengths, that were ranked highest in the Agilent software, were selected. The highest-ranked wavelength was used for data processing, as indicated in Table 4.3. When measuring in 1 M KOH, insensitive wavelengths were chosen for K to avoid overloading the axial detector. Ar, marked as the internal standard, was determined as the temperature sensor of the plasma. Drifts in the Ar signal likely result in a shift of the other elements' signals, falsely suggesting a change in element concentration. Drifts of the Ar signal can occur from a change in the sample matrix, too little stabilization time, or long-term plasma operation and a change in the Ar plasma temperature over time.

Table 4.3. Measured Ar, Ba, Fe, K, and Ni wavelengths with ICP-OES for online and *ex-situ* measurements.

Material	Wavelengths (nm)
Ar	420.067
Ba	**455.408**, 493.408
Fe	**238.204**, 259.94
K	404.721, **404.414**
Ni	**231.604**, 216.555, 221.648

For *ex-situ* ICP-OES to determine the Fe content in 1 M KOH, quantitative wavelength calibration was performed by adjusted standard addition. Calibration by standard addition is required when the sample matrix is complex and cannot be reproduced for the calibration standards or when the reproduced sample matrix for the calibration standards contains an unknown amount of the analyte. Here, the latter is the case. For calibration by standard addition, the calibration standards are made from the sample solution, and the analyte of interest is added in different amounts (addition A1-A3). It needs to be noted that the volume of the sample solution is fixed for all additions A0-A3 and its volume fraction of the total calibration solution should be as high as possible (> 90%). Figure 4.11 shows how the concentration of the sample can then be determined by extrapolating the calibration curve to the x-axis.[104]

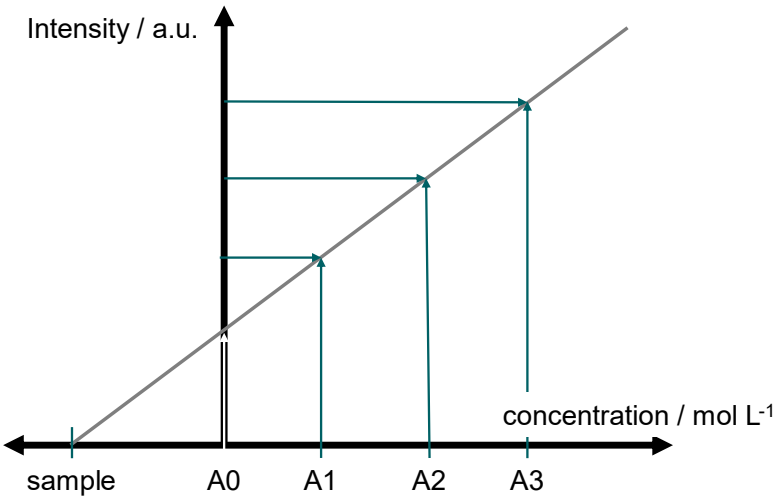

Figure 4.11. Schematic illustration of how to determine a sample's analyte concentration when performing standard addition calibration. By extrapolating the calibration curve to the x-axis, the concentration of the sample is determined.

In this work, the sample solution was not used as a solvent for the calibration standards, but any commercial 1 M KOH, which contained an unknown amount of Fe. The Fe concentration of the calibration standards was then adjusted to 10+x ppb, 100+x ppb, and 500+x ppb, with x being the unknown Fe concentration of the commercial 1 M KOH. In the Agilent software, the following calibration settings were chosen: calibration by standard addition, no consideration of a blank solution, the minimum correlation was set to 0.9, and the calibration error to 100%. No weighted fit was used. It is important to note that by choosing "calibration by standard addition" the first sample measured is defined as the blank sample solution (addition A0), in

this case, the commercial 1 M KOH. Between each (calibration) sample, ICP-OES was run with ultrapure water. When assessing the data, it is vital to ensure that the Ar-ratio (internal standard) is 1±0.1, indicating a constant plasma temperature during calibration and sample measurement.

Online ICP-OES of the electrolyte coupled to the iEFC was applied to investigate the behavior of $Ni_{99.99}$ and $Ni_{70}Fe_{30}$ as OER anodes in 1 M KOH. The WE electrode preparation, CE and RE choice, and cell assembly were employed according to the procedure described in *Investigation of Electrochemical Conditioning in the iEFC* in chapter 4.3.2. The electrolyte ran through the vertically aligned flow cell into the ICP-OES with 1 mL min^{-1} from the Ar-purged PTFE reservoir. Before starting the electrochemical protocol, a baseline of at least 5 min was recorded. The setup can be seen in Figure 4.12. The time required for the electrolyte to travel from the iEFC to the torch was determined by correlating the performed electrochemical operations to the observed concentration changes. Alternatively, a separate calibration experiment, such as Ni dissolution in 0.1 M $HClO_4$, can be performed to correlate the electrochemical operation with the respective concentration change. In this case, it is important that the same tubing is taken for the calibration and the experiment of interest. Calibration (3 points between 10-500 ppb [*e.g.* 10, 100, 500 ppb] + blank, in 1 M KOH, 5 min per calibration point) was performed separately, and ICP-OES was run with ultrapure water between the calibration points. The signal was averaged over 3 min. Data evaluation was done with a custom Python script. Spectra were smoothed with a moving average over 3 data points. If intense gas evolution was observed, the outlying data points were omitted with no trends modified. The Python script further offers the possibility of integrating the peaks with respect to the baseline between manually defined timeframes.

In order to elucidate the peak smearing behavior when coupling the ICP-OES with the herein-designed iEFC, a Ni dissolution experiment was conducted with a $Ni_{99.99}$ WE, a glassy carbon CE, and a $Hg/HgSO_4$ RE in 0.1 M $HClO_4$. The experimental procedure as described above was conducted. Before the experiment, the CE was additionally ground (2500, 5000 grit size), ultrasonicated in ultrapure water for 5 min, and dried. The calibration was performed with 0.1 M $HClO_4$ as solvent. As electrochemical protocol, an OCP was applied first, followed by CV conditioning (0.056-1.256 V *vs*. RHE, 200 mV s^{-1}, 30 cycles), a 15 min pause, and 10x a CP at 1 mA cm^{-2} for 10 s with a 10 min pause each time.

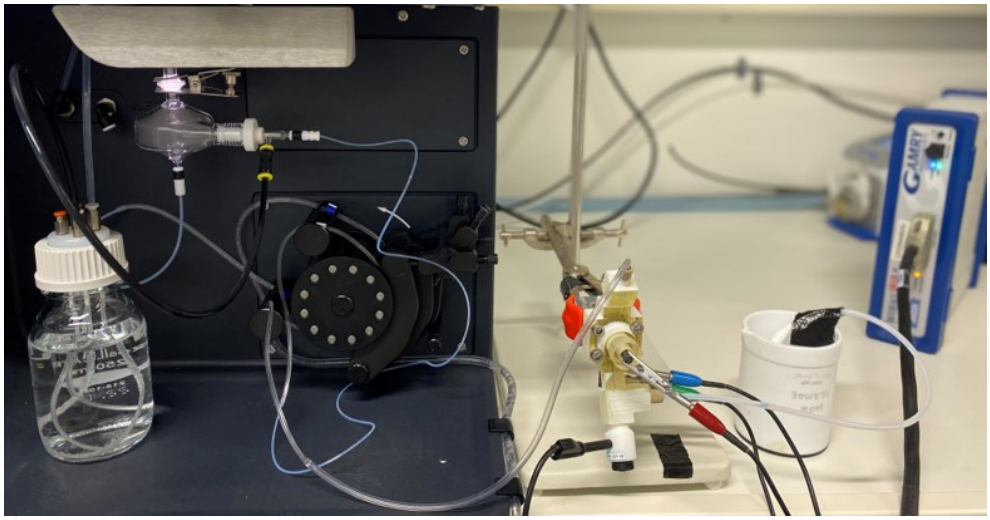

Figure 4.12. Picture of online electrolyte monitoring by ICP-OES during electrochemical operation in iEFC.

4.4.6. Fourier Transform alternating current Voltammetry

Theoretical Background

In Fourier Transform alternating current Voltammetry (FTacV), a sine wave with an amplitude and a frequency *f* is superimposed on a direct current (dc) ramp $E_{dc} = E_{t=0} + vt$, as seen in Figure 4.13.[105–107]

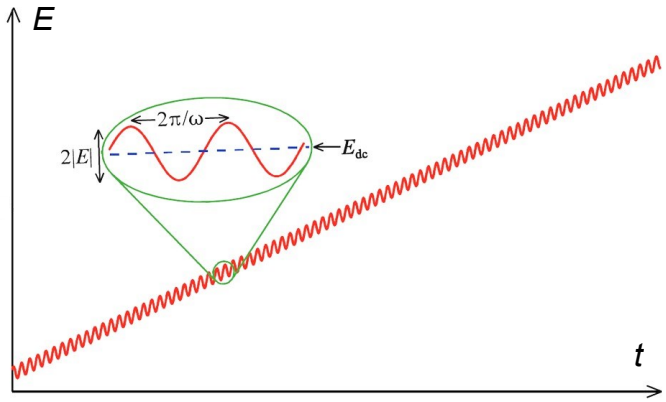

Figure 4.13. Schematic illustration of the applied potential in a FTacV. A sine wave is superimposed on a dc ramp. [adapted from ref. [106] with permission from American Chemical Society]

If the amplitude is small, the current response will be pseudo-linear with respect to the potential and will give a single sine wave over time at the applied frequency. If the amplitude is large enough, non-linearity from charge transfer reactions is introduced. The resulting current over time can be represented by a sum of sinewaves each with a frequency at a multiple of the fundamental (applied) frequency. These sinewaves at the respective frequencies translate into the harmonic components. The data analysis process to filter out these harmonics is illustrated in Figure 4.14.

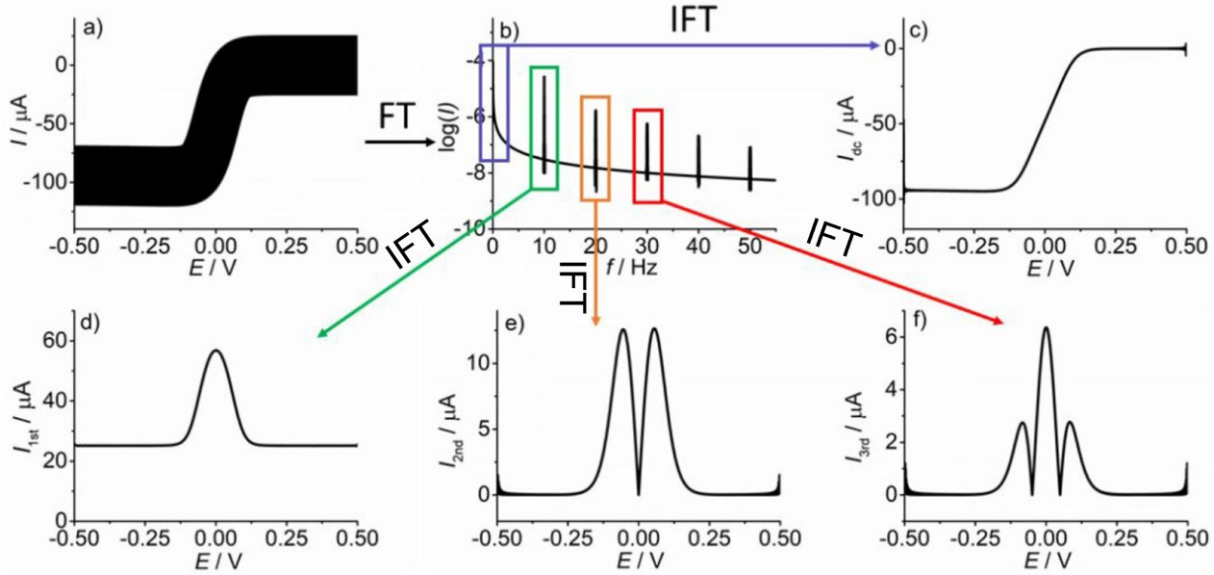

Figure 4.14. Schematic representation of how to extract the harmonics from the measured total current during FTacV. a) Raw data from FTacV measurement is converted by FT into the b) power spectrum. Each harmonic is filtered by applying a window filter at a multiple of the fundamental (applied) frequency. IFT reconverts the data from the frequency in the time domain obtaining sinusoidal perturbations with a multiple of the fundamental frequency. The positive envelope of these sinusoidal perturbations gives the depicted c) dc voltammogram, d) fundamental, e) second, and f) third harmonics. The time domain is converted into the potential scale by $E = E_{t=0} + vt$. [adapted from ref. [106] with permission from American Chemical Society]

For data analysis, 2^N data points are required, with N being an integer between 14-20. First, FT converts the current–time data into a power spectrum over frequency. Note that the time domain is converted into the potential scale by $E = E_{t=0} + vt$. Each n^{th} harmonic is extracted by using a bandwidth (BW) filter (nf - BW < nf < nf + BW), which nulls the contributions outside this window.[105–107] This rectangular window can be convoluted with a Gaussian profile to minimize contributions at the edges of the window, also referred to as 'ringing'.[108] By inverse FT (IFT), the data is converted back to the time domain obtaining sinusoidal perturbations with a multiple of the fundamental frequency. The positive envelope of these sinusoidal perturbations gives the dc, fundamental, and higher harmonics.[105–107]

The dc, fundamental, and higher alternating current (ac) harmonics are differently sensitive to (non-)linear processes. The dc and fundamental harmonic are more sensitive to linear processes such as capacitive current. Higher harmonics are mainly dominated by non-linear electrochemical processes such as electron transfers and are insensitive to contributions from slow electron transfers and background charging. Thus, FTacV is a tool to detect dc underlying processes, to separate overlapping processes based on differences in kinetics or linearity of response, and to determine the electrochemically active site density, turn-over-frequency, and kinetics of a redox reaction. dc Voltammetry can be used to determine E^0 of the redox reaction, the catalytic current, the charge passed to quantify the number of species involved in the charge transfer, and to estimate the diffusion coefficient. From the fundamental harmonic, C_{dl} can be extracted, and from higher harmonics, the kinetic parameters, such as the reaction rate constant k_0, the charge transfer coefficient, and the diffusion coefficient of the reactants. For that, the shape, position, and magnitude of the peaks in the harmonics are evaluated. These are affected by the scan rate, amplitude, and frequency of the FTacV and the uncompensated resistance R_u, double layer capacitance C_{dl}, and kinetics of the redox reaction. This complex interplay makes interpretation difficult and is often assisted by simulating the system.[105–107,109] Still, in the following, the effect of scan rate, amplitude, and frequency of the FTacV, as well as the uncompensated resistance, double layer capacitance, and kinetics of the redox reaction on the harmonics will be qualitatively described for a one-step charge transfer following: O* + $e^- \rightleftharpoons$ R*. Figure 4.15 gives an exemplary visual overview of different scenarios when varying R_u, C_{dl}, and k_0.

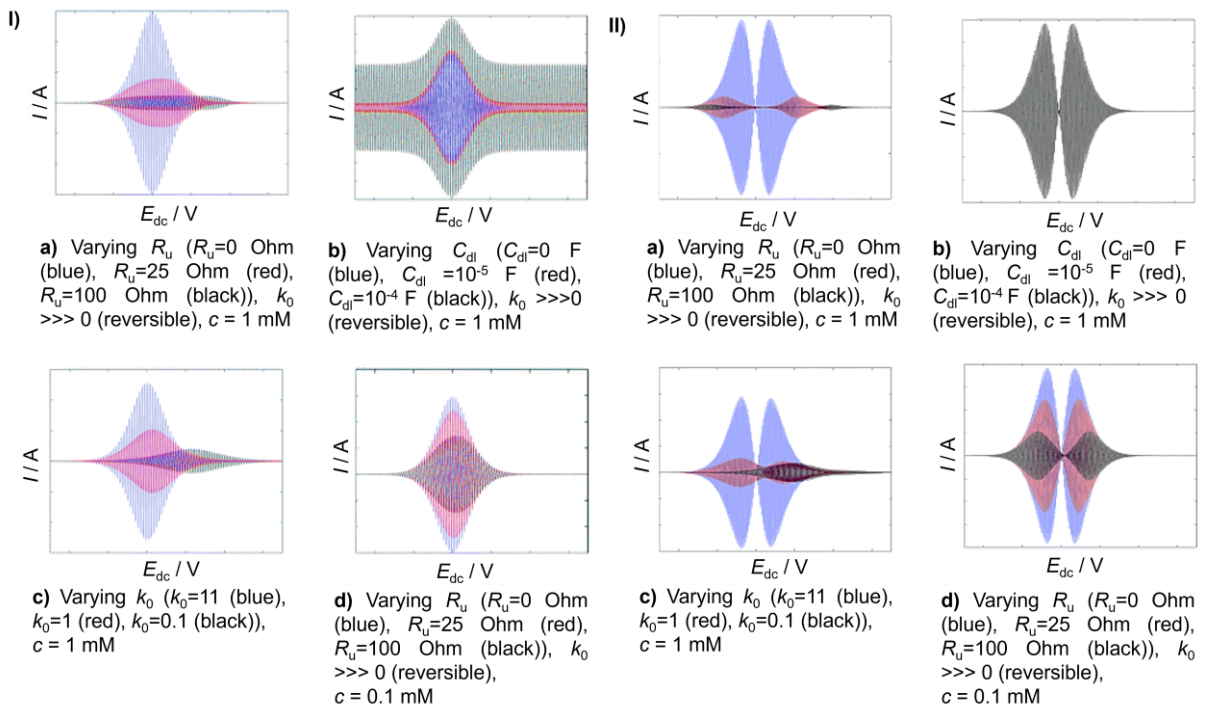

Figure 4.15. Comparison of simulated a) fundamental and b) second harmonics from FTacV for a one-step charge transfer process with varying R_u, C_{dl}, and k_0. [adapted from ref. [109] with permission from American Chemical Society]

Uncompensated resistance

The uncompensated resistance R_u reduces the absolute magnitude of harmonic currents. Further, it can distort the shape of the higher harmonics. Figure 4.15 illustrates in (I)a,d and (II)a,d this decrease in magnitude and an additional flattening of the fundamental and second harmonics with increasing R_u. The peaks of the second harmonic (Figure 4.15(II)a) move apart from one another with increasing R_u.[105–107,109] Previous reports further stated that for a very large R_u of 200 Ohm, peak splitting can be observed in the uneven higher harmonics (3rd, 5th, *etc.*).[107,110] Thus, knowledge of the R_u by independent determination is vital for interpretation.[105–107,109]

Double layer charging capacity

Capacitive currents add to the total current and lift the baseline in the dc and fundamental harmonic envelope, as seen in Figure 4.15(I)b. This increases the influence of the IR_u drop on the harmonics.[106,109] Higher harmonics (> 1st) are usually insensitive to such a contribution from C_{dl}. However, it is also possible that capacitive currents change with potential, as shown exemplarily in Figure 4.16, producing a non-linearity, which induces a response in the higher-order harmonics. This effect, however, usually occurs only up to the 3rd harmonic, allowing the fourth and higher harmonic components to remain unaffected by capacitive currents. The lower harmonics can also be corrected by empirically fitting the fundamental harmonic and incorporating the results for the experiment's simulation.[111]

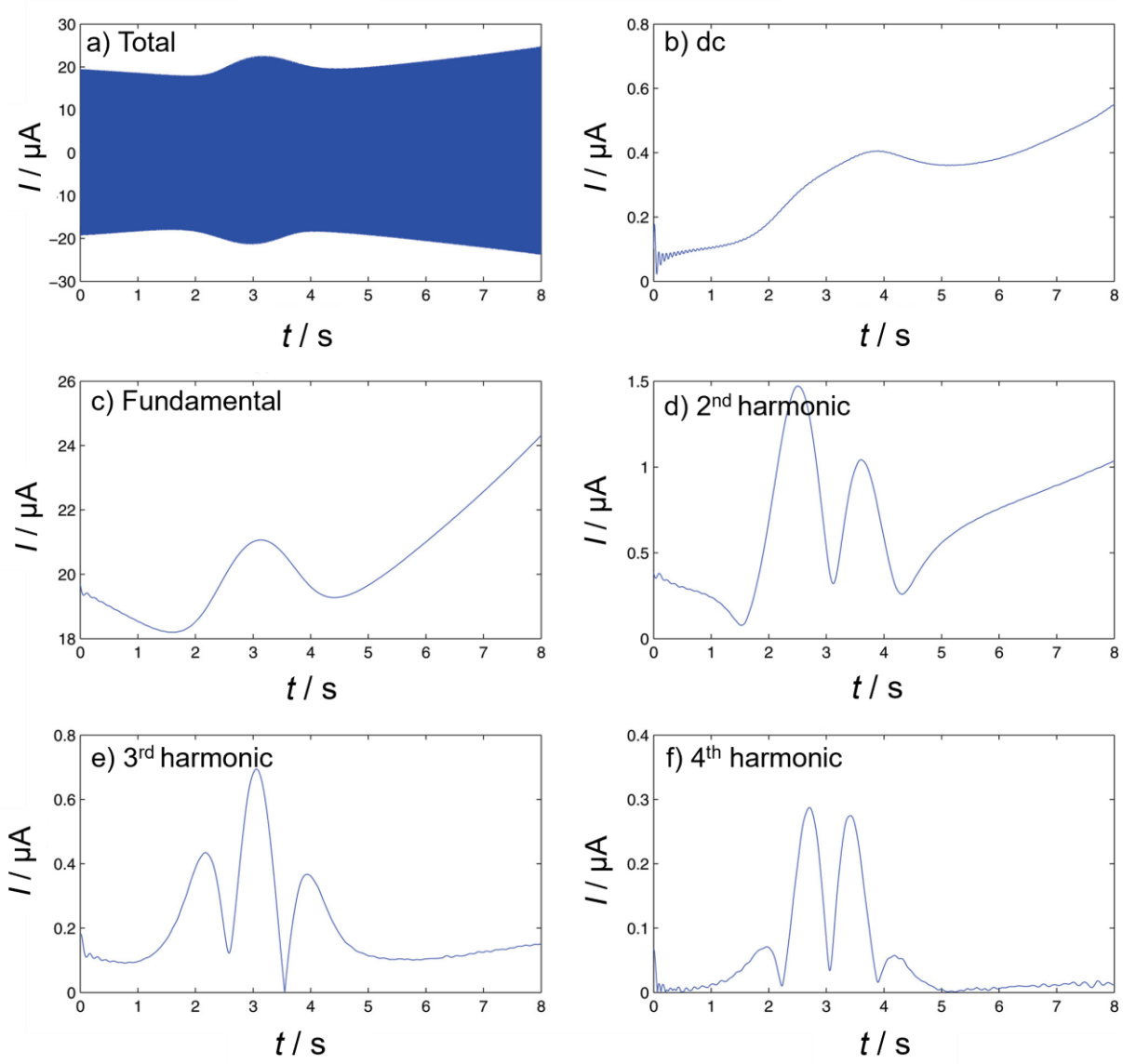

Figure 4.16. Exemplary FTacV, showing the influence of a nonlinear background capacitance on a) total current, b) dc component, c) fundamental, d) 2nd, e) 3rd, and f) 4th harmonics. The presented data shows ac LSV for the oxidation of ferrocene monocarboxylic acid (0.087 mM) at a glassy carbon electrode in aqueous 1.0 M NaCl at 295 K. [adapted from ref. [111] with permission from American Chemical Society]

Number of active sites, reaction rate constant, and charge transfer coefficient

Regarding the influence of the reaction kinetics on the harmonics, it needs to be considered that the apparent reaction rate of a redox reaction is the result of the number of active sites, mass transport phenomena, and intrinsic activity (reaction rate constant, charge transfer coefficient). Applying FTacV with a low frequency to a comparably fast faradaic process, the process can be considered reversible and the harmonics are less sensitive to changes in the intrinsic activity. Instead, the magnitude of the harmonic peak grows as the number of active sites increases.[112] Applying FTacV with a high frequency to a relatively slow faradaic process, the process behaves quasi-reversible and the harmonics become highly sensitive to changes in the intrinsic activity. Compared to fast and reversible redox kinetics, slow kinetics (small k_0) decrease the signal magnitude, can deform the harmonics, and shift the peak potential to higher potentials, as seen in Figure 4.15(I)c and (II)c.[107,109] For very large reaction rates

(reversible), the harmonic components are symmetrical. Smaller reaction rates (quasi-reversible) and a current response sensitive to the reaction rate cause the symmetry of the even harmonics to be highly sensitive to the charge transfer coefficient. This sensitivity intensifies with higher harmonics.[107] A symmetrical harmonic implies a charge transfer coefficient *α* of 0.5 and a non-symmetrical an α smaller or larger than 0.5.[109]

Scan rate and frequency

To ensure that the dc and ac time scales do not overlap, the applied frequency needs to be sufficiently large compared to the applied scan rate. The higher the applied frequency is, the faster charge transfers can be analyzed. A low sine wave frequency would be sufficient to determine the reaction rate constant of a slow charge transfer process. For fast charge transfers, high frequencies are required.[106] A higher frequency improves the signal-to-noise ratio since the overall noise stays constant, but the noise is spread across more frequencies.[105]

An overlap of the dc and ac time scales would be visible in the power spectrum by an exponentially decaying baseline instead of a horizontal line and a low harmonic contribution. In order to extract the harmonics in case of an overlap, the dc component can be experimentally fitted from the signal and subtracted.[109] In any case, it must be considered that the aperiodic dc components from the FTacV measurement will not be identical to the respective dc voltammogram since large amplitude FTacV accentuates the non-linear processes (amplitude-dependent Faradaic rectification).[105]

Sine wave amplitude

Increasing the amplitude generates higher harmonics and increases the harmonic currents, including the capacitive current. This will also increase the IR_u potential drop, lowering the harmonic currents and deforming their shape. If multiple redox species with similar redox potentials are present, an increase in amplitude decreases resolution due to an overlapping of the generated currents. Therefore, the amplitude should be just large enough to generate analyzable harmonics. Typically, applied amplitudes for large amplitude FTacV vary between 80-250 mV.[106]

Experimental

This work used FTacV as a highly sensitive technique for characterizing the electrochemical surface transformations occurring on $Ni_{99.99}$ and $Ni_{70}Fe_{30}$ from conditioning. The same procedure, regarding electrode choice and preparation, cell setup, and electrochemical protocol, as in chapter 4.3.2, *Investigation of electrochemical conditioning in iEFC,* was applied. The experiments were performed in the iEFC (Design C), shown in Figure 4.1c, with a Biologic VSP-300 potentiostat. The WE ($Ni_{99.99}$, $Ni_{70}Fe_{30}$) was downsized to 0.126 cm^2 by using a rod electrode to reduce the absolute currents generated.

FTacV was conducted at the start and end of the electrochemical protocol and before and after conditioning, as seen in Figure 4.17. FTacV was performed as CV between 1-2 V *vs.* RHE at 19.073 mV s^{-1} at approx. 9, 39, and 89 Hz. Each CV with a respective parameter set was repeated three times.

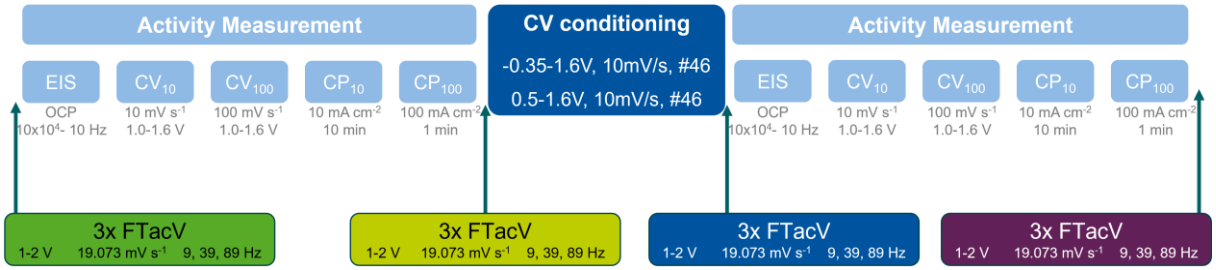

Figure 4.17. Schematic representation of the applied electrochemical protocol to investigate the electrochemical conditioning of $Ni_{99.99}$ and $Ni_{70}Fe_{30}$ by FTacV. FTacV was performed as CV between 1-2 V *vs*. RHE at 19.073 mV s^{-1} at 9, 39, and 89 Hz at the start of the electrochemical protocol (green), before conditioning (light green), after conditioning (blue), and at the end of the electrochemical protocol (purple). All CVs were repeated three times.

The exact FTacV parameters (frequency *f*, scan rate *v,* sampling frequency f_s) were determined by the relations in equations (4.6) and (4.7). These can be deduced from the different definitions of the total time t_{FTacV} of the FTacV:

$$t_{\mathrm{FTacV}} = \frac{B}{f} = \frac{2^N}{f_s} = \frac{\Delta E}{\nu} \tag{4.5}$$

The total time equals the number of sine waves *B* divided by the frequency of these sine waves *f*. Further, it can be calculated by the ratio of the overall number of data points (2^N) to the sampling frequency f_s. Lastly, the total time corresponds to the potential window screened ΔE (for CV: $\Delta E = 2(E_{high}-E_{low})$) divided by the scan rate *v*.

To solve equations (4.6) and (4.7), the premise was that *B* and *N* are integers, with *N* required to be between 16-20. The more data points (2^N), the higher harmonics can be resolved.[113]

$$v = \frac{2f_s(E_{\mathrm{high}} - E_{\mathrm{low}})}{2^N} \tag{4.6}$$

$$f = \frac{f_s B}{2^N} \tag{4.7}$$

Data evaluation was performed by a self-written Python script. The power spectrum (= $\log(I^2)$) was calculated from the absolute FT current, normalized to the length of the signal. For the envelope of the harmonic currents, the positive part of the real IFT current was taken.

5. Results and Discussion

5.1. Design of an Electrochemical Flow Cell with 1 cm² Electrodes for Performance Studies of Electrocatalytic Reactions

The following chapter discusses the simulation-assisted design of an EFC with a WE area of 1 cm^2 for coupling with online downstream analysis and simultaneous activity determination of the electrocatalyst, the so-called iEFC. Parts of this chapter are published in *J. Electrochem. Soc.* **2025,** *172,* 126501.[114] To evaluate the flow cell design, COMSOL Multiphysics is used to model fluid flow velocity, concentration distribution, and particle flux of the reactive species over the electrode surface. The simulations and data analysis were performed by C. Marcks and their methodology can be read in chapter 4.3.1 *Simulative Procedures*. Flow velocity, concentration, and species flux distribution were analyzed qualitatively. Quantitatively, the precision of the activity determination was measured by the deviation of the KL slope from one and the so-called *G* value. The *G* value describes the deviation of the simulated kinetic current density $i_{kin,sim}$, obtained from the KL plot, from the kinetic current density $i_{kin,input}$, calculated with the input parameter according to Butler-Volmer. It served as evaluation parameter *G* for the homogeneity of the mass transport and, thus, i_{lim} over the electrode, and it is defined as:

$$G = \frac{i_{\mathrm{kin,sim}} - i_{\mathrm{kin,input}}}{i_{\mathrm{kin,input}}} \cdot 100 \qquad (5.1)$$

First, the reported iEFCs, namely the scaled-up versions of the SFC from Mayrhofer *et al.* and the V-shaped EFC (V-EFC) from Schlögl *et al*. with an electrode area of 1 cm^2, are simulated. Based on this, criteria are established for designing an iEFC and ensuring a precise activity determination over a wide potential range and minimal dilution of reaction products. To investigate the influence of mass transport of the reactive species to the electrode on the precision of the activity determination, uniform accessibility and uniformity of convective mass transport over the WE are varied. A prototype of the final design is 3D-printed. The simulations and applicability of the kinetic analysis for electrocatalysts are experimentally verified for the ferricyanide reduction as an electrochemical model reaction. Based on this designed iEFC, options for defining the WE's and CE's surface area are tested. Additionally, it is explored how the potential can be precisely controlled and determined for the OER during constant current operation at industrially relevant conditions. Lastly, online monitoring of the Fe concentration during CV and CP at 10 mA cm^{-2} is tested with a Ni-Fe WE in 1 M KOH at RT.

5.1.1. Simulation and Experimental Validation of Mass Transport

Simulation of the Scale-up of the reported SFC[38,40] and V-EFC[37]

In order to find a suitable iEFC for 1 cm^2 electrodes, the prominent flow cells for coupling with ICP-OES were investigated for scale-up. The flow geometry of the SFC from Mayrhofer *et al*. and the V-EFC from Schlögl *et al*. can be seen in Figure 5.1. The SFC cell design consists of two intersecting channels in a V-geometry with 60° between the channels, forming an elliptical opening at the bottom of the cell. The CE is placed into one of the channels and the RE is connected to the respective other channel by a capillary or T-connector.[36,38,40] In contrast to the SFC, the flow channels of the V-EFC intersect at their outer walls and it features a circular

opening, resulting from an O-ring-sealing. The RE and CE are placed in the channels.[37] For the scale-up, the electrode area was fixed to 1 cm^2.

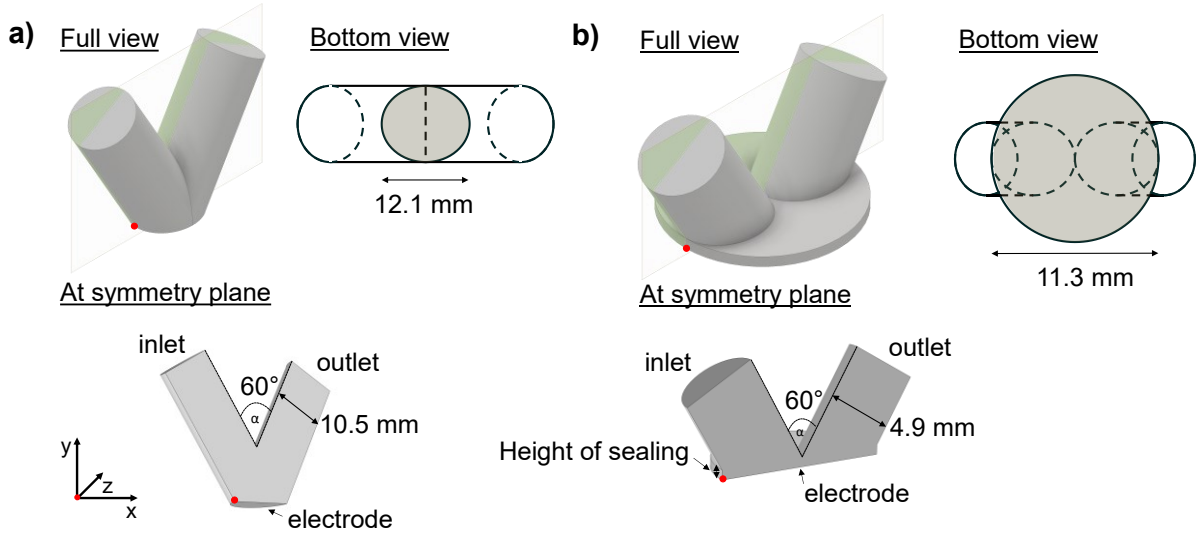

Figure 5.1. Scheme of flow geometries utilized for the numerical simulations of a) the SFC and b) the V-EFC, with a) α = 60°, *d*(channel) = 10.5 mm, 1 cm^2 electrode b) α = 60°, *d*(channel) = 4.9 mm, 1 cm^2 electrode, sealing height of 0.64 mm.

The simulation results for the flow velocity distribution, concentration distribution, and species flux in a mass-transport-limited case can be seen in Figure 5.2 for a volume flow of 1.45 mL min^{-1} at the inlet and an overpotential of 1.5 V. Please note that here and in the following, the volume flow is defined for the inlet's cross-section of the simulated cell width, which is half of the entire cell due to the symmetry plane. Hence, the flow rate is given for half of the inlet's cross-section. The flow velocity (a, d) and concentration (b, e) distribution are shown at the central x-y plane of the cell (z = 0), corresponding to the symmetry plane in the middle of the channel. The species flux at the electrode is shown in the x-z plane (y = 0) from the channel wall to the symmetry plane.

In Figure 5.2a, the flow velocity distribution for the SFC shows a maximum velocity of 1.1 mm s^{-1} in the middle of the channel and no turbulences, such as a vortex. Note that due to the V-shaped channels, the flow velocity distribution is not uniform over the WE. The highest velocity can be found at the intersection of the channels, while there are regions with lower flow velocity toward the outer channel walls (toward x = 0 and x = 12). The corresponding concentration distribution (see Figure 5.2b) shows a non-uniform distribution over the WE. At the electrode, the concentration of active species is zero due to its consumption. Along the electrode with increasing x, the reaction species is continuously consumed, the concentration gradient decreases, and the diffusion layer grows as diffusion is too slow for equilibration. At the symmetry plane (z = 0, central x-y plane), the diffusion layer thickness varies from approx. 1 mm at the inlet (x ≈ 0) to 3 mm at the outlet (x ≈ 12). Figure 5.2c shows the species flux at the electrode and demonstrates more clearly how this non-uniformity evolves along the electrode in the x-direction. The maximum species flux of 22 µmol m^{-2} s^{-1} occurs at the start of the electrode (x ≈ 0) and rapidly drops to approx. 5 µmol m^{-2} s^{-1} after less than 1 µm along the electrode. Until approx. 3 mm (x ≈ 3), the species flux stays relatively constant with a slight increase in the species flux resulting from the increase in flow velocity over the WE toward the center of the electrode. After that, the species flux continues to decrease to a minimum of

0.9 µmol m^{-2} s^{-1}. The increase of species flux at the end of the electrode cannot be explained physically and is probably an artifact from simulation. It should also be noted that only a few data points that have been connected to form a surface lead to this behavior. Along the z-axis, the species flux decreases toward the cell walls (toward z = –5). The average species flux over the WE is 3.8 µmol m^{-2} s^{-1}.

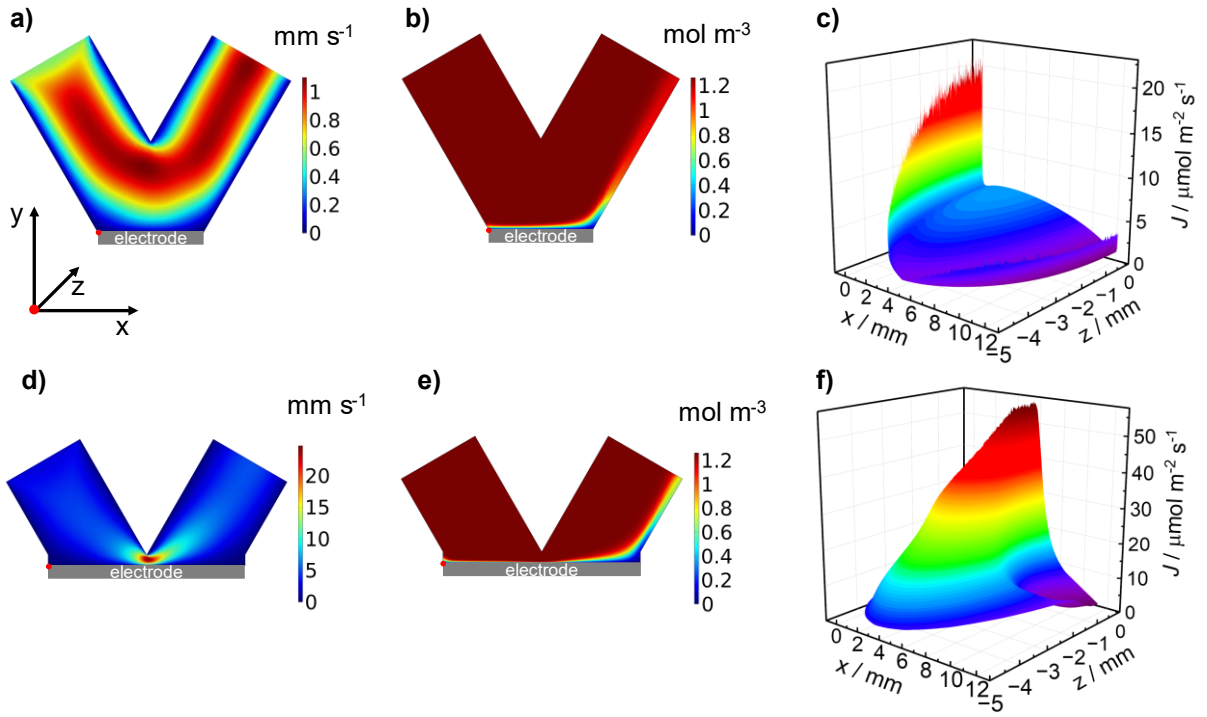

Figure 5.2. Flow velocity distribution (a, d) and concentration distribution (b, e) at the central x-y plane of the cell (symmetry plane) and species flux at the electrode (c, f) for the SFC from Mayrhofer *et al*. (a-c) and the V-EFC from Schlögl *et al*. (d-f). The average inlet volume flow is 1.45 mL min^{-1} (for half of the inlet's cross-section), and the overpotential is 1.5 V. The scale ranges from 0-1.1 mm s^{-1} (a), 0-24.7 mm s^{-1} (d), and 0-1.26 mol m^{-3} (b, e).

Qualitatively, these results reflect the previous simulations for the smaller SFC version by Kulyk *et al*.[38] However, the absolute maximum velocity and, thus, i_{lim} is about 17x lower for the scaled-up version despite the larger inlet volume flow of 1.45 mL min^{-1} compared to 1 mL min^{-1}. This indicates a smaller kinetic regime, in which the material properties can be analyzed. The KL evaluation identifies a KL slope of 1.0, which indicates a more homogeneous i_{lim} over the electrode area and, thus, a better applicability of the KL analysis compared to the reported 0.94 in the case of the small cell model.[38] However, the discrepancy between the small cell model and the one simulated here is more likely due to slight differences in the simulation, *e.g*. the meshing. When applying downstream online analysis such as ICP-OES, the maximum volume flow is restricted to avoid non-spectral interferences, as described in chapter 4.4.5. Such a low volume flow would result in a lower mass-transport-limited current and, thus, an earlier onset of the mass transport limitation. The resulting small kinetic regime of the scaled-up SFC would, therefore, highly limit its applicability for the analysis of the catalyst's kinetics.

For the V-EFC, the flow velocity distribution in Figure 5.2d shows a laminar flow in the channels with a maximum of 4.5 mm s^{-1} in the middle of the channel. When meeting the electrode, the flow accelerates at the intersection of the channels to a maximum of 25 mm s^{-1}. The flow velocity decreases toward the cell walls (toward x = 0, x = 11, z = –5, and z = 5). The resulting

concentration distribution (Figure 5.2e) is non-uniform and asymmetrical. The smallest diffusion layer thickness of 0.14 mm is allocated at the highest flow velocity over the WE. The largest diffusion layer thickness of 2.3 mm is obtained at the outlet (toward x = 11). The corresponding species flux (Figure 5.2f) shows a maximum of 56 µmol m^{-2} s^{-1} in the center of the electrode, where also the highest flow velocity over the WE and smallest diffusion layer thickness is. The centrally allocated and high species flux decreases in all directions. Along the x-axis, it decreases slowly toward the beginning of the electrode and more rapidly toward the end of the electrode. The asymmetrical distribution of species flux and concentration might result from a trade-off between high flow velocity, which is very localized in the center over the electrode, and axial diffusion along the electrode in the direction of the flow. The average species flux over the electrode is 19 µmol m^{-2} s^{-1}, which is significantly higher than that of the scaled-up SFC and indicates a larger kinetic regime. The KL evaluation identifies a small deviation of the KL slope of 1% from one. To evaluate the geometries further, a more sensitive measure is required, and for that, the *G* value is taken in the following. For the scaled-up SFC, the *G* value equals 5%, and for the V-EFC, *G* is 7%, which is still comparable to the SFC. Thus, the scaled-up V-EFC features a sufficiently large kinetic regime and precise activity determination. However, it must be considered that this high precision results from the i_{lim} being scattered around the median and does not refer to a homogeneous species flux over the electrode area. The identified regions of this design with an extremely low flow velocity and species flux (= dead zones) should not be neglected. Depending on the application, these can be a challenge, if *e.g.* the aimed product is converted further at the electrode, affecting the product distribution, or inhomogeneous catalyst usage and degradation can occur. Such an inhomogeneous catalyst usage might falsify the catalyst performance data. Additionally, the current distribution at the WE could become difficult with a rod cathode in only one channel. Since the tip of the CE rod would be the closest to the WE, the potential drop due to the electrolyte resistance would be the smallest there. Thus, the circular area of the rod would need to increase to approx. 1 cm^2, which would again increase the channel and the WE. Similar considerations for the herein-designed iEFC are discussed in chapter 5.1.2. Lastly, the discrepancy between the V-EFC and the cell designs in the industry and classical lab-scale testing needs to be considered.

Criteria to Scale Up an iEFC

Based on the scale-up of these reported flow cells, a first flow geometry for the iEFC, as seen in Figure 5.3, was designed, considering the possibility of kinetic analysis and combinability with downstream analysis. Online downstream analysis, such as an ICP-OES, restricts the maximum electrolyte flow to avoid non-spectral interferences (see chapter 4.4.5) and the dilution of the electrochemical products. For the kinetic analysis, a large kinetic regime and uniform mass transport over the WE are important for applying the KL analysis. Thus, a minimal reaction volume over the electrode is required for high convection and minimal dilution of reaction products. Additionally, planar, parallel electrodes with electrolyte flow parallel to the electrode are included as industrial characteristics for this design. Thus, it needs to be considered that cross-contaminations from CE reactions cannot be excluded. As seen in Figure 5.3, these considerations resulted in two interconnected rectangular channels, tilted in a V-shape. This channel geometry allows the minimal reaction volume over the WE and fewer dead zones.

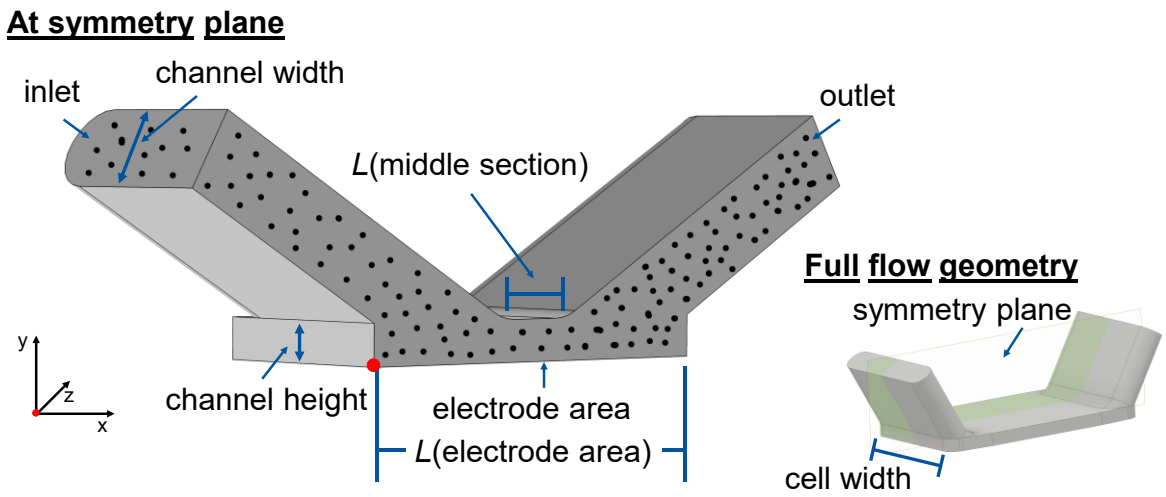

Figure 5.3. Schematic flow geometry, utilized for the numerical simulations to design the iEFC. Simulations were performed with 1 mm channel height, varying channel widths of the in- and outlet, varying electrode lengths, and 2.5 mm cell width (symmetry plane at 1.25 mm).

Now, to adjust the dimensions of this design for the applicability of the KL analysis, the mass transport of reactive species to the electrode was characterized. Here, two effects were looked at separately: the flow velocity distribution over the WE due to convection and the electrode's accessibility with a uniform flow velocity distribution over the WE. For the simulations, a geometry model with a reduced cell width was used to minimize calculation time, assuming the width does not influence the model (width (z) = 0.25 cm, length (x) = 1-4 cm, A = 0.25-1 cm^2, symmetry plane at z = 0.125 cm, simulated: 0 < z_{sim} < 0.125 cm, A_{sim} = 0.125-0.625 cm^2). Thus, please note that the absolute flow velocities, concentrations, and species fluxes are not comparable to the scaled-up SFC and V-EFC (Figure 5.2) and the final EFC design presented here (Figure 5.6).

Influence of Flow Velocity Distribution over the WE

When evaluating the influence of the flow velocity distribution over the WE on the KL analysis, it is known that the more uniform the flow velocity distribution over the WE, the narrower the distribution of i_{lim} and the better the applicability of the KL analysis.[46] Herein, the extent of imprecision introduced by inhomogeneous convective mass transport on the kinetic analysis was estimated for different versions of the iEFC's flow geometry, which is presented in Figure 5.3.

Therefore, the uniformity of the flow velocity distribution over the WE was varied by changing the channel width (CW) of the in- and outlet, while the WE covered the entire bottom part of the cell. The transition zone between the connecting middle section and the channels introduced inhomogeneity of the flow velocity distribution. Thus, the ratio U between the length of the middle section L(middle section) and the length of the electrode L(electrode) was defined to quantify the share of the electrode with parallel flow:

$$U = \frac{L(\text{middle section})}{L(\text{electrode})} \cdot 100\% \qquad (5.2)$$

In Figure 5.4, the velocity flow distribution and species flux for CWs of 2 mm (a, b), 1 mm (c, d), and 0.5 mm (e, f) for 1.14 mL min^{-1} at 1.5 V are displayed, corresponding to the mass-

transport-limited case. The respective concentration distributions are shown in Figure S2. The smallest CW of 0.5 mm corresponds to the largest *U* of 73.3%. For a CW of 2 mm, less than a quarter of the electrode (13.3%) features a parallel flow to the electrode.

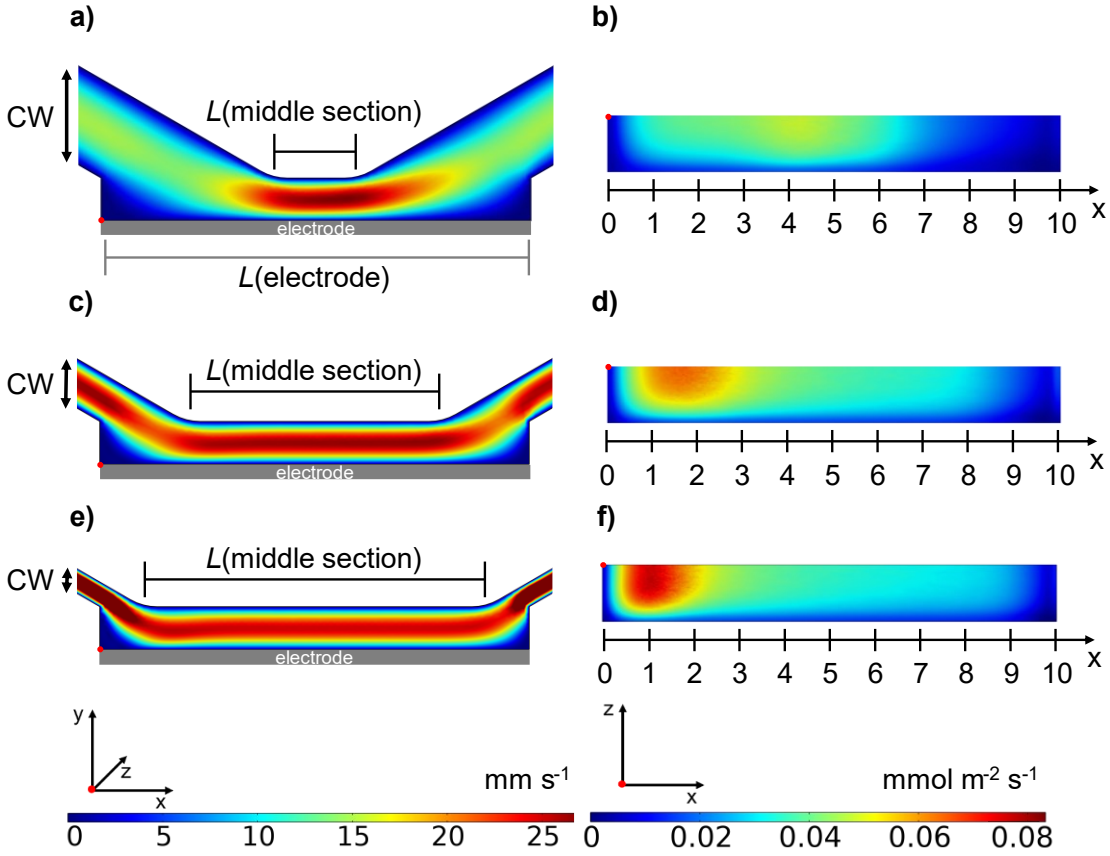

Figure 5.4. Flow velocity distribution at the central x-y plane (a, c, e) and species flux distribution at the electrode (b, d, f) in the mass-transport-limited regime for a CW of 2 mm (a, b), 1 mm (c, d) and 0.5 mm (e, f). The inlet volume flow is 1.14 mL min^{-1} (for half of the inlet's cross-section), and the overpotential is 1.5 V. The channel height is 1 mm, and the cell width is 2.5 mm (symmetry plane at 1.25 mm). The scale ranges from 0-27 mm s^{-1} (a, c, e) and 0-83.3 µmol m^{-2} s^{-1} (b, d, f).

Figure 5.4 identifies in a), c), and e) a uniform flow velocity distribution over the electrode in the middle section with a maximum velocity of 27 mm s^{-1}. The species flux distribution at the electrode is shown in Figure 5.4b, d) and f). If *U* is large (CW = 0.5 mm, Figure 5.4f), the maximum flux of 83 µmol m^{-2} s^{-1} will be closest to the beginning of the electrode at the inlet (x≈1 mm). If the CW is increased (compare Figure 5.4b, d) and *U* gets smaller, the point of maximum species flux moves toward the center of the electrode. For the largest CW of 2 mm (Figure 5.4b), the maximum species flux of 49.4 µmol m^{-2} s^{-1} is at 4 mm along the electrode. As previously discussed, the homogeneity of species flux over the electrode is directly correlated to the uniformity of the convective and diffusional mass transport. The larger *U*, the more the species flux distribution is dominated by axial diffusion limitation (see Figure 5.5 for comparison). The smaller *U*, the more the species flux distribution shows a trade-off between the limitation by convection and axial diffusion. The KL analysis supports this visual correlation. The evaluation parameter *G* for the homogeneity of the mass transport increases with decreasing *U* from 0.5% (*U* = 73%, 0.5 mm CW) to 3% (*U* = 53%, 1 mm CW) to 8% (*U* = 13%, 2 mm CW). This evaluation shows that even if only 13% of the electrode features a uniform flow velocity distribution, the imprecision of the i_{kin} determination *via* the KL analysis is still acceptable. This can be seen when comparing the KL slopes, which were all ranging between

0.986-0.990, to the reported 0.94 from Kulyk *et al*.[38] and Scherson *et al*.[43] Still, to obtain the highest possible precision in the activity determination, the WE should be placed in the connecting middle section with parallel flow to the electrode.

Influence of Uniform Accessibility

Even though EFCs do not have a uniformly accessible electrode, the KL analysis was previously applied to EFCs.[43,47,48] This work seeks to evaluate the significance of uniform accessibility in determining reaction kinetics within laboratory-scale EFCs. For that, the electrode length was increased from 1 to 4 cm with a parallel flow and a uniform flow velocity distribution over the entire electrode, which is ensured by placing it in the middle section.

Figure 5.5 shows the concentration distribution (a, b) and species flux (e, f) at the central x-y plane for an electrode length of 1 cm (a, e) and 4 cm (b, f) for an inlet volume flow of 1.14 mL min^{-1} at 1.5 V, corresponding to the mass-transport-limited case. The flow velocity distribution is given in Figure S3. For better visualization of the reactive species' depletion along the length of the electrode, the concentration distribution at a lower flow rate (14.4 µl min^{-1}) is shown in Figure 5.5c and d). For the 1 cm and 4 cm long electrodes, Figure 5.5 indicates an increasing diffusion layer thickness along the electrode length in the direction of the flow with a maximum diffusion layer thickness at the end of the electrode of 0.4 mm (*L*(electrode) = 1 cm, a) and >1 mm (*L*(electrode) = 4 cm, b). Additionally, the species flux in Figure 5.5e and f) indicates more clearly the evolution of the diffusion layer thickness along the electrode. For both electrode lengths, the species flux shows a maximum at the very beginning of the electrode. At the central x-y plane, the species flux of approx. 0.5 mmol m^{-2} s^{-1} rapidly drops down to 1/10 of its original value after 130 µm, after which it stays comparatively constant along x. This profile is relatively constant along the z-axis, with a decreasing species flux toward the cell walls. Thus, the depicted concentration distribution and species flux clearly reflect the expected gradual stabilization of the diffusion layer along the electrode. It is interesting to point out that this species flux profile shows similarities to the one from the SFC (compare Figure 5.2), where the species flux is also strongly influenced by the diffusion layer growth along the electrode.

The KL analysis identified deviations of $i_{kin,sim}$ from $i_{kin,input}$ of 1% for 1 cm and 3% for 4 cm long electrodes. Comparing this to the *G* values discussed above, this indicates that uniform accessibility can be neglected for the herein-investigated system when studying the reaction kinetics. In comparison to the variation of convection, the variation of the electrode length had a less significant impact on *G*.

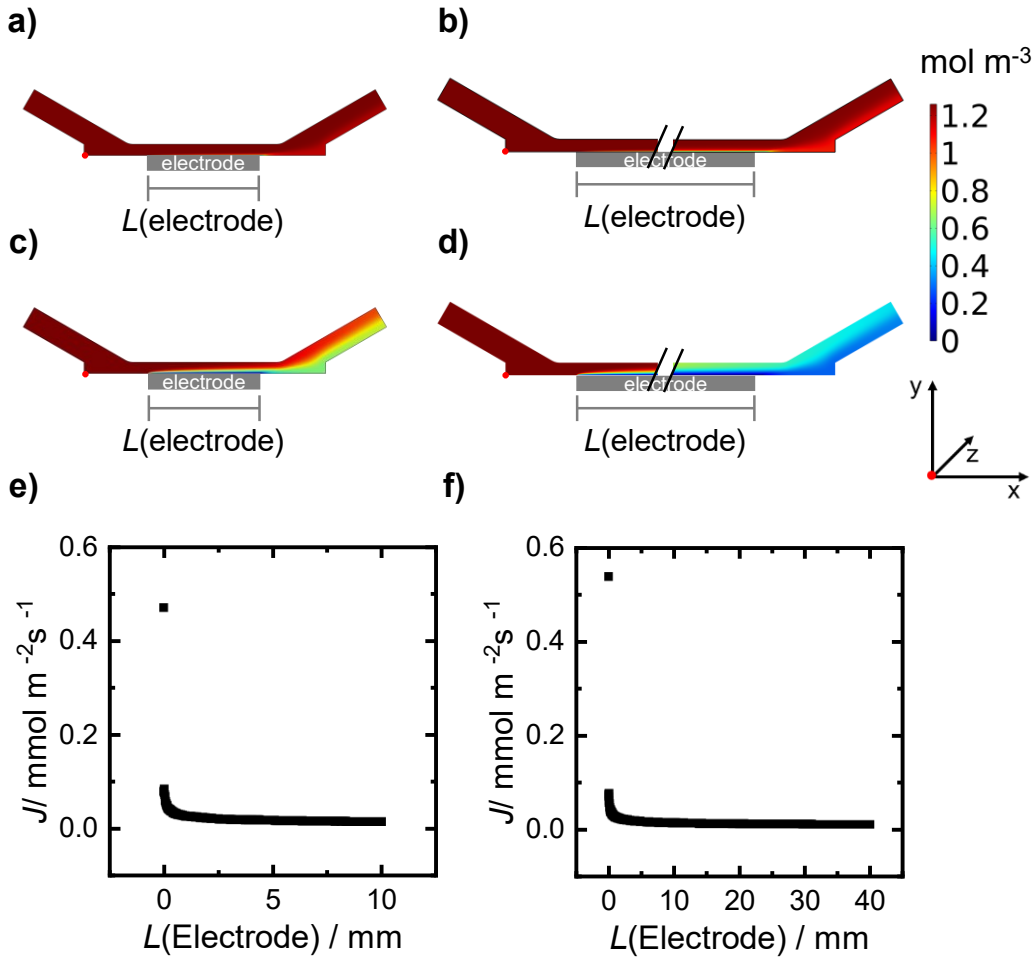

Figure 5.5. Concentration distribution at the central x-y plane (a, b, c, d) and species flux distribution at the electrode (e, f) in the mass-transport-limited regime for a 1 cm (a, c, e) and 4 cm (b, d, f) long electrode. The inlet flow is 1.14 mL min^{-1} for a), b), e), and f) (for half of the inlet's cross-section). For better visualization, (c) and (d) are shown with an inlet volume flow rate of 14.4 µl min^{-1}. The respective *G* values are 1% (*L*(electrode) = 1 cm) and 3% (*L*(electrode) = 4 cm). The channel height is 1 mm, and the cell width is 2.5 mm (symmetry plane at 1.25 mm). The overpotential is 1.5 V. The scale ranges from 0-1.26 mol m^{-3} (a-d). Note that the slight deviation of the maximum species flux at the central x-y plane between the 1 cm (e) and 4 cm (f) long electrode is an artifact of the simulation as the simulation mesh is different for each geometry and, therefore, the data points do not necessarily coincide.

Final Design

For the iEFC design, these two investigations highlight that the WE needs to be placed in the middle-section between the channels for a uniform flow profile over the WE and for the deviation of i_{lim} over the WE to be negligible. With the WE in the middle section, the influence of the non-uniform accessibility on the KL analysis was found negligible for 1-4 cm long electrodes. When combining the iEFC with downstream analysis, which is limited in the flow velocity, the electrode's width is limited to obtain sufficiently high flow velocities over the WE and, thus, high species fluxes. Because of this, and for practicality in handling, an electrode size of 1 x 1 cm was chosen.

The final flow geometry of the iEFC with a 1 x 1 cm WE in the connecting middle section was simulated. The geometry (a) and the simulation results for the velocity distribution (b) and concentration distribution (c) at the central x-y plane of the cell and the species flux over the

electrode (d) are shown in Figure 5.6. Note that since the WE is placed in the middle section of the flow cell, where parallel flow with a uniform distribution is given, the channel angle to the x-z plane should not affect mass transport to the electrode and can be varied between 30°-90°. For constructive reasons, a minimum of 30° is needed for a channel height of 1 mm over the WE. By increasing the angle, the dead zones at the edges increase, which can be problematic, *e.g.* for gas bubble removal. The simulated *G* value is 2%, and the average species flux over the electrode is 23 µmol m^{-2} s^{-1}, which gives the smallest deviation of $i_{kin,sim}$ from $i_{kin,input}$ and the largest kinetic regime for the 1-cm^2-models presented herein.

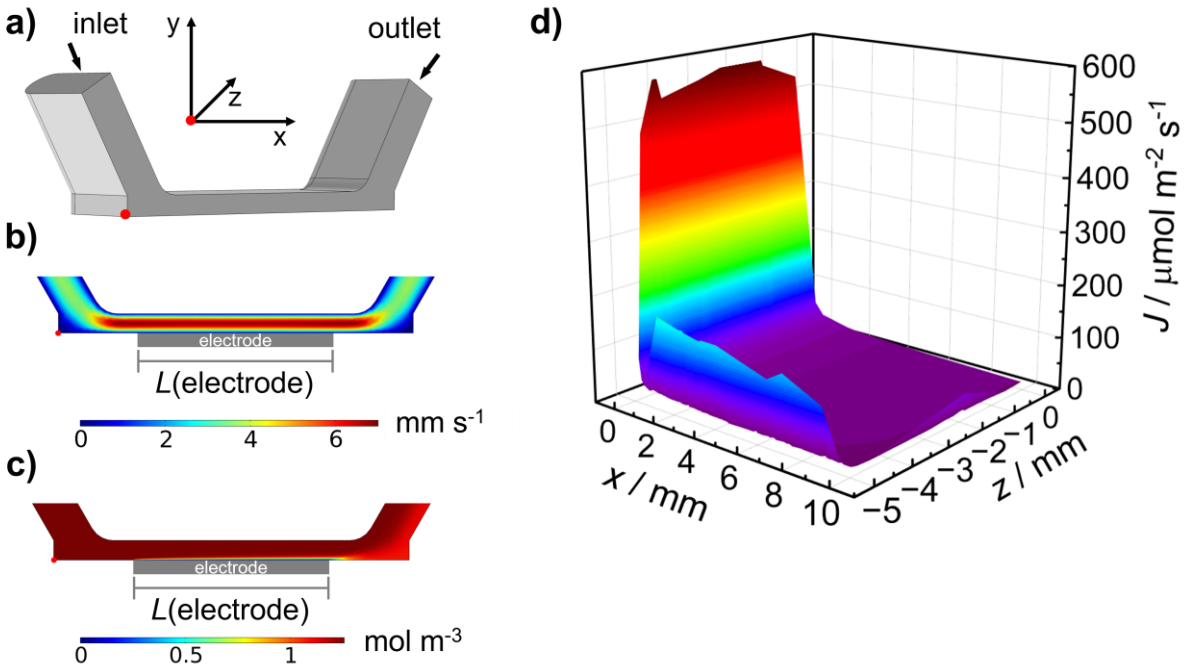

Figure 5.6. a) Flow geometry of the final flow cell design, b) flow velocity distribution at the central x-y plane, c) concentration distribution at the central x-y plane, and d) species flux distribution at the electrode. The inlet volume flow is 1.45 mL min^{-1} (for half of the inlet's cross-section), and the overpotential is 1.5 V. The channel height is 1 mm, and the cell width is 10 mm (symmetry plane at 5 mm). The scale ranges from 0-7.01 mm s^{-1} (b) and 0-1.26 mol m^{-3} (c). The simulated *G* value is 2%, and the average species flux over the electrode is 23 µmol m^{-2} s^{-1}.

Experimental Validation

Based on these theoretical simulations, the flow velocity distribution, concentration distribution, and species flux of the final iEFC flow geometry were validated experimentally. For that, the applicability of the Levich analysis for EFCs and the KL relationship was tested by recording polarization curves at different flow velocities for the ferricyanide reduction. The respective polarization curves can be found in Figure S4. The results for the Levich analysis for EFCs and the KL plot in the mixed kinetic-mass-transport-limited regime at a potential of 0.593 V *vs.* RHE can be seen in Figure 5.7 for four different trials (V1-V4*)*. It must be noted that the potential regime for the applicability of the KL analysis to the ferricyanide reduction is very narrow due to its fast reaction kinetics.

The Levich analysis for EFCs (a) and the KL plots (b) in Figure 5.7 show a linear relationship with an averaged slope of 0.39±0.03 and 0.96±0.02, respectively. From the KL plots in Figure 5.7b, $|1/I_{kin}|$ (y-intercept) of 0.37±0.07 can be identified, corresponding to a kinetic current of 2.7±0.3 mA. The slight variations between the different trials in Figure 5.7a and b) might be

associated with different $Fe(CN)_6^{3+}$-concentrations present in the electrolyte as the solution was not long-term stable. Another source of error could be the varying precision of the flow rates since those are very sensitive to hydrostatic pressure, meaning the electrolyte level in the reservoir, the position of the tubing and the iEFC, and the influence of the pump. Still, this overall reproducible linearity of the Levich analysis for EFCs and the KL relationship, in combination with a slope close to one for the KL plot, proves the applicability of the Levich analysis for EFCs and KL relationship for this cell design. The 4% deviation of the KL slope from one is in line with previous reports, suggesting a systematic deviation between uniform accessible electrodes and electrodes in EFCs.[38,43] Thus, the herein-designed flow cell proves to be a channel electrode according to equation (2.2). When all parameters are known, incl. the geometry-dependent constant, the diffusion coefficient of $Fe(CN)_6^{3+}$ can be determined for this reaction system. On the other hand, when investigating a different system with a known diffusion coefficient of the reactive species, valuable predictions about the mass transport (diffusion layer and i_{lim}) are now possible with the herein-designed iEFC. Further, the KL analysis in Figure 5.7b shows that the kinetics of a catalyst can be evaluated in the kinetic-mass-transport-limited regime with this iEFC.

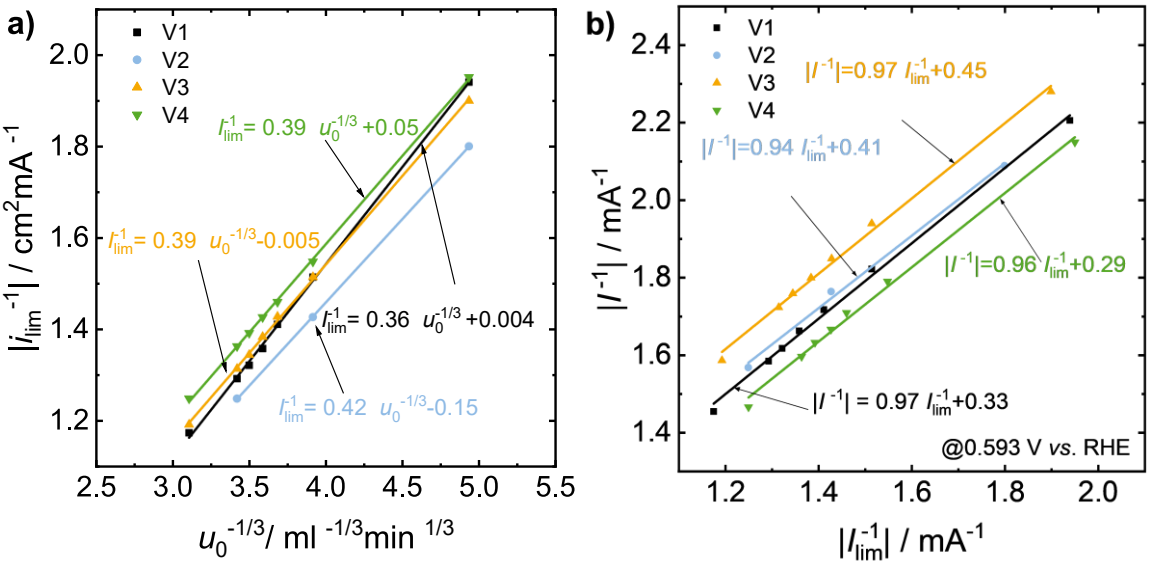

Figure 5.7. a) Experimental Levich analysis for EFCs and b) KL plot for the ferricyanide reduction in 0.1 M $HClO_4$ with 10 mM $K_3[Fe(CN)_6]$ in the final iEFC design for four different trials 1-4 (V1-V4). The KL plot was evaluated at an overpotential of 0.593 V *vs.* RHE. The inlet volume flow was varied between 0.5 – 2 mL min^{-1}. The Levich and KL relationship proved to be applicable for the herein-designed iEFC with a KL slope of 0.96±0.02.

Conclusion

To summarize, an iEFC with a 1 cm^2 WE for simultaneous activity measurement and downstream analysis of the electrolyte was designed. COMSOL simulations of the flow velocity, concentration, and species flux distribution were performed to evaluate different cell geometries. Simulations of the scaled-up versions of the previously reported SFC from Mayrhofer *et al*. and V-shaped EFC from Schlögl *et al*. identified a limited kinetic regime and formation of large dead zones, respectively, in combination with an incompatibility with classical lab cell designs. The herein-designed iEFC features 1 cm^2 planar and parallel

electrodes with a 1 mm electrode distance as industrial characteristics. To ensure minimal dilution of the reaction products and maximized flow velocity over the WE, the reaction volume over the WE was minimized by tilting the in- and outlet channels with an angle of 30-90° to the x-z plane. A laminar flow, which is parallel to the electrodes and uniform over the WE, is ensured by placing the electrode in the middle of the connecting channel. Thereby, precision in activity determination is maximized. For the herein-designed iEFC, it was further shown that the uniform accessibility of the electrode can be neglected for an electrode length of less than 4 cm when calculating the activity *via* the KL relation. The simulation of the final iEFC cell design revealed a *G* value of 2% for the determination of i_{kin}. This indicates that the KL analysis can be applied with high accuracy. This applicability of the Levich analysis for EFCs and the KL relationship was validated experimentally for the ferricyanide reduction.

5.1.2. Relative Electrode Positioning

While designing, simulating, and experimentally validating an iEFC with a 1 cm^2 WE, the relative electrode positioning was found to be of great importance and significantly influenced the electrochemical measurement, primarily high-frequency measurements such as EIS. Thus, four different geometries, as seen in Figure 5.8, were investigated to identify the dominating effects for successful EIS measurements in EFCs where the electrodes are separated by narrow and winded channels. In all cases, the RE was connected to the inlet by a capillary with a diameter of 1 mm.

For the herein-developed flow geometry of the iEFC, two electrode configurations are theoretically plausible: parallel WE and CE (Figure 5.8a) or the CE as a rod in the outlet (Figure 5.8b). While parallel WE and CE are standard in the industry, the CE is, however, favored in the outlet in analytical electrochemistry to avoid any contaminations at the WE. Further, two additional cell designs based on the V-EFC were tested for more insight: the original (Figure 5.8c) and a variation with two additional turns between WE and CE (Figure 5.8d). In all cell designs, the WE is positioned at the bottom.

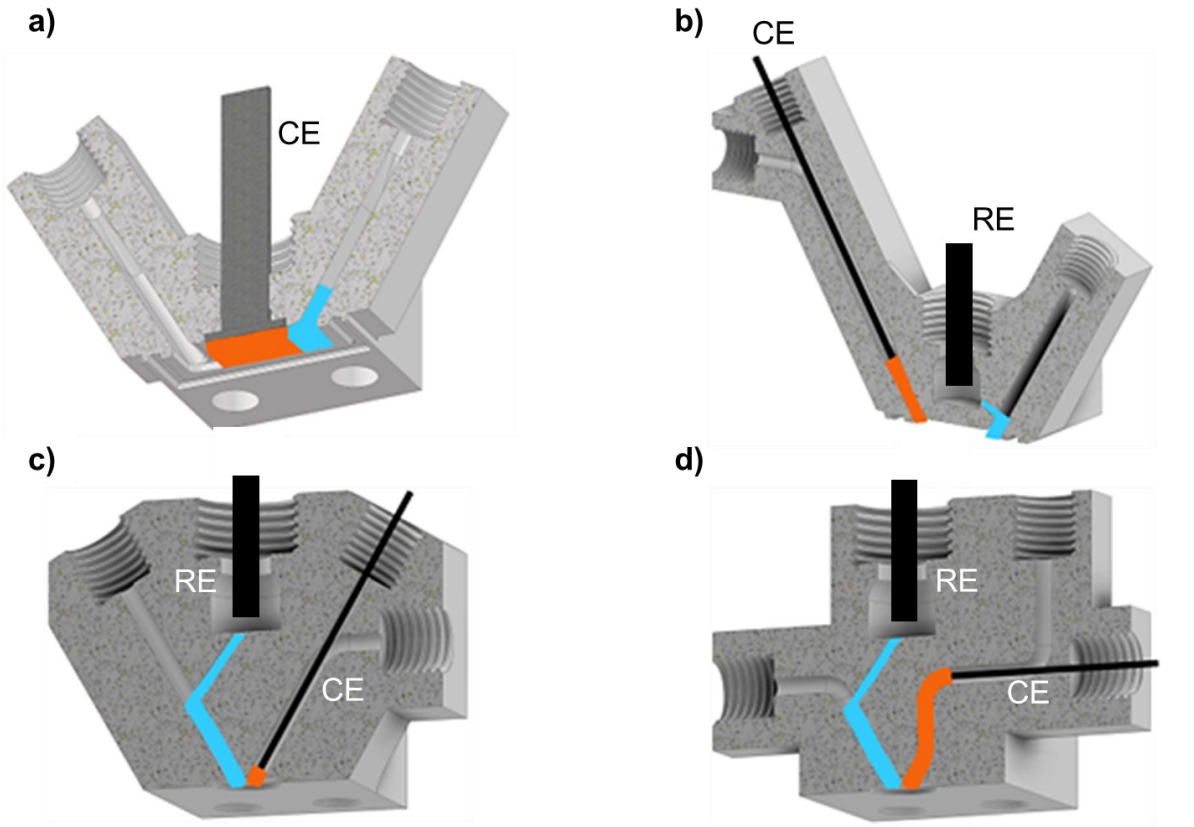

Figure 5.8. Schematic illustration of the RE capillary (blue) and the suggested regions of equidistant parallel potential lines between WE and CE (orange) for different electrode positionings in EFCs with narrow and winded channels. The WE is positioned at the bottom. a) Herein-designed iEFC with parallel WE and CE electrodes, b) herein-designed iEFC with the CE in the outlet as a rod, c) V-EFC with the CE in the outlet as a rod, d) variation of the V-EFC with two additional channel windings between the WE and CE.

Previous reports stated that for precise potential control at the WE, a uniform current distribution over the WE is required.[116] Here, it is important to know that potential lines are perpendicular to the current lines.[117] When using a RE with a capillary, the capillary distorts the potential lines near it. The measured potential reflects the undistorted field in the distance of $d/3$ from the capillary-tip position, with d being the diameter of the capillary.[118] In this work, this knowledge is applied and tested for EFCs with narrow and winded channels. When performing EIS measurements for the four different setups in Figure 5.8, EIS was only successful for the parallel electrode arrangement (Figure 5.8a) and the original V-EFC (Figure 5.8c). This might be due to the homogeneous current distribution at the WE and a convenient point of potential measurement by the capillary of the RE. The capillary of the RE presumably detects homogeneous equidistant and parallel potential lines between WE and CE. The reason for the unsuccessful EIS measurement with the adjusted V-EFC in Figure 5.8d is not fully understood. Potentially, the current response might be too slow for the timescale of the EIS or the IR_u drop too large for the electronics of the EIS. For the iEFC design in Figure 5.8b, the suggested region of parallel and uniform current lines between CE and WE is spatially separated from the region of potential measurement by the RE. This potentially hinders the EIS measurement.

To summarize, electrodes in EFCs with narrow and winded channels need to be placed in a way that a uniform current distribution over the WE is possible and that the RE can sense

parallel, equidistant, and uniform potential lines. Practically, this means that the projection of the capillary of the RE onto the WE needs to intersect with a region of parallel and equidistant current and potential lines between CE and WE. This is also in line with previous reports.[116–118] Further, the WE and CE need to be in direct sight of one another.

5.1.3. Introduction of Working and Counter Electrode

When introducing the WE and CE into the iEFC, the definition of the surface area and electrode contacting have to be considered.

To define the active surface area, flat seals (adhesive PTFE foil, Kapton tape), varnish (insulating spray, PTFE spray, Lacomit, nail polish), and embedding were tested. Figure 5.9 shows the definition of the surface area by insulating spray and adhesive PTFE foil when oxidizing Ta, which irreversibly turns brown upon oxidation. The detailed experimental procedure can be read in chapter 4.3.2. Both, the insulating spray and the adhesive PTFE foil, resulted in a deviation from the desired 1 cm^2. Figure 5.9a demonstrates that the insulating spray delaminated strongly, making a reproducible surface area determination impossible. In Figure 5.9b, four independent tests for defining the surface area using adhesive PTFE foil are illustrated. The electrolyte crept underneath the adhesive PTFE foil, enlarging the surface to an average of 1.25 cm^2. This corresponds to a 25% larger surface area than anticipated. Embedded electrodes can be seen in Figure 5.10. The geometric area of the embedded electrodes is assumed to correspond to the active surface area without any additional areas of the electrode being exposed. A detailed experimental description of how those embedded WEs in Figure 5.10c are fabricated can be found in chapter 4.2.1.

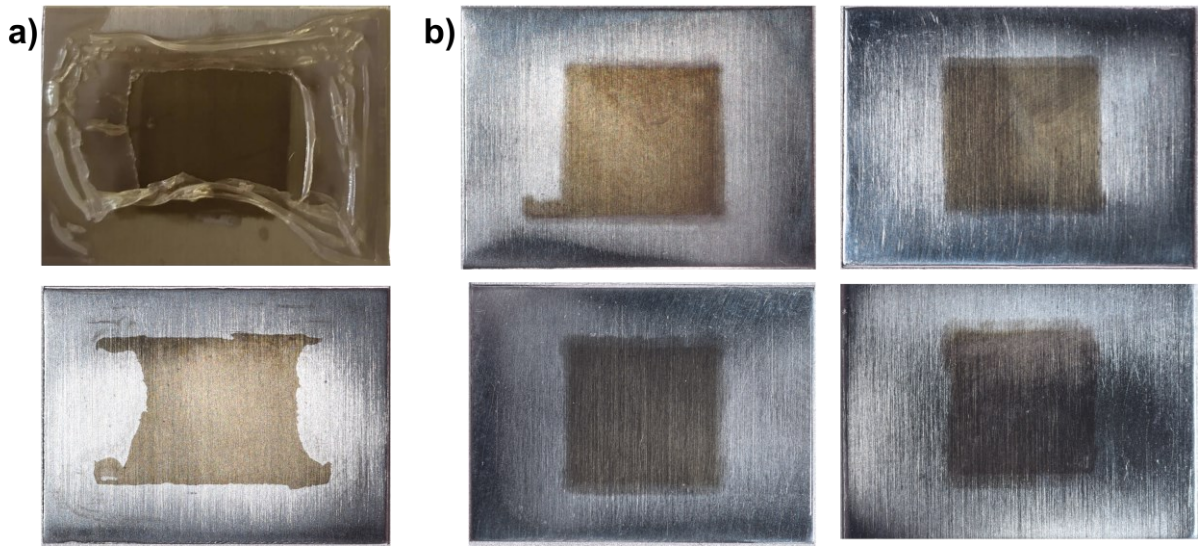

Figure 5.9. Definition of the electrode surface area by a) PTFE spray and b) adhesive PTFE foil (four independent tests) shows deviation from 1 cm^2, when tested under electrochemical operation in the iEFC with 0.1 M $HClO_4$. Deviations from 1 cm^2 resulted because a) the PTFE spray delaminated and b) electrolyte crept underneath the PTFE foil. [adapted from C. Marck's master thesis[91]]

Figure 5.10 compares the three tested electrode contacting and embedding methods. Initially, the electrode was contacted by attaching a wire with copper tape, as seen in Figure 5.10a. Disadvantages were the fracture point of the wire at the entry point into the embedding material and the poor adhesion between the copper tape, wire, and electrode. This poor adhesion led

to reduced conductivity and sometimes the inclusion of embedding material between tape, wire, and electrode, which further deteriorated the conductivity. Thus, this contacting method was substituted by a metal glued to the electrode with Ag-containing conducting adhesive, as demonstrated in Figure 5.10b and c).

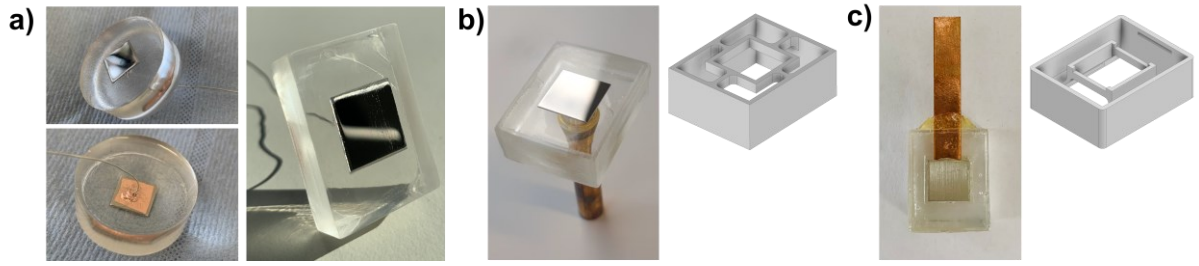

Figure 5.10. Developments in the fabrication of embedded WEs. a) WE is embedded in commercial round form and contacted by wire and copper tape. The embedded WE is cut to the respective dimensions in the next step. b) WE is embedded in a 3D-printed form with a holding structure, open to the electrolyte. Electrode contacting is done by a metal rod and Ag-containing conducting adhesive. c) WE is embedded in a 3D-printed form with a holding structure, not open to the electrolyte. Electrode contacting is done using a metal sheet and Ag-containing conducting adhesive. [a) is adapted from V. Schulte's bachelor thesis,[119] b) is reprinted from J. Kautz's bachelor thesis][120]

Next, the embedding form was optimized. First, a commercially available, removable, round form was used for embedding, and the resulting hardened epoxy block was cut down with a saw and ground to the respective size, as seen in Figure 5.10a. This was, however, a waste of material and time- and labor-intensive. As a second approach, a 3D-printed form (VeroClear, DraftGrey) with a holding structure for the WE was tested, which cannot be removed after embedding (see Figure 5.10b). Here, a metal rod contacted the WE. It was observed that the 3D-printing material corroded slightly from the cleaning procedure and the alkaline environment, which acted as a starting point for pitting. After a while, parts of the electrode and the contacting metal came in contact with the electrolyte. Thus, the design in Figure 5.10c was developed, where no 3D-printing material is open to the electrolyte, and a metal sheet contacts the WE. This design is also easier to handle concerning electrode contacting and pre- and post-analysis by, for example, optical microscopy, SEM, or EDX.

5.1.4. Adapted Design to Study the Alkaline Water Electrolysis

Recently, Spanos *et al.* proposed the coupling of an iEFC and ICP-OES as a setup to characterize simultaneously a catalyst's activity and stability for the AWE, more specifically for the OER. Although not yet widely used, this technique is very promising as it can address the discrepancy between high activity and low stability. In particular, the stability of the electrocatalyst is of crucial importance for industrial application, and, therefore, a deep understanding of the deactivation mechanisms is required.[37] These could be elucidated with the help of online ICP-OES. Hence, the herein-developed iEFC should be adapted to the needs of studying AWE electrocatalysts at lab- (up to 10 mA cm^{-2}, RT, 1 M KOH) and industrially more relevant (up to 100 mA cm^{-2}, 80 °C, 30 wt% KOH) conditions. When applying industrially more relevant conditions, additional challenges arise such as gas evolution, incl. possible electrode blockage or trapped gas bubbles, and the cell's material stability toward highly concentrated alkaline electrolytes (up to 30 wt% KOH) and high temperatures (up to 80 °C).

Regarding the cell's material stability, different embedding and 3D-printing materials were screened. One requirement was that the material is transparent to see and react to trapped

gas bubbles. Further, the 3D-printing material had to be applicable for the PolyJet printer for a sufficiently thin layer thickness of 16 µm[121] and a manufacturing tolerance of 0.1 mm.[122] Table S7 in the appendix summarizes the material study and identifies AR-H1 (Keyence) as a suitable 3D-printing material and EpoHeat Clear (Buehler) as embedding material. These materials did not show any significant weight loss, embrittlement, deformation, or visual change when leaving it in 30 wt% at 80 °C for 24 h.

Regarding gas evolution, Figure 5.11 indicates the spots of gas accumulation in the iEFC with 60° between the channels, a 1 mm spacing between WE and CE, and a seamless inserted CE. Gas accumulation occurred between the CE and WE (1), behind the CE in the transition to the outlet (2), and at the bottom in the transition to the outlet (3).

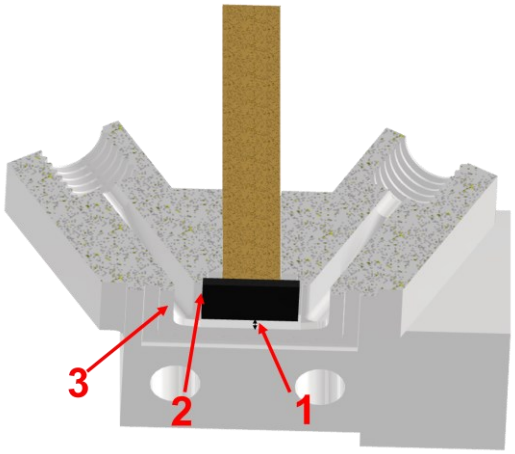

Figure 5.11. Critical areas for gas bubble accumulation in the herein-designed iEFC. These are between the CE and WE (1), behind the CE in the transition to the outlet (2), and at the bottom in the transition to the outlet (3).

The effect of gas bubbles on the activity determination can be clearly seen in Figure 5.12a by the unstable CP at 10 and 100 mA cm^{-2}. To achieve a more efficient gas removal, the interelectrode distance was increased to 3 mm, the angle between the in- and outlet channel was maximized to 120°, and the middle section was prolonged, increasing the distance between CE and the outlet channel. It needs to be considered that increasing the interelectrode distance raises the dilution of the reaction and electrode dissolution products, which could become problematic for their detection by the ICP-OES. Further, the fluid velocity over the WE is decreased. This would correspond to an increased mass transport limitation, which is, however, a) counteracted by the turbulence introduced by the gas evolution and b) not relevant for the OER due to the high availability of hydroxide ions (= reactants). The adapted design to study AWE electrocatalysts can be seen in Figure 5.12b and Figure 5.13a. By these adaptations, a stable CP measurement to determine the OER activity at up to 100 mA cm^{-2} is possible, as shown in Figure 5.12b.

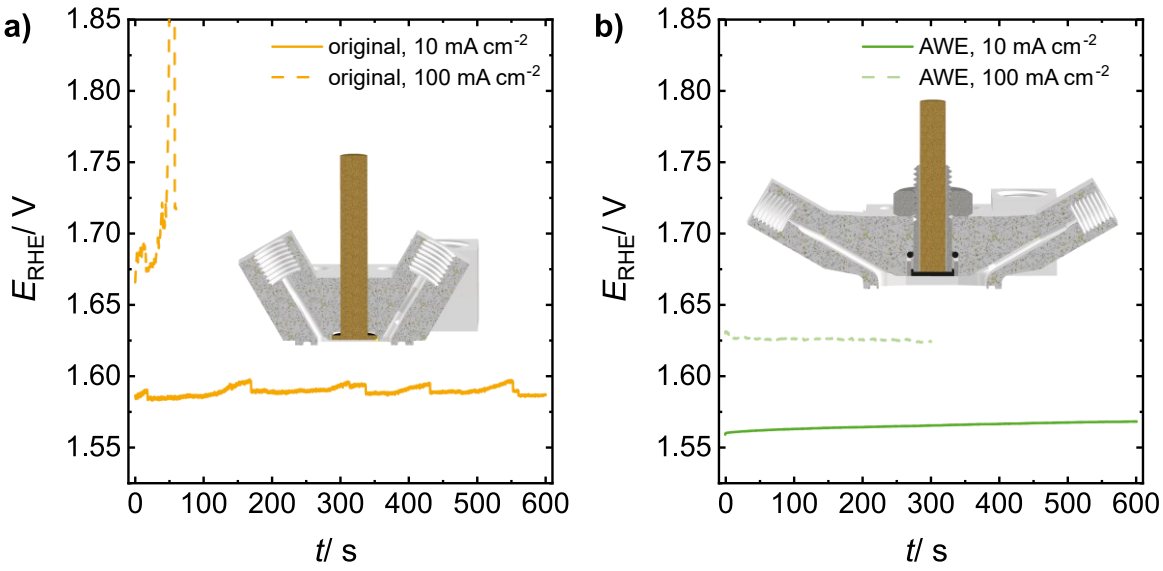

Figure 5.12. CP at 10 and 100 mA cm^{-2} for a 1 cm^2 unconditioned $Ni_{70}Fe_{30}$ in a) the original herein-designed iEFC and b) the adjusted iEFC to study AWE catalysts (AWE-iEFC). Experiments were conducted in 1 M KOH at RT.

For more flexibility, practicability in handling, and reproducibility, an exchangeable CE and possibilities for different REs and their placing were implemented, as illustrated in Figure 5.13. Figure 5.13a (also seen in Figure 5.12b) shows that a RE with a diameter of 6 mm can be introduced into a separate reservoir, which is connected to the inlet channel by a 1.5 mm wide capillary. This has the advantage that the RE sees no contaminations or passing gas bubbles. On the contrary, during its introduction, gas bubbles can get trapped. Further, the insertion depth of the RE into the reservoir is not fixed, and thus, the distance between WE and RE can vary slightly. The CE is held by a nut and an O-ring within the cell. It should be noted that the thread represents a potential fracture point with the current dimensions due to the thin material. For the next generation, the material thickness needs to be increased. As an alternative, the CE can be introduced through a hollow screw, which compresses an O-ring for sealing. This can be seen in Figure 5.13b and c). Here, the RE is directly placed in the inlet. Figure 5.13b shows this for a RE with a 6 mm diameter and Figure 5.13c for a miniRHE from Gaskatel with a 1.6 mm diameter. For the RE with the 6 mm diameter, the introduction is now easier compared to Figure 5.13a, but the RE is not sheltered from passing gas bubbles and contaminations. While the capillary characteristics vary slightly in length and diameter, no significant difference was observed experimentally for EIS at OCP in 1 M KOH at RT. The introduction of the entire shaft of the miniRHE into the inlet channel, as seen in Figure 5.13c, has the benefit of minimizing the distance and temperature gradient between the WE and RE when industrial temperatures of 80 °C are applied. The reproducibility of the activity and activation determination of OER catalysts with these cell designs is discussed in chapter 5.1.5.

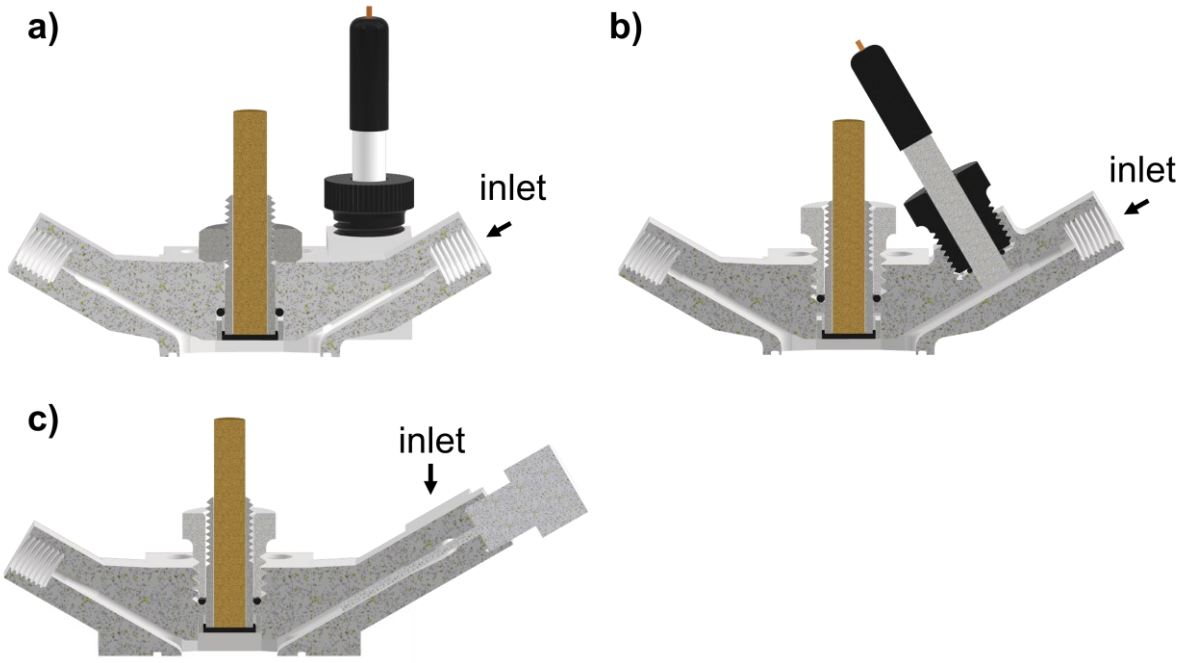

Figure 5.13. iEFC designs, suitable for studying AWE catalysts, with a 3 mm spacing between the 1 cm^2 WE and CE, 120° between the channels, and a prolonged connecting channel (increased distance between CE and channels). All designs feature an exchangeable CE and RE. a) CE is held by a nut. RE (d = 6 mm) is placed in a separate reservoir and connected to the channel by a capillary (d = 1.5 mm). b) CE is introduced through a hollow screw, which compresses an O-ring. RE (d = 6 mm) is placed directly in the channel. c) CE is introduced through a hollow screw, which compresses an O-ring. miniRHE from Gaskatel (d =1.6 mm, G1/8 thread, length = 3 or 4 cm) is placed with its entire shaft in the channel.

Lastly, the applicability of coupling the AWE-iEFC to the ICP-OES for online monitoring of the electrolyte during electrochemical operation was tested. For that, the Ni dissolution from a Ni electrode ($Ni_{99.99,}$ 99.99 wt% Ni) in 0.1 M $HClO_4$ was first measured as a reference. A ground glassy carbon electrode was used as CE. The electrochemical protocol consisted of an OCP, followed by CV conditioning (0.056-1.256 V *vs.* RHE, 200 mV s^{-1}, 30 cycles), a 15 min delay, and 10x a CP at 1 mA cm^{-2} for 10 s with each a 10 min delay. To align the electrochemical and spectroscopic timescale, the starting time of the CP pulse was set to the onset time of the Ni dissolution peak. Figure 5.14 shows the Ni concentration when applying the series of 10 CPs at 1 mA cm^{-2} for 10 s separated by a 10 min delay.

In Figure 5.14, the first two peaks differ in peak shape and area slightly from the following eight peaks, suggesting an initial equilibration. Disregarding the first two peaks and averaging over the remaining eight peaks, the maximum of the Ni dissolution peak follows the current pulse with a delay of 50±4 s. The concentration drops back to the initial concentration and reaches it after approx. 4.0±0.3 min. These times need to be considered when interpreting future ICP-OES results with the herein-designed iEFC. In literature, the concentration drop back to the baseline was reported to be between 4-5 min when using the SFC.[36,123,124] This proves that the herein-designed iEFC is suitable for studying electrode stability and dissolution despite the larger electrode area and the cell design with more dead zones and transitions.

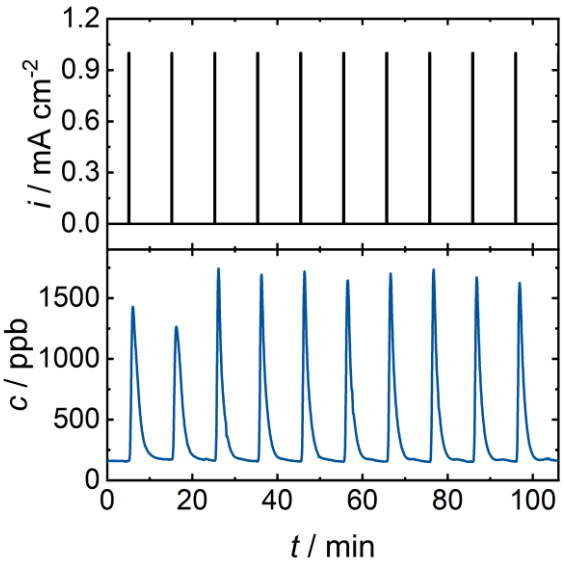

Figure 5.14. Ni dissolution in Ar-purged 0.1 M $HClO_4$ from a $Ni_{99.99}$ anode, when applying a series of 10 CPs at 1 mA cm^{-2} for 10 s. A glassy carbon CE was used, and 1 ml min^{-1} was applied. The experiment was conducted at RT.

In the next step, the potential- and time-dependent dissolution of a Ni-Fe alloy anode with 30 wt% Fe ($Ni_{70}Fe_{30}$) in 1 M KOH was studied to characterize its behavior for the AWE. Glassy carbon was used as a CE. Two different studies were performed: a) CV between –0.35-1.6 V *vs*. RHE at 2 mV s^{-1} (Figure 5.15a) and b) CP at 10 mA cm^{-2} for 30 min, followed by 30 min OCP (Figure 5.15b). Figure 5.15a shows the potential-dependent dissolution of Fe from $Ni_{70}Fe_{30}$ during CV for the anodic and cathodic sweep. Sharp signal drops can be seen at the HER (< –0.1 V) and OER (> 1.5 V) potentials. This might be because of a decrease in electrolyte supply at the ICP-OES due to gas bubbles. From the baseline Fe concentration of 115 ppb, the Fe concentration starts to increase at 0.2 V *vs*. RHE on the oxidative sweep. At 0.55 V, it reaches its maximum of 123 ppb, and it decreases afterward to 119 ppb at 1.3 V. On the cathodic sweep, the Fe concentration goes down linearly back to the initial Fe concentration. Figure 5.15b shows the time-dependent Fe dissolution from a $Ni_{70}Fe_{30}$ anode during CP at 10 mA cm^{-2}, followed by OCP. In Figure 5.15b, the baseline concentration is about 119 ppb. A sharp increase in Fe concentration to 130 ppb is visible when applying 10 mA cm^{-2}, followed by a drop of the Fe concentration below the baseline to 116 ppb. After the CP ends and the potential is reversed to OCP, the Fe concentration spikes to approx. 135 ppb and then drops back to 120 ppb. This suggests an initial Fe dissolution from $Ni_{70}Fe_{30}$, which is followed by an Fe uptake at the anode or cathode during the CP. A simultaneous dissolution from the $Ni_{70}Fe_{30}$ anode cannot be excluded. After the CP, the Fe seems to be released again. The noise probably results from the high KOH concentration and gas bubble interferences. Overall, Figure 5.15 proves the possibility of deconvoluting metal dissolution from AWE electrocatalysts or rather incorporation from the electrolyte in 1 M KOH at RT. Further investigations on the Fe dissolution from $Ni_{70}Fe_{30}$ as anode during CV and CP in 1 M KOH are discussed in chapter 5.2.3.

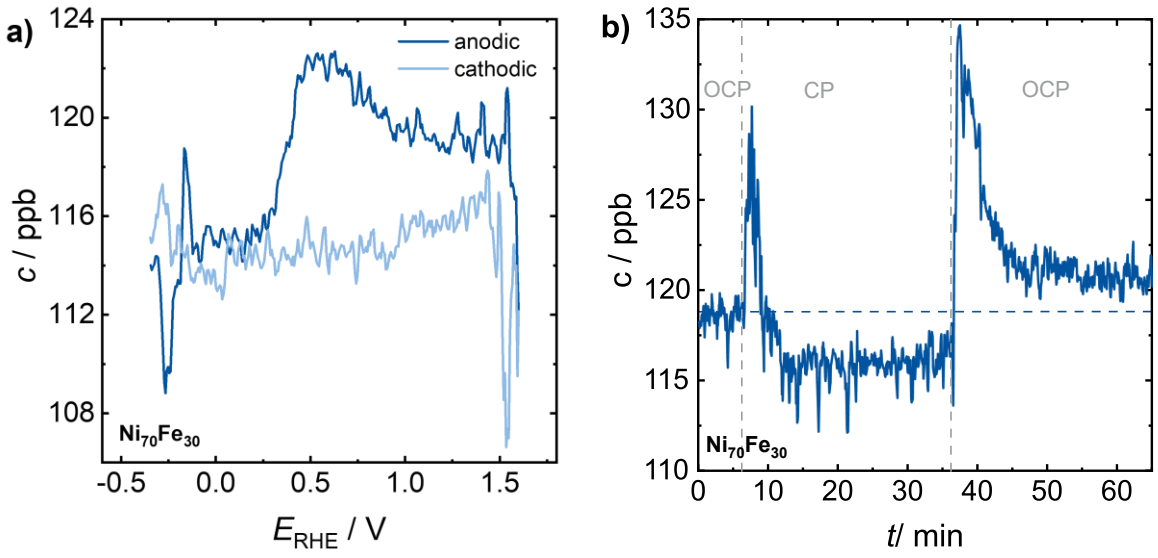

Figure 5.15. Fe concentration in 1 M KOH, measured by ICP-OES, during a) CV between –0.35-1.6 V at 2 mV s^{-1}, and b) the application of, first, a CP at 10 mA cm^{-2} and then an OCP for each 30 min. A 1 cm^2 $Ni_{70}Fe_{30}$ electrode was used as anode and glassy carbon as cathode. Data was cleaned from spikes to low concentrations due to gas evolution (no trends were modified) and data was smoothed over 3 data points. Experiments were conducted in 1 M KOH at RT. a) is also displayed in Figure 5.25 and b) in Figure 5.38. a) is part of more extensive online ICP-OES study and the full sequence is shown for Fe in Figure 5.39 and Figure S7.

To conclude, the iEFC was adapted for the operation under gas evolution and the harsh environment of AWE studies by increasing the electrode spacing, maximizing the angle between the in- and outlet channel to 120°, and prolonging the middle section. As a next step, possibilities for introducing the RE and the CE were evaluated, and different iEFC versions were designed. While these designs feature different (dis)advantages, all can be applied as is to characterize electrocatalysts for the AWE. Lastly, the online electrolyte monitoring by ICP-OES during CV and CP at 10 mA cm^{-2} in 1 M KOH at RT was successfully demonstrated with the iEFC. The prior conducted Ni dissolution experiment identified a peak smearing behavior similar to that reported in literature.

5.1.5. Reproducibility when Studying the Alkaline Oxygen Evolution Reaction

When investigating AWE electrocatalysts in the herein-designed iEFC, electrochemical activity and activation by conditioning of the WE are subject to multiple influences, which may affect (ir)reproducibility. In the following, possible causes for the irreproducibility of electrochemical activation of electrodes by conditioning are discussed. Figure 5.16 shows the influence of the applied cell design, CE, and flow conditions on the activation of a $Ni_{70}Fe_{30}$ electrode by conditioning (–0.35-1.6 V, 100 mV s^{-1}, 30 min, 46 cycles). The potential difference at 10 mA cm^{-2} before and after conditioning was here defined as activation $-\Delta E_{10}$ (for more details see chapter 4.3.2, *Investigation of Electrochemical Conditioning*).

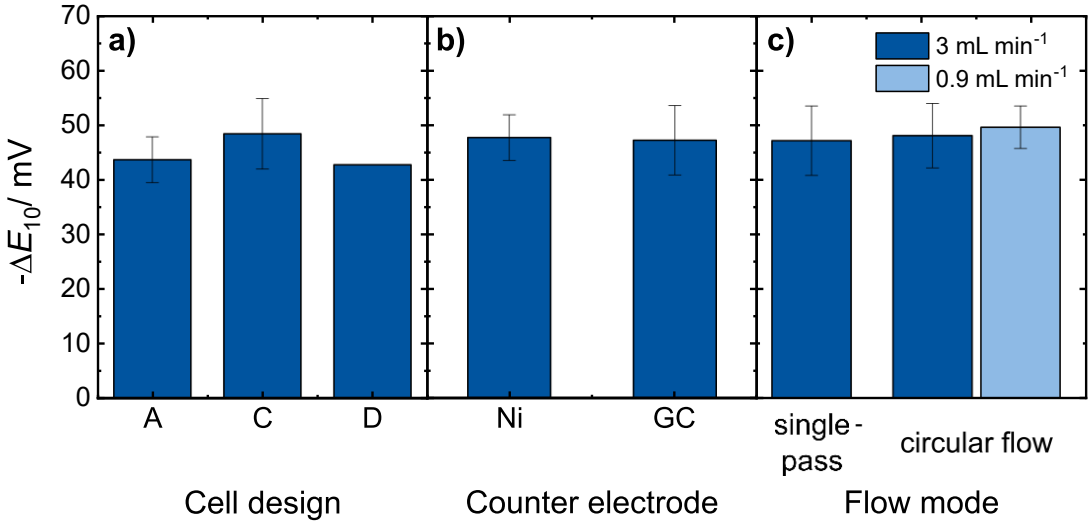

Figure 5.16. a) Influence of the cell design on the electrode activation of $Ni_{70}Fe_{30}$ by conditioning. Cell design A refers to an angle of 60 ° between the in- and outlet channel, an electrode spacing of 1 mm, and the RE is placed in a reservoir and connected to the channel by a capillary. Designs C and D feature 120 ° between the in- and outlet channels and an electrode spacing of 3 mm. For C, the RE is placed in a reservoir and connected to the channel by a capillary. For D, the RE is placed directly in the channel. For all designs, a Hg/HgO RE was employed. b) Influence of the CE material ($Ni_{99.2}$ and glassy carbon) on the electrode activation of $Ni_{70}Fe_{30}$ by conditioning. c) Influence of flow conditions (circular *vs.* single-pass flow) and flow rate (3 *vs.* 0.9 mL min^{-1}) on the electrode activation of $Ni_{70}Fe_{30}$ by conditioning. For all experiments, conditioning was performed between –0.35-1.6 V at 100 mV s^{-1} for 30 min (46 cycles). The experiments were conducted in 1 M KOH at RT.

For the investigation of electrochemical activation by conditioning, different cell designs were used within this work. Figure 5.16a shows that deviations in activation between the different designs are within the error range. However, a source of irreproducibility can be the iEFC 3D-printing material. It was observed that after 3D-printing, iEFCs made from VeroClear performed initially irreproducible in the OER and required a long period to run smoothly (> 10 experiments).

Regarding the electrodes, grinding and polishing of the WE were implemented to define the surface area reproducibly. Slight variations can, however, still be present, causing irreproducibility in electrode activity and activation. As CE, Ni or glassy carbon (GC) were tested. As seen in Figure 5.16b, electrode activation is constant irrespective of the applied CE. Still, it needs to be noted that the choice of CE can become relevant depending on the material and protocol. When conditioning the WE between –0.35-1.6 V, the CE is oxidized in the low potential regime. If an element is chosen as CE, which is not present in the WE, it will be oxidized, possibly dissolve and, hence, contaminate the electrolyte and might interact with the WE.

Further, unknown impurities in the electrolyte or the iEFC can influence the electrochemical measurements and cause irreproducibility. Here, it needs to be considered that the iEFC is only rinsed with and ultrasonicated in ultrapure water for cleaning, and the tubing is rinsed with ultrapure water. Ar purging of the electrolyte was reported to improve reproducibility.[125] However, in this work, Ar purging of the electrolyte did not significantly influence the standard error of the mean activation. A possible explanation might be that the observed standard error of the mean activation is too large for this effect to dominate and be visible.

Regarding the electrolyte flow, different flow conditions, namely single-pass (SP) *vs.* circular flow (CF) at different flow rates (3 *vs.* 0.9 mL min^{-1}), were tested. Both did not significantly influence the electrode activation, as seen in Figure 5.16c. Still, variations in gas quantities passing the electrodes, accumulating, or blocking the surface can be a source of irreproducibility. Insufficient gas removal can also result in noisy data, which hampers the potential determination.

Reproducibility of the electrode activity and activation is further affected by shifts of the RE and the IR_u drop as these change the applied potential, which can result in differently conditioned surfaces. The R_u is influenced by slightly different positions of the RE, different resistances of the WE depending on the electrical contact, and different resistances of the cables or potentiostat periphery.

To conclude, this systematic investigation showed that neither the choice of cell design, CE, flow mode, nor the flow rate had a significant impact on the (ir)reproducibility of the electrochemical activation of electrodes. It is, therefore, suggested that a complex interplay of the above-discussed reasons is responsible for the obtained error bars.

5.2. Electrochemical Conditioning of Ni-(Fe)-based Electrodes at Lab-scale Conditions

The following chapter discusses the systematic investigation of the electrochemical conditioning for a Ni-Fe alloy electrode with 30 wt% Fe (31 at% Fe). 30 wt% Fe was selected because it falls within the optimal range for Fe content.[17–22] This is expected to minimize the adjustment of the Ni:Fe ratio during conditioning. The correlation between electrochemical protocol parameters and electrochemical activation is explored by varying the potential window, scan rate, hold times at the upper and lower potential limit, and the number of cycles. The correlation between activation and potential window is linked to the induced material changes, characterized by direct current cyclic voltammetry (dcCV), FTacV, optical microscopy, SEM, EDX, XPS, FTIR, and ICP-OES. To further understand the role of Fe in the activation, the influence of the Fe content in the electrode and electrolyte on the electrode activation is evaluated. Lastly, the long-term effect of conditioning on the activity of $Ni_{70}Fe_{30}$ during 100 h electrolysis at 100 mA cm^{-2} is explored. Parts of this chapter are published in *ChemElectroChem* **2024**, *11*, e202400318.[126]

5.2.1. Optimization of the Electrochemical Conditioning of $Ni_{70}Fe_{30}$ as Model Electrode

To study the influence of the conditioning parameters on the OER performance of Ni-Fe-based electrodes, the conditioning of $Ni_{70}Fe_{30}$ ($Ni_{70wt\%}Fe_{30wt\%}$, $Ni_{69at\%}Fe_{31at\%}$) as a model electrode was systematically optimized. As an evaluation parameter, the activation by conditioning was defined as the difference between the potentials at a certain current density, *e.g.* 10 mA cm^{-2}, before and after conditioning, ΔE_{10} (for more details see chapter 4.3.2, Investigation *of Electrochemical Conditioning*). An increase in activation will result in a negative ΔE_{10} ($E_{10,after} < E_{10,before}$). For better readability, $-\Delta E_{10}$ is plotted in the following. First, the conditioning of the electrode under constant operation at OCP and 100 mA cm^{-2} was tested for reference. Figure 5.17a compares the activation from operation at OCP and 100 mA cm^{-2} to CV

conditioning between different potential limits at 100 mV s^{-1}. All procedures were performed for 30 min.

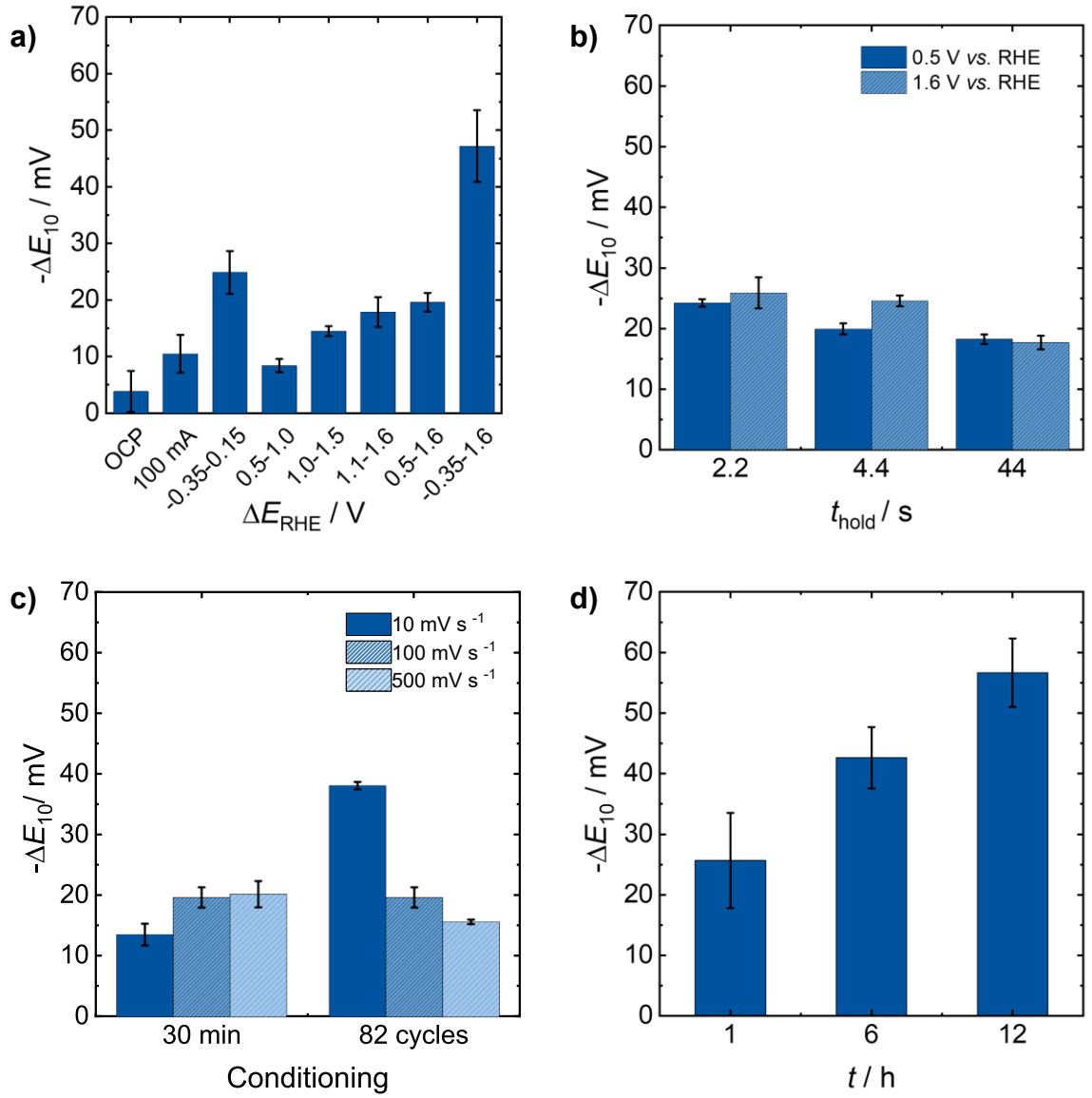

Figure 5.17. a-d) Activation of $Ni_{70}Fe_{30}$ resulting from different conditioning. a) Conditioning for 30 min at OCP, 100 mA, and by CV with different potential limits. Conditioning time and scan rate are constant at 30 min and 100 mV s^{-1}. b) CV conditioning with different hold times at the upper (1.6 V) and lower (0.5 V) potential limit. Conditioning potential window, scan rate, and time are constant at 0.5-1.6 V, 100 mV s^{-1}, and 30 min. c) CV conditioning at different scan rates for a fixed conditioning time of 30 min and a fixed number of 82 CV cycles. Conditioning was performed in the potential range of 0.5-1.6 V. With the time fixed to 30 min, 9, 82, and 402 CV cycles were completed for 10, 100, and 500 mV s^{-1}, respectively. d) CV conditioning for 1, 6, and 12 h, which corresponds to 804, 4819, and 9638 cycles. Conditioning potential window and scan rate are constant at 0.5-1.6 V and 500 mV s^{-1}.

As seen in Figure 5.17a, conditioning the electrode at OCP or by CV cycling within the capacitive regime (0.5-1.0 V) did not show a significant activation (< 10 mV). A slight activation of 10±4 mV could be obtained when applying a constant current of 100 mA cm^{-2}. This could be significantly improved to >14 mV by CV cycling in potential regions with relevant redox features of Ni or Fe. In alkaline electrolytes, the following redox potentials *vs.* RHE were reported, which are intensively discussed in the chapters 2.2.1 and 2.2.2 (see Figure 2.2 and Figure 2.3): Ni(0) to Ni(II): 0.0-0.5 V,[29,55] Ni(II) to Ni(0): –0.2-0.1 V,[55] Ni(II) to Ni(III) / Ni(III) to

Ni(II): 1.2-1.5 V,[29,53,76] Fe(0) to Fe(III) *via* Fe(I/II) and *vice versa* between –0.2-0.6 V.[59,60] As discussed in chapter 2.2.4, the formation of a thin and compact anhydrous oxide layer with a hydrous oxide layer on top is suggested to form during constant current operation at 100 mA cm^{-2}. The diffusive oxidation process is, however, comparably slow at these conditions, and a stronger activation would only be visible after a longer conditioning time. At OCP, hence without a forced oxidative current, this surface oxidation process is much slower, resulting in no visible activation. During CV conditioning with relevant redox features of Ni or Fe, the activation is proposed to be enhanced compared to the application of a constant oxidative current, because the respective hydrous oxides are formed more efficiently. The reductive sweep reduces the anhydrous layer and facilitates rearrangement and the formation of a larger hydrous oxide layer during the oxidative sweep.

Figure 5.17a shows that when comparing the potential windows with the same size of 0.5 V, the largest activation of 25±4 mV was achieved when cycling between –0.35-0.15 V, followed by 1.1-1.6 V, 1.0-1.5 V, and 0.5-1.0 V. This indicates that the application of low as well as high potentials seems to be beneficial for activation. Within the low potential window between –0.35-0.15 V, the redox couple Fe(0)/Fe(II) is reported.[29,55,59,60] Hence, Fe dissolution might be favored in this regime, resulting in an increase in surface area. This is in line with a previous report, which stated that CV cycling of steel electrodes in the lower potential regime (–0.074-0.924 V *vs*. RHE) resulted in an increased Fe leaching and, thus, a larger surface area.[33] The increase in surface area is supported by the qualitative comparison of the Ni(II)/Ni(III) redox peak areas after conditioning of $Ni_{70}Fe_{30}$ between –0.35-1.6 V and 0.5-1.6 V at 100 mV s^{-1} for 30 min, as shown in Figure 5.18. Figure 5.18 illustrates the CV (1-1.6 V, 100 mV s^{-1}) of $Ni_{70}Fe_{30}$ before and after conditioning.

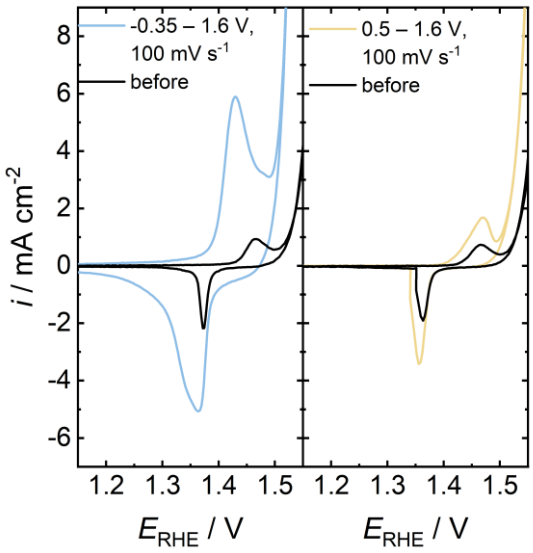

Figure 5.18. CV (1-1.6 V, 100 mV s^{-1}) of $Ni_{70}Fe_{30}$ before and after conditioning between –0.35-1.6 V and 0.5-1.6 V at 100 mV s^{-1} for 30 min (46 and 82 cycles, respectively). The larger oxide charge capacity of the Ni(II)/Ni(III) redox peaks for conditioning between –0.35-1.6 V compared to 0.5-1.6 V indicates more accessible Ni sites and a larger surface area.

In Figure 5.18, the Ni(II)/Ni(III) redox peak areas increase due to conditioning with the large (–0.35-1.6 V) and small (0.5-1.6 V) potential window. The increase in peak area is, however, more significant when including the HER (–0.35-1.6 V). This indicates more accessible Ni-

oxide sites. A more detailed quantitative analysis of the Ni(II)/Ni(III) redox peak areas in correlation to the obtained activation will be discussed later in this chapter.

Figure 5.17a shows that also the higher potentials are very significant for the activation by electrochemical conditioning. At higher potentials, Ni(II) to Ni(III) oxidation and reduction take place between 1.2-1.5 V in 1 M KOH.[29,53,76] When including the OER in the CV conditioning, additional or different oxides might be formed or transformed, and a deeper oxygen penetration or uptake of excess oxygen might occur.[12,28,74] One can see that conditioning with a 0.5 V potential window within the Fe(0)/Fe(II) regime resulted in a larger activation compared to cycling at higher potentials, where the oxidation of Ni(II)/Ni(III) and OER occurs. At higher potentials, the lower potential limit might be too high for sufficient reduction of the formed anhydrous oxides and the subsequent rearrangement of the oxide structure. Additionally, less Fe might be dissolved. This implies the importance of the lower potential limit over the upper potential limit.

The activation was maximized to 47±7 mV when enlarging the potential window and combining the HER and OER regime (see Figure 5.17a). This summarizes the above-stated observation and is in line with previous works on hydrous oxide films on Fe,[12] stating that a low lower and a high upper potential limit are beneficial for an efficient hydrous oxide formation. The lower potential limit in the HER enhances the formation of the hydrous oxide by partially reducing the anhydrous oxide layer formed at higher potentials. The upper potential limit in the OER regime produces the required multilayer of (an)hydrous oxide and ensures deep penetration of oxygen. Further, it is interesting to note that these potential limits of –0.35 V and 1.6 V approx. coincide with the reported optimum lower and upper potential limit for the hydrous oxide growth when cycling Ni (< –0.4 V, ≥ 1.6 V)[58,75] and Fe (–0.2 V, high E_{high}).[28]

For an increased focus on the upper and lower potential limits, the effect of introducing hold times at these potential limits was investigated. A schematic representation of the potential profiles is illustrated in Figure 4.8e. While now more time is spent at the upper or lower potential limit during the fixed conditioning time of 30 min, the number of cycles is reduced. Figure 5.17b shows the resulting activation. A slightly decreasing trend for the activation with increasing hold times can be seen, independent of the potential during the hold time. This is in line with the results in Figure 5.17a, where little to no significant activation at constant operation at higher (100 mA cm^{-2}) and lower (OCP) potentials was observed. This supports the hypothesis that potential cycling is decisive for efficient surface oxidation. Thus, for a fixed conditioning time, the number of cycles showed a superior influence compared to the additional reduction/oxidation occurring at the lower or upper potential limits.

When the conditioning time is fixed, the number of cycles can alternatively be varied by the scan rate. Figure 5.17c shows the influence of the scan rate on the activation of the $Ni_{70}Fe_{30}$ electrode when cycling for a constant time of 30 min or a constant number of 82 CV cycles. When conditioning for a constant time, the activation increased from 14±2 mV at 10 mV s^{-1} to 20±2 mV at 100 mV s^{-1} and 500 mV s^{-1}. Applying a higher scan rate for a fixed conditioning time results in a higher number of performed CV cycles. Hence, assuming no kinetic limitation of the surface oxidation, the increased activation with increasing scan rate is probably a result of the higher number of cycles being performed. When conditioning for a constant number of 82 CV cycles, this trend was reversed, and the conditioning at 10 mV s^{-1} with 38±1 mV outperformed the activation when conditioning at 100 and 500 mV s^{-1}. This corresponds to an increased oxide growth per cycle for lower scan rates. The saturation of the activation with

increasing scan rate when conditioning for a fixed time illustrates the trade-off between increased oxide growth per cycle and the absolute oxide growth, which also depends on the total number of cycles.

To assess the impact of conditioning time or rather the number of cycles, the conditioning was extended to 12 h. Conditioning was performed between 0.5-1.6 V at 500 mV s^{-1}. The resulting activation in dependence on the time can be seen in Figure 5.17d. An increase of activation with time from 26±8 mV after 1 h to 57±6 mV after 12 h was observed. Although the activation from 6 h to 12 h was less than for the first 6 h, a final saturation after 12 h was not visible, suggesting that an ongoing activation with further cycling would be possible.

Summarizing, the conditioning of $Ni_{70}Fe_{30}$ would yield the largest activation when performing CV cycling between –0.35-1.6 V at 10 mV s^{-1} for a high number of cycles (≥ 50). For a fixed conditioning time of 30 min, a high scan rate (≥ 100 mV s^{-1}) without hold times at the upper or lower potential limit was beneficial. Thus, CV cycling between –0.35-1.6 V at 100 mV s^{-1} for 30 min was used as optimized conditioning for further studies in the following.

To better understand the influence of the scan rate, the conditioning between –0.35-1.6 V was performed at 10, 100, and 1000 mV s^{-1} over 24 h with a CP at 10 mA cm^{-2} every hour to track the activity, as demonstrated in Figure 5.19.

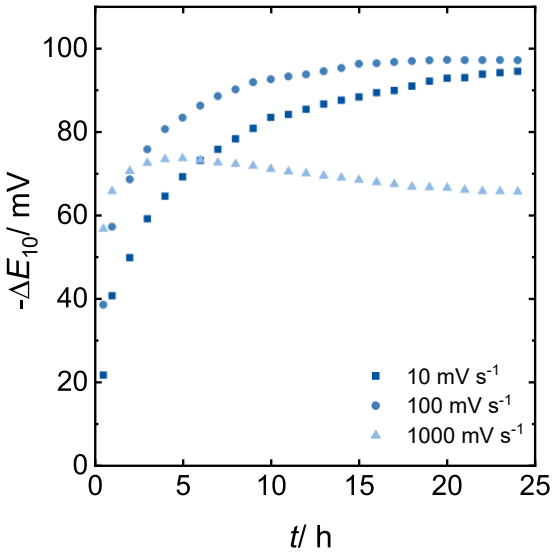

Figure 5.19. Time dependency of the activation of $Ni_{70}Fe_{30}$ when conditioning between –0.35-1.6 V at 10, 100, and 1000 mV s^{-1}. Experiments were performed in 1 M KOH at RT. A CP was conducted every 0.5-1 h. $Ni_{99.99}$ was used as CE. The electrolyte was circulated. The experiments are single measurements.

Figure 5.19 shows that activation increased and saturated with time for all scan rates. After 30 min conditioning, using a high scan rate of 1000 mV s^{-1} during conditioning resulted in an activation of 57 mV, outperforming 100 and 10 mV s^{-1}. After 2 h, the activation from conditioning at 1000 mV s^{-1} was maximized and dropped slightly thereafter, possibly due to degradation of the oxide film. In Figure 5.19, this results in a cross-over with 100 mV s^{-1} after 2 h and 10 mV s^{-1} after 6 h. Over 24 h, 100 mV s^{-1} consistently outperformed 10 mV s^{-1}. After 24 h, the activation for conditioning with these two scan rates is, however, almost the same with 97 mV (100 mV s^{-1}) and 94 mV (10 mV s^{-1}). As the slope (activation per hour) is greater for 10 mV s^{-1} than 100 mV s^{-1}, there might be a crossing point of these two curves after 24 h. While the activation per hour for 10 mV s^{-1} is larger than for 100 mV s^{-1}, it still decreases with

time and indicates that the activation will saturate soon. These activation trends with time for the different scan rates support the hypothesis of a trade-off between efficient and absolute oxide growth. A thin oxide layer can most efficiently form at high scan rates. Thicker oxide layers can, however, only form when conditioning at lower scan rates for a longer time since these low scan rates allow more time for the reduction and oxidation of the surface to disperse through the entire oxide film.

The observed correlations between activation and conditioning parameters are hypothesized to primarily result from forming a hydrous oxide layer on the electrode surface. In order to support this hypothesis, the change in oxide charge capacity of the Ni(II)/Ni(III) redox peaks by conditioning was evaluated and correlated to the activation. For that, the oxidative and reductive Ni(II)/Ni(III) redox peak areas were integrated for the activity CVs (1-1.6 V, 100 mV s^{-1}) before and after conditioning. All tested CV conditionings without hold times (Figure 5.17a, c, d) were considered. For the time-resolved conditioning (–0.35-1.6 V, 100 mV s^{-1}, 0.5-24 h), the conditioning CVs were evaluated. The change in the peak area from before to after conditioning is defined as dQ_{ox} or dQ_{red}, respectively. Figure 5.20 shows the dependency of the activation of $Ni_{70}Fe_{30}$ on the change in the oxide charge capacity dQ_{ox} for various conditioning parameter sets. While in Figure 5.17 the activation was averaged over three measurements, here in Figure 5.20, each data point represents a single measurement. As the peak integration is very prone to errors, the shown oxide charge capacities need to be considered carefully.

Figure 5.20 demonstrates an increase of activation with the increase in oxide charge capacity dQ_{ox}, which saturates after dQ_{ox} reaches approx. 60 mC and an activation of 83 mV. It needs to be noted that saturation is primarily indicated by one time-resolved experiment. Still, in the regime of lower activation (ΔE_{10} < 60 mV), where most conditioning sequences show their activation, the trend of increasing activation with the change in oxide charge capacity can be seen clearly. However, scattering around this trend is also visible, reflecting the error-proneness of the integration method and the experiment. The activation in dependence on the oxide charge capacity of the reductive Ni(II)/Ni(III) peak is shown in Figure S5 in the appendix and shows the same trends. This correlation between activation and change in oxide charge capacity supports the hypothesis that activation is primarily dominated by forming a (hydr)oxide film on the electrode and, thus, a larger active surface area. Lyons *et al.* demonstrated a similar correlation between OER activity and the oxide charge capacity for Ni and Fe electrodes.[28,29] Also, Mattinen *et al*. showed that for different Ni-based pre-catalysts, the OER activity is strongly correlated to the oxide charge capacity and that when normalized to it, the same OER activity for all pre-catalysts was obtained.[68] Still, it needs to be noted that even though this formation of a (hydr)oxide film might dominate the observed activation trends, different surface processes such as Fe dissolution/incorporation or phase changes probably occur additionally and should not be neglected. It is even very likely that this observed correlation between activation and hydroxide layer formation is only as pronounced since the starting material is an unoxidized metal. Whereas if the starting material would be a $Ni(OH)_2$-based catalyst, the predominating effects for activation during electrochemical conditioning might be different, such as phase transitions and Fe incorporation from the electrolyte. Concluding, while the activation trends of $Ni_{70}Fe_{30}$ due to conditioning seem to be primarily dominated by $Ni(OH)_2$ formation, further induced surface changes for $Ni_{70}Fe_{30}$ by conditioning will be characterized in chapter 5.2.3 to gain a deeper understanding of the occurring processes.

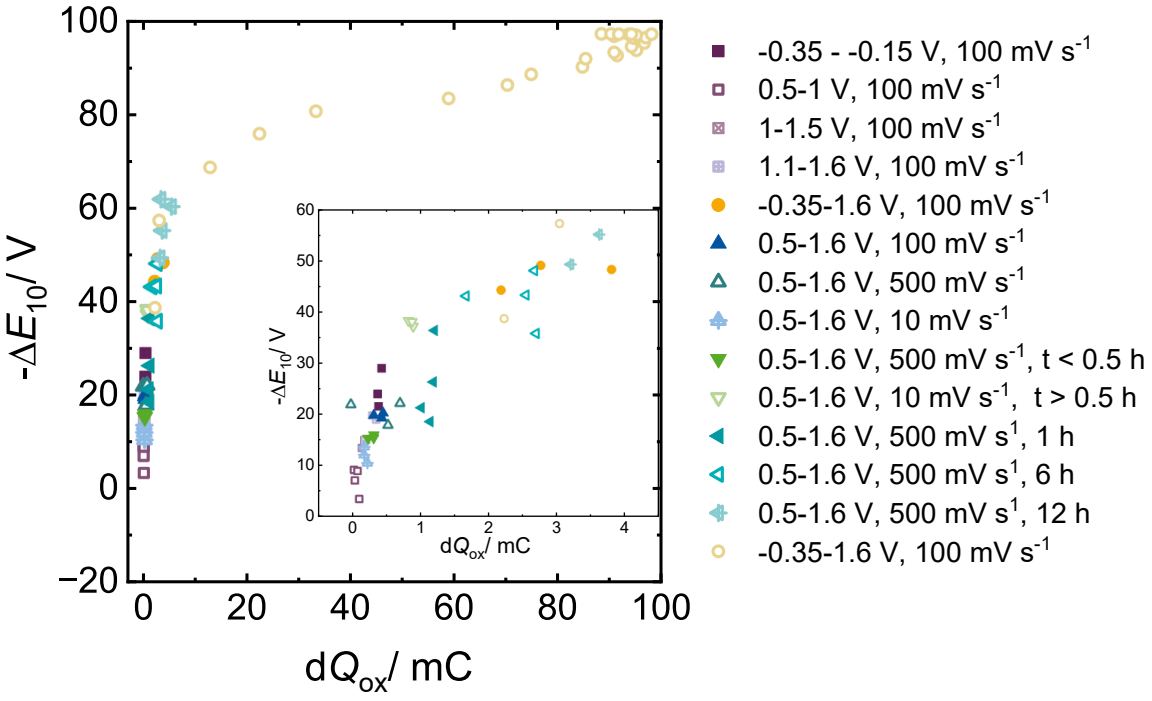

Figure 5.20. Electrode activation of $Ni_{70}Fe_{30}$, depending on the change in oxide charge capacity of the oxidative Ni(II)/Ni(III) peak (1.2-1.5 V *vs.* RHE). The oxide charge capacity was determined by integrating the oxidative Ni(II)/Ni(III) peak for the activity CVs (1-1.6 V, 100 mV s^{-1}) before and after conditioning. For the time-resolved conditioning (–0.35-1.6 V, 100 mV s^{-1}, 0.5-24 h), the conditioning CVs were evaluated. The conditioning sequences correspond to those from Figure 5.17a, c), d), and Figure 5.19 (100 mV s^{-1}). All experiments were conducted in 1 M KOH at RT.

Lastly, the sustainability of the activation by the optimized conditioning (–0.35-1.6 V, 100 mV s^{-1}, 30 min, 46 cycles) over time was determined. Therefore, an unconditioned and a conditioned $Ni_{70}Fe_{30}$ electrode were tested at 100 mA cm^{-2} for 100 h during continuous operation and the results can be seen in Figure 5.21.

Figure 5.21 shows that for the unconditioned electrode, the potential started at 1.62 V, deactivated to 1.78 V after about 1.4 h, and then dropped again to 1.76 V after approx. 7.1 h. Within the next 30 h, the potential increased continuously. In the last 20 h, the potential increase decreased to 0.4 mV h^{-1} and the final potential after 100 h electrolysis was 1.94 V. The conditioned electrode, on the contrary, showed a stable performance with an initial potential of 1.58 V and a constant degradation rate of 0.4 mV h^{-1}. Consequently, with a potential difference of 0.32 V after 100 h of electrolysis, it is evident that conditioning yields a beneficial impact on the electrode activity even in the long term. This indicates that while the oxide layer formed by CV conditioning is stable during constant current operation, the unconditioned electrode surface undergoes dynamic changes, which show first an activating and then a deactivating effect.

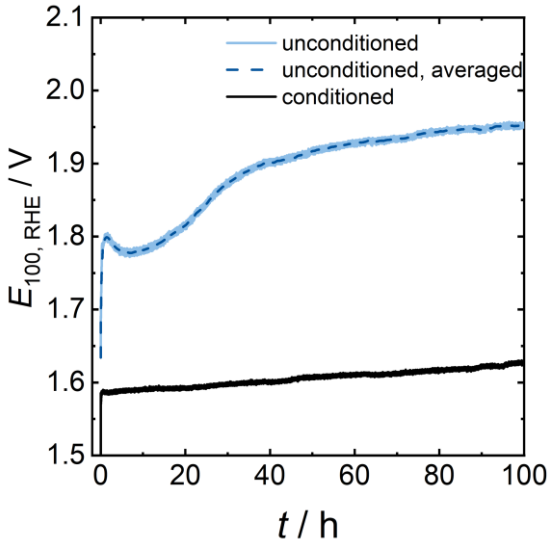

Figure 5.21. Long-term stability (100 mA cm^{-2} for 100 h) of an unconditioned and CV-conditioned $Ni_{70}Fe_{30}$ electrode. CV conditioning was performed between –0.35-1.6 V at 100 mV s^{-1} for 30 min (46 cycles). Experiments were performed in 1 M KOH at RT. The electrolyte was circulated.

In conclusion, systematic parameter variation for the conditioning of $Ni_{70}Fe_{30}$ revealed that cycling with a high upper and low lower potential limit (–0.35-1.6 V) is most beneficial for the electrode activation. Which scan rate enhances activation most depends on the number of cycles or instead on the conditioning time. Activation saturates with conditioning time. For short conditioning times of less than 2 h, a high scan rate is most beneficial (1000 > 100, 10 mV s^{-1}). However, the activation is inhibited faster when conditioning at 1000 mV s^{-1}, and saturation is already visible after 2 h. For longer conditioning times (2-24 h), slower scan rates achieve a larger activation (100 > 10 > 1000 mV s^{-1}). From the observed trends, it can be anticipated that 10 mV s^{-1} might even outperform 100 mV s^{-1} for conditioning times longer than 24 h. The correlation between conditioning parameters and activation is suggested to primarily result from surface oxidation and enlargement, which is supported by the increasing activation with increasing oxide charge capacity of $Ni(OH)_2$.

5.2.2. Influence of the Fe content of the WE and the Electrolyte

Variation of Fe Content in the Electrode

Based on the optimization of the conditioning for $Ni_{70}Fe_{30}$ as a model electrode, the identified trends were applied to Ni and Ni-Fe electrodes with different Fe contents. Figure 5.22 compares the activation of $Ni_{99.99}$ and $Ni_{70}Fe_{30}$ resulting from CV conditioning with three different sequences, each for a) 30 min and b) 46 cycles. The conditioning was performed with two different potential windows, –0.35-1.6 V and 0.5-1.6 V, at 100 mV s^{-1} and at two different scan rates, 10 and 100 mV s^{-1}, for –0.35-1.6 V.

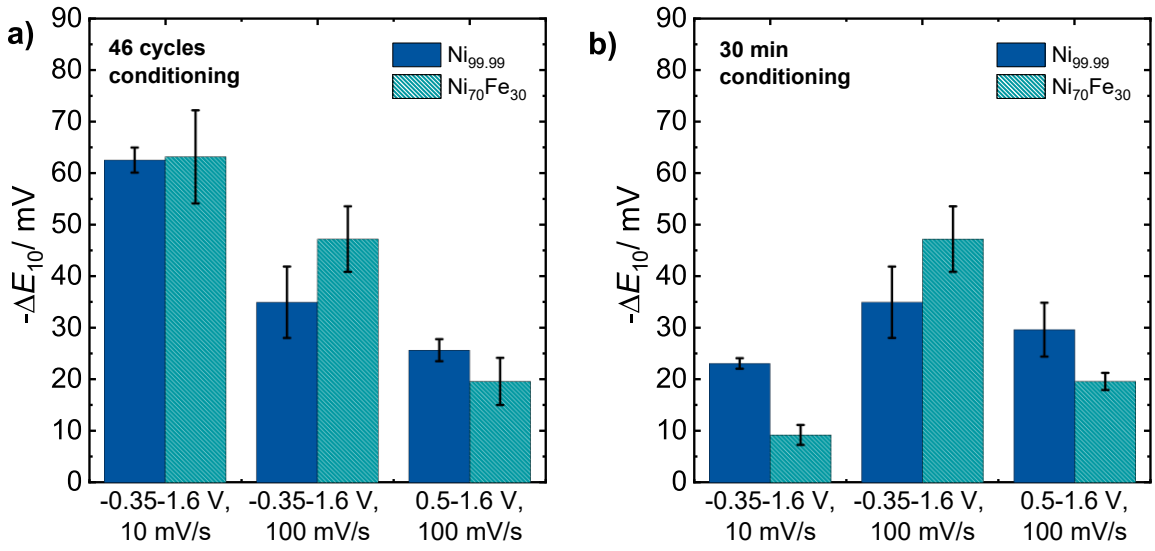

Figure 5.22. Activation of $Ni_{99.99}$ and $Ni_{70}Fe_{30}$ resulting from CV conditioning between –0.35-1.6 V at 10 mV s^{-1}, –0.35-1.6 V at 100 mV s^{-1}, and 0.5-1.6 V at 100 mV s^{-1} for a) 46 cycles and b) 30 min. With a fixed numer of cycles of 46, the conditioning time was 16.9 min (0.5-1.6 V, 100 mV s^{-1}), 29.9 min (–0.35-1.6 V, 100 mV s^{-1}), and 299 min (–0.35-1.6 V, 10 mV s^{-1}). With a fixed time of 30 min, 82 (0.5-1.6 V, 100 mV s^{-1}), 46 (–0.35-1.6 V, 100 mV s^{-1}), and 5 (–0.35-1.6 V, 10 mV s^{-1}) CV cycles were performed. Experiments were performed in 1 M KOH at RT.

In Figure 5.22a, for a constant number of cycles, the activation of $Ni_{99.99}$ and $Ni_{70}Fe_{30}$ shows the same trend. Namely, the highest activation was found for the largest potential window with the low scan rate (–0.35-1.6 V, 10 mV s^{-1}), followed by the same potential window with the high scan rate (–0.35-1.6 V, 100 mV s^{-1}), and lastly the smaller potential window (0.5-1.6 V, 100 mV s^{-1}). This trend is in line with the conditioning optimization for $Ni_{70}Fe_{30}$. Interestingly, similar trends were observed for various Ni-Fe compositions (compare Figure 5.24) and were also reported for the conditioning of different steels, as well as pure Ni and Fe.[12,28,29,31,59,60,74] Upon closer examination, it becomes apparent that the impact of the lower potential limit on the activation was more pronounced for $Ni_{70}Fe_{30}$ in contrast to $Ni_{99.99}$. Possibly, this potential regime favors Fe dissolution. Since within the tested Ni-Fe alloys, 10-20 wt% Fe were favorable for the absolute OER activity (Figure S6), the Fe-dissolution from $Ni_{70}Fe_{30}$ during conditioning results not only in a larger active surface area but also in a slightly more beneficial Ni:Fe ratio. Comparing the different scan rates, one can see that the difference between the activation at 10 and 100 mV s^{-1} was larger for $Ni_{99.99}$ than for $Ni_{70}Fe_{30}$. This indicates that the activation of $Ni_{99.99}$ is kinetically more hindered. In chapter 5.2.1, the activation trends when conditioning $Ni_{70}Fe_{30}$ were suggested to result primarily from surface oxidation and enlargement, which was supported by the correlation between activation and the increase of the $Ni(OH)_2$ amount. The kinetic limitation for the activation of $Ni_{99.99}$ then suggests that the oxidation of Ni is slower than that of a Ni-Fe alloy. In the case of the oxidation of Ni centers, their oxidation from Ni(II) to Ni(III) was reported to be rather suppressed than enhanced with Fe present in the electrode.[61,67,69] Hence, it might be rather the Ni to $Ni(OH)_2$ conversion at lower potentials, which is kinetically limited. The presence of Fe in the electrode could either enhance this reaction or the Fe dissolution, which occurs at the lower potentials as well, might generate a larger surface and more accessible Ni sites, facilitating mass transport of hydroxide and water. This in turn might enhance the mass-transport-limited reaction. An alternative explanation is based on the fact that the formation of mixed Ni-Fe-oxides or Fe-oxides within

a $Ni(OH)_2$ structure is responsible for the activation. While Fe is already present in the Ni-Fe alloy and the formation of Ni-Fe-oxides is not limited by Fe availability, Fe still needs to be incorporated in the case of $Ni_{99.99}$. Hence, it could be that this kinetic limitation of the activation might be due to a slow Fe incorporation from the electrolyte into the forming $Ni(OH)_2$ layer.

For a constant time of 30 min, as depicted in Figure 5.22b, a different trend was observed. Here, the highest activation resulted when conditioning with the large potential window at a high scan rate (–0.35-1.6 V, 100 mV s^{-1}), followed by the smaller potential window at the same scan rate (0.5-1.6 V, 100 mV s^{-1}), and lastly the large potential window at the low scan rate (–0.35-1.6 V, 10 mV s^{-1}). The order is changed since the number of cycles varies between the different conditionings. 82 (0.5-1.6 V, 100 mV s^{-1}), 46 (–0.35-1.6 V, 100 mV s^{-1}), and 5 (–0.35-1.6 V, 10 mV s^{-1}) CV cycles were performed for the respective conditioning. This explains why the smallest activation resulted for the conditioning with 10 mV s^{-1} since here the number of cycles is an order of magnitude lower than for the other two. Interestingly, the activation of $Ni_{99.99}$ was approximately double that of $Ni_{70}Fe_{30}$ under these conditions. This hints at the activation of $Ni_{99.99}$ increasing more rapidly within the first few cycles and supports the hypothesis of a kinetically limited activation. Comparing the two potential windows, it becomes evident that for $Ni_{70}Fe_{30}$, the lower potential limit demonstrated a more substantial impact on the activation than a higher frequency of cycles over the Ni-redox peak. For $Ni_{99.99}$, the increased cycling over the Ni(II)/Ni(III) redox peaks showed a similarly beneficial effect as conditioning with a lower potential limit and a reduced number of cycles. This supports the hypothesis that the importance of the lower limit for the activation depends on the amount of Fe content in the electrode.

To better resolve the impact of the HER regime and the scan rate during conditioning on the activation of $Ni_{99.99}$, the activation was analyzed over time, as illustrated in Figure 5.23. Conditioning was performed between 0.5-1.6 V and –0.35-1.6 V at 10 and 100 mV s^{-1} for a maximum of 24 h with a CP at 10 mA cm^{-2} every hour. Figure 5.23 shows that independent of which conditioning was used, activation increases first rapidly and then levels off over time. Conditioning between 0.5-1.6 V resulted in a lower activation compared to conditioning between –0.35-1.6 V. At 100 mV s^{-1}, activation saturated at 37±2 mV after 14 h conditioning between 0.5-1.6 V and at 70±2 mV after 9 h conditioning between –0.35-1.6 V. This highlights that even though conditioning with the HER regime might be more important for $Ni_{70}Fe_{30}$ than for $Ni_{99.99}$ (see Figure 5.22), it is also significantly important for the absolute activation of $Ni_{99.99}$. This is particularly evident during longer conditioning times as the saturation limit for activation appears to vary depending on the lower potential limit. Interestingly, the influence of the scan rate on activation is different depending on the potential window. When conditioning between –0.35-1.6 V, activation saturated at 67±2 mV after 16 h conditioning at 10 mV s^{-1} and was, thus, slightly lower than that at 100 mV s^{-1}. For the conditioning window of 0.5-1.6 V, the saturated activation of 53 mV after 16 h conditioning at 10 mV s^{-1} was higher than that at 100 mV s^{-1}. A possible explanation could be that Fe incorporation from the electrolyte into Ni (hydr)oxides is stabilized at lower potentials. Lowering the scan rate increases the time spent at these low potentials. Since significantly more time is spent at the lower potentials for the potential window –0.35-1.6 V, a low scan rate might not be as influential here. It must be noted that during the conditioning between 0.5-1.6 V at 10 mV s^{-1}, the electrolyte flow was shortly disconnected, and the electrodes were exposed to air between the 4^{th} and 5^{th} hour of conditioning. This might have led to the sudden increase in activation at this point.

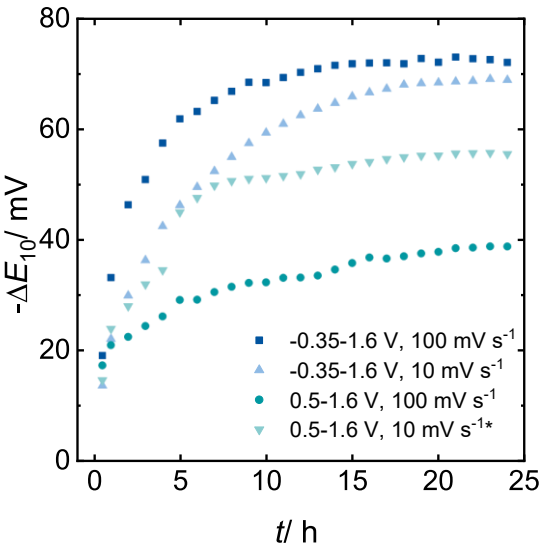

Figure 5.23. Time dependency of the activation of $Ni_{99.99}$, when conditioning between 0.5-1.6 V and –0.35-1.6 V at 10 and 100 mV s^{-1}. A CP was conducted every 0.5-1 h. Experiments were performed in 1 M KOH at RT. The asterisk (*) indicates that during this experiment, the electrolyte flow was shortly disconnected, and the electrodes were exposed to air between the 4th and 5th hour of conditioning. The experiments are single measurements.

Regarding the activation of $Ni_{99.99}$, $Ni_{99.2}$, $Ni_{90}Fe_{10}$, $Ni_{80}Fe_{20}$, and $Ni_{70}Fe_{30}$ resulting from CV conditioning with the same sequences shown in Figure 5.22b, activation is compared in Figure 5.24. For all materials, the same trends as in Figure 5.22b were found. Figure 5.24 identifies that $Ni_{99.99}$ and $Ni_{99.2}$ perform similarly, as well as the Ni-Fe alloys among one another.

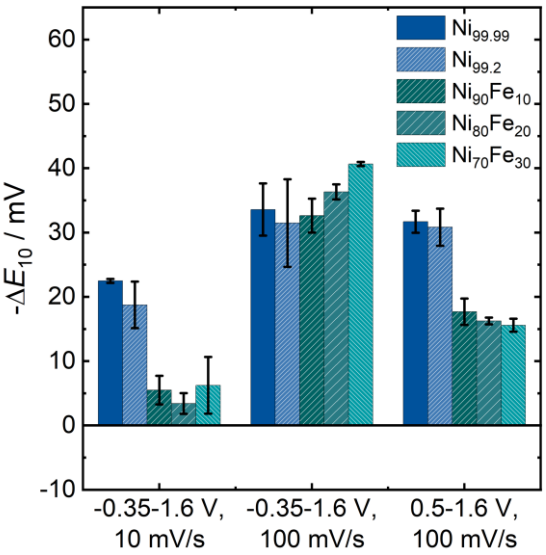

Figure 5.24. Activation of different Ni-(Fe)-electrodes ($Ni_{99.99}$, $Ni_{99.2}$, $Ni_{90}Fe_{10}$, $Ni_{80}Fe_{20}$, $Ni_{70}Fe_{30}$) resulting from CV conditioning between –0.36-1.6 V at 10 mV s^{-1}, –0.35-1.6 V at 100 mV s^{-1}, 0.5-1.6 V at 100 mV s^{-1} for 30 min. 82 (0.5-1.6 V, 100 mV s^{-1}), 46 (–0.35-1.6 V, 100 mV s^{-1}), and 5 (–0.35-1.6 V, 10 mV s^{-1}) cycles were performed. Note that this Figure represents a coherent data set. Thus, single data points can deviate within the error range from the values in Figure 5.17.

Similarly as in Figure 5.22b, the activation of Ni was more than double compared to all Ni-Fe alloys at the low scan rate. Also in line with Figure 5.22b, the lower potential limit showed a larger impact on the activation of the Ni-Fe alloys than a higher frequency of cycles over the

Ni-redox peak. Interestingly, activation increased with rising Fe content in the electrode when conditioning between –0.35-1.6 V at 100 mV s^{-1}. This supports the hypothesis that the lower potential limit is of increasing importance for the activation with rising Fe content in the electrode. This could be attributed to an increased Fe dissolution in electrodes with higher Fe content. The Fe dissolution might result in a larger surface area, more accessible Ni centers, and a subtle improvement in the Ni:Fe ratio.

To validate this hypothesis, the Fe dissolution was investigated *in-situ* by ICP-OES during the conditioning of $Ni_{70}Fe_{30}$ between –0.35-1.6 V and 0.5-1.6 V. Three analysis CVs at a scan rate of 2 mV s^{-1} were performed, followed by a 30 min conditioning at 100 mV s^{-1}, and lastly again one analysis CV at 2 mV s^{-1}. K was measured as an internal standard. The Fe and K concentrations for the entire sequence can be seen in Figure S7 in the appendix and in Figure 5.39 in chapter 5.2.3**.** The K concentration is constant over the course of the experiment for both sequences. The sharp intensity drops are associated with gas evolution. The Fe concentration remains relatively constant over most of the experiment. Only during the first analysis CV and during the 30 min CV conditioning between –0.35-1.6 V a significant Fe dissolution is visible. Thus, Figure 5.25 focuses on a) the first analysis CV and b) the 30 min CV conditioning at 100 mV s^{-1}.

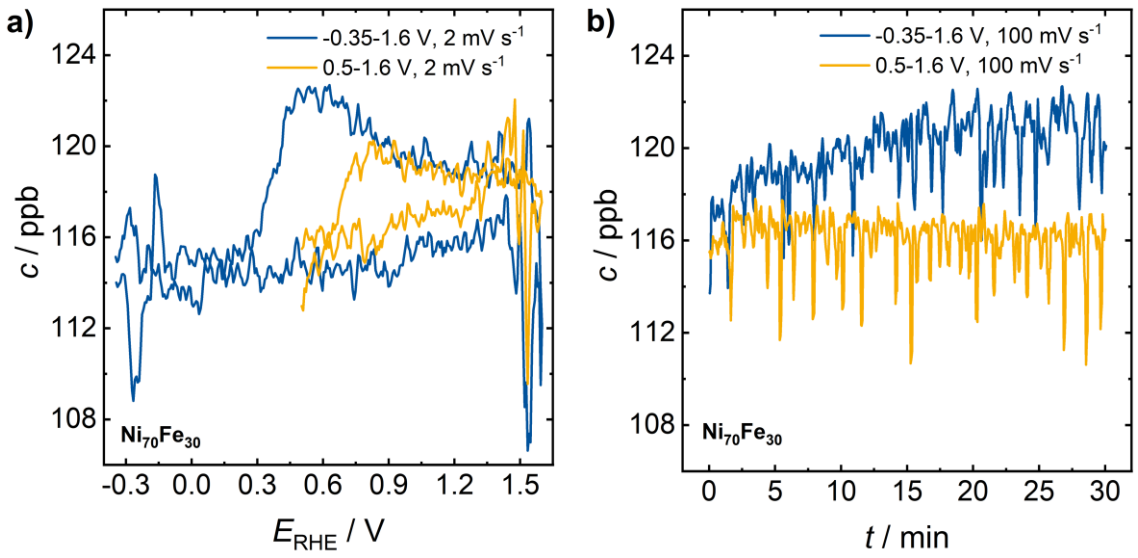

Figure 5.25. Fe concentration, measured *in-situ* by ICP-OES, while performing a) CV at 2 mV s^{-1} and b) CV conditioning at 100 mV s^{-1} on $Ni_{70}Fe_{30}$. CV was conducted between –0.35-1.6 V and 0.5-1.6 V in 1 M KOH at RT. The Fe and K concentrations for the entire sequence can be seen in Figure S7 and also in Figure 5.39 and Figure S20. The potential window –0.35-1.6 V in a) is also displayed in Figure 5.15.

Figure 5.25a shows that Fe dissolution occurs during the oxidative potential sweep between 0.3-1.2 V. As the conditioning between 0.5-1.6 V covers only a part of this potential window, the Fe dissolution appears to be smaller compared to the conditioning between –0.35-1.6 V. This enhanced Fe dissolution for the conditioning between –0.35-1.6 V becomes more evident when comparing the course of the Fe concentration during the CV conditioning at 100 mV s^{-1} for 30 min in Figure 5.25b. While the Fe concentration stays constant at 116 ppb when conditioning between 0.5-1.6 V, the Fe concentration increases to approx. 121 ppb when cycling between –0.35-1.6 V. This supports the hypothesis that conditioning with –0.35 V as a lower potential limit enhances Fe dissolution for Ni-Fe electrodes. Such an increased Fe

dissolution at lower potentials aligns with the works by Zuo *et al*. on the conditioning of steel electrodes.[33]

Variation of Fe Concentration

In addition to varying the Fe content in the electrode, the impact of different Fe contents in the electrolyte on activity and activation was investigated. Figure 5.26 displays the OER potential at 10 mA cm^{-2} for $Ni_{99.99}$ and $Ni_{70}Fe_{30}$ before and after CV conditioning at different Fe concentrations. Conditioning was performed between –0.35-1.6 V at 100 mV s^{-1} for 30 min (46 cycles). The Fe concentrations were set to approx. 10±5, 110±10, and 950±10 ppb by choosing a KOH batch with a low Fe concentration (10 ppb) and by $Fe(NO)_3$ addition (110 ppb, 950 ppb). The detailed electrolyte preparation can be found in chapter 4.1. For the previously discussed conditioning optimization for $Ni_{70}Fe_{30}$, 1 M KOH with 110 ppb Fe was used.

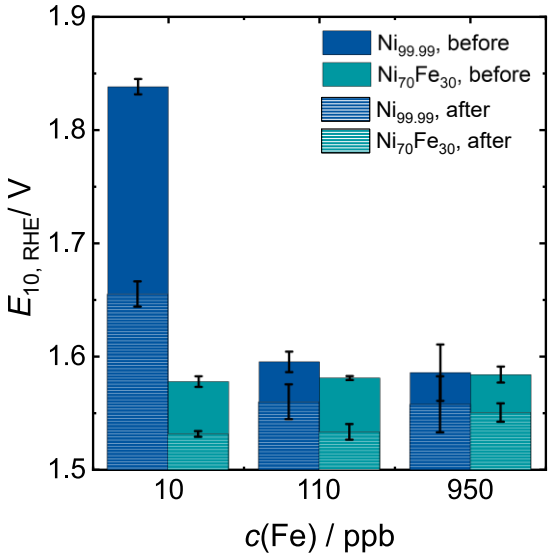

Figure 5.26. Potential at 10 mA cm^{-2}, $E_{10,RHE}$, before and after CV conditioning with different Fe concentrations of approx. 10, 110, and 950 ppb in the electrolyte. Conditioning was performed between –0.35-1.6 V at 100 mV s^{-1} for 30 min (46 cycles) in 1 M KOH at RT.

In Figure 5.26, it is evident that at very low Fe concentrations in the electrolyte of approx. 10 ppb, the potential of unconditioned $Ni_{99.99}$ was very high at 1.84±0.01 V in contrast to Fe concentrations larger than 100 ppb. At Fe concentrations of 110 ppb and 950 ppb, no significant differences in potentials were observed within the margin of error, resulting in an average potential of approx. 1.59±0.03 V. This aligns with previous reports, which state that the activity of Ni hydr(oxy)oxide only depends on the Fe concentration for concentrations smaller than 100 ppb.[72] It is important to note that determining the potential at 10 ppb Fe proved challenging as the potential increased significantly during its 10 min measurement time, as shown in Figure S8. This indicates an instability of the electrode-electrolyte interface. Such pronounced deactivation was not observed for the electrolytes with higher Fe concentrations. After conditioning, the potential at 10 ppb Fe was decreased. It was, however, still 100 mV higher than for electrolytes containing ≥110 ppb Fe, where an average potential of 1.56±0.03 V was obtained after conditioning, as seen in Figure 5.26 (also compare Figure S8). This suggests that Fe incorporation and stabilization of a dynamic Fe equilibrium might be difficult during constant current operation of $Ni_{99.99}$ at 10 ppb without conditioning. During conditioning,

a (hydr)oxide layer grows, which might enable a slight Fe incorporation, stabilizing the surface-electrolyte interface. This aligns with previous reports stating that a stable dynamic Fe-dissolution-redeposition equilibrium is required for stable OER performance.[72,127] However, it needs to be noted that Son *et al*. reported a deactivation of Ni when conditioning (CP: 5 mA cm^{-2} for 24 h, CV: 1.1-1.63 V *vs*. RHE, >1000 cycles) in Fe-free electrolyte.[63] The deactivation during conditioning by CP is in line with the herein-reported instability of the CP at 10 ppb Fe before conditioning. Comparing the CV conditioning, it becomes clear that the conditioning from Son *et al*. does not cover the lower potential regime, while the conditioning used in this work includes the OER and HER regime. Thus, this suggests that the lower potential regime might be responsible for generating a more active and stable oxide. If sufficient Fe is present in the electrolyte (110, 950 ppb), a stable dynamic Fe-dissolution-redeposition equilibrium is suggested to establish even before conditioning, resulting in a similar activity of $Ni_{99.99}$ in these two electrolytes. Chung *et al*. suggested that for each MO_xH_y surface, there is an Fe saturation coverage. When this coverage is achieved, a further increase in Fe concentration does not affect the electrode activity or Fe incorporation.[72] As seen in Figure 5.26, the activation of Ni by conditioning was not limited by the Fe concentration in the electrolyte bulk at Fe concentrations of 110 and 950 ppb. This could be due to different reasons. For once, this observation supports the hypothesis of a stable dynamic Fe-equilibrium at the surface. Another possible explanation is that instead of the Fe incorporation from the electrolyte, the amount of formed $Ni(OH)_2$ is limiting activation. $Ni(OH)_2$ acts as a host and only if sufficient $Ni(OH)_2$ is present, Fe can be incorporated. Since the conditioning parameters are the same and it is assumed that the Fe concentration does not affect the $Ni(OH)_2$ formation, a similar activation would result due to a similar amount of $Ni(OH)_2$ present. This is in line with previous reports from Mattinen *et al*., who showed a strong correlation between the amount of $Ni(OH)_2$ and of Fe being incorporated. However, they also showed that the oxide charge capacity, *i.e*. the amount of formed $Ni(OH)_2$, did indeed depend on the Fe concentration in the electrolyte. In their study, the oxide charge capacity was lower in Fe-containing electrolyte compared to Fe-free electrolyte, probably due to a suppression of the Ni(II)/Ni(III) oxidation.[68] However, it needs to be noted that their cycling conditions were different from the ones reported here. They did not cycle to potentials lower than 0.8 V *vs*. RHE (0.855-1.655 V *vs*. RHE, 10 mV s^{-1}, up to 150 cycles). Hence, the cycling to lower potentials seems to be essential to not lose oxide charge capacity when conditioning Ni in (highly) Fe-containing electrolytes. Going to lower potentials might be required for the Ni(0) to $Ni(OH)_2$ transformation, which increases the $Ni(OH)_2$ layer into the bulk metal and ensures a stable $Ni(OH)_2$ layer also at elevated Fe concentrations.

For $Ni_{70}Fe_{30}$, the potential before conditioning of 1.58±0.01 V was unaffected by changes in Fe concentrations. This suggests that there is enough Fe present to ensure a stable dynamic Fe-equilibrium at the electrode surface. At low Fe concentrations in the electrolyte bulk, the dynamic Fe-equilibrium might be sustained by an enhanced Fe dissolution from the Ni-Fe alloy, which increases the local Fe concentration at the electrode interface. By conditioning, a similar activation for Fe concentrations of 10 and 110 ppb was obtained with 46±7 mV for 10 ppb and 47±6 mV for 110 ppb. The activation in an electrolyte with 950 ppb Fe was lower with 33±2 mV. A possible explanation for the lower activation at 950 ppb Fe might be that at these high Fe concentrations, less Fe dissolution occurs, resulting in a smaller increase of active surface area by conditioning. Alternatively, the Ni oxidation could become more suppressed with increasing Fe concentration in the electrolyte and at the electrode interface. This is in line with

previous reports, which stated an increased suppression of the Ni oxidation with a larger Fe content in the electrode and electrolyte.[61,67–69] The suppressed Ni oxidation directly corresponds to a decreased activation since the activation is correlated to the amount of formed $Ni(OH)_2$, as discussed in chapter 5.2.1.

Conclusion

To summarize, conditioning Ni and Ni-Fe alloys with an Fe content between 10-30 wt% revealed that all materials show similar correlations between activation and conditioning parameters, though the absolute extent of these activation trends varied slightly. For example, while $Ni_{99.99}$ and $Ni_{70}Fe_{30}$ showed the most significant activation at low scan rates (10 mV s^{-1}) for a fixed number of cycles, low scan rates were particularly important for Ni. This suggests that the activation of $Ni_{99.99}$ is kinetically more hindered or that more time in the lower potential regime is required for efficient oxide growth and stabilization of Fe incorporation. Kinetic limitation could result from a slow Ni to $Ni(OH)_2$ formation and a slow Fe incorporation.

Investigating the influence of the Fe concentration on the activation, it was observed that if sufficient Fe is present in the electrolyte (c(Fe) ≥ 110 ppb), the activity and activation of $Ni_{99.99}$ were independent of the Fe concentration. This could be due to a stable dynamic Fe equilibrium at the electrode interface, which results in a stable rate of Fe incorporation. Alternatively, activation might be limited by the availability of $Ni(OH)_2$. If very little Fe is present in the electrolyte, strong deactivation occurs for an unconditioned $Ni_{99.99}$ electrode. Conditioning, especially at lower potentials, is suggested to stabilize the surface by oxide formation and Fe incorporation. For $Ni_{70}Fe_{30}$, the activity of the unconditioned electrode is unaffected by the Fe concentration in the electrolyte. Activation is slightly lower when conditioning with a high Fe concentration (950 ppb), potentially because of a decreased Fe dissolution at the electrode, resulting in a smaller surface area increase. Alternatively, higher Fe concentrations in the electrolyte might lead to an inhibition of Ni oxidation.

5.2.3. Understanding the Electrode Material Changes Induced by Electrochemical Conditioning

To better understand the processes occurring during the conditioning of bulk Ni-(Fe)-based electrodes at lab conditions, the induced surface changes will be analytically characterized in the following chapter. More specifically, the surface changes of $Ni_{99.99}$ and $Ni_{70}Fe_{30}$ from conditioning with two different potential windows, with (–0.35-1.6 V) and without (0.5-1.6 V) the HER regime, are investigated by

- dcCV (= regular direct current CV)
- FTacV
- FTIR spectroscopy
- Optical microscopy, SEM, and EDX
- XPS
- ICP-OES

The activation of $Ni_{99.99}$ and $Ni_{70}Fe_{30}$ from CV conditioning between –0.35-1.6 V and 0.5-1.6 V at 10 and 100 mV s^{-1} for 46 cycles is illustrated in Figure 5.27. For both materials, activation was enhanced when conditioning between –0.35-1.6 V compared to conditioning between 0.5-

1.6 V at the same scan rate. For $Ni_{99.99}$, the difference in activation between the two potential windows was smaller. Further, Figure 5.27 shows that conditioning at a low scan rate of 10 mV s^{-1} yielded a larger activation for $Ni_{99.99}$. For $Ni_{70}Fe_{30}$, the scan rate had only a minor impact on the activation. In the previous chapters 5.2.1 and 5.2.2,[126] it is hypothesized that an improvement in activation correlates with an enhanced formation of a hydrous (oxy)hydroxide layer, such as α-$Ni(OH)_2$/γ-NiOOH. For $Ni_{99.99}$, the formation of such a hydrous oxide layer is suggested to be kinetically limited, resulting in the observed scan rate dependency. Considering that most likely mixed Ni-Fe oxides are being formed, a slow Fe incorporation could also limit the process. The increased importance of the lower potential limit for $Ni_{70}Fe_{30}$ compared to $Ni_{99.99}$ could be due to an enhanced Fe dissolution for $Ni_{70}Fe_{30}$ in the lower potential regime, as was also recently proposed by Zuo *et al.*[33] This, in turn, would lead to a larger surface area, more accessible Ni sites, and a subtle improvement of the Ni:Fe ratio. When comparing the conditioning without the HER regime for the two materials, activation of $Ni_{70}Fe_{30}$ is lower than for $Ni_{99.99}$ as the Fe in the electrode might suppress Ni oxidation, as was previously stated by others.[61,67,69] Activation of $Ni_{99.99}$ could also increase initially stronger with the growth of the hydrous oxide layer than for $Ni_{70}Fe_{30}$.

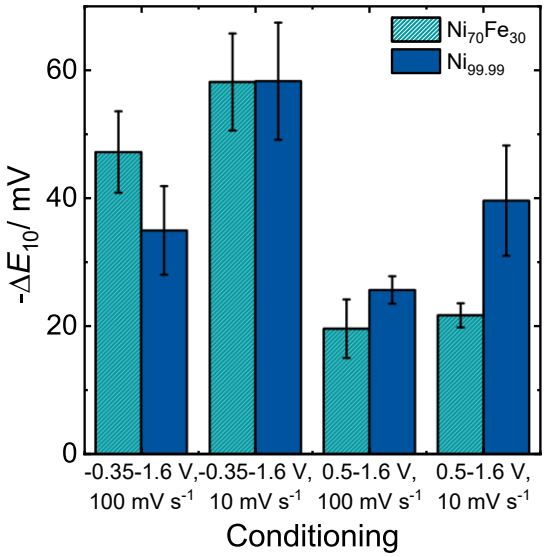

Figure 5.27. Activation of $Ni_{99.99}$ and $Ni_{70}Fe_{30}$ resulting from CV conditioning between –0.35-1.6 V and 0.5-1.6 V at 10 and 100 mV s^{-1} for 46 cycles in 1 M KOH at RT. The conditioning was 16.9 min (0.5-1.6 V, 100 mV s^{-1}), 168.7 min (0.5-1.6 V, 10 mV s^{-1}), 29.9 min (–0.35-1.6 V, 100 mV s^{-1}), and 299 min (–0.35-1.6 V, 10 mV s^{-1}).

dcCV

To get a first insight into the occurring surface changes, the redox peaks of the conditioning and activity CVs were evaluated. Figure 5.28 shows the 2nd and 46th conditioning CV cycle when conditioning $Ni_{99.99}$ (a) and $Ni_{70}Fe_{30}$ (b) with –0.35-1.6 V and 0.5-1.6 V at 10 and 100 mV s^{-1} for 46 cycles.

In Figure 5.28, different redox peaks are visible for $Ni_{70}Fe_{30}$ (a) and $Ni_{99.99}$ (b) before (black) and after (in color) conditioning. All apparent redox peaks are enhanced by electrochemical conditioning, independent of the applied conditioning parameters. Hence, primarily the redox features after conditioning are discussed in the following. When conditioning $Ni_{70}Fe_{30}$ between

–0.35-1.6 V at either 10 or 100 mV s^{-1}, Figure 5.28a shows a broad redox peak between –0.2-0.5 V, indicating the Ni(0)/Ni(II) redox couple [29,55] and the Fe(0) to Fe(III) oxidation *via* Fe(I/II) and the reduction *vice versa* between –0.2-0.6 V.[59,60] This redox peak between –0.2-0.5 V is relatively broad with little fine structure, making further interpretation difficult. When conditioning $Ni_{99.99}$ (b) between –0.35-1.6 V at 100 mV s^{-1}, an oxidative peak between 0-0.5 V can be seen in the 46th CV. At 10 mV s^{-1}, this peak is visible only with very little intensity due to the decreased scan rate. Based on previous reports, this peak can be assigned to the oxidation of Ni(0) to α-$Ni(OH)_2$.[29] It is interesting to note that this suggests a continuous Ni(0) to Ni(II) oxidation and, hence, a growth of the oxide layer into the bulk material. The reductive counter-reaction cannot be identified, suggesting an irreversible phase transformation of the formed α-$Ni(OH)_2$ to β-$Ni(OH)_2$ at intermediate potentials[29,53,55] or that the counter-reaction is covered by background current and the HER onset.[29,58] The studies from Alsabet *et al.*[53,55] and Lyons *et al.*[29] reported that the potential needs to be reversed <0.7 V *vs.* RHE to prevent the phase transformation of α-$Ni(OH)_2$ to β-$Ni(OH)_2$. Only then the respective reduction peak from α-$Ni(OH)_2$ to Ni(0) would be visible.

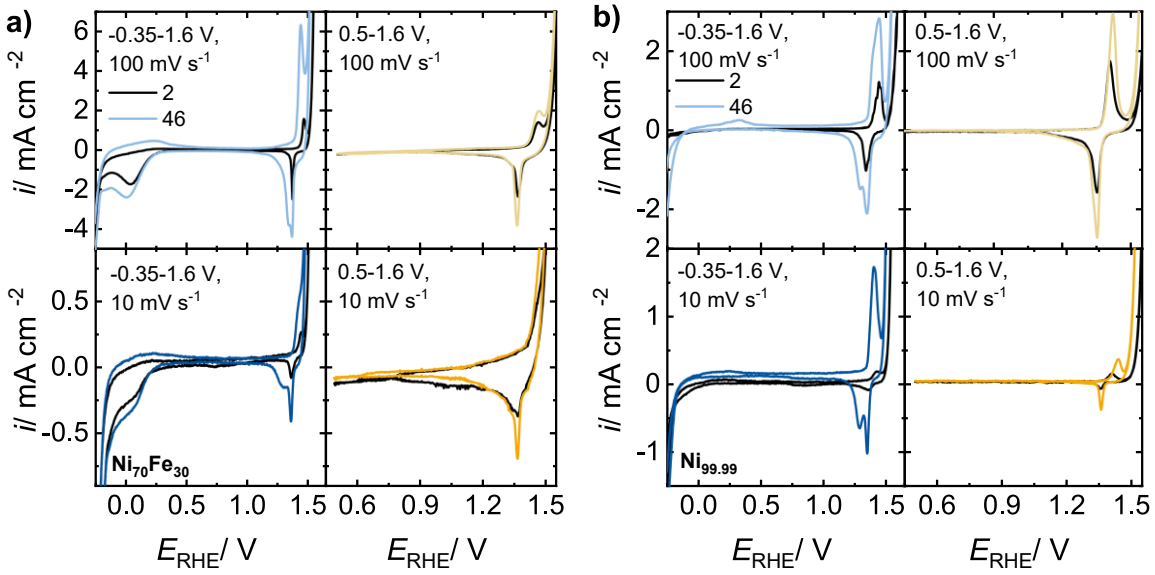

Figure 5.28. Conditioning CVs (2nd and 46th cycle) of a) $Ni_{70}Fe_{30}$ and b) $Ni_{99.99}$. Conditioning was performed between –0.35-1.6 V and 0.5-1.6 V at 10 and 100 mV s^{-1} for 46 cycles. Experiments were performed in 1 M KOH at RT. The redox peaks between –0.2-0.5 V could be assigned to Ni(0)/Ni(II) and/or Fe(0) to Fe(III) *via* Fe(I/II) and vice versa. The Ni(II)/Ni(III) redox peaks are visible between 1.2-1.5 V.

At higher potentials, Figure 5.28 shows a redox feature between 1.2-1.5 V for $Ni_{70}Fe_{30}$ (a) and $Ni_{99.99}$ (b), irrespective of the conditioning parameters. This redox peak corresponds to the Ni(II)/Ni(III) redox couple.[29,53,76] This Ni(II)/Ni(III) redox peak is sensitive to a change in the conditioning potential window. Two Ni(II)/Ni(III) reduction peaks are obtained after 46 CV cycles when conditioning $Ni_{70}Fe_{30}$ or $Ni_{99.99}$ between –0.35-1.6 V and only one when conditioning between 0.5-1.6 V.

To study the Ni(II)/Ni(III) peak behavior more closely, the activity CVs before and after conditioning of a) $Ni_{70}Fe_{30}$ and b) $Ni_{99.99}$ are compared in Figure 5.29. The activity CVs were performed before and after conditioning between 1-1.6 V at 100 mV s^{-1}.

In Figure 5.29, one can observe that before conditioning (black), only one oxidative and one reductive peak can be seen with peak potentials at 1.40-1.44 V (oxidation) and 1.35-1.36 V

(reduction) for $Ni_{99.99}$, respectively, and for $Ni_{70}Fe_{30}$, 1.47-1.48 V (oxidation) and 1.36-1.37 V (reduction). The shift of the oxidative peak toward higher potentials in the case of $Ni_{70}Fe_{30}$ could be explained by a suppressed Ni oxidation due to the Fe in the electrode, as suggested in previous reports.[61,67,69]

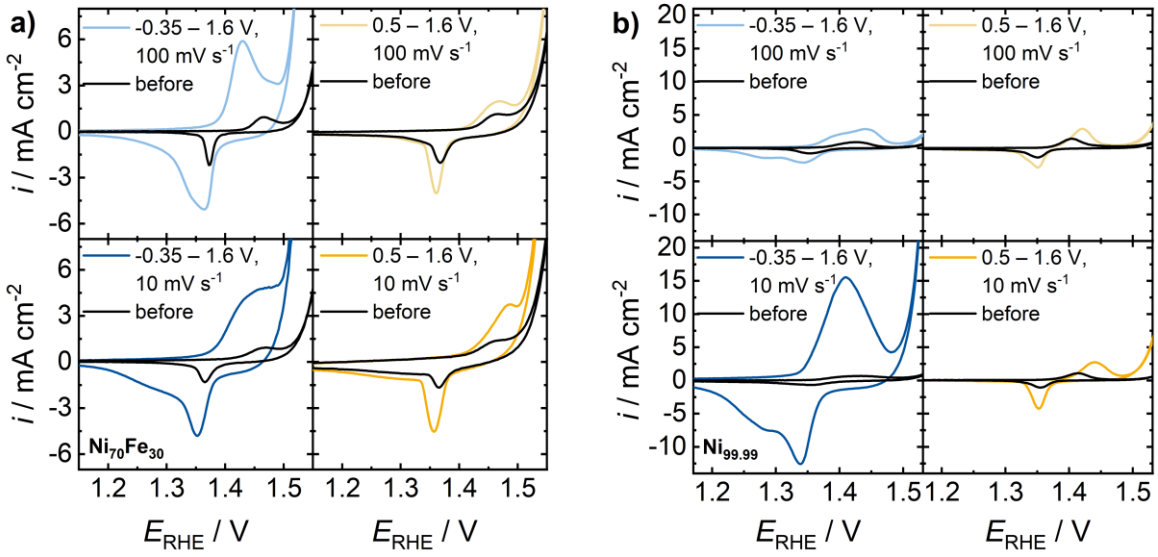

Figure 5.29. Activity CVs (1-1.6 V, 100 mV s^{-1}) before and after conditioning a) $Ni_{70}Fe_{30}$ and b) $Ni_{99.99}$. Conditioning was performed between –0.35-1.6 V and 0.5-1.6 V at 10 and 100 mV s^{-1} for 46 cycles in 1 M KOH at RT.

By conditioning without the HER regime at 10 and 100 mV s^{-1}(sand and orange), the redox peaks for both materials (Figure 5.29a and b) increase in intensity. The increase in intensity relates to a larger oxide layer and, thus, surface area.

When including the HER during conditioning (light and dark blue), the redox peaks increase in intensity, and an additional reduction peak appears for both materials. For $Ni_{99.99}$ (Figure 5.29b), the reduction peak potentials after conditioning are allocated at 1.29 V and 1.34 V. For $Ni_{70}Fe_{30}$ (Figure 5.29a), these peaks are less clearly resolved and are located around 1.29-1.34 V and 1.35-1.36 V. The appearance of a second reduction peak for both materials could be due to the evolution of a second phase. According to the duplex layer model,[12,27–29] a hydrous oxide layer, equivalent to α-$Ni(OH)_2$/γ-NiOOH, forms during CV conditioning. Based on this, the formation of the second reduction peak could correspond to the aging of this hydrous α-$Ni(OH)_2$/γ-NiOOH into the anhydrous β-$Ni(OH)_2$/NiOOH form. In line with this, Lyons *et al*. suggested the lower reductive peak to indicate the β-NiOOH reduction.[29] Regarding the oxidative peak, one oxidative peak with a peak potential at 1.44-1.46 V and a peak current density of 4.2-4.8 mA cm^{-2} is seen for $Ni_{70}Fe_{30}$ (Figure 5.29a), independent of the scan rate. Only when conditioning $Ni_{99.99}$ (Figure 5.29b) between –0.35-1.6 V at 100 mV s^{-1}, two oxidative peaks instead of one can be observed, with their peak potentials at 1.40 V and 1.44 V. Here, the peak intensities are low with 2.2 mA cm^{-2} and 2.9 mA cm^{-2}, respectively, compared to 16 mA cm^{-2} at 1.41 V when conditioning with 10 mV s^{-1}. A possible explanation might be that these two oxidative peaks are only visible for 100 mV s^{-1} due to their low peak intensity. When the peak intensity increases, both peaks might overlay and cannot be resolved, which is also in line with previous reports.[29] Interestingly, it needs to be pointed out that the oxide charge capacity of $Ni_{99.99}$ is significantly enhanced when conditioning between –0.35-1.6 V at 10 mV s^{-1} compared to the other conditionings. The difference between the two potential

windows suggests that the time spent at the lower potentials (–0.35-0.5 V) might be more relevant for the activation of $Ni_{99.99}$ potentially because the oxide structure is specifically tailored within this potential regime. One known Ni oxidation process occurring at these low potentials is the Ni(0) to $Ni(OH)_2$ oxidation, suggesting that its kinetic limitation might be the cause of this observed different scan rate dependency for the two potential windows. Alternatively, Fe might be slowly incorporated and stabilized in the low potential regime, which enhances the Ni oxidation.

For the correlation between the oxide charge capacity of the Ni(II)/Ni(III) redox peak and the activation (see Figure 5.20), both reduction peaks and, if applicable, both oxidative peaks were considered. This suggests that the phase and, thus, its hydrous character is of secondary importance for the activating effect. This is in line with the study from Stevens *et al*. who stated that the Ni(II)/Ni(III) peak behavior, such as a changing Ni-phase, is not reflected in the OER performance.[64]

Further, different peak shifts by conditioning were obtained depending on the electrode material and applied potential window. However, it needs to be noted that these are influenced by multiple effects such as redox kinetics, uncompensated resistance, capacitance, and surface changes. Thus, their interpretation is often difficult and needs to be considered carefully. The trends of the activity CVs shown were cross-checked by two repeat experiments, and in the following, only the common observed peak shifts are discussed. When conditioning without the HER regime (0.5-1.6 V), the oxidative peaks for both materials shift to higher potentials, irrespective of the applied scan rate. The shift of the oxidative peak indicates a surface change. For $Ni_{99.99}$, Fe is potentially incorporated and the increased Fe content in the electrode suppresses the Ni oxidation.[61,67,69] Since the peak shift is larger at 10 mV s^{-1} compared to 100 mV s^{-1}, this surface change might be kinetically limited. That the reductive peak remains constant might be due to the compensation of two counteracting effects. On the one side, the Ni(II)/Ni(III) redox peak might be shifted to more positive potentials due to a surface change. On the other side, the R_u is slightly increased by conditioning (<0.1 Ohm), resulting in an increased peak separation, which shifts the oxidation peak to even higher potentials and the reduction peak to lower potentials. For $Ni_{70}Fe_{30}$, a less significant oxidative peak shift is observed. Here, the reduction peak is also slightly shifted but to more negative potentials. This increased peak separation might result from the increased R_u. For 10 mV s^{-1}, the oxidative and reductive peak, however, do not shift symmetrically to more positive or rather negative potentials. The surplus shift of the oxidative peak to more positive potentials could theoretically also be explained by Fe incorporation. However, it is highly questionable that a Ni-Fe electrode with 30 wt% Fe, which is slightly higher than the herein-identified optimum Ni:Fe ratio (see Figure S6), would still incorporate Fe from the electrolyte. It is, thus, more likely that a different surface change is involved as well, leading to this peak shift. To clarify this, further analytical characterization is necessary. When conditioning with the HER regime (–0.35-0.5 V), the Ni(II)/Ni(III) redox peak is shifted to lower potentials for $Ni_{70}Fe_{30}$, indicating a surface change such as a Fe dissolution. For $Ni_{99.99}$, no common peak shift toward lower or higher potentials of the reductive or oxidative peak could be identified for the three performed repeat experiments. Considering the peak shifts from $Ni_{99.99}$ and $Ni_{70}Fe_{30}$ in either potential window with respect to their activation, it can be concluded that these peak shifts cannot be correlated to the activation. This is in line with the study from Stevens *et al*., which stated that the activation of NiO_xH_y catalysts is not distinctly correlated with the behavior of the Ni(II)/Ni(III) redox peaks.[64] Further, from the conditioning of $Ni_{70}Fe_{30}$ without HER and $Ni_{99.99}$ with HER, it

can be deduced that the peak shifts do not only result from an adjustment of the Ni:Fe ratio in the electrode and are highly complex, challenging interpretation. Hence, further investigations such as FTacV or spectroscopic analyses are necessary to clarify the occurring surface changes.

To sum up, dcCV indicates that conditioning with the HER regime results in stronger surface oxidation and the evolution of a second Ni phase, which might correlate to β-$Ni(OH)_2$. The amount of generated hydroxide is primarily important for the activation, and the type of phase is suggested to play a secondary role. The formation of a Ni oxide charge depends on the scan rate primarily for $Ni_{99.99}$ when conditioned with the HER, suggesting a kinetic limitation of the Ni(0) to $Ni(OH)_2$ oxidation. Alternatively, Fe incorporation and stabilization at low potentials can be the kinetically limiting factor, assuming it would enhance the Ni oxidation. The occurring peak shifts when conditioning $Ni_{99.99}$ and $Ni_{70}Fe_{30}$ are highly complex due to many interacting factors and can not be correlated to the activation.

In order to validate these hypotheses, FTacV, optical microscopy, SEM, EDX, XPS, and FTIR measurements were performed before and after conditioning for both discussed potential windows (–0.35-1.6 V and 0.5-1.6 V at 10 mV s^{-1}).

FTacV

Determining the extent and the kinetics of oxide formation by peak analysis of the dcCVs can be significantly distorted by capacitive currents, IR_u drop, and overlapping of faradaic currents. Additionally, processes can be masked. FTacV can be used to deconvolute these different processes and differentiate between redox kinetics, capacitive currents, and IR_u drop. Thus, FTacV was applied before and after conditioning to identify the occurring electrochemical processes on Ni-(Fe)-based electrodes and their changes due to electrochemical conditioning. The detailed methodology for the FTacV measurements can be found in chapter 4.4.6. The entire electrochemical protocol started with FTacV, followed by the standard dc activity determination (CV at 10 and 100 mV s^{-1}, CP at 10 and 100 mA cm^{-2}), FTacV before conditioning, electrochemical conditioning, FTacV after conditioning, standard dc activity determination, and again FTacV at the end of the experiment. In the following, only the results from before and after conditioning are discussed as the harmonics from FTacV at the start of the experiment and before conditioning as well as after conditioning and at the end of the experiment were similar. FTacV was conducted as CV between 1-2 V at 19.073 mV s^{-1} at 9, 39, and 89 Hz. The results from 9 and 89 Hz are compared, while the results from 39 Hz are not discussed as they do not contain any additional information. Each CV was repeated three times, and the data from the 1st CV is displayed. The power spectra, corresponding to the FT of the recorded current-time data, are in the appendix (Figure S9 and Figure S11). These indicate the quality of the FTacV measurement by showing *e.g.* the signal-to-noise ratio and the influence of the scan rate on the harmonics. Further, the number of resolved harmonics can be seen.

Many variables impact the behavior of the harmonics, which complicates the evaluation of FTacV. For example, the peak current of the FTacV-generated harmonics can be influenced by the uncompensated resistance, capacitance, charge transfer coefficient, thermodynamic and kinetic dispersion, temperature, amplitude, and frequency. Thus, Table 5.1 gives a short and simplified overview to guide the qualitative interpretation of the following FTacV results.

More details can be read in chapter 4.4.6. An increased uncompensated resistance R_u leads to a decrease in the harmonics' magnitude and a distortion of the peak shape.[105–107,109] A higher double layer capacitance C_{dl} would magnify the influence of the R_u and it would show as a baseline shift in the 1st harmonic.[106,109] With increasing harmonic, the sensitivity to C_{dl} decreases. Higher harmonics (>1st) are usually insensitive to C_{dl}, unless C_{dl} depends on the potential.[111] Regarding the influence of the reaction kinetics on the harmonics, two scenarios need to be differentiated. If the reaction rate k is fast (reversible process) in comparison to the applied frequency (*i.e*. low frequency), the sensitivity of the harmonics to changes in k is reduced. Instead, the harmonic peak magnitude depends on the number of active sites N_{sites}. If the reaction rate k is slow (quasi-reversible process) in comparison to the applied frequency (*i.e*. high frequency), the harmonics become highly sensitive to changes in k. In contrast to fast reaction rates, slow reaction rates will lead in this case to a decreased peak magnitude, distortions in peak shape, and a peak shift to higher potentials in the harmonics (see Figure 4.15, chapter 4.4.6).[107,109,112]

Table 5.1. Simplified overview to guide the qualitative interpretation of the FTacV results.

Parameter	Change in harmonics
R_u	↑ R_u → decreased magnitude & shape distortion
C_{dl}	↑ C_{dl} → increased influence of R_u & elevated baseline The higher the harmonic, the more insensitive it is to C_{dl}
k	↓ k → decreased magnitude, shape distortion, shift to higher potentials (at higher frequencies)
N_{sites}	↑ N_{sites} → increased magnitude (at low frequencies)

Figure 5.30 illustrates the extracted dc and harmonics at a) 9 Hz and b) 89 Hz for $Ni_{70}Fe_{30}$ before and after conditioning between 0.5-1.6 V at 10 mV s^{-1}. By conditioning between 0.5-1.6 V, the R_u stayed constant at 0.64 Ohm. Hence, changes in the peak magnitude or shape in the harmonics are probably due to a change in the process' reaction kinetics.

In Figure 5.30a (9 Hz, before conditioning, forward scan, light green curve), the fundamental (1st) harmonic displays a peak in current density at approx. 1.4 V and an increase and then leveling off of the current density for potentials higher than 1.5 V. In the 2nd harmonic, a doublet at 1.4 V and a peak at 1.6 V is visible. The 3rd harmonic shows a peak with shoulders, a triplet, at 1.4 V and a doublet at 1.6 V. These peaks in the different harmonics indicate that two main processes are occurring, which can possibly be assigned to the OER (process I at 1.6 V) and the Ni(II)/Ni(III) redox reaction (process II at 1.4 V). These two processes are recognizable in the forward and backward sweep at 9 Hz (Figure 5.30a) and 89 Hz (Figure 5.30b) before and after conditioning. The comparison between 9 and 89 Hz before conditioning (light green) shows that the peak shape and position for both processes remain relatively unchanged for the different harmonics. The peak magnitude for process I (OER) also stays approx. constant. For process II (Ni(II)/Ni(III)), the peak magnitude increases slightly from 9 Hz to 89 Hz. The increase in magnitude with frequency is reported to be an indicator of a reversible process with a fast reaction rate if the relation between peak current and frequency is linear.[112] Please note that this comparison between the harmonics at 9 Hz (Figure 5.30a) and 89 Hz (Figure 5.30b) is also a first indication that the influence of the R_u of 0.64 Ohm on the harmonics does not

change when increasing the frequency. When comparing the harmonics before (light green) and after (dark blue) conditioning in Figure 5.30a (9 Hz) and b) (89 Hz) for the forward and backward scan, peak position, magnitude, and shape do not change significantly. This indicates that conditioning between 0.5-1.6 V shows little effect on oxide growth and OER kinetics. The 2nd and 3rd harmonics at 9 Hz (Figure 5.30a) and 89 Hz (Figure 5.30b) show a deformation of the process II peak in the forward sweep after conditioning (dark blue), which recovers during the backward sweep. This deformation is also slightly visible before conditioning but is considerably enhanced by conditioning. It could originate from a negative interference of the sine-waves from process II and I. Potentially, a third process (process III) is also involved, which causes this negative interference. The fundamental (1st) harmonic at 89 Hz in Figure 5.30b shows high currents between processes I and II and a peak at 1.46 V, which supports the hypothesis of a third process.

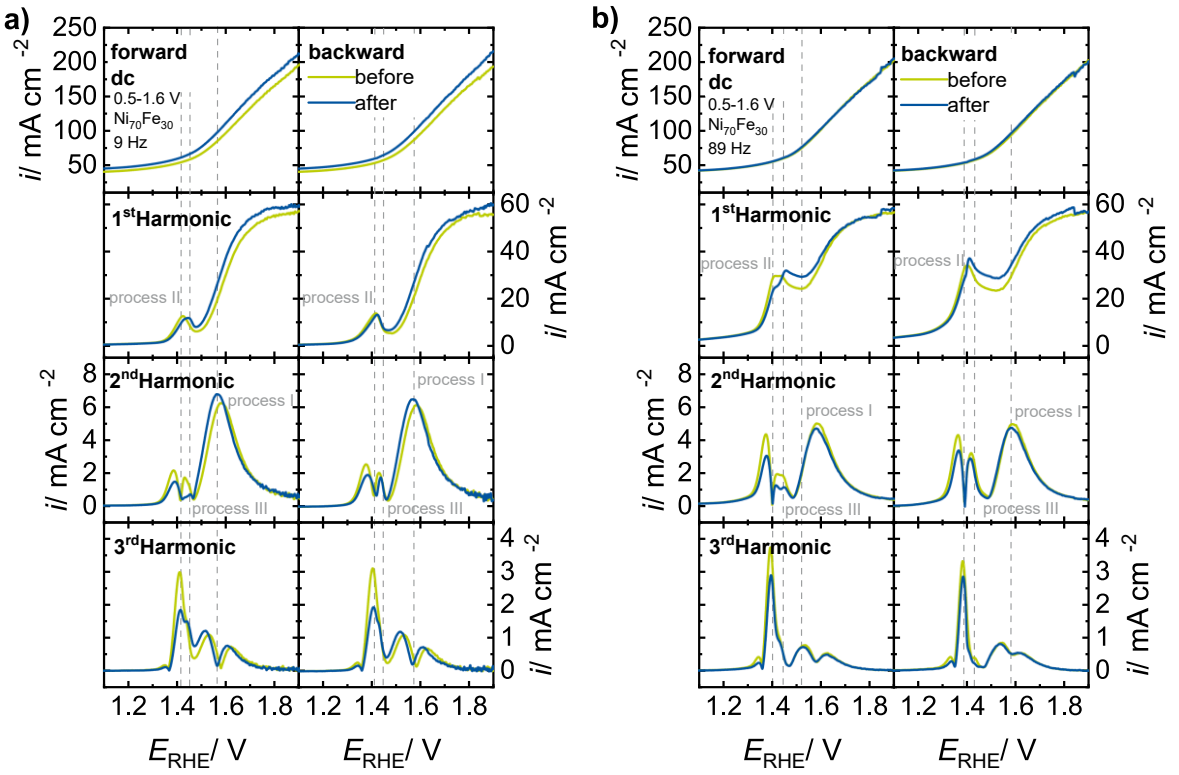

Figure 5.30. dc, fundamental (1st), 2nd-3rd harmonics from FTacV before and after conditioning $Ni_{70}Fe_{30}$ between 0.5-1.6 V at 10 mV s^{-1}. FTacV was performed as CV between 1-2 V at 19.073 mV s^{-1} at a) 9 and b) 89 Hz. Experiments were conducted in 1 M KOH at RT. The potentials are not iR_u corrected. The R_u stayed constant at 0.64 Ohm before and after conditioning.

Figure 5.31 shows the dc and harmonics at 9 Hz (Figure 5.31a) and 89 Hz (Figure 5.31b) for $Ni_{70}Fe_{30}$ before and after conditioning between –0.35-1.6 V at 10 mV s^{-1}. The measured R_u increased slightly from 0.73 to 0.75 Ohm from before to after conditioning. Thus, a slight lowering of the peak magnitude and a shape distortion after conditioning due to the R_u cannot be excluded.

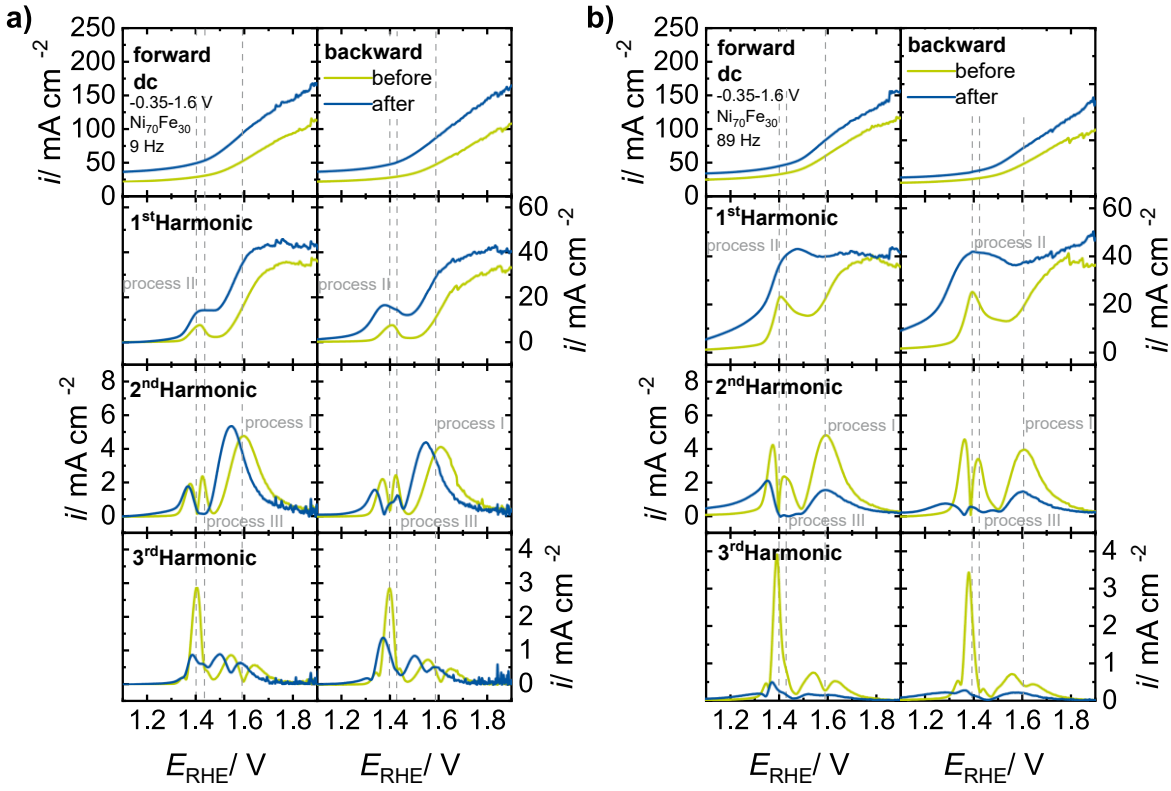

Figure 5.31. dc, fundamental (1st), 2nd-3rd harmonics from FTacV before and after conditioning $Ni_{70}Fe_{30}$ between –0.35-1.6 V at 10 mV s^{-1}. FTacV was performed between 1-2 V at 19.073 mV s^{-1} at a) 9 and b) 89 Hz. Experiments were conducted in 1 M KOH at RT. The potentials are not iR_u corrected. The R_u increased slightly from 0.73 to 0.75 Ohm from before to after conditioning.

In Figure 5.31, the 1st-3rd harmonics before conditioning (light green) indicate again the two main processes for 9 Hz (a) and 89 Hz (b): process I (OER) at 1.6 V and process II (Ni(II)/Ni(III)) at 1.4 V. Also, the comparison of the harmonics between 9 (a) and 89 Hz (b) before conditioning (light green) in Figure 5.31 shows the same trends as in Figure 5.30. This supports that the influence of the R_u on the harmonics does not change with the applied frequency for a R_u between 0.6-0.8 Ohm. Comparing the harmonics from before (light green) to after (dark blue) conditioning at 9 Hz (a) and 89 Hz (b), it can be seen that by conditioning the peak position, shape, and magnitude change for both processes. Process I (OER) shifts to lower potentials at 9 Hz (Figure 5.31a) in the 2nd and 3rd harmonics, but shape and magnitude remain unchanged upon conditioning. At 89 Hz (Figure 5.31b) in the 2nd and 3rd harmonics, the peak position of process I (OER) stays constant from before to after conditioning while the magnitude decreases and peak distortion occurs. Due to the different behavior at 9 and 89 Hz, it is proposed that the decrease in magnitude and shape distortion at 89 Hz does not result from the R_u but from a change in the kinetics of process I (OER). This decreased peak magnitude and distortion suggest that the apparent reaction rate is now slow compared to the frequency (*i.e.* quasi-reversible process with a small k/f ratio). It indicates that the induced surface changes from conditioning slow down the apparent OER reaction rate on the $Ni_{70}Fe_{30}$ electrode. None of these effects are observed at 9 Hz, proposing that the harmonics are influenced differently at 9 Hz. This could be since at 9 Hz the k/f ratio is larger and, thus, the harmonics are more sensitive to the number of active sites. By conditioning, the number of active sites is suggested to increase. Hence, the different peak behavior in the 2nd

and 3rd harmonics after conditioning at 9 Hz could be explained by the increased number of active sites compensating for the decreased apparent reaction rate. The decreased reaction rate is in line with a study from Son *et al.*, which showed an increase in the Tafel slope due to the conditioning of Ni.[63] However, others demonstrated an invariant Tafel slope from before to after conditioning of Ni[29] or even a decreasing Tafel slope at low potentials when conditioning Fe.[77]

For process II (Ni(II)/Ni(III)) at 9 Hz (Figure 5.31a) and 89 Hz (Figure 5.31b), the peak position stays constant, and the peak current increases in the 1st and decreases in the 2nd and 3rd harmonics by conditioning (comparison light green *vs.* dark blue). This decreased magnitude in the 2nd and 3rd harmonics suggests a decreased apparent reaction rate of the Ni(II)/Ni(III) redox reaction. Furthermore, a shape deformation in the 2nd and 3rd harmonics is visible after conditioning (dark blue) in the forward sweep at 9 Hz (a) and 89 Hz (b), which is partly recovered in the backward sweep. This deformation is similar to the behavior when conditioning with 0.5-1.6 V (compare with Figure 5.30). Similar to Figure 5.30, the current between process I and II in the fundamental (1st) harmonic is increased and broadens the feature of process II, indicating a potential process III. In Figure 5.31, the fundamental (1st) harmonic could also suggest a potential-dependent C_{dl}, which would show as a sloped or rather uneven baseline. Combined with Figure 5.30, a process III between processes I and II is, however, more likely. Summing up, Figure 5.31 indicates that by conditioning between –0.35-1.6 V, the oxide growth and OER reaction are slowed down and that the overall increased OER activity gain results from an increased number of active sites.

For $Ni_{99.99}$, similar trends were observed, and the graphs can be found in Figure S9 - Figure S12. One significant difference needs to be noted: By conditioning between 0.5-1.6 V, process I (OER) and process II (Ni(II)/Ni(III)) are shifted to higher potentials. As was shown by Bonke *et al.*[128], such a shift suggests a worsening of the OER activity.

Indeed, it is essential to note that the dc components in Figure 5.30 and Figure 5.31 do not show the expected Ni(II)/Ni(III) redox peaks or activation. Further, large offsets from 0 are visible, indicated by a shifted baseline. This could be associated with capacitive currents.

To investigate this, the dc activity CVs (1-1.6 V at 10 mV s^{-1}) and CPs at 10 mA cm^{-2} were evaluated, which were performed before and after conditioning in addition to the FTacV (see Figure 4.17 in chapter 4.4.6). In Figure 5.32, the dcCVs for $Ni_{70}Fe_{30}$ before and after conditioning between –0.35-1.6 V are shown in a). Figure 5.32b demonstrates the activation $-\Delta E_{10}$ of $Ni_{70}Fe_{30}$ and $Ni_{99.99}$ when conditioning with and without HER regime.

In Figure 5.32a, the dcCVs for $Ni_{70}Fe_{30}$ before and after conditioning between –0.35-1.6 V clearly show Ni(II)/Ni(III) redox peaks, which are enlarged by conditioning. Also, activation by conditioning is visible by the shift of the OER to lower potentials and an increase of the maximum current. Similarly, this was also observed for the conditioning of $Ni_{70}Fe_{30}$ between 0.5-1.6 V, as shown in Figure S13 in the appendix. This suggests that the dc component, seen in Figure 5.30 and Figure 5.31, is altered by the applied ac, which accentuates the non-linear processes.[105]

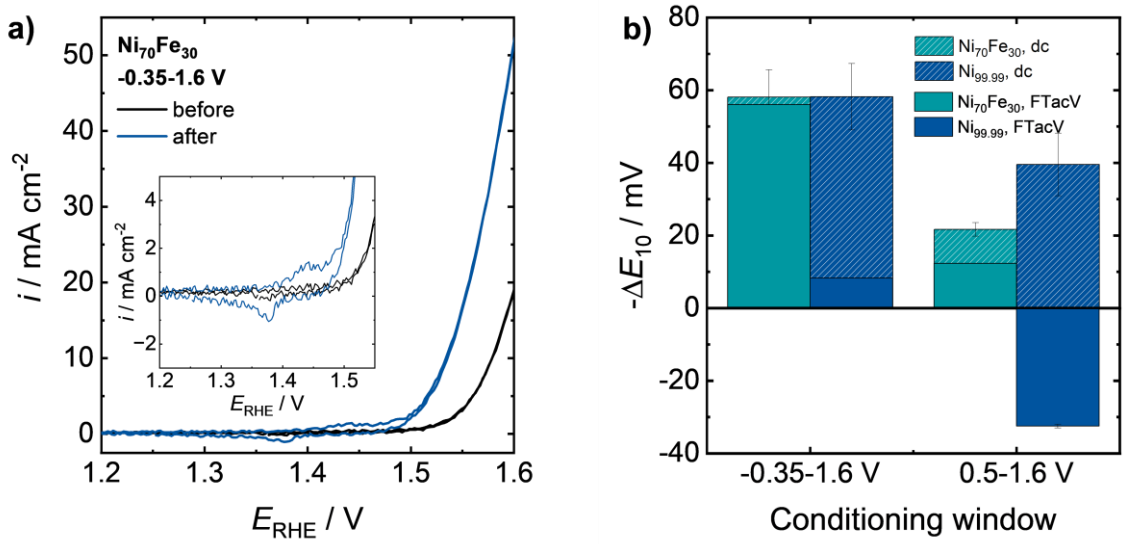

Figure 5.32. a) dcCV (1-1.6 V, 10 mV s^{-1}) during the FTacV experiment before and after conditioning of $Ni_{70}Fe_{30}$ between –0.35-1.6 V at 10 mV s^{-1} for 46 cycles. b) Effect of including FTacV into the electrochemical measurement procedure on the activation of $Ni_{99.99}$ and $Ni_{70}Fe_{30}$ when conditioning between –0.35-1.6 V and 0.5-1.6 V at 10 mV s^{-1} for 46 cycles. Experiments were conducted in 1 M KOH at RT.

In Figure 5.32b, the activation during the FTacV experiments was compared to the activation obtained when performing the experiment without FTacV with 1 cm^2 electrodes according to the standard procedure (see chapter 4.3.2 *Investigation of Electrochemical Conditioning*). For $Ni_{70}Fe_{30}$, Figure 5.32b shows that the activation is not significantly influenced by the inclusion of FTacV into the electrochemical protocol when conditioning between –0.35-1.6 V, with an activation of 56 mV (FTacV) compared to 58±8 mV (dc). During conditioning between 0.5-1.6 V, the activation in FTacV experiments is 9 mV lower than the 22±2 mV observed without FTacV. For $Ni_{99.99}$, the activation is significantly decreased by FTacV when conditioning between –0.35-1.6 V. An activation of 8 mV (FTacV) compared to 58±10 mV (dc) can be seen. When conditioning between 0.5-1.6 V, even a deactivation of –33 mV is visible, while without FTacV an activation of 40±9 mV is observed. This deactivation is in line with the observed shift of the Ni(II)/Ni(III) redox and the OER peaks to higher potentials in the harmonics in Figure S10. This different behavior from $Ni_{99.99}$ and $Ni_{70}Fe_{30}$ could be because the formation of mixed Ni-Fe oxides is responsible for the electrode activation. While these mixed Ni-Fe oxides might be stable under FTacV for the Ni-Fe alloy, the Fe incorporated from the electrolyte in the Ni-oxide structure might be destabilized by FTacV. Further investigations are required to validate this, such as performing the electrochemical sequence with FTacV replaced with the respective dc equivalent and performing FTacV only after conditioning.

In summary, the performed FTacV suggests that conditioning of $Ni_{70}Fe_{30}$ and $Ni_{99.99}$ between 0.5-1.6 V for 46 cycles does not significantly alter the kinetics of the OER and the Ni(II)/Ni(III) redox process. Conditioning between –0.35-1.6 V for 46 cycles seems to decrease the Ni(II)/Ni(III) redox reaction rate and the OER reaction rate, probably due to the higher degree of surface oxidation. This decreased Ni(II)/Ni(III) and OER kinetics correlates with the activation only for $Ni_{70}Fe_{30}$. This might be because mixed Ni-Fe oxides are responsible for the activation, which are stable under FTacV conditions for the Ni-Fe alloy but not for Ni with Fe incorporated from the electrolyte. For $Ni_{70}Fe_{30}$, the overall observed activation is suggested to result from the high number of generated active sites. Furthermore, a third process, which

occurs at potentials between the OER and Ni(II)/Ni(III) redox reaction, could be deconvoluted. It is enhanced during conditioning with either sequence. However, since this third process behaves similarly when conditioning with and without the HER and, thus, does not correlate with an increased activation, it seems to be not significantly relevant for the activating effect.

FTIR spectroscopy

To study the evolution of the Ni (hydr)oxide phase owing to conditioning with and without the HER regime, $Ni_{99.99}$ and $Ni_{70}Fe_{30}$ were analyzed by FTIR after conditioning between 0.5-1.6 V and –0.35-1.6 V at 10 mV s^{-1}. This was done in collaboration with Julia Gallenberger (AG Hofmann) from TU Darmstadt. The respective spectra are displayed in Figure 5.33.

In Figure 5.33, the peaks at 850, 1550, 1610-1620, and 3400 cm^{-1} can be correlated to the existence of α-$Ni(OH)_2$. More specifically, these wavenumbers correspond to α-$Ni(OH)_2$, lattice O-H in α-$Ni(OH)_2$, and water and OH^- intercalated in amorphous α-$Ni(OH)_2$, respectively. The peaks at 3400 cm^{-1} (OH^- intercalated in α-$Ni(OH)_2$) and 1610-1620 cm^{-1} (water intercalated in α-$Ni(OH)_2$) in Figure 5.33 show clearly that α-$Ni(OH)_2$ is present for both materials independent from the potential window used during conditioning. The Ni(II)/Ni(III) redox peak behavior analyzed by the activity dcCVs in Figure 5.29 shows that the reduction peak at 1.34 V ($Ni_{99.99}$) and 1.35-1.36 V ($Ni_{70}Fe_{30}$) is also present independent from the potential window used during conditioning. Hence, this reduction peak could correspond to the α-$Ni(OH)_2$ formation. This supports the hypothesis that a hydrous oxide layer forms during conditioning, which might be responsible for the activation. β-$Ni(OH)_2$ can be identified in the FTIR spectrum by a sharp peak at 3644 cm^{-1}, as seen when conditioning $Ni_{99.99}$ and $Ni_{70}Fe_{30}$ including the HER regime (–0.35-1.6 V). When conditioning without the HER regime (0.5-1.6 V), no significant amount of β-$Ni(OH)_2$ was detected for $Ni_{99.99}$. For $Ni_{70}Fe_{30}$, a peak at 3644 cm^{-1} with little intensity compared to the conditioning between –0.35-1.6 V was obtained. When relating the detection of β-$Ni(OH)_2$ to the dc Ni(II)/Ni(III) peak behavior, it needs to be noted that the dcCVs of the FTIR samples differed slightly from the earlier presented CVs. The dcCVs of the FTIR samples, shown in Figure S14, indicate a second reduction peak at 1.29-1.34 V with little intensity also for the conditioning between 0.5-1.6 V. The reason behind this deviation is not fully understood yet. The differences in the CVs might be due to the slightly different measurement conditions, poorer polishing, and thus, starting potentially already with β-$Ni(OH)_2$ present, or due to influences of the Ag-containing conducting glue in the case of the FTIR measurements. Correlating the dcCVs of the FTIR samples and the FTIR results, the existence of β-$Ni(OH)_2$ could correspond to the second reduction peak at 1.29 V ($Ni_{99.99}$) and 1.29-1.34 V ($Ni_{70}Fe_{30}$). It is hypothesized that α-$Ni(OH)_2$, formed during conditioning, ages to β-$Ni(OH)_2$, which aligns with the Bode scheme.[54,65] This aging seems to primarily occur when including the HER regime during conditioning.

Concluding, FTIR validated that a hydrous oxide layer (α-$Ni(OH)_2$) is formed during conditioning independent of the applied potential window. Little β-$Ni(OH)_2$ is formed, potentially due to the aging of α-$Ni(OH)_2$. According to the dcCV peak analysis, conditioning including the HER generates a significantly higher β/α-$Ni(OH)_2$ ratio than without the HER.

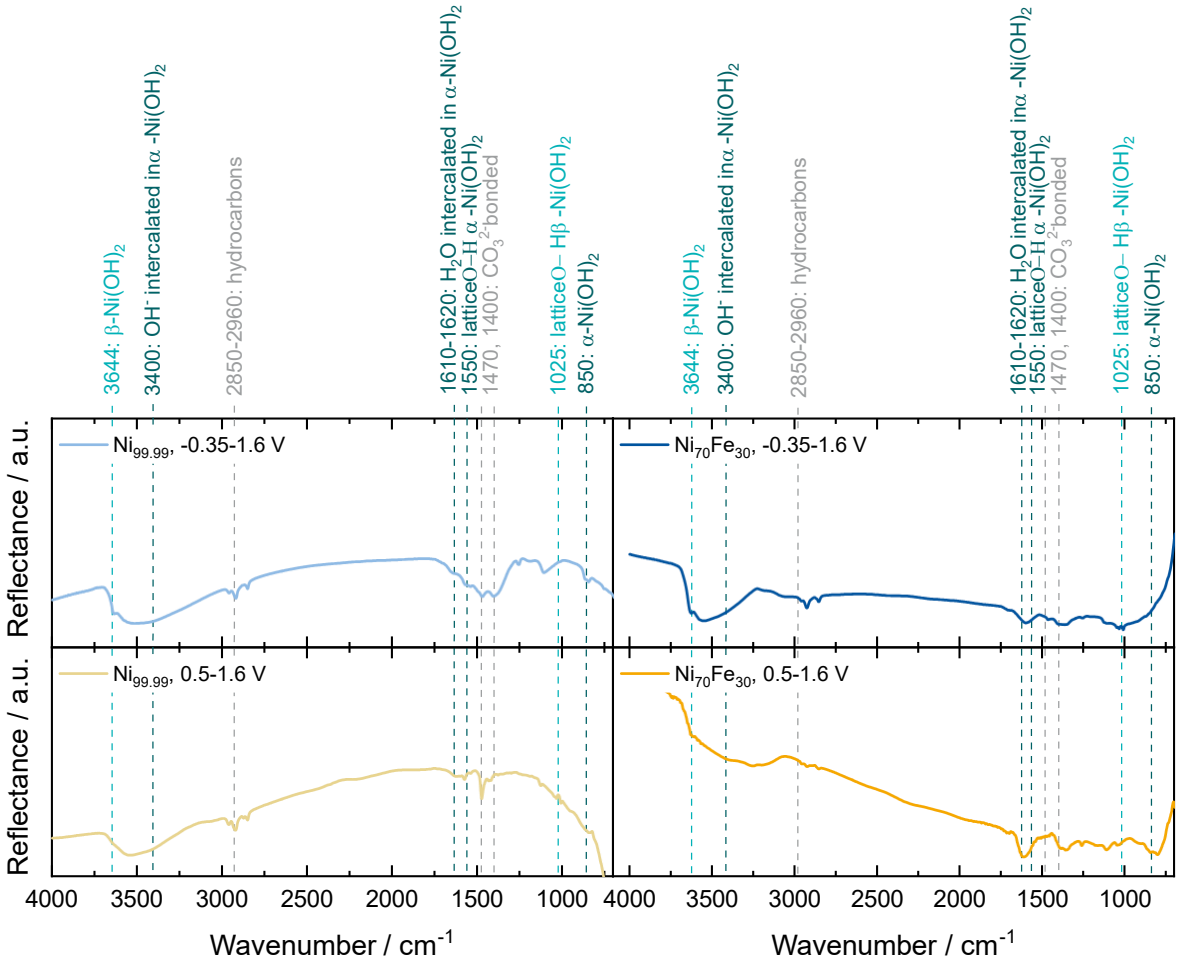

Figure 5.33. FTIR spectra for $Ni_{99.99}$ and $Ni_{70}Fe_{30}$ measured *ex-situ* after conditioning. Conditioning was conducted between –0.35-1.6 V and 0.5-1.6 V at 10 mV s^{-1} for 46 cycles. Experiments were performed in 1 M KOH at RT.

Optical microscopy, SEM, and EDX

To investigate the visual and compositional change of the electrodes, optical microscopy, SEM, and EDX were employed for $Ni_{99.99}$ and $Ni_{70}Fe_{30}$ before and after conditioning between –0.35-1.6 V and 0.5-1.6 V at 10 mV s^{-1}. The optical microscopy and SEM images reveal similar changes in the electrode surface for $Ni_{99.99}$ and $Ni_{70}Fe_{30}$. Hence, these will be jointly and exemplary discussed for $Ni_{99.99}$. The optical microscopy and SEM images for $Ni_{70}Fe_{30}$ can be found in Figure S15.

The SEM images (g-i) in Figure 5.34 reveal that by conditioning with either potential window, no structures grew microscopically (3,000x magnification). Visual optical microscopy (Figure 5.34a-c) shows that macroscopically, the color of the electrode changed when conditioning between –0.35-1.6 V but did not for 0.5-1.6 V. $Ni_{99.99}$ and $Ni_{70}Fe_{30}$ were colored golden-brown after conditioning. For $Ni_{70}Fe_{30}$, this coloration was persistent for multiple days. For $Ni_{99.99}$, a few additional dark grey marks could be observed. The coloration of $Ni_{99.99}$ disappeared more quickly than for $Ni_{70}Fe_{30}$, especially the dark grey marks. The origin of the golden-brown coloration is not fully clear, but it probably results from mixed Ni-Fe-oxides. Based on previous reports, the dark grey color from $Ni_{99.99}$ after conditioning could be assigned to NiOOH, which

decomposes quickly in air without polarization.[126,129] Figure 5.34 shows in d)-f) that a macroscopic structure change occurred when conditioning between –0.35-1.6 V but did not for 0.5-1.6 V. This structural change could possibly be due to intercalated electrolyte and introduced grain boundaries of different facets. A similar structure and color change was reported when conditioning $Ni_{99.99}$ and $Ni_{70}Fe_{30}$ between –0.35-1.6 V at 100 mV s^{-1} for 46 cycles in 1 M KOH at RT.[126]

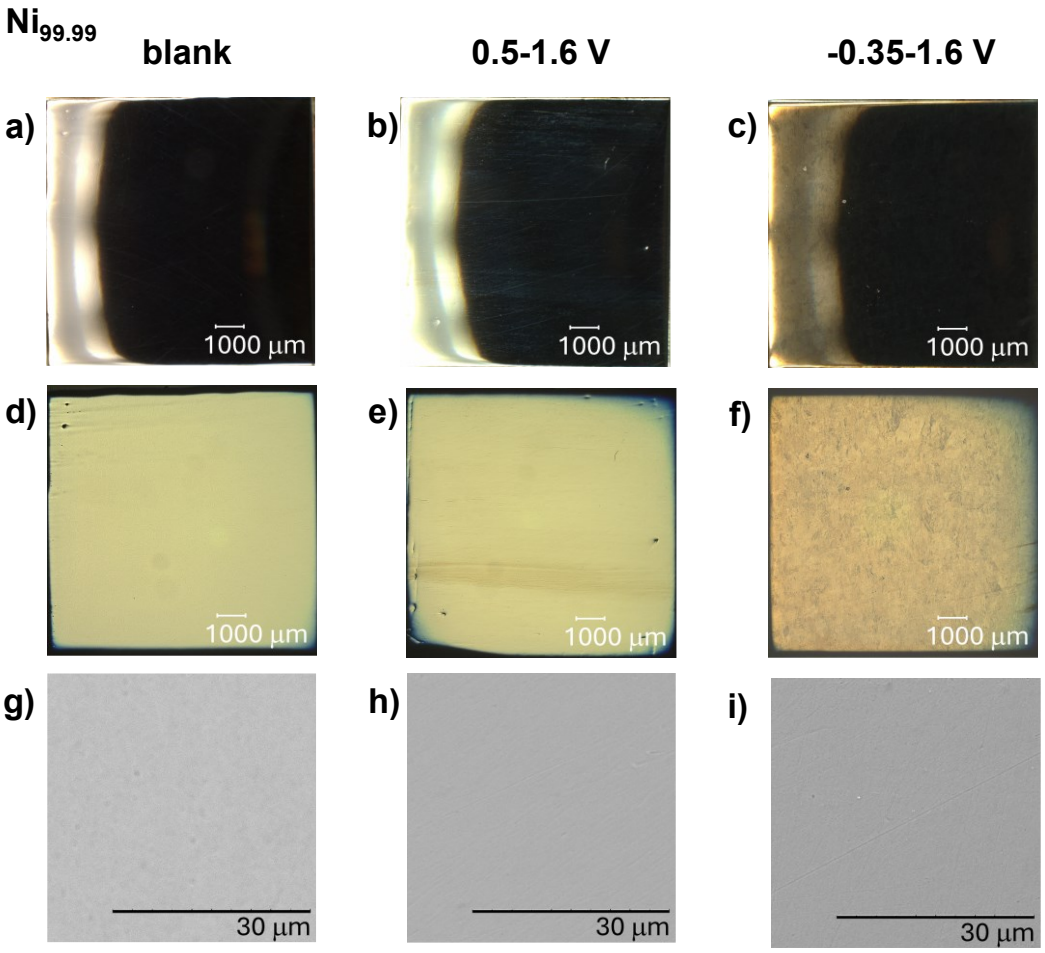

Figure 5.34. Optical microscopy images (a-f) at 20x magnification and SEM images (g-i) at 3,000x magnification showing the surface structure of $Ni_{99.99}$ as blank (a, d, g), after conditioning between 0.5-1.6 V at 10 mV s^{-1} for 46 cycles (b, e, h), and after conditioning between –0.35-1.6 V at 10 mV s^{-1} for 46 cycles (c, f, i). For the optical microscope images, two modes were used: full-ring illumination measured at an angle of 12° (mode 1: a-c) and coaxial illumination measured at a 0° angle (mode 2: d-f). Mode 1 shows the color of the electrode on the left side of the image. This color is only visible due to the light reflection caused by tilting the microscope. Illumination from the top only shows a black color, as seen for the rest of the electrode. Mode 2 indicates the structural change. The color change can, here, not be seen as clearly.

The Ni, Fe, and O contents of the electrodes before and after conditioning were determined by EDX and are illustrated in Figure 5.35. Detected C was not considered as it was likely caused by atmospheric contamination. The respective EDX spectra are shown in Figure S16 in the appendix.

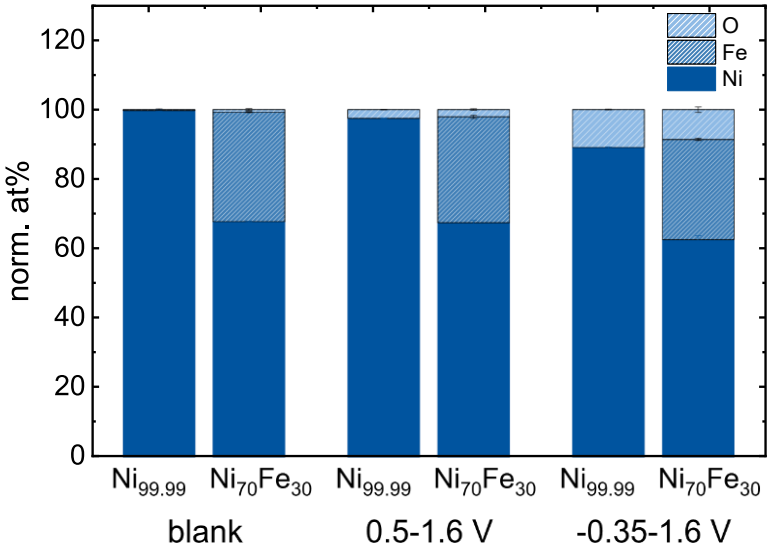

Figure 5.35. Average norm. at% of Ni, Fe, O detected by EDX for $Ni_{99.99}$ and $Ni_{70}Fe_{30}$ before (blank) and after conditioning. Conditioning was performed between 0.5-1.6 V and –0.35-1.6 V at 10 mV s^{-1} for 46 cycles in 1 M KOH at RT. The error bars represent the standard deviation from three measurements for one electrode. The corresponding EDX spectra can be seen in Figure S16.

Figure 5.35 shows that before conditioning, 0.3±0.2 norm. at% and 0.7±0.3 norm. at% O were detected for $Ni_{99.99}$ and $Ni_{70}Fe_{30}$, respectively. These small amounts of O could be surface oxidation due to exposure to air. The atomic Ni:Fe ratio for $Ni_{70}Fe_{30}$ was 2.1±0.1, which corresponds to the calculated Ni:Fe ratio of 2.2 from stoichiometry. After conditioning, the O-content increased for $Ni_{99.99}$ and $Ni_{70}Fe_{30}$ irrespective of the applied conditioning window, as seen in Figure 5.35. When conditioning between 0.5-1.6 V, the resulting O contents were much smaller ($Ni_{99.99}$: 2.5±0.1 norm. at%, $Ni_{70}Fe_{30}$: 2.1±0.3 norm. at%) compared to when including the HER regime in the conditioning ($Ni_{99.99}$: 10.9±0.2 norm. at%, $Ni_{70}Fe_{30}$: 8.6±0.8 norm. at%). Irrespective of the applied conditioning potential window, the Ni:Fe ratio remained stable for $Ni_{70}Fe_{30}$, and no Fe was incorporated for $Ni_{99.99}$. The increase in O content and the stable Ni:Fe ratio align with the composition changes observed by EDX when conditioning between –0.35-1.6 V at 100 mV s^{-1}.[126] It suggests that conditioning leads to the oxidation of both $Ni_{99.99}$ and $Ni_{70}Fe_{30}$ without significantly altering the Ni:Fe ratio. However, it is essential to note that EDX is primarily sensitive to the bulk composition, meaning that slight metal dissolution or Fe deposition on the surface might not be detected.

In conclusion, optical microscopy, SEM, and EDX showed that when conditioning with the HER, the structure and color of $Ni_{99.99}$ and $Ni_{70}Fe_{30}$ change macroscopically, and a more substantial surface oxidation occurs.

XPS

To investigate the effect of the lower potential regime during conditioning on the surface composition, XPS of $Ni_{99.99}$ and $Ni_{70}Fe_{30}$ after conditioning between 0.5-1.6 V and –0.35-1.6 V at 10 mV s^{-1} for 46 cycles was performed in collaboration with Julia Gallenberger (AG Hofmann) at TU Darmstadt. Figure 5.36 and Figure 5.37 present the Ni 2p, Ni 3p, Fe 3p, and O 1s spectra. The Fe 2p core level peak analysis was excluded due to interference with the dominant $L_3M_{23}M_{45}$ Auger line of Ni when using Al K_α X-ray radiation. The survey XPS spectra,

C 1s XPS spectra, and the activity dcCVs (1-1.6 V, 100 mV s^{-1}, before and after conditioning) of the electrodes can be seen in Figure S17 and Figure S18.

The Ni 2p spectra of $Ni_{99.99}$ and $Ni_{70}Fe_{30}$ in Figure 5.36a show signals from the Ni $2p_{1/2}$ above 870 eV and the Ni $2p_{3/2}$ below 870 eV. Both show the same trends, although the Ni $2p_{3/2}$ is more clearly resolved.[130] Thus, only the Ni $2p_{3/2}$ will be discussed in the following.

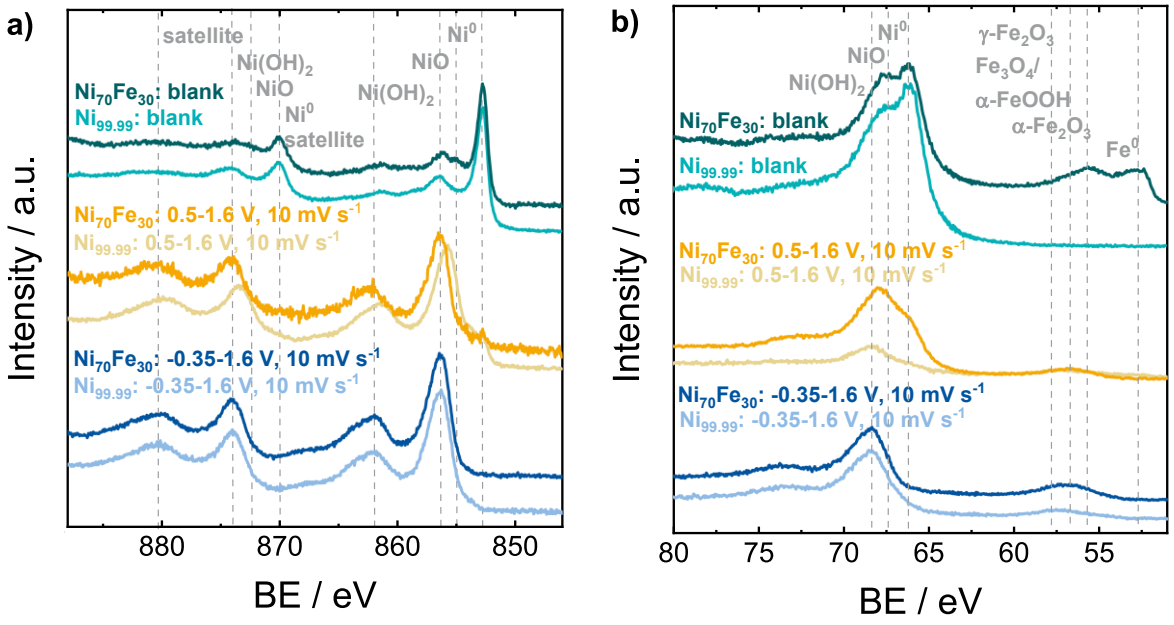

Figure 5.36. a) Ni 2p and b) Ni 3p, Fe 3p spectra for $Ni_{99.99}$ and $Ni_{70}Fe_{30}$, measured *ex-situ* before (blank) and after conditioning. Conditioning was performed between 0.5-1.6 V and –0.35-1.6 V at 10 mV s^{-1} for 46 cycles. Experiments were performed in 1 M KOH at RT.

In Figure 5.36a, the strong signal at a binding energy (BE) of 852.7 eV[130] corresponds to Ni^0 and proves the predominant metallic character of $Ni_{99.99}$ and $Ni_{70}Fe_{30}$ after polishing and before conditioning. The peaks at 856.3 eV[130] and 854.7 eV[130] indicate the presence of small amounts of $Ni(OH)_2$ and NiO, probably formed by exposure to air. When Fe acts as a ligand in NiO, the main Ni(Fe)O peak appears 1.6 eV above the pure NiO main peak.[131,132] Such a peak cannot be resolved in the present spectra as the peak is expected to be small and overlaying with the $Ni(OH)_2$ peak. It needs to be further noted that the $Ni(OH)_2$ signal is shifted to higher binding energies by 0.9 eV compared to reported values in the literature. The corresponding peaks in the C 1s and O 1s spectra (see Figure S17) are similarly shifted. Thus, this shift might correspond to the charging of the layers above the uncharged and unconverted Ni metal. After conditioning, Figure 5.36 shows a signal from metallic Ni^0 as a peak shoulder at 852.7 eV only when conditioning $Ni_{99.99}$ and $Ni_{70}Fe_{30}$ between 0.5-1.6 V.[130] For the conditioning with the HER regime, the metal surface is completely oxidized within the measurement depth of the XPS (~10 nm).[94] The stronger signal at a BE of 856.3 eV[130], indicating $Ni(OH)_2$, is visible irrespective of the applied conditioning. A contribution from NiO cannot be excluded, which would show a peak at 854.7 eV.[130] These Ni $2p_{3/2}$ spectra indicate that Ni is oxidized to $Ni(OH)_2$ for both electrode materials during conditioning, with stronger oxidation occurring when the HER regime is included. These results align with the above presented dcCV, FTacV, and EDX analyses.

Figure 5.36b depicts the Ni 3p and Fe 3p spectra of $Ni_{99.99}$ and $Ni_{70}Fe_{30}$ before and after conditioning with the two different potential windows. The Ni 3p spectra reflect the same

observations as the Ni 2p spectra. Before conditioning, a strong signal at a BE of 66.2 eV with a shoulder at 67.5-68.4 eV was detected for both electrodes. The peak at lower BEs is linked to Ni^0 and the peak at higher BEs to both its satellite peak and $NiO/Ni(OH)_2$.[130] After conditioning with either sequence, a strong and broad signal from $NiO/Ni(OH)_2$ can be seen for both materials. When conditioning between 0.5-1.6 V, both materials show a shoulder at 66.2 eV, which indicates the presence of metallic Ni^0, whose intensity is remarkably lower when conditioning between –0.35-1.6 V.[130] In the Fe 3p spectra, metallic Fe and a mixture of various Fe oxides, potentially α-Fe_2O_3, at a BE of 52.7 eV and 55.6 eV for $Ni_{70}Fe_{30}$ can be identified before conditioning.[130] For $Ni_{99.99}$, no Fe species were detected in the unconditioned state. After conditioning, metallic Fe^0 could no longer be detected for $Ni_{70}Fe_{30}$, and only a broad peak between 56.5-58 eV can be seen when conditioning $Ni_{70}Fe_{30}$ with either potential window. This broad peak corresponds to a mixture of various Fe-oxides, such as Fe_3O_4 (56.7 eV), α-FeOOH (57.0 eV), or γ-Fe_2O_3 (57.8 eV).[130] Conditioned $Ni_{99.99}$ shows the same broad peak at 56.7 eV with little intensity, verifying Fe incorporation from the electrolyte by conditioning. To quantify the Ni and Fe content, the areas of the Ni 3p and Fe 3p spectra were integrated. When conditioning with the HER regime, a more substantial Fe dissolution from the Ni-Fe electrode or rather incorporation from the electrolyte was detected, with Ni:Fe ratios of 7.3 for $Ni_{99.99}$ and 4 for $Ni_{70}Fe_{30}$ (–0.35-1.6 V) compared to 11.5 for $Ni_{99.99}$ and 3.3 for $Ni_{70}Fe_{30}$ (0.5-1.6 V).

The O 1s spectra, shown in Figure 5.37, allow the quantification of the oxide formation during conditioning. The present metal hydroxide (M-OH) and metal oxide (M-O) can be identified by the peaks at 531.9 eV ($Ni(OH)_2$) and 529.8 eV (NiO, FeO), respectively.[130]

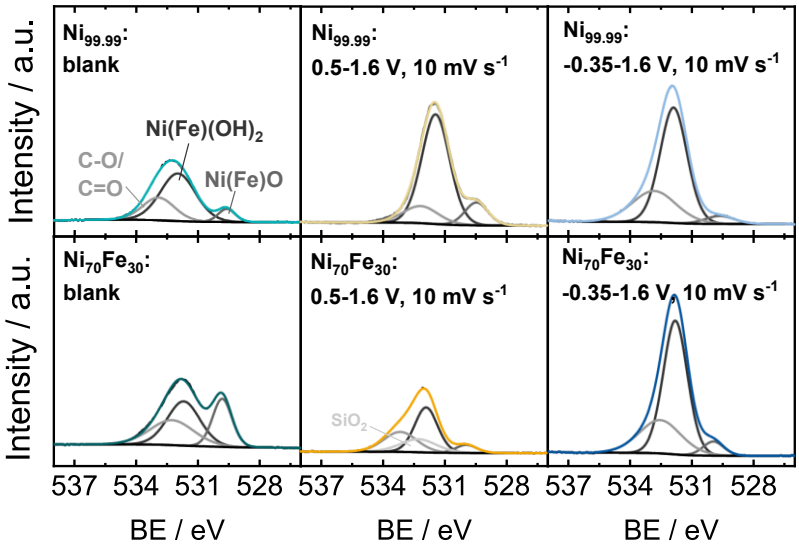

Figure 5.37. O 1s XPS spectra for $Ni_{99.99}$ and $Ni_{70}Fe_{30}$, measured *ex-situ* before (blank) and after conditioning. Conditioning was performed between 0.5-1.6 V and –0.35-1.6 V at 10 mV s^{-1} for 46 cycles in 1 M KOH at RT.

Conditioning with the HER regime resulted in a larger M-OH:M-O ratio of 13.5 ($Ni_{99.99}$) and 11.0 ($Ni_{70}Fe_{30}$) compared to 5.7 ($Ni_{99.99}$) and 6.1 ($Ni_{70}Fe_{30}$) for conditioning between 0.5-1.6 V. This supports the hypothesis that activation is driven by the formation of a hydroxide layer by simultaneously minimizing the oxide layer.

Summing up, XPS demonstrated that conditioning including the HER regime results in a higher degree of surface oxidation, a higher M-OH:M-O ratio, and a stronger Fe dissolution for $Ni_{70}Fe_{30}$ or incorporation for $Ni_{99.99}$.

ICP-OES

To study the Ni and Fe dissolution and incorporation behavior of $Ni_{70}Fe_{30}$ and $Ni_{99.99}$ during conditioning with and without HER, online ICP-OES of the electrolyte was performed. Additionally, K was measured as an internal standard. The K spectra were always constant if not stated otherwise. Sharp signal drops were observed and associated with gas evolution. The Ni spectra showed no dependency on the applied protocols, independent of the utilized electrode. The Ni concentration stayed mainly constant. The respective spectra for K and Ni are shown in Figure S19 and Figure S20 in the appendix.

First, the Fe concentration of the electrolyte was studied while performing CP at 10 mA cm^{-2} with $Ni_{70}Fe_{30}$ and $Ni_{99.99}$ anodes, which can be seen in Figure 5.38a. For $Ni_{70}Fe_{30}$, the effect of conditioning before the CP was additionally investigated and is shown in Figure 5.38b. Here, conditioning was performed between –0.35-1.6 V at 10 and 100 mV s^{-1} and between 0.5-1.6 V at 10 mV s^{-1}.

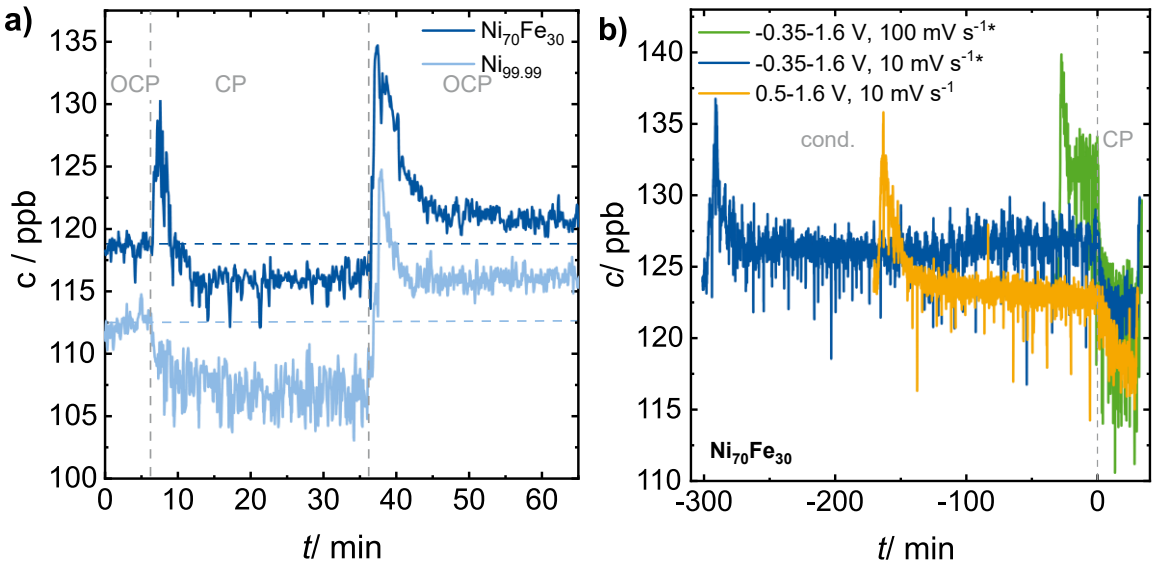

Figure 5.38. a) Fe concentration, measured by ICP-OES, during a 30 min CP at 10 mA cm^{-2}, followed by a 30 min OCP, on $Ni_{70}Fe_{30}$ and $Ni_{99.99}$. b) Fe concentration, measured by ICP-OES, during conditioning of $Ni_{70}Fe_{30}$ between –0.35-1.6 V at 10 and 100 mV s^{-1} and 0.5-1.6 V at 10 mV s^{-1}, followed by a CP at 10 mA cm^{-2} for 30 min. The asterisk (*) indicates that the starting concentrations were manually adjusted to be the same. $Ni_{70}Fe_{30}$ in a) is also displayed in Figure 5.15.

In Figure 5.38a, the Fe concentration during CP at 10 mA cm^{-2} followed by an OCP for $Ni_{70}Fe_{30}$ and $Ni_{99.99}$ is shown. For both anodes, the Fe concentration drops during the CP by approx. 5 ppb and peaks afterward when changing to OCP. In the case of $Ni_{99.99}$, this decreased Fe concentration could be due to an increased Fe uptake from the anode and/or cathode. For $Ni_{70}Fe_{30}$, the decreased Fe concentration could result from a lower Fe dissolution from the anode and an Fe uptake at the anode and/or cathode. Since the dissolution behavior during the CP is independent of the anode potential, it is likely due to the Fe uptake at the cathode, which is released when stopping the electrolysis. This aligns with previous studies, which

reported the Fe uptake at the cathode during constant current operation.[133,134] At OCP and after the Fe release, the Fe concentration remains constant. The slightly higher Fe concentration by 2-4 ppb during OCP compared to the baseline is within the range of measurement error and, thus, difficult to interpret. It could be that the remaining concentration drop to the baseline is a slow process, and 30 min at OCP is too short to observe it. When using $Ni_{70}Fe_{30}$ as the anode (dark blue), the Fe concentration additionally peaks when the current is applied initially. Since this is not visible for the $Ni_{99.99}$ electrode, this rise in Fe concentration is associated with Fe dissolution from the anode.

Figure 5.38b shows the Fe concentration during conditioning of $Ni_{70}Fe_{30}$ with different sequences (–0.35-1.6 V at 10 and 100 mV s^{-1}; 0.5-1.6 V at 10 mV s^{-1}) for $t < 0$ min followed by a CP at 10 mA cm^{-2} for 30 min. In Figure 5.38b, the drop in Fe concentration during the CP remains unchanged independent of the prior applied conditioning. This supports the hypothesis that this concentration drop originates from the Fe uptake at the cathode. It further indicates that changes in the Fe dissolution/incorporation behavior at the anode during CP cannot be resolved with an undivided EFC. Figure 5.38b also suggests an increased Fe dissolution from the anode when conditioning with the HER regime (blue and green) at a high scan rate (green). This different Fe dissolution behavior during CV cycling proposes that the Fe uptake at the cathode is not as pronounced during CV and changes in the Fe concentration are rather due to electrode processes at the anode than the cathode.

In order to investigate this further, the Fe concentration of the electrolyte was determined *ex-situ* by ICP-OES before and after the electrochemical conditioning of $Ni_{70}Fe_{30}$ and $Ni_{99.99}$ between –0.35-1.6 V at 100 mV s^{-1}. The electrolyte was circulated from a 150 mL reservoir with 3 mL min^{-1}. No change in Fe concentration could be detected with 118 ppb before and 117 ppb after conditioning. Thus, the Fe dissolution and incorporation during conditioning, discussed in Figure 5.38 and Figure 5.39 seems to be only visible during online investigation when the concentration changes are not diluted in the bulk reservoir. The concentration change in the entire reservoir is too small to be detected at these conditioning parameters.

For a more detailed comparison of the conditioning with and without the HER regime, three analysis CVs at 2 mV s^{-1} were performed with the respective potential window. At such a low scan rate, the Fe concentration can be correlated to the applied potentials. Subsequently, the scan rate was increased to 100 mV s^{-1} for 30 min to induce significant surface changes. After this period, another analysis CV was carried out at the initial rate of 2 mV s^{-1} to see whether these surface changes altered the Fe concentration behavior. Figure 5.39 shows the entire sequences for cycling $Ni_{99.99}$ and $Ni_{70}Fe_{30}$ between a) 0.5-1.6 V and b) –0.35-1.6 V. In all spectra, sharp concentration drops or increases can be seen, which are associated with gas evolution during the HER and OER. It is important to note that these spikes serve as a reliable marker of the current position within the CV.

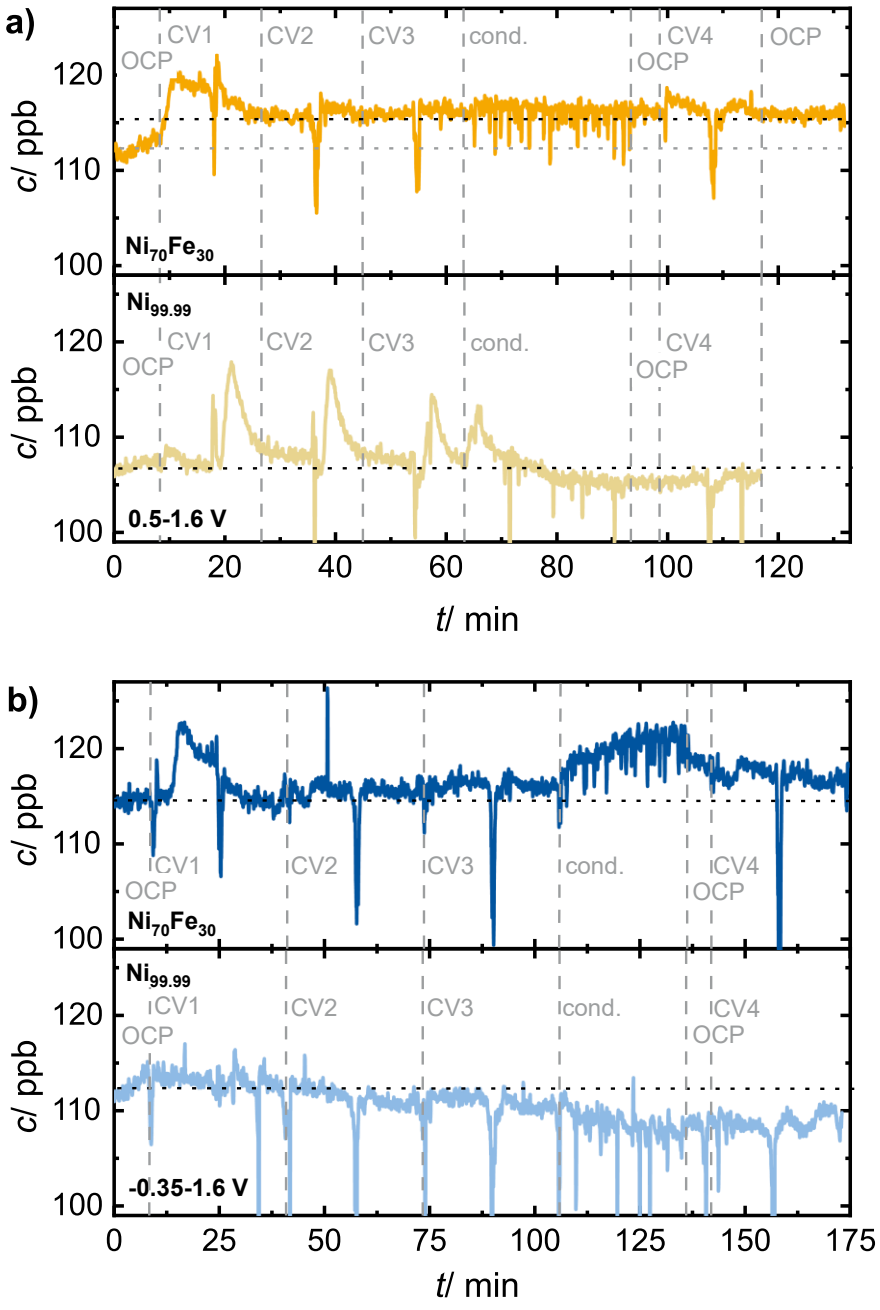

Figure 5.39. Fe concentration, analyzed by ICP-OES, while conditioning $Ni_{70}Fe_{30}$ and $Ni_{99.99}$ by first three analysis CVs at 2 mV s^{-1}, a 30 min conditioning at 100 mV s^{-1}, and again an analysis CV at 2 mV s^{-1}. CV was performed between –0.35-1.6 V and 0.5-1.6 V. All experiments were performed in 1 M KOH at RT. The plots for the $Ni_{70}Fe_{30}$ anode are also displayed in Figure S7.

For $Ni_{99.99}$, Figure 5.39 indicates that the course of Fe concentration differs depending on which potential window is applied during conditioning. For the conditioning between 0.5-1.6 V (Figure 5.39a), the Fe concentration stays constant on the oxidative sweep of the first analysis CV (CV1). In the middle of the CV in the OER region, the Fe concentration shows a sharp increase due to gas evolution. On the reductive sweep, the Fe concentration increases, peaks, and decreases afterward. All of the first three analysis CVs show a similar behavior of the Fe concentration. The Fe dissolution peak on the reductive sweep decreases with each cycle. During the conditioning at 100 mV s^{-1}, Fe is initially dissolved. The dissolution rate, however,

decreases and, after approx. 15 min, reverses so as to Fe is taken up. After conditioning, the Fe dissolution on the reductive sweep can no longer be observed in the analysis CV at 2 mV s^{-1} (CV4, Figure 5.39a). The reason for this behavior of the Fe concentration is not yet fully understood. This Fe dissolution behavior could theoretically originate from the anode or the cathode. Glassy carbon was used as a cathode and is assumed to not change its surface chemistry significantly due to electrochemical conditioning. Hence, since the Fe dissolution behavior differs from before to after conditioning, this change is suggested to be due to a modified anode surface. This further supports that the observed behavior of the Fe concentration during CV is primarily due to the interaction of the Fe in the electrolyte with the anode. This proposes that the metal deposition at the cathode is too slow for the timescale of the CV. Based on this, one possible explanation is that Fe is incorporated at the $Ni_{99.99}$ anode from the electrolyte during the OER while only stable in a particular surface environment. When NiOOH is reduced on the reductive sweep during CV between 0.5-1.6 V, Fe seems to be destabilized on the surface. This aligns with previous reports, which state that $Ni(OH)_2$/NiOOH acts as a host for Fe incorporation[10,135] and that Fe incorporation is superior at OER potential compared to lower potentials.[62] Further, Mattinen *et al*. stated that more Fe is incorporated for larger $Ni(OH)_2$ layers, which similarly suggests that the amount of present $Ni(OH)_2$ defines how much Fe is incorporated. However, it should be noted that integration of the analysis CVs to the baseline indicates purely Fe dissolution from the electrodes, which decreases with the number of performed CVs. Thus, the proposed Fe uptake during the OER does not match the quantity of recorded Fe dissolution on the reductive sweep after the OER. This could result from the Fe incorporation being too slow to affect the bulk Fe concentration, whereas Fe dissolution is comparable fast. An alternative explanation could be that small amounts of NiO_xH_y are formed by exposing the Ni electrode to air and the alkaline electrolyte, and Fe is directly incorporated into these structures before the online ICP-OES measurement is started. The observed Fe dissolution during the reductive sweep after the OER might occur since the OER introduces stress and movement in the oxide layer for rearrangement. This would, however, contradict the previous reports, which stated that Fe incorporation is significantly enhanced during electrochemical operation and even more so by CV.[19,61,63] Considering this context, it appears doubtful that a significant amount of Fe would be incorporated in a short period (<30 min) without applied potential but would then dissolve rather than be incorporated during the electrochemical CV conditioning process. Another possible explanation for the mismatch between Fe incorporation and dissolution during the activity CV could be an artifact from the online ICP-OES measurement methodology. For example, peak smearing and falsified signal enhancement or reduction might result from the gas evolution during the OER and the associated turbulent flow in this potential regime. Further, the switching between air and electrolyte could influence the plasma properties, affecting the sample excitation.

When cycling between –0.35-1.6 V (Figure 5.39b), the initial Fe concentration decreases constantly throughout the entire sequence. Since a similar trend is observed for the Ni concentration (see Figure S19), a baseline shift, probably due to a decreased plasma temperature, is suggested to be the cause for this concentration decrease. Hence, comparing the four different analysis CVs in Figure 5.39a, no significant Fe dissolution or incorporation depending on the applied potential is visible before, during, or after the cycling at 100 mV s^{-1}. This might be because a) no Fe is incorporated or dissolved or b) Fe incorporation is a very slow process, which is difficult to detect by ICP-OES. Under the assumption that Fe is incorporated into the $Ni_{99.99}$ anode during the oxidative sweep when conditioning between 0.5-

1.6 V, which is then released on the reductive sweep, it seems unlikely that when enlarging the potential, no Fe would be incorporated anymore. Thus, it is rather suggested that Fe incorporation is a slow process, which cannot be properly detected by ICP-OES under these conditions. As no Fe dissolution is observed on the reductive sweep, the lower potentials during conditioning might stabilize the Fe incorporation. To conclude, with increasing conditioning time, independent of the potential window, a distinct phase seems to be formed, stabilizing the Fe incorporation. According to the conducted XPS and FTIR analyses, this phase could be α-$Ni(OH)_2$.

For $Ni_{70}Fe_{30}$, a deviation from the baseline toward higher Fe concentrations can be seen for both conditioning sequences, indicating Fe dissolution from the electrode. Please note that the difference between baseline and the overall Fe concentration level during CV cycling between 0.5-1.6 V (Figure 5.39a) is suggested to be artificial as indicated by the comparison of the OCP before and after the electrochemical procedure (also compare Figure 5.39a with Figure S21). Based on this, the ICP-OES spectra of Fe show a significant Fe dissolution for the first analysis CV (CV1) for both conditioning sequences (Figure 5.39a, b). When conditioning between –0.35-1.6 V, Fe dissolution can also be observed when cycling at 100 mV s^{-1}, suggesting a dependency of the Fe dissolution on the scan rate when including the HER regime in the conditioning. The Fe dissolution behavior when conditioning $Ni_{70}Fe_{30}$ with or without the HER regime was already discussed in chapter 5.2.2 (subchapter: *Variation of Fe Content in the Electrode*). There, in Figure 5.25, the first analysis CV can be seen in more detail. Figure 5.25 shows that Fe dissolution occurs during the oxidative potential sweep between 0.3-1.2 V. As the conditioning between 0.5-1.6 V covers only a part of this potential window, the Fe dissolution appears to be smaller here compared to the conditioning between –0.35-1.6 V. This increased Fe dissolution for the conditioning between –0.35-1.6 V becomes more evident when comparing the course of the Fe concentration during the CV conditioning at 100 mV s^{-1} for 30 min between the 63th to 93th minute in Figure 5.39. While the Fe concentration stays constant at 116 ppb when conditioning between 0.5-1.6 V, the Fe concentration increases to approx. 121 ppb when cycling between –0.35-1.6 V. This supports the hypothesis that conditioning with the HER regime enhances Fe dissolution for Ni-Fe electrodes, as was also observable in the XPS analysis. The increased Fe dissolution might result in a larger surface area and a subtle Ni:Fe ratio improvement. The different behavior of the Fe concentration when conditioning $Ni_{99.99}$ or $Ni_{70}Fe_{30}$ supports the hypothesis that the course of Fe concentration during CV reflects the interaction of the Fe in the electrolyte with the anode rather than the cathode.

Summarizing, $Ni_{70}Fe_{30}$ seems to leach more Fe if conditioned between –0.35-1.6 V at intermediate scan rates of 100 mV s^{-1} compared to conditioning between 0.5-1.6 V at any scan rate. However, the observed scan rate dependency was minor and needs to be considered carefully. *Ex-situ* ICP-OES before and after the conditioning suggested that the Fe dissolution at the electrodes is only observable by online ICP-OES as no dilution by the bulk reservoir occurs. When conditioning the iron-free $Ni_{99.99}$ electrode, Fe is suggested to be incorporated from the electrolyte. This incorporation could not be properly detected by ICP-OES but it seems to occur during the OER. Incorporated Fe might be stabilized in the Ni (hydr)oxide when cycling to lower potentials between –0.35-0.5 V during the conditioning procedure and when cycling for an extended period with either potential window. This stabilization possibly occurs due to the formation of $Ni(OH)_2$ during conditioning. Without this stabilization, Fe is directly re-dissolved after OER on the reductive sweep. During constant current operation, the Fe

dissolution/incorporation behavior at the anode cannot be resolved with an undivided EFC as the Fe ions are suggested to migrate to the cathode, concealing other effects. After CP, this deposited Fe at the cathode is released at OCP. During CV, the influence from CE processes could not be seen, suggesting that the metal deposition at the cathode is too slow to be detected on the timescale of the CV.

Conclusion

In this chapter, the induced surface changes by conditioning were characterized analytically by dcCV, FTacV, optical microscopy, SEM, EDX, XPS, FTIR spectroscopy, and ICP-OES. In chapter 5.2.1, it was demonstrated that the observed activation trends strongly correlate with the amount of formed $Ni(OH)_2$. This supports the hypothesis that the activation trends result from a tailored growth of a (hydr)oxide layer.

When comparing the conditioning of $Ni_{99.99}$ and $Ni_{70}Fe_{30}$ between –0.35-1.6 V (with HER) and 0.5-1.6 V (without HER) at 10 mV s^{-1}, conditioning with the HER regime resulted in a more extensive electrochemical activation. Conditioning with the HER regime was, furthermore, associated with a macroscopic structure and color change (optical microscopy, SEM), a more substantial surface oxidation (EDX, XPS), a more significant Fe dissolution for $Ni_{70}Fe_{30}$ or rather Fe incorporation from the electrolyte for $Ni_{99.99}$ (XPS, ICP-OES), and a larger M(OH):M(O) (XPS) and β/α-$Ni(OH)_2$ ratio (FTIR). FTacV suggested that the conditioning including the HER regime decreases the apparent OER reaction rate due to the strong surface oxidation. The overall activation is then proposed to occur from an overcompensation by the large number of active sites created by conditioning. Regarding Fe incorporation into the Ni (hydr)oxide layers, ICP-OES revealed that Fe might be incorporated during the OER and stabilized by cycling to lower potentials (–0.35-0.5 V) and by cycling with either potential window for an extended period. Stabilization might occur due to the formation of $Ni(OH)_2$ during conditioning. Overall, the analytical characterization of the surface changes of $Ni_{99.99}$ and $Ni_{70}Fe_{30}$ suggests that the activation trends are dominated by forming a hydroxide layer with partly anhydrous and hydrous character. This hydroxide formation is accompanied by Fe dissolution and incorporation and a decrease in the apparent OER reaction rate, which is compensated by the large number of generated active sites.

5.3. Electrochemical Conditioning at Industrially More Relevant Conditions

In order to exploit the full potential of electrochemical conditioning as an electrode manufacturing technique, its *in-situ* application in the electrolyzer under industrial conditions needs to be addressed. By incorporating electrochemical conditioning into the ramp-up procedure of the electrolyzer, electrode manufacturing can be significantly simplified and applied more easily for electrode reactivation. This can potentially save electrode manufacturing and electricity costs and resources. Hence, as a first step, the electrochemical conditioning was herein tested under industrially more relevant conditions. To implement these conditions, a new EFC setup was developed, which is based on the flex-E-cell and described in detail in chapter 4.2.2. Several factors change when transitioning from the previously used iEFC at lab conditions to the flex-E-cell at industrially more relevant conditions. These changes involve scaling up from 1 cm^2 to a 12 cm^2 electrode, employing separated anode and cathode

half-cells, operating in 30 wt% KOH at 80 °C, utilizing higher current densities during the activity determination, and using mesh electrodes. In the following, these changes are systematically investigated. In all cases, conditioning was performed using the optimized protocol, applying potentials between –0.35-1.6 V at 100 mV s^{-1} for 30 min.

First, the conditioning of a 12 cm^2 $Ni_{70}Fe_{30}$ plate electrode in the flex-E-cell, with and without a separator, is compared to the conditioning of a 1 cm^2 $Ni_{70}Fe_{30}$ plate electrode in the iEFC, as seen in Figure 5.40. The activation at 10 mA cm^{-2} is comparable for the 1 cm^2 (iEFC) and 12 cm^2 (flex-E-cell) electrode within the error range with 47±7 mV (1 cm^2, iEFC) and 46±3 mV (12 cm^2, flex-E-cell). This proves the scalability of the electrode activation by electrochemical conditioning and indicates a similar activation, *i.e.* surface oxidation, per cm^2, corresponding to a similar homogenous current and potential distribution across the electrode. Interestingly, the activation achieved by conditioning does not seem to be influenced by the various other changes introduced with the new setup. These changes include *e.g.* a different electrode contacting method, a longer RE capillary, altered flow conditions such as larger dead zones, higher flow rates, greater flow pulsation, and more difficult electrode polishing due to the increased electrode size. The insensitivity of the electrode activation to those changes suggests that the electrode contacting in the flex-E-cell seems to sufficiently supply the current without taking part in the reaction, and the potential is precisely controlled over the entire electrode by the RE. Further, the insensitivity of the electrode activation to the altered flow conditions is in line with the tested flow rate variation in the iEFC discussed in chapter 5.1.5. Figure 5.40 also demonstrates the influence of separating the anode and cathode half-cells by a separator on the activation. The activation for the divided flex-E-cell with 44±2 mV is comparable to the undivided one with 46±3 mV. This first test indicates that the separator can withstand CV cycling and ensure a fast current supply. It further suggests that activation is not significantly influenced by processes and cross-contamination from the cathode.

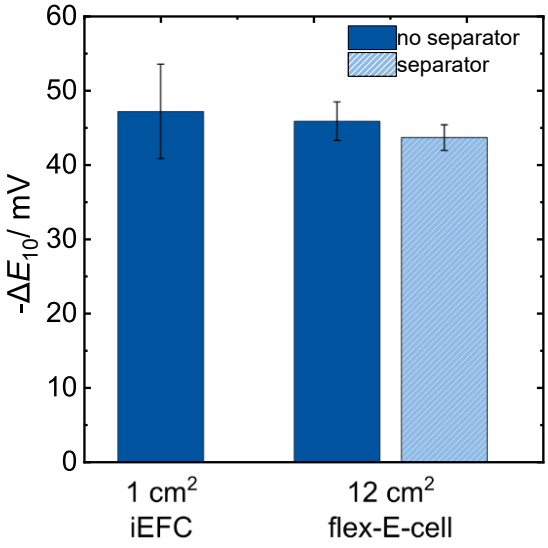

Figure 5.40. Activation of $Ni_{70}Fe_{30}$ by conditioning between –0.35-1.6 V at 100 mV s^{-1} for 30 min (46 cycles) in the undivided iEFC (1 cm^2) and the flex-E-cell (Design PLATE, 12 cm^2) with and without separator. Experiments were conducted in 1 M KOH at RT. Flow rates of 3 mL min^{-1} (iEFC) and 80 mL min^{-1} (flex-E-cell, per half-cell) were applied. The potentials recorded in the flex-E-cell are not iR_u corrected.

Industrial AWE is performed at current densities up to 1 A cm^{-2} in highly concentrated electrolyte with 30 wt% KOH, and at elevated temperatures of 80 °C. Thus, as a second step toward industrially more relevant conditions, the influence of conditioning on the activity determination at elevated current densities of 100 and 500 mA cm^{-2} is analyzed for a $Ni_{70}Fe_{30}$ plate electrode, as shown in Figure 5.41. Additionally, this figure compares the activation from conditioning in 1 M KOH at RT with that obtained in 30 wt% KOH at 80 °C.

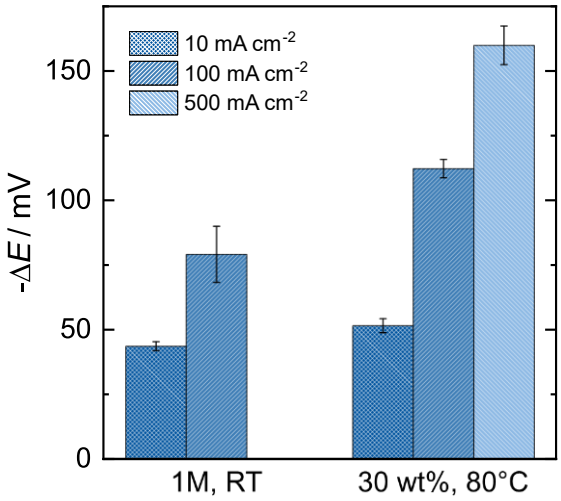

Figure 5.41. Activation (–Δ*E* at 10, 100, and 500 mA cm^{-2}) of $Ni_{70}Fe_{30}$ by conditioning between –0.35-1.6 V at 100 mV s^{-1} for 30 min (46 cycles) in the flex-E-cell (divided Design PLATE with separator, 12 cm^2) in 1 M KOH at RT and 30 wt% KOH at 80 °C. A flow rate of 80 mL min^{-1} per half-cell (*i.e.* 160 mL min^{-1} total) was applied. The potentials are not iR_u corrected.

Figure 5.41 shows an activation of 44±2 mV at 10 mA cm^{-2} and 79±11 mV at 100 mA cm^{-2} when conditioning in 1 M KOH at RT. In 30 wt% KOH at 80 °C, an activation of 52±3 mV at 10 mA cm^{-2}, 112±4 mV at 100 mA cm^{-2}, and 159±8 mV at 500 mA cm^{-2} was observed. Hence, for both conditions, 1 M KOH at RT and 30 wt% KOH at 80 °C, Figure 5.41 shows that the activation is larger under high loads. This could hint at an improved intrinsic activity due to conditioning. However, an increased intrinsic would contradict the characterization by FTacV and previous works, which stated that the Tafel slope of the OER stayed constant or even worsened when conditioning Ni electrodes.[29,63,77] An alternative explanation could be that the OER follows a different reaction mechanism at higher current densities and that the *E-I*-regimes for these different mechanisms do not match before and after conditioning. To fully understand the changing OER kinetics during conditioning, an in-depth analysis of the Tafel slope, the electrochemically active surface area, and EIS would be required. However, for industrial applications, the key requirement is that activation at higher current densities matches or exceeds that at low current densities. This has been successfully demonstrated. Figure 5.41 further demonstrates that the application of industrial KOH concentration and temperature resulted in a slightly higher activation compared to 1 M KOH and RT. This might be because the higher KOH concentration and temperature favor thermodynamics and enhance the kinetics of the OER and surface oxidation, potentially also metal dissolution. Thus, the oxide layer might grow faster at these conditions, which aligns with previous works.[12,28,58,60] Previous works on oxide films on Fe, however, also mentioned that the oxide growth is faster inhibited in highly concentrated hydroxide solutions with respect to the number of performed

CV cycles.[12,28,60] This was possibly not observed here as too few cycles were conducted. While interpreting Figure 5.41, it needs to be noted that the electrode surface area was increased at industrial KOH concentration and temperature due to reduced sealing efficiency. This probably distorted the activation and conditioning parameters slightly since the applied current densities during conditioning and activity determination were lower than at lab conditions. For future investigations on how the temperature and KOH concentration affect the activation, further cell optimization is required.

The final step in transitioning from the iEFC at laboratory conditions to the flex-E-cell under industrially relevant conditions involves evaluating the effect of electrode geometry on electrode activation, as shown in Figure 5.42. This is done by comparing the conditioning of a Ni mesh electrode to that of a $Ni_{99.99}$ plate electrode. The 1 cm^2 $Ni_{99.99}$ plate electrode was measured in the undivided iEFC at lab conditions (1 M KOH, RT), and the 12 cm^2 Ni mesh in the divided flex-E-cell at lab (1 M KOH, RT) and industrially more relevant (30 wt% KOH, 80 °C) conditions. In Figure 5.42, it can be seen that the activation of the Ni mesh at lab conditions is much smaller with 6±1 mV compared to the activation of the $Ni_{99.99}$ plate with 35±7 mV. This might be due to pre-existing oxides on the Ni mesh from exposure to air since no polishing can be performed before the experiment. Also, the Ni current collector, which was exposed to the electrolyte, may have distorted the results and the conditioning since the potential distribution is unknown. Further, it is important to consider that the activation was defined at a current density calculated for the projected surface area, which is 0.625 times that of the geometric surface as estimated from the mesh geometry. Since Figure 5.41 indicates that the activation depends on the current density at which it is compared, the lower activation of the meshes could be due to an overestimation of the current density. Also, it needs to be noted that the Ni-mesh probably has a lower purity than $Ni_{99.99}$. This should, however, only have a minor impact as the activation of $Ni_{99.99}$ and $Ni_{99.2}$ was similar in a previous comparison (see chapter 5.2.2). Comparing the activation of the Ni mesh at lab (1 M KOH, RT) and industrially more relevant (30 wt% KOH, 80 °C) conditions in Figure 5.42, the activation from conditioning at industrially more relevant conditions is superior to that at lab conditions. This trend aligns with the observations for the conditioning of the $Ni_{70}Fe_{30}$ plate electrode at these conditions in Figure 5.41, supporting the hypothesis that stronger surface oxidation and restructuring occurs in 30 wt% KOH at 80 °C with this conditioning sequence.

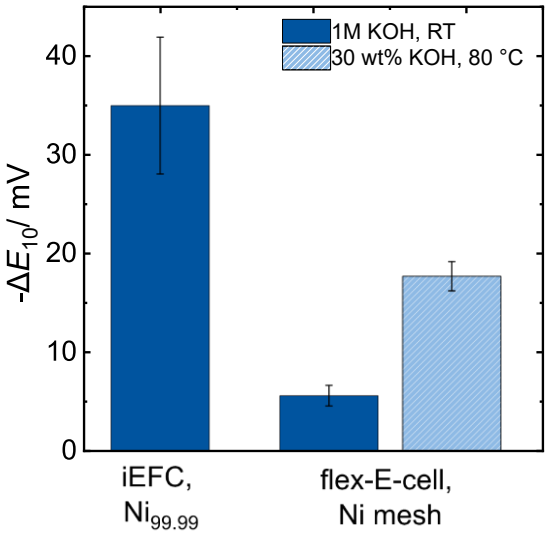

Figure 5.42. Activation of a 1 cm^2 $Ni_{99.99}$ plate and a 12 cm^2 Ni mesh by conditioning between –0.35-1.6 V at 100 mV s^{-1} for 30 min (46 cycles). The 1 cm^2 $Ni_{99.99}$ plate electrode was measured in 1 M KOH at RT at 3 mL min^{-1} in the undivided iEFC. The 12 cm^2 Ni mesh electrode was measured in 1 M KOH at RT and in 30 wt% KOH at 80 °C at 80 mL min^{-1} per half-cell (*i.e.* 160 mL min^{-1} in total) in the divided flex-E-cell (Design MESH, divided). The potentials of the flex-E-cell are not iR_u corrected.

Summarizing, the scalability of electrochemical conditioning was successfully demonstrated as the activation remained unaffected by scaling the electrode from 1 to 12 cm^2. Introducing a separator showed that the separator could endure CV cycling and that activation is not significantly influenced by processes at the CE. Applying higher current densities during the activity measurements resulted in a significantly greater activation. The origin of this effect has yet to be determined, especially since others suggested a constant or worsening of the Tafel slope due to the conditioning of Ni in 1 M KOH at RT.[29,63,77] Activation from conditioning in 30 wt% KOH at 80 °C was superior to that in 1 M KOH at RT, potentially due to increased surface oxidation. However, previous reports stated that increased KOH concentration and temperature can be disadvantageous in creating larger oxide layers.[12,28,60] This might be observed when conditioning for longer. Lastly, the conditioning of the Ni mesh yielded significantly lower activations compared to activating a $Ni_{99.99}$ plate electrode. This most likely occurred due to the higher degree of surface oxidation before the experiment, an influence by the backplate during the conditioning, and an overestimation of the current density in activity determination.

6. Conclusion

To increase cost and resource efficiency for large-scale green hydrogen production by AWE, the development of cost-effective, active, and stable electrodes for the alkaline OER is of utmost importance. This work addressed this challenge in three steps. First, an EFC was designed for the simultaneous activity measurement of electrocatalysts and downstream analysis of the electrolyte, which was herein termed iEFC (= electrochemical flow cell suitable for *in-situ* downstream electrolyte monitoring). In comparison to the previously reported iEFCs, the herein-designed one enables the characterization of new electrocatalysts' activity and stability under industrially more relevant conditions, *i.e*. 1 cm^2 parallel and planar electrodes. Second, the electrochemical conditioning of Ni-(Fe)-based electrodes was examined in this iEFC as a tool to (re)activate electrocatalysts for the alkaline OER. Electrochemical conditioning was identified as a promising technique to not only lower the required cell potential for the AWE but also make the anode manufacturing process significantly simpler and more versatile, saving resources, electricity, and production costs. Thus, electrochemical conditioning was herein systematically investigated by correlating electrode activation, surface changes, and electrochemical conditioning parameters. Finally, to get one step closer to industrial application, the electrochemical conditioning was scaled up and tested under industrially more relevant conditions, *i.e*. application of a separator, an electrode area of 12 cm^2, 30 wt% KOH, and 80 °C.

For the design of the iEFC, a precise activity determination over a wide potential range and minimal dilution of reaction products with a restricted volume flow needed to be ensured. This was realized by minimizing the reaction volume over the WE and the inhomogeneities of mass transport of the reactive species to the WE **(research question 1.1)**. Thus, when working with this iEFC, the influence of mass transport on the activity determination can be neglected and the kinetic current can be determined with >95% accuracy (=KL slope) in the mixed-kinetic-mass-transport-limited regime with the KL relation **(research question 1.2)**. This was validated by simulations and experimental KL analysis. The key design features of the iEFC include parallel 1 cm^2 electrodes, a parallel and uniform flow velocity distribution over the WE, an electrode spacing of 1-3 mm, and a tilted angle of 60-120° between the inlet and outlet channels. When investigating AWE electrocatalysts at industrial electrolyte concentration and temperature, the iEFC needed to be adjusted for efficient gas removal and material stability **(research question 1.4)**. During the design of this iEFC, valuable insights could be gained, which are of great importance for the future design of such specialized EFCs. First, precise and fast potential control in an EFC with narrow and winded channels can be ensured when the projection of the RE's capillary onto the WE intersects with a region of parallel and equidistant current and potential lines between CE and WE. Additionally, WE and CE are to be in direct sight of one another **(research question 1.3)**. Second, the surface area of the WE and CE can be accurately defined by embedding **(research question 1.3)**.

With this iEFC, the electrochemical conditioning of Ni-(Fe)-based electrodes to enhance the alkaline OER was investigated. Indeed, conditioning showed an outstanding and long-lasting impact on their electrochemical activity. To gain a deeper understanding of the occurring activation, the correlations between electrochemical conditioning parameters, surface changes, and activation were systematically investigated for Ni- and Ni-Fe-based electrodes with Ni:Fe ratios in the optimum regime. All materials showed similar trends between activation and conditioning parameters, suggesting a common activation mechanism and guidelines

(research question 2.2). Precisely, when aiming for the most significant activation, conditioning is to be performed by CV with a high upper (1.6 V) and a low lower (–0.35 V) potential limit, a slow scan rate (≤100 mV s^{-1}), and many cycles (≥ 200) **(research question 2.1)**. Conditioning for a fixed time identified a trade-off between efficient activation per cycle and the number of cycles. Thus, the optimum scan rate varies depending on the available time. Out of the tested parameters, the choice of the potential limits was the most significant to maximize activation. However, an increase of the potential limits beyond the herein-tested limits needs to be considered carefully, not only for safety reasons, but also since too high currents and stress are hypothesized to be disadvantageous for the activation. These correlations between electrochemical conditioning parameters and activation can now be used to tailor the oxides of any pre-catalyst to (re)activate them and exploit their full potential. By studying Ni as Fe-incorporating material and Ni-Fe electrodes with the Ni:Fe ratio in the optimum regime as a material, which incorporates or dissolves Fe only minimally, a wide and important material class was covered. The importance of this material class is highlighted by the Ni:Fe ratio often being reported as activity determining factor for OER electrocatalysts. Thus, since both, Ni as well as Ni-Fe-based, electrodes showed similar activation trends, the transferability of these activation trends to any Ni-based pre-catalyst is suggested to be very likely. This is further supported by the works from other groups, which found similar activation trends for Ni, Fe, and steel electrodes. When transferring these activation trends to different Ni-based pre-catalysts, it is hypothesized that while the overall activation trends remain similar, the importance of certain parameters, such as the scan rate, will vary. For non-Fe-containing electrodes (*i.e*. Ni), it was found that the importance of the scan rate to obtain a high activation is increased, with a lower scan rate being more beneficial for the activation. Also, for oxide catalysts the importance of a lower scan rate is proposed to be increased. On the contrary, for Fe-containing electrodes (*i.e*. herein: Ni-Fe alloys), the importance of the scan rate is decreased.

It appeared that the primary reasons for these correlations between activation and conditioning parameters are surface oxidation and enlargement **(research question 2.3)**. Based on the characterization of the resulting oxides after conditioning, to achieve the greatest activation, a thick (hydr)oxide layer with a high M(OH):M(O) ratio needs to be produced, with the character of the $Ni(OH)_2$ phase (α or β) being of secondary importance. The correlation between the $Ni(OH)_2$ phase and the activity or activation could not be clearly deduced and needs further investigation. For non-Fe-containing electrodes (Ni), the oxide layer thickness is especially sensitive to the scan rate likely due to a kinetically limited Ni(0) to $Ni(OH)_2$ oxidation. If an anhydrous rigid oxide is present as a pre-catalyst, a low scan rate is also suggested to be more beneficial for the activation since the rigid oxide will require restructuring, which is likely kinetically limited. In addition to the oxide growth during conditioning, Fe is incorporated for non-Fe-containing electrodes and dissolved for Fe-containing electrodes. Since both, Fe incorporation for non-Fe-containing electrodes (Ni) as well as Fe dissolution for Fe-containing electrodes ($Ni_{70}Fe_{30}$), were closely linked with the $Ni(OH)_2$ formation, the correlation between activation and Fe incorporation or rather dissolution could not be differentiated from the relation between $Ni(OH)_2$ formation and activation. Online ICP-OES coupled to the iEFC **(research question 1.5)** combined with XPS identified that more Fe is incorporated for Ni or rather dissolved for $Ni_{70}Fe_{30}$ with increased $Ni(OH)_2$ formation. Such an increased $Ni(OH)_2$ formation and Fe incorporation (Ni) or rather dissolution (Ni-Fe) is the case when cycling for example to lower potentials and including the HER regime. Online ICP-OES further showed Fe

incorporation to be a slow or even mass-transport-limited process and Fe dissolution a comparable fast one. Hence, slow scan rates are more important for the activation of non-Fe-containing electrodes. The role of the electrolyte's Fe content in causing differences in electrode activation was, however, found to be minor under the herein-tested conditions **(research question 2.2)**. When the Fe concentration in the electrolyte was higher than approx. 110 ppb, changes in the Fe concentration had no significant impact on the potential or activation of $Ni_{99.99}$ and $Ni_{70}Fe_{30}$. From this, a stable dynamic Fe equilibrium and a constant thick $Ni(OH)_2$ layer as a host for Fe incorporation at the different Fe concentrations can be concluded **(research question 2.2)**. These correlations between conditioning parameters and surface changes contribute to a deeper understanding of the occurring processes during the conditioning of Ni-based electrocatalysts. This knowledge is considered essential for future catalyst design and tailoring.

Having achieved a thorough understanding and optimization of electrode conditioning of Ni-(Fe)-based electrodes in the iEFC at lab conditions, the next step was to transition toward industrial-scale implementation **(research question 3.1)**. Hence, in this work, it was shown that the electrochemical conditioning can be performed at industrially more relevant conditions (flex-E-cell, separator, 12 cm^2, 30 wt% KOH, 80 °C) with a similar or even higher activation than at lab conditions (iEFC, no separator, 1 cm^2, 1 M KOH, RT). Further, since in industry higher current densities are applied during AWE, the effect of conditioning on the OER potential during electrolysis at higher current densities was tested. Increased activation was observed, which additionally supported the successful scale-up of electrochemical conditioning as an *in-situ* electrode manufacturing technique. This first proof-of-concept brings electrochemical conditioning one step closer to industrial application, where it could save resources, electricity, and manufacturing costs.

Overall, this work demonstrates that enhancing the OER efficiency through conditioning is vital for improving the catalysts' effectiveness throughout extended AWE processes. This underscores the critical role of conditioning in catalyst preparation and electrochemical characterization.

7. Outlook

In this work, the electrochemical conditioning of Ni-(Fe)-based bulk electrodes was systematically investigated in a self-designed iEFC and scaled up to industrially more relevant conditions. While working on these topics and gaining valuable insights, a few challenges remained open, and new research questions arose. Figure 7.1 shows an overview of these open research topics, grouping them into the coupling of the iEFC with ICP-OES, the understanding and transferability of electrochemical conditioning, and the industrialization of electrochemical conditioning.

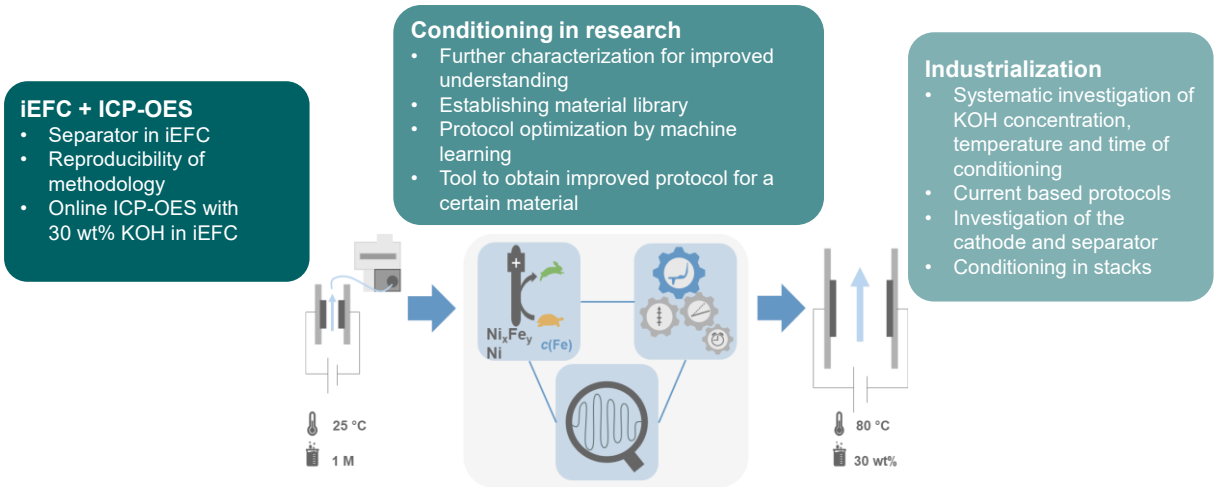

Figure 7.1. Schematic outlook of this thesis, defining the research topics that emerged from this thesis in the fields of coupling the herein-designed iEFC with the ICP-OES, understanding and transferability of an electrocatalysts' electrochemical conditioning for the alkaline OER, and industrialization of the electrochemical conditioning.

First, an iEFC was designed in this work to enable the characterization of the electrocatalytic activity of new electrocatalysts with online electrolyte monitoring under industrially more relevant conditions. These industrially more relevant conditions refer to 1 cm^2 parallel, planar electrodes and parallel flow to the electrodes, representing unique features compared to the previously reported iEFCs. Further, the iEFC was successfully linked with ICP-OES to monitor the electrolyte concentration online in 1 M KOH at RT while studying the activity and stability of electrocatalysts for the alkaline OER. Interesting insights on potential-dependent Fe dissolution and incorporation during CV cycling of a $Ni_{99.99}$ and $Ni_{70}Fe_{30}$ electrode could be gained, but some methodologic challenges remained. First, metal dissolution or incorporation at the electrodes could only be determined for the anode and cathode together. Ideally, the anode and cathode chambers would be separated, allowing their separate investigation. This is detrimental to an increased understanding of the occurring electrode processes. Second, reproducibility was sometimes limited by a shifting baseline, gas bubbles, and a low signal-to-noise-ratio. One explanation for the baseline shift is a temperature change in the plasma related to a varying flow rate due to prolonged tubing from aging, more salt residues at the torch and cone, gas bubbles, or fluctuations in the ventilation. The low signal-to-noise ratio could be due to the high salt concentration of the electrolyte in combination with unoptimized plasma settings. Hence, optimization potential is apparent. Since high reproducibility is crucial for correct data interpretation, a systematic investigation of the causes of irreproducibility and the low signal-to-noise ratio is required. Optimization potential could be *e.g.* introducing a baseline recording of at least 30 min at the beginning and end of the experiment, incorporating

a bubble trap to remove as many bubbles as possible, and adding an internal standard, that behaves similarly to the element of interest regarding plasma temperature changes. Going one step further, the herein-designed iEFC coupled to ICP-OES can be used in the future to investigate the OER catalyst's stability at an industrially applied concentration (30 wt% KOH) and temperature (80 °C). However, since the ICP-OES can only endure salt loadings up to 20 wt%, a dilution of the outlet stream from the iEFC needs to be implemented. For that, the following questions need to be addressed step-by-step: What dilution is necessary to record Fe-concentration changes with an acceptable signal-to-noise ratio, and do the plasma settings need to be adjusted accordingly? Can the dilution and, thus, the KOH concentration, be kept constant over an extended period of time under the influence of a varying gas evolution and tube aging? How can a suitable calibration be performed? By answering these questions and performing the required adjustments, the gap between industrial AWE and academic research can be reduced, significantly enhancing the importance of online ICP-OES. By being then able to simultaneously study the electrocatalysts' activity and stability under industrially more relevant conditions (1 cm^2 parallel, planar electrodes with parallel flow and separator, 30 wt% KOH, 80 °C), the highly interesting question of why many electrocatalysts perform well at lab and worse at industrial conditions can be addressed.

The herein-developed iEFC was used in this work to systematically investigate the correlations between conditioning parameters, activation, and surface changes for Ni-(Fe)-based bulk electrodes. While activation was strongly correlated with an increase of the Ni-hydroxide layer, the role of its phase character was not 100% clear. The hypothesis was that the $Ni(OH)_2$ phase character is of secondary importance for the electrode activation and activity. Interestingly, it was further observed that the Ni(II)/Ni(III) redox peaks of a Ni electrode behave differently depending on the amount of Fe in the electrolyte, suggesting that different Ni-phases are formed. With no Fe in the electrolyte during conditioning between –0.35-1.6 V, only one phase, potentially β-$Ni(OH)_2$, formed. At medium to high Fe concentrations, two to three peaks were visible, respectively. This raises the questions: Which phase or phase mix is more active when compared in an electrolyte with the same Fe content? How can these phases be tailored by an interplay of the electrolyte's Fe-concentration, scan rate, and potential window? These questions can be addressed by a systematic parameter variation of the Fe-concentration, scan rate, and potential window during conditioning coupled with a post-characterization by FTIR and XPS. Knowing which phase forms at what conditions and how that is correlated with the activity is vital to tailor other Ni-based catalysts for such a phase change and activity boost. This understanding would, further, significantly improve efficient catalyst design. Even more so, if the relations between intrinsic activity and the number of active sites were known precisely. In this thesis, the hypothesis was established that the apparent reaction rate decreases or stays constant, but the number of active sites increases during conditioning. This, however, did not fully align with the lowered slope of the galvanostatic *i-E*-curve by conditioning. Thus, it would be interesting to study whether the same *i-E*-slope occurs when performing a potentiostatic measurement instead of galvanostatic. As the FTacV suggested the intrinsic activity loss due to conditioning, these results need to be questioned as well and supported by additional experiments. Such experiments include *e.g.* performing the electrochemical sequence with FTacV replaced with the respective dc equivalent and performing FTacV only after the entire sequence. To further validate the increase of active species and decrease of intrinsic activity, the electrochemically active surface area (ECSA) needs to be determined and the activity has to be normalized to it. To answer these questions,

detailed Tafel, EIS, FTacV, and ECSA analyses are required. Ideally, this profound understanding of electrochemical conditioning of Ni-(Fe)-based electrodes and the induced surface changes can be used, in the next step, to tailor specific surface changes and the respective activation for any Ni-based pre-catalyst.

Indeed, based on this work, the herein-observed correlations between conditioning parameters, activation, and surface changes can already be tested for other electrocatalysts. If this is done systematically for different elements and multi-element electrodes, one can investigate whether those elements show similar activation trends, suggesting a common activation mechanism, and obtain a conditioning library for various materials and element combinations. Here, machine learning approaches can be applied to find a suitable protocol faster. This approach can also enlarge the pool of protocol parameters that can be tested, incl. testing potential switching instead of cycling and combinations of different parameter sets. It needs to be noted that when expanding the parameter space, industrial relevance needs to be considered, *i.e*. the scan rate increase is limited and when increasing the potential limits further into the HER and OER, mixing of H_2 and O_2 could become critical. The material screening and the obtained conditioning library would not only contribute to a deeper understanding of how certain elements and their combinations activate, but it would also be essential for the research community to estimate which activation protocol could be best suited for their electrocatalyst. Going one step further, an interactive tool to find a suitable conditioning protocol depending on the elements present in the catalyst could be implemented. In addition to variations of the conditioning parameters to enhance activation, the addition of additives in the ppb range could also be an interesting alternative. Here, the activity gain and stability for different additives would need to be tested systematically.

Based on this, successful activation of any Ni-based pre-catalyst is anticipated to be possible, exploiting their full potential. During AWE, these will, however, likely deactivate, potentially due to oxide restructuring, phase changes, metal dissolution, or deposition at the electrode. To not invest in an activation technique, whose effect can not be maintained long-term, the deactivation mechanisms are of great interest to be investigated by long-term measurements at high current densities, accelerated stress tests, and spectroscopic analysis. After deactivation, conditioning might again be a suitable tool for reactivation, which could be very promising for industry to prolong the electrode's lifetime. Thus, it is very important to investigate whether the electrodes can be reactivated and under what conditions, including clarifying whether reactivation depends on the type of deactivation.

With such a well-understood and established conditioning of electrodes, the next step toward application is the industrialization of the process. For the industrialization of electrochemical conditioning as an electrode preparation technique, the currently potential-based protocols need to be transferred to current-based protocols, and depending on the cycling parameters the mixing of H_2 and O_2 needs to be investigated and circumvented. Industrial electrochemical conditioning can theoretically be applied as an *ex-situ* and *in-situ* electrode preparation technique. The advantage of *ex-situ* application is, for once, that the process parameters, such as the KOH concentration, additive, and temperature, can be adjusted more flexibly than for *in-situ* application. Here, a process parameter optimization is still required. Another advantage is that the implications of conditioning on the other cell components are not as decisive. For *ex-situ* application, it still needs to be clarified whether the conditioned electrodes retain their electrocatalytic activity during storage, and if so, under which conditions. *In-situ* conditioning

in a full cell, on the contrary, has the promising potential of simplifying electrode manufacturing and reactivation one step further and, thus, saving manufacturing costs. For *in-situ* conditioning, it is then important to study what happens at the cathode and the separator. If the cathode or separator is degrading, *in-situ* conditioning will not be suitable. Degradation of the cathode can occur by *e.g.* metal dissolution/deposition or surface restructuring. The separator might degrade by an increase of pinholes, ripping, gas cross-over, or property changes. Further, conditioning could affect the electrolyte quality by increasing or decreasing the metal ion concentration when recirculating the electrolyte. This might pose an additional challenge as industrial AWE electrolyzers are often tied to a certain electrolyte quality. If a purification system would be needed, the overall cost-effectiveness of this *in-situ* technique needs to be re-evaluated. In any case, it is absolutely important to investigate these phenomena, especially during long-term operation (> 100 h). If the cathode and separator do not degrade, the next question to answer is how *in-situ* conditioning can be applied in an electrolyzer stack. Questions to clarify would be: If an entire stack is conditioned, are all single cells activated similarly? How would stray currents evolve and interfere with the conditioning and the stack activity? How fast is the response time of an electrolyzer, does it differ from a single cell? How can single cells be controlled and conditioned within a stack? Lastly, it needs to be evaluated what the investment and operating costs of this technique are for *in-situ* and *ex-situ* application. If all of these research questions are answered, electrochemical conditioning might be able to be applied industrially to Ni-based electrodes to boost their activity and potentially make electrode manufacturing simpler and more agile. Thereby, electrode manufacturing and electricity costs and resources could be saved.

8. References

[1] S. Chu, A. Majumdar, Opportunities and challenges for a sustainable energy future, *Nature* **2012**, *488*, 294, DOI 10.1038/nature11475.

[2] Z.-P. Wu, X. F. Lu, S.-Q. Zang, X. W. Lou, Non-Noble-Metal-Based Electrocatalysts toward the Oxygen Evolution Reaction, *Adv. Funct. Mater.* **2020**, *30*, 1910274, DOI 10.1002/adfm.201910274.

[3] T. Reier, H. N. Nong, D. Teschner, R. Schlögl, P. Strasser, Electrocatalytic Oxygen Evolution Reaction in Acidic Environments - Reaction Mechanisms and Catalysts, *Adv. Energy Mater.* **2017**, *7*, 1601275, DOI 10.1002/aenm.201601275.

[4] J. Song, C. Wei, Z.-F. Huang, C. Liu, L. Zeng, X. Wang, Z. J. Xu, A review on fundamentals for designing oxygen evolution electrocatalysts, *Chem. Soc. Rev.* **2020**, *49*, 2196, DOI 10.1039/C9CS00607A.

[5] R. Frydendal, E. A. Paoli, B. P. Knudsen, B. Wickman, P. Malacrida, I. E. L. Stephens, I. Chorkendorff, Benchmarking the Stability of Oxygen Evolution Reaction Catalysts: The Importance of Monitoring Mass Losses, *ChemElectroChem* **2014**, *1*, 2075, DOI 10.1002/celc.201402262.

[6] N. Thissen, J. Hoffmann, S. Tigges, D. A. M. Vogel, J. J. Thoede, S. Khan, N. Schmitt, S. Heumann, B. J. M. Etzold, A. K. Mechler, Industrially Relevant Conditions in Lab-Scale Analysis for Alkaline Water Electrolysis, *ChemElectroChem* **2024**, *11,* DOI 10.1002/celc.202300432.

[7] M. Chatenet, B. G. Pollet, D. R. Dekel, F. Dionigi, J. Deseure, P. Millet, R. D. Braatz, M. Z. Bazant, M. Eikerling, I. Staffell et al., Water electrolysis: from textbook knowledge to the latest scientific strategies and industrial developments, *Chem. Soc. Rev.* **2022**, *51*, 4583, DOI 10.1039/d0cs01079k.

[8] J. Wang, Y. Gao, H. Kong, J. Kim, S. Choi, F. Ciucci, Y. Hao, S. Yang, Z. Shao, J. Lim, Non-precious-metal catalysts for alkaline water electrolysis: operando characterizations, theoretical calculations, and recent advances, *Chem. Soc. Rev.* **2020**, *49*, 9154, DOI 10.1039/d0cs00575d.

[9] N. Yuan, Q. Jiang, J. Li, J. Tang, A review on non-noble metal based electrocatalysis for the oxygen evolution reaction, *Arabian J. Chem.* **2020**, *13*, 4294, DOI 10.1016/j.arabjc.2019.08.006.

[10] M. S. Burke, L. J. Enman, A. S. Batchellor, S. Zou, S. W. Boettcher, Oxygen Evolution Reaction Electrocatalysis on Transition Metal Oxides and (Oxy)hydroxides: Activity Trends and Design Principles, *Chem. Mater.* **2015**, *27*, 7549, DOI 10.1021/acs.chemmater.5b03148.

[11] De Nora, Electrodes. Alkaline Water Electrolysis Solutions, can be found under https://energytransition.denora.com/en/offerings/electrodes-for-alkaline-water-electrolysis?_gl=1*13d10u1*_gcl_au*NzYwMDQ2OTAwLjE3MzE1NzY0MTU. (accessed on: 15.11.2024).

[12] R. L. Doyle, I. J. Godwin, M. P. Brandon, M. E. G. Lyons, Redox and electrochemical water splitting catalytic properties of hydrated metal oxide modified electrodes, *Phys. Chem. Chem. Phys.* **2013**, *15*, 13737, DOI 10.1039/c3cp51213d.

[13] L. Bertuccioli, A. Chan, D. Hart, F. Lehner, B. Madden, E. Standen, Development of Water Electrolysis in the European Union, **2014**, element energy & E4tech Sàrl.

[14] The International Renewable Energy Agency (IRENA), Green hydrogen cost reduction: Scaling up electrolysers to meet the 1.5C climate goal, Abu Dhabi, **2020**.

[15] International Energy Agency (IEA), The Future of Hydrogen. Seizing today's opportunities, France, **2019**.

[16] De Nora, H_2 Production by Water Electrolysis, can be found under https://www.denora.com/applications/H2-production-by-water-electrolysis.html (accessed on: 14.11.2024).

[17] M. Steimecke, G. Seiffarth, M. Bron, In Situ Characterization of Ni and Ni/Fe Thin Film Electrodes for Oxygen Evolution in Alkaline Media by a Raman-Coupled Scanning Electrochemical Microscope Setup, *Anal. Chem.* **2017**, *89*, 10679, DOI 10.1021/acs.analchem.7b01060.

[18] R. Wang, C. Wang, S. Yin, Y. Peng, J. Chen, Y. Deng, J. Li, Hierarchically devising $NiFeO_xH_y$ catalyst with surface Fe active sites for efficient oxygen evolution reaction, *Catal. Today* **2021**, *364*, 140, DOI 10.1016/j.cattod.2020.04.013.

[19] S. Klaus, Y. Cai, M. W. Louie, L. Trotochaud, A. T. Bell, Effects of Fe Electrolyte Impurities on $Ni(OH)_2$/NiOOH Structure and Oxygen Evolution Activity, *J. Phys. Chem. C* **2015**, *119*, 7243, DOI 10.1021/acs.jpcc.5b00105.

[20] S. Klaus, M. W. Louie, L. Trotochaud, A. T. Bell, Role of Catalyst Preparation on the Electrocatalytic Activity of $Ni_{1-x}Fe_xOOH$ for the Oxygen Evolution Reaction, *J. Phys. Chem. C* **2015**, *119*, 18303, DOI 10.1021/acs.jpcc.5b04776.

[21] F. Le Formal, L. Yerly, E. Potapova Mensi, X. Pereira Da Costa, F. Boudoire, N. Guijarro, M. Spodaryk, A. Züttel, K. Sivula, Influence of Composition on Performance in Metallic Iron–Nickel–Cobalt Ternary Anodes for Alkaline Water Electrolysis, *ACS Catal.* **2020**, *10*, 12139, DOI 10.1021/acscatal.0c03523.

[22] H. Schäfer, S. Sadaf, L. Walder, K. Kuepper, S. Dinklage, J. Wollschläger, L. Schneider, M. Steinhart, J. Hardege, D. Daum, Stainless steel made to rust: a robust water-splitting catalyst with benchmark characteristics, *Energy Environ. Sci.* **2015**, *8*, 2685, DOI 10.1039/C5EE01601K.

[23] Z. Lu, W. Xu, W. Zhu, Q. Yang, X. Lei, J. Liu, Y. Li, X. Sun, X. Duan, Three-dimensional NiFe layered double hydroxide film for high-efficiency oxygen evolution reaction, *Chem. Commun.* **2014**, *50*, 6479, DOI 10.1039/c4cc01625d.

[24] Z. Cai, D. Zhou, M. Wang, S.-M. Bak, Y. Wu, Z. Wu, Y. Tian, X. Xiong, Y. Li, W. Liu et al., Introducing Fe^{2+} into Nickel-Iron Layered Double Hydroxide: Local Structure Modulated Water Oxidation Activity, *Angew. Chem. Int. Ed. Engl.* **2018**, *57*, 9392, DOI 10.1002/anie.201804881.

[25] Z. Lu, L. Qian, W. Xu, Y. Tian, M. Jiang, Y. Li, X. Sun, X. Duan, Dehydrated layered double hydroxides: Alcohothermal synthesis and oxygen evolution activity, *Nano Res.* **2016**, *9*, 3152, DOI 10.1007/s12274-016-1197-4.

[26] J. Mohammed-Ibrahim, A review on NiFe-based electrocatalysts for efficient alkaline oxygen evolution reaction, *J. Power Sources* **2020**, *448*, 227375, DOI 10.1016/j.jpowsour.2019.227375.

[27] L. D. Burke, E. J. M. O'Sullivan, Oxygen gas evolution on hydrous oxides — An example of three-dimensional electrocatalysis?, *J. Electroanal. Chem. Interfacial Electrochem.* **1981**, *117*, 155, DOI 10.1016/S0022-0728(81)80459-7.

[28] R. L. Doyle, M. E. G. Lyons, Kinetics and Mechanistic Aspects of the Oxygen Evolution Reaction at Hydrous Iron Oxide Films in Base, *J. Electrochem. Soc.* **2013**, *160*, H142-H154, DOI 10.1149/2.015303jes.

[29] M. E. G. Lyons, R. L. Doyle, I. Godwin, M. O'Brien, L. Russell, Hydrous Nickel Oxide: Redox Switching and the Oxygen Evolution Reaction in Aqueous Alkaline Solution, *J. Electrochem. Soc.* **2012**, *159*, H932-H944, DOI 10.1149/2.078212jes.

[30] G.-R. Zhang, L.-L. Shen, P. Schmatz, K. Krois, B. J. Etzold, Cathodic activated stainless steel mesh as a highly active electrocatalyst for the oxygen evolution reaction with self-healing possibility, *J. Energy Chem.* **2020**, *49*, 153, DOI 10.1016/j.jechem.2020.01.025.

[31] S. Zhu, C. Chang, Y. Sun, G. Duan, Y. Chen, J. Pan, Y. Tang, P. Wan, Modification of stainless steel fiber felt via in situ self-growth by electrochemical induction as a robust catalysis electrode for oxygen evolution reaction, *Int. J. Hydrogen Energy* **2020**, *45*, 1810, DOI 10.1016/j.ijhydene.2019.11.052.

[32] N. Todoroki, T. Wadayama, Heterolayered Ni-Fe Hydroxide/Oxide Nanostructures Generated on a Stainless-Steel Substrate for Efficient Alkaline Water Splitting, *ACS Appl. Mater. Interfaces* **2019**, *11*, 44161, DOI 10.1021/acsami.9b14213.

[33] Y. Zuo, V. Mastronardi, A. Gamberini, M. I. Zappia, T.-H.-H. Le, M. Prato, S. Dante, S. Bellani, L. Manna, Stainless Steel Activation for Efficient Alkaline Oxygen Evolution in Advanced Electrolyzers, *Adv. Mater.* **2024,** DOI 10.1002/adma.202312071.

[34] N. Todoroki, T. Wadayama, Dissolution of constituent elements from various austenitic stainless steel oxygen evolution electrodes under potential cycle loadings, *Int. J. Hydrogen Energy* **2022**, *47*, 32753, DOI 10.1016/j.ijhydene.2022.07.175.

[35] L. Magnier, G. Cossard, V. Martin, C. Pascal, V. Roche, E. Sibert, I. Shchedrina, R. Bousquet, V. Parry, M. Chatenet, Fe-Ni-based alloys as highly active and low-cost oxygen evolution reaction catalyst in alkaline media, *Nat. Mater.* **2024**, 1, DOI 10.1038/s41563-023-01744-5.

[36] O. Kasian, S. Geiger, K. J. J. Mayrhofer, S. Cherevko, Electrochemical On-line ICP-MS in Electrocatalysis Research, *Chem. Rec.* **2019**, *19*, 2130, DOI 10.1002/tcr.201800162.

[37] I. Spanos, A. A. Auer, S. Neugebauer, X. Deng, H. Tüysüz, R. Schlögl, Standardized Benchmarking of Water Splitting Catalysts in a Combined Electrochemical Flow Cell/Inductively Coupled Plasma–Optical Emission Spectrometry (ICP-OES) Setup, *ACS Catal.* **2017**, *7*, 3768, DOI 10.1021/acscatal.7b00632.

[38] N. Kulyk, S. Cherevko, M. Auinger, C. Laska, K. J. J. Mayrhofer, Numerical Simulation of an Electrochemical Flow Cell with V-Shape Channel Geometry, *J. Electrochem. Soc.* **2015**, *162*, H860-H866, DOI 10.1149/2.0261512jes.

[39] J. A. Cooper, R. G. Compton, Channel Electrodes — A Review, *Electroanalysis* **1998**, *10*, 141, DOI 10.1002/(SICI)1521-4109(199803)10:3<141::AID-ELAN141>3.0.CO;2-F.

[40] A. K. Schuppert, A. A. Topalov, I. Katsounaros, S. O. Klemm, K. J. J. Mayrhofer, A Scanning Flow Cell System for Fully Automated Screening of Electrocatalyst Materials, *J. Electrochem. Soc.* **2012**, *159*, F670, DOI 10.1149/2.009211jes.

[41] A. J. Bard, L. R. Faulkner, Electrochemical methods. Fundamentals and applications, Wiley, New York, **2001**, ISBN 0471043729.

[42] D. J. Pickett, Electrochemical reactor design, Elsevier, Amsterdam, **1979**, ISBN 0444418148.

[43] V. M. Schmidt, Elektrochemische Verfahrenstechnik, Wiley-VCH, Hoboken, **2012**, ISBN 9783527299584.

[44] N. Wakabayashi, M. Takeichi, M. Itagaki, H. Uchida, M. Watanabe, Temperature-dependence of oxygen reduction activity at a platinum electrode in an acidic electrolyte solution investigated with a channel flow double electrode, *J. Electroanal. Chem.* **2005**, *574*, 339, DOI 10.1016/j.jelechem.2004.08.013.

[45] G. R. Engelhardt, R. Biswas, Z. Ahmed, S. N. Lvov, D. D. Macdonald, The use of channel flow cells for electrochemical kinetic studies in high temperature aqueous solutions, *Electrochim. Acta* **2007**, *52*, 4124, DOI 10.1016/j.electacta.2006.11.027.

[46] Daniel A. Scherson, Yuriy V. Tolmachev, Zhenghao Wang, Jun Wang, Attila Palencsar, Extensions of the Koutecky–Levich Equation to Channel Electrodes, *Electrochem. Solid-State Lett.* **2007**, *11*, F1, DOI 10.1149/1.2818649.

[47] S. E. Temmel, S. A. Tschupp, T. J. Schmidt, A highly flexible electrochemical flow cell designed for the use of model electrode materials on non-conventional substrates, *Rev. Sci. Instrum.* **2016**, *87*, 45115, DOI 10.1063/1.4947459.

[48] J. P. Kollender, M. Voith, S. Schneiderbauer, A. I. Mardare, A. W. Hassel, Highly customisable scanning droplet cell microscopes using 3D-printing, *J. Electroanal. Chem.* **2015**, *740*, 53, DOI 10.1016/j.jelechem.2014.12.043.

[49] T. F. O'Brien, T. V. Bommaraju, F. Hine, Handbook of Chlor-Alkali Technology. Volume I: Fundamentals, Springer, New York, **2005**, ISBN 9780306486241.

[50] A. Godula-Jopek, Hydrogen production by electrolysis, Wiley-VCH, Weinheim, Germany, **2015**, ISBN 9783527676521.

[51] M. Alsabet, M. Grdeń, G. Jerkiewicz, Electrochemical Growth of Surface Oxides on Nickel. Part 3: Formation of β-NiOOH in Relation to the Polarization Potential, Polarization Time, and Temperature, *Electrocatalysis* **2015**, *6*, 60, DOI 10.1007/s12678-014-0214-1.

[52] H. Bode, K. Dehmelt, J. Witte, Zur kenntnis der nickelhydroxidelektrode—I.Über das nickel (II)-hydroxidhydrat, *Electrochim. Acta* **1966**, *11*, 1079, DOI 10.1016/0013-4686(66)80045-2.

[53] M. Alsabet, M. Grden, G. Jerkiewicz, Electrochemical Growth of Surface Oxides on Nickel. Part 1: Formation of α-$Ni(OH)_2$ in Relation to the Polarization Potential, Polarization Time, and Temperature, *Electrocatalysis* **2011**, *2*, 317, DOI 10.1007/s12678-011-0067-9.

[54] Z. Angeles-Olvera, A. Crespo-Yapur, O. Rodríguez, J. Cholula-Díaz, L. Martínez, M. Videa, Nickel-Based Electrocatalysts for Water Electrolysis, *Energies* **2022**, *15*, 1609, DOI 10.3390/en15051609.

[55] Y. Zhou, N. López, The Role of Fe Species on NiOOH in Oxygen Evolution Reactions, *ACS Catal.* **2020**, *10*, 6254, DOI 10.1021/acscatal.0c00304.

[56] L. D. Burke, T. Twomey, Voltammetric behaviour of nickel in base with particular reference to thick oxide growth, *J. Electroanal. Chem. Interfacial Electrochem.* **1984**, *162*, 101, DOI 10.1016/S0022-0728(84)80158-8.

[57] M. E. G. Lyons, M. P. Brandon, Redox switching and oxygen evolution electrocatalysis in polymeric iron oxyhydroxide films, *Phys. Chem. Chem. Phys.* **2009**, *11*, 2203, DOI 10.1039/b815338h.

[58] L. D. Burke, M. E. Lyons, The formation and stability of hydrous oxide films on iron under potential cycling conditions in aqueous solution at high pH, *J. Electroanal. Chem. Interfacial Electrochem.* **1986**, *198*, 347, DOI 10.1016/0022-0728(86)90010-0.

[59] L. Trotochaud, S. L. Young, J. K. Ranney, S. W. Boettcher, Nickel–Iron Oxyhydroxide Oxygen-Evolution Electrocatalysts: The Role of Intentional and Incidental Iron Incorporation, *J. Am. Chem. Soc.* **2014**, *136*, 6744, DOI 10.1021/ja502379c.

[60] C. Kuai, C. Xi, A. Hu, Y. Zhang, Z. Xu, D. Nordlund, C.-J. Sun, C. A. Cadigan, R. M. Richards, L. Li et al., Revealing the Dynamics and Roles of Iron Incorporation in Nickel Hydroxide Water Oxidation Catalysts, *J. Am. Chem. Soc.* **2021**, *143*, 18519, DOI 10.1021/jacs.1c07975.

[61] Y. J. Son, S. Kim, V. Leung, K. Kawashima, J. Noh, K. Kim, R. A. Marquez, O. A. Carrasco-Jaim, L. A. Smith, H. Celio et al., Effects of Electrochemical Conditioning on Nickel-Based Oxygen Evolution Electrocatalysts, *ACS Catal.* **2022**, *12*, 10384, DOI 10.1021/acscatal.2c01001.

[62] M. B. Stevens, C. D. M. Trang, L. J. Enman, J. Deng, S. W. Boettcher, Reactive Fe-Sites in Ni/Fe (Oxy)hydroxide Are Responsible for Exceptional Oxygen Electrocatalysis Activity, *J. Am. Chem. Soc.* **2017**, *139*, 11361, DOI 10.1021/jacs.7b07117.

[63] J. R. Swierk, S. Klaus, L. Trotochaud, A. T. Bell, T. D. Tilley, Electrochemical Study of the Energetics of the Oxygen Evolution Reaction at Nickel Iron (Oxy)Hydroxide Catalysts, *J. Phys. Chem. C* **2015**, *119*, 19022, DOI 10.1021/acs.jpcc.5b05861.

[64] D. Friebel, M. W. Louie, M. Bajdich, K. E. Sanwald, Y. Cai, A. M. Wise, M.-J. Cheng, D. Sokaras, T.-C. Weng, R. Alonso-Mori et al., Identification of highly active Fe sites in (Ni,Fe)OOH for electrocatalytic water splitting, *J. Am. Chem. Soc.* **2015**, *137*, 1305, DOI 10.1021/ja511559d.

[65] M. W. Louie, A. T. Bell, An investigation of thin-film Ni-Fe oxide catalysts for the electrochemical evolution of oxygen, *J. Am. Chem. Soc.* **2013**, *135*, 12329, DOI 10.1021/ja405351s.

[66] M. Mattinen, J. Schröder, G. D'Acunto, M. Ritala, T. F. Jaramillo, M. B. Stevens, S. F. Bent, Dynamics of precatalyst conversion and iron incorporation in nickel-based alkaline oxygen evolution reaction catalysts, *Cell Rep. Phys. Sci.* **2024**, 102284, DOI 10.1016/j.xcrp.2024.102284.

[67] S. Lee, L. Bai, X. Hu, Deciphering Iron-Dependent Activity in Oxygen Evolution Catalyzed by Nickel-Iron Layered Double Hydroxide, *Angew. Chem. Int. Ed. Engl.* **2020**, *59*, 8072, DOI 10.1002/anie.201915803.

[68] F. Dionigi, Z. Zeng, I. Sinev, T. Merzdorf, S. Deshpande, M. B. Lopez, S. Kunze, I. Zegkinoglou, H. Sarodnik, D. Fan et al., In-situ structure and catalytic mechanism of NiFe

and CoFe layered double hydroxides during oxygen evolution, *Nat. Commun.* **2020**, *11*, 2522, DOI 10.1038/s41467-020-16237-1.

[69] R. Farhat, J. Dhainy, L. I. Halaoui, OER Catalysis at Activated and Codeposited NiFe-Oxo/Hydroxide Thin Films Is Due to Postdeposition Surface-Fe and Is Not Sustainable without Fe in Solution, *ACS Catalysis* **2020**, *10*, 20, DOI 10.1021/acscatal.9b02580.

[70] D. Y. Chung, P. P. Lopes, P. Farinazzo Bergamo Dias Martins, H. He, T. Kawaguchi, P. Zapol, H. You, D. Tripkovic, D. Strmcnik, Y. Zhu et al., Dynamic stability of active sites in hydr(oxy)oxides for the oxygen evolution reaction, *Nat Energy* **2020**, *5*, 222, DOI 10.1038/s41560-020-0576-y.

[71] C. Feng, F. Wang, Z. Liu, M. Nakabayashi, Y. Xiao, Q. Zeng, J. Fu, Q. Wu, C. Cui, Y. Han et al., A self-healing catalyst for electrocatalytic and photoelectrochemical oxygen evolution in highly alkaline conditions, *Nat. Commun.* **2021**, *12*, 5980, DOI 10.1038/s41467-021-26281-0.

[72] S. Rebouillat, M. E. Lyons, M. P. Brandon, R. L. Doyle, Paving the way to the integration of smart nanostructures: part II: nanostructured microdispersed hydrated metal oxides for electrochemical energy conversion and Storage Applications, *Int. J. Electrochem. Sci.* **2011**, 5830, DOI 10.1016/S1452-3981(23)18448-3.

[73] L. D. Burke, D. P. Whelan, Growth of electrochromic film on nickel in base under potential cycling conditions, *J. Electroanal. Chem. Interfacial Electrochem.* **1980**, *109*, 385, DOI 10.1016/S0022-0728(80)80139-2.

[74] M. E. Lyons, A. Cakara, P. O'Brien, I. Godwin, R. L. Doyle, Redox, pH sensing and Electrolytic Water Splitting Properties of Electrochemically Generated Nickel Hydroxide Thin Films in Aqueous Alkaline Solution, *Int. J. Electrochem. Sci.* **2012**, *7*, 11768, DOI 10.1016/S1452-3981(23)16503-5.

[75] M. E. G. Lyons, R. L. Doyle, M. P. Brandon, Redox switching and oxygen evolution at oxidized metal and metal oxide electrodes: iron in base, *Phys. Chem. Chem. Phys.* **2011**, *13*, 21530, DOI 10.1039/C1CP22470K.

[76] M. Vuković, Voltammetry and anodic stability of a hydrous oxide film on a nickel electrode in alkaline solution, *J. Appl. Electrochem.* **1994**, *24*, 878, DOI 10.1007/BF00348775.

[77] P. Zhou, H. Bai, J. Feng, Di Liu, L. Qiao, C. Liu, S. Wang, H. Pan, Recent progress on bulk Fe-based alloys for industrial alkaline water electrolysis, *J. Mater. Chem. A* **2023**, *11*, 1551, DOI 10.1039/D2TA09052J.

[78] H. R. Zamanizadeh, S. Sunde, B. G. Pollet, F. Seland, Tailoring the oxide surface composition of stainless steel for improved OER performance in alkaline water electrolysis, *Electrochim. Acta* **2022**, *424*, 140561, DOI 10.1016/j.electacta.2022.140561.

[79] N. Todoroki, T. Wadayama, Electrochemical stability of stainless-steel-made anode for alkaline water electrolysis: Surface catalyst nanostructures and oxygen evolution overpotentials under applying potential cycle loading, *Electrochem. commun.* **2021**, *122*, 106902, DOI 10.1016/j.elecom.2020.106902.

[80] F. Moureaux, P. Stevens, G. Toussaint, M. Chatenet, Timely-activated 316L stainless steel: A low cost, durable and active electrode for oxygen evolution reaction in concentrated alkaline environments, *Appl. Catal. B* **2019**, *258*, 117963, DOI 10.1016/j.apcatb.2019.117963.

[81] H. Schäfer, D. M. Chevrier, P. Zhang, J. Stangl, K. Müller-Buschbaum, J. D. Hardege, K. Kuepper, J. Wollschläger, U. Krupp, S. Dühnen et al., Electro-Oxidation of Ni42 Steel: A Highly Active Bifunctional Electrocatalyst, *Adv. Funct. Mater.* **2016**, *26*, 6402, DOI 10.1002/adfm.201601581.

[82] N. M. Kubo, F. Ketter, S. Palkovits, R. Palkovits, Nickel and Commercially Available Nickel-Containing Alloys as Electrodes for the Electrochemical Oxygen Evolution, *ChemElectroChem* **2024**, *11,* DOI 10.1002/celc.202300460.

[83] T. B. Ferriday, S. Nuggehalli Sampathkumar, M. D. Mensi, P. H. Middleton, J. van Herle, M. L. Kolhe, Tuning Stainless Steel Oxide Layers through Potential Cycling─AEM Water Electrolysis Free of Critical Raw Materials, *ACS Appl. Mater. Interfaces* **2024**, *16*, 29963, DOI 10.1021/acsami.4c01107.

[84] Y. Deo, N. Thissen, V. Seidl, J. Gallenberger, J. Hoffmann, J. P. Hofmann, B. J. M. Etzold, A. K. Mechler, Thin Nickel Coatings on Stainless Steel for Enhanced Oxygen Evolution and Reduced Iron Leaching in Alkaline Water Electrolysis, *Electrochemical Science Adv* **2024,** DOI 10.1002/elsa.202400023.

[85] De Nora, De Nora electrodic package for Alkaline Water Electrolysis, can be found under https://denora.com/applications/H2-production-by-water-electrolysis.html, **2016** (accessed on: 01.02.2023).

[86] Stratasys, VeroClear, can be found under https://www.stratasys.com/de/materials/materials-catalog/polyjet-materials/veroclear/ (accessed on: 24.12.2024).

[87] H. Ingendae, Influence of Operating Conditions on Electrochemical Activation of NiFe based Electrodes for Alkaline Oxygen Evolution, *master thesis*, **2023**, RWTH Aachen University, Aachen.

[88] J. Schmitt, Scale-up of water electrolysis: electrode activation under industrial conditions, *master thesis*, **2024**, RWTH Aachen University, Aachen.

[89] C. Marcks, Simulation and validation of an Electrochemical Flow Cell for in-situ activity studies of electrocatalytic reactions, *master thesis*, **2021**, RWTH Aachen University, Aachen.

[90] R. G. Compton, P. R. Unwin, Channel and tubular electrodes, *J. Electroanal. Chem. Interfacial Electrochem.* **1986**, *205*, 1, DOI 10.1016/0022-0728(86)90219-6.

[91] G. D. O'Neil, S. Ahmed, K. Halloran, J. N. Janusz, A. Rodríguez, I. M. Terrero Rodríguez, Single-step fabrication of electrochemical flow cells utilizing multi-material 3D printing, *Electrochem. commun.* **2019**, *99*, 56, DOI 10.1016/j.elecom.2018.12.006.

[92] S. K. Sharma, D. Singh Verma, L. Ullah Khan, S. Kumar, S. Bahadar Khan (Eds.), Handbook of Materials Characterization, Springer, Cham, Switzerland, **2018**.

[93] D. J. D. Sullivan, E. J. Carleton in *Failure Analysis* (Eds.: D. J. D. Sullivan, E. J. Carleton), De Gruyter, **2022**, pp. 101–104.

[94] F. A. Stevie, C. L. Donley, Introduction to x-ray photoelectron spectroscopy, *J. Vac. Sci. Technol. A* **2020**, *38,* DOI 10.1116/6.0000412.

[95] P. van der Heide, X-ray photoelectron spectroscopy. An introduction to principles and practices, Wiley, Hoboken, N.J., **2012**, ISBN 9781118062531.

[96] N. Fairley, V. Fernandez, M. Richard-Plouet, C. Guillot-Deudon, J. Walton, E. Smith, D. Flahaut, M. Greiner, M. Biesinger, S. Tougaard et al., Systematic and collaborative approach to problem solving using X-ray photoelectron spectroscopy, *Applied Surface Science Advances* **2021**, *5*, 100112, DOI 10.1016/j.apsadv.2021.100112.

[97] J. H. Scofield, Hartree-Slater subshell photoionization cross-sections at 1254 and 1487 eV, *J. Electron Spectros. Relat. Phenomena* **1976**, *8*, 129, DOI 10.1016/0368-2048(76)80015-1.

[98] S. A. Khan, S. B. Khan, L. U. Khan, A. Farooq, K. Akhtar, A. M. Asiri in *Handbook of Materials Characterization*, Springer, Cham, **2018**, pp. 317–344.

[99] Bruker, FT-IR or IR Spectroscopy?, can be found under https://www.bruker.com/en/products-and-solutions/infrared-and-raman/ft-ir-routine-spectrometer/what-is-ft-ir-spectroscopy/difference-ir-vs-ftir.html, **2024** (accessed on: 20.11.2024).

[100] J. Olesik, ICP-OES Capabilities, Developments, Limitations, and Any Potential Challengers?, *Spectroscopy* **2020**, *35*, 18.

[101] Jobin Yvon S.A.S, Horiba Group (Geoff Tyler), ICP-OES, ICP-MS and AAS Techniques Compared, can be found under https://www.horiba.com/fileadmin/uploads/Scientific/Downloads/OpticalSchool_CN/TN/ICP/ICP-OES__ICP-MS_and_AAS_Techniques_Compared.pdf (accessed on: 28.12.2024).

[102] J. Nölte, ICP emission spectrometry. A practical guide, Wiley-VCH, Weinheim, **2021**, ISBN 9783527823635.

[103] S. Cherevko, K. Mayrhofer in *Encyclopedia of Interfacial Chemistry* (Ed.: K. Wandelt), Elsevier, Oxford, **2018**, pp. 326–335.

[104] S. Kaushik, B. Kumar (Eds.), Analytical Methods in Chemical Analysis: An Introduction, De Gruyter, **2023**.

[105] N. G. Baranska, B. Jones, M. R. Dowsett, C. Rhodes, D. M. Elton, J. Zhang, A. M. Bond, D. Gavaghan, H. O. Lloyd-Laney, A. Parkin, Practical Guide to Large Amplitude Fourier-Transformed Alternating Current Voltammetry─What, How, and Why, *ACS Meas. Sci. Au* **2024**, *4*, 418, DOI 10.1021/acsmeasuresciau.4c00008.

[106] R. Z. Snitkoff-Sol, A. M. Bond, L. Elbaz, Fourier-Transformed Alternating Current Voltammetry (FTacV) for Analysis of Electrocatalysts, *ACS Catal.* **2024**, *14*, 7576, DOI 10.1021/acscatal.4c01526.

[107] S.-X. Guo, A. M. Bond, J. Zhang, Fourier Transformed Large Amplitude Alternating Current Voltammetry: Principles and Applications, *Rev. Polarogr.* **2015**, *61*, 21, DOI 10.5189/revpolarography.61.21.

[108] E. A. Mashkina, A. N. Simonov, A. M. Bond, Optimisation of windowing for harmonic recovery in large-amplitude Fourier transformed a.c. voltammetry, *J. Electroanal. Chem.* **2014**, *732*, 86, DOI 10.1016/j.jelechem.2014.08.028.

[109] A. A. Sher, A. M. Bond, D. J. Gavaghan, K. Harriman, S. W. Feldberg, N. W. Duffy, S.-X. Guo, J. Zhang, Resistance, capacitance, and electrode kinetic effects in Fourier-transformed large-amplitude sinusoidal voltammetry: emergence of powerful and intuitively obvious tools for recognition of patterns of behavior, *Anal. Chem.* **2004**, *76*, 6214, DOI 10.1021/ac0495337.

[110] J. Zhang, S.-X. Guo, A. M. Bond, Discrimination and evaluation of the effects of uncompensated resistance and slow electrode kinetics from the higher harmonic components of a fourier transformed large-amplitude alternating current voltammogram, *Anal. Chem.* **2007**, *79*, 2276, DOI 10.1021/ac061859n.

[111] A. M. Bond, N. W. Duffy, D. M. Elton, B. D. Fleming, Characterization of nonlinear background components in voltammetry by use of large amplitude periodic perturbations and fourier transform analysis, *Anal. Chem.* **2009**, *81*, 8801, DOI 10.1021/ac901318r.

[112] A. Friedman, R. Z. Snitkoff-Sol, H. C. Honig, L. Elbaz, Simplified FTacV model to quantify the electrochemically active site density in PGM-free ORR catalysts, *Electrochim. Acta* **2023**, *463*, 142865, DOI 10.1016/j.electacta.2023.142865.

[113] R. Z. Snitkoff-Sol, A. Friedman, H. C. Honig, Y. Yurko, A. Kozhushner, M. J. Zachman, P. Zelenay, A. M. Bond, L. Elbaz, Quantifying the electrochemical active site density of precious metal-free catalysts in situ in fuel cells, *Nat. Catal.* **2022**, *5*, 163, DOI 10.1038/s41929-022-00748-9.

[114] C. Gohlke, C. Marcks, V. Seidl, M. Padligur, A. K. Mechler, Simulation-Assisted Design of an Analytical Flow Cell for Industrially Relevant Performance Studies, *J. Electrochem. Soc.* **2025**, *172*, 126501, DOI 10.1149/1945-7111/ae215e.

[115] P. L. Domingo, B. García, J. M. Leal, Acid–base behaviour of the ferricyanide ion in perchloric acid media. Spectrophotometric and kinetic study, *Can. J. Chem.* **1990**, *68*, 228, DOI 10.1139/v90-030.

[116] S. Barnartt, Primary Current Distribution Around Capillary Tips Used in the Measurement of Electrolytic Polarization, *J. Electrochem. Soc.* **1952**, *99*, 549, DOI 10.1149/1.2779650.

[117] J. E. Harrar, I. Shain, Electrode Potential Gradients and Cell Design in Controlled Potential Electrolysis Experiments, *Anal. Chem.* **1966**, *38*, 1148, DOI 10.1021/ac60241a008.

[118] S. Barnartt, Magnitude of IR-Drop Corrections in Electrode Polarization Measurements Made with a Luggin-Haber Capillary, *J. Electrochem. Soc.* **1961**, *108*, 102, DOI 10.1149/1.2427994.

[119] V. Schulte, Optimization of an Electrochemical Flow Cell for Activity Measurements of Electrocatalytic Reactions, *bachelor thesis*, **2022**, RWTH Aachen University, Aachen.

[120] J. Kautz, Electrochemical Modification of Nickel-Iron Electrodes for Alkaline Water Electrolysis, *bachelor thesis*, **2023**, RWTH Aachen University, Aachen.

[121] versus, Stratasys Objet Eden 260VS Test: Technische Daten und Preis, can be found under https://versus.com/de/stratasys-objet-eden-260vs (accessed on: 24.12.2024).

[122] rapidobject GmbH, Fertigungstoleranzen. Additive Fertigung / 3D Druck, can be found under https://www.rapidobject.com/downloads/#zu-beachten, **2023** (accessed on: 22.06.2024).

[123] L. Rossrucker, K. J. J. Mayrhofer, G. S. Frankel, N. Birbilis, Investigating the Real Time Dissolution of Mg Using Online Analysis by ICP-MS, *J. Electrochem. Soc.* **2014**, *161*, C115-C119, DOI 10.1149/2.064403jes.

[124] S. Cherevko, G. P. Keeley, N. Kulyk, K. J. J. Mayrhofer, Pt Sub-Monolayer on Au: System Stability and Insights into Platinum Electrochemical Dissolution, *J. Electrochem. Soc.* **2016**, *163*, H228-H233, DOI 10.1149/2.0981603jes.

[125] S. Bhandari, P. V. Narangoda, S. O. Mogensen, M. F. Tesch, A. K. Mechler, Effect of Experimental Parameters on the Electrocatalytic Performance in Rotating Disc Electrode Measurements: Case Study of Oxygen Evolution on Ni−Co-Oxide in Alkaline Media, *ChemElectroChem* **2022**, *9,* DOI 10.1002/celc.202200479.

[126] C. Gohlke, J. Gallenberger, N. Niederprüm, H. Ingendae, J. Kautz, J. P. Hofmann, A. K. Mechler, Boosting the Oxygen Evolution Reaction Performance of Ni-Fe-Electrodes by Tailored Conditioning, *ChemElectroChem* **2024**, *11,* DOI 10.1002/celc.202400318.

[127] Q. Zhang, W. Xiao, H. C. Fu, X. L. Li, J. L. Lei, H. Q. Luo, N. B. Li, Unraveling the Mechanism of Self-Repair of NiFe-Based Electrocatalysts by Dynamic Exchange of Iron during the Oxygen Evolution Reaction, *ACS Catal.* **2023**, 14975, DOI 10.1021/acscatal.3c03804.

[128] S. A. Bonke, A. M. Bond, L. Spiccia, A. N. Simonov, Parameterization of Water Electrooxidation Catalyzed by Metal Oxides Using Fourier Transformed Alternating Current Voltammetry, *J. Am. Chem. Soc.* **2016**, *138*, 16095, DOI 10.1021/jacs.6b10304.

[129] J. Gallenberger, H. Moreno Fernández, A. Alkemper, M. Li, C. Tian, B. Kaiser, J. P. Hofmann, Stability and decomposition pathways of the NiOOH OER active phase of NiO_x electrocatalysts at open circuit potential traced by ex situ and in situ spectroscopies, *Catal. Sci. Technol.* **2023**, *13*, 4693, DOI 10.1039/D3CY00674C.

[130] B. V. Crist, Handbook of Monochromatic XPS Spectra. Volume 2: Commercially Pure Binary Oxides, XPS International LLC, **2005**.

[131] M. A. van Veenendaal, G. A. Sawatzky, Nonlocal screening effects in 2p x-ray photoemission spectroscopy core-level line shapes of transition metal compounds, *Phys. Rev. Lett.* **1993**, *70*, 2459, DOI 10.1103/PhysRevLett.70.2459.

[132] C. Gort, P. W. Buchheister, M. Klingenhof, S. D. Paul, F. Dionigi, R. van de Krol, U. I. Kramm, W. Jaegermann, J. P. Hofmann, P. Strasser et al., Effect of Metal Layer Support Structures on the Catalytic Activity of NiFe(oxy)hydroxide (LDH) for the OER in Alkaline Media, *ChemCatChem* **2023**, *15,* DOI 10.1002/cctc.202201670.

[133] M. Riley, P. Moran, The Influence of Iron Deposition on the Voltage-Time Behavior of Nickel Cathodes in Alkaline Water Electrolysis, *J. Electrochem. Soc.* **1986**, *133*, 760, DOI 10.1149/1.2108670.

[134] M. Demnitz, Y. M. Lamas, R. L. Garcia Barros, A. de Leeuw den Bouter, J. van der Schaaf, M. Theodorus de Groot, Effect of iron addition to the electrolyte on alkaline water electrolysis performance, *iScience* **2024**, *27*, 108695, DOI 10.1016/j.isci.2023.108695.

[135] F. Bao, E. Kemppainen, I. Dorbandt, F. Xi, R. Bors, N. Maticiuc, R. Wenisch, R. Bagacki, C. Schary, U. Michalczik et al., Host, Suppressor, and Promoter—The Roles of Ni and Fe on Oxygen Evolution Reaction Activity and Stability of NiFe Alloy Thin Films in Alkaline Media, *ACS Catal.* **2021**, *11*, 10537, DOI 10.1021/acscatal.1c01190.

[136] J. N. Hausmann, B. Traynor, R. J. Myers, M. Driess, P. W. Menezes, The pH of Aqueous NaOH/KOH Solutions: A Critical and Non-trivial Parameter for Electrocatalysis, *ACS Energy Lett.* **2021**, *6*, 3567, DOI 10.1021/acsenergylett.1c01693.

9. Appendix

9.1. Experimental

Chemicals, materials, devices, and software

Table S1. Materials and chemicals, utilized for the experiments.

Name	Material	Manufacturer/ Ordered from	Purity/ Specification	Application
Ag-plated Cu wire	Ag on Cu	BKL electronic (Conrad)	n.a.	Electrode contacting
Al-slurry	Al_2O_3	Buehler	n.a.	Polishing
Ar gas	Ar	Air Products	99.99%	Electrolyte purging, ICP-OES
AR-H1	n.a.	Keyence	n.a.	3D-printing material
AR-M2	n.a.	Keyence	n.a.	3D-printing material
Cu tape (25 mm x 10 m)	Cu	Conrad	n.a.	Electrode contacting
DLP HI TEMP 300-AMB	n.a.	3D Systems	n.a.	3D-printing material
Ethanol	C_2H_5OH	Th. Geyer	99.8%	Cleaning
Ferricyanide	$K_3Fe(CN)_6$	Sigma-Aldrich	99%	Simulation validation
ICP-OES Iron Standard	10,000 μg mL^{-1} Fe in diluted HNO_3	Agilent Technologies	ICP-026	ICP-OES standard, adjusting *c*(Fe) in electrolyte
ICP-OES Wavelength Calibration Solution	50 mg L^{-1} Al, As, Ba, Cd, Co, Cr, Cu, Mn, Mo, Ni, Pb, Se, Sr, Zn, 500 mg L^{-1} K in 5% HNO_3	Agilent Technologies	6610030000	ICP-OES
$HClO_4$, RotipuranSupra 70%	$HClO_4$	Carl Roth	n.a.	Electrolyte
Hg/HgO RE	Hg/HgO	ALS	RE-61AP	RE
$Hg/HgSO_4$ RE	$Hg/HgSO_4$	ALS	RE-2CP	RE
Kapton tape	Polyimide	MaoXinTek (Amazon)	n.a.	Defining electrode surface area
KOH pellets	KOH	CHEMSOLUTE (Th. Geyer)	≥85%	Electrolyte
Lacomit varnish & remover	n.a.	Agar Scientific Ltd. (Plano)	n.a.	Defining electrode surface area

Name	Material	Manufacturer/ Ordered from	Purity/ Specification	Application
miniRHE	H_2/H^+	Gaskatel	Length: 3 cm, 4 cm	RE
N_2 gas	N_2	Air Products	99.99%	Electrolyte purging, ICP-OES
NaOH flakes	NaOH	Carl Roth	98%	Cleaning after 3D-printing
Ni mesh	Ni	De Nora	n.a.	WE
Ni plate, 1 mm thickness	Ni	Goodfellow	99.0%	WE
Ni plate, 1 mm thickness	Ni	HMW Hauner	99.2, 99.99+ wt%	WE
Ni rod (d = 4 mm)	Ni	HMW Hauner	99.99+ wt%	WE
Ni-Fe alloy plate, 1 mm thickness	$Ni_{90}Fe_{10}$, $Ni_{80}Fe_{20}$, $Ni_{70}Fe_{30}$	HMW Hauner	made from $Ni_{99.9}$ and $Fe_{99.99}$	WE
Ni-Fe alloy rod (d = 4 mm)	$Ni_{70}Fe_{30}$	HMW Hauner	made from $Ni_{99.9}$ and $Fe_{99.99}$	WE
PP, clear	PP	3D-Printe (printing service)	n.a.	3D-printing
PTFE foil, adhesive (0.127 mm thickness)	PTFE	High-tech-flon	n.a.	Defining electrode surface area
PTFE spray	PTFE	Ballistol	n.a.	Defining electrode surface area
RGD 525-High Temperature	n.a.	Stratasys	n.a.	3D-printing material
Sandpaper (<5000 grit size)	SiC	wolcraft	n.a.	Grinding (electrode preparation)
Sandpaper (5000-7000 grit size)	SiC	STARCKE (Hoffmann)	n.a.	Grinding (electrode preparation)
Glassy carbon (plates [1 mm thick], rods [d = 1 mm])	C	HTW	SIGRADUR G	WE, CE
Ta, 0.5 mm thickness	Ta	HMW Hauner	99.9%	Determining active surface area
Tropicoat, Insulating spray	n.a.	ITW Spraytec	n.a.	Defining electrode surface area
Ultrapure water	H_2O	Purified with purification system	Type 1, 0.05 µS cm^{-1}	n.a.

Table S2. Materials used in the iEFC.

Item	Material	Ordered from	Application
3D-printed EFC	VeroClear RD810 (Stratasys)	AVT-3D-printing (Object Eden260VS)	EFC top
Adhesive tape (double-sided, extra strong)	n.a.	tesa	Embedding
Brass rod (d = 4 mm)	Cu_xZn_y	Obi	CE contacting
CaldoFix-2 Resin & Hardener	n.a.	Struers	Embedding
Cu plate (0.5 mm)	Cu	Obi	WE contacting
EpoHeat CLR Resin & Hardener	n.a.	Buehler	Embedding
Flangeless PEEK fittings incl. nut, 5/16-24 flat bottom port, for 4 mm outer diameter tubing, XP-132	PEEK	VWR	Tubing
Flangeless PEEK fittings, 1/2-20 flat bottom port, for 1/4" outer diameter tubing, XU-655	PEEK	VWR	RE (d = 6 mm)
O-Ring, 1.5 x 5.5 mm, EPDM	EPDM	Landefeld	RE (d = 6 mm)
Screws (M5 x 50 mm DIN912) & nuts (M5)	Steel (A2)	SWG Schraubenwerk Galsbach	Sealing EFC
Silver Epoxy 8330-21G	n.a.	MG Chemicals	Electrode contacting
Tubing, d_{inner} = 2 mm, d_{outer} = 4 mm	PVC	VWR	Tubing
Design A			
3D-printed WE holder (20 x 25 mm)	VeroClear RD810 (Stratasys)	AVT-3D-printing (Object Eden260VS)	WE
3D-printed EFC bottom (20 x 25 mm)	VeroClear RD810 (Stratasys)	AVT-3D-printing (Object Eden260VS)	EFC bottom
O-Ring, 1 x 21 mm	EPDM	Landefeld	Bottom to top
UHU Plus sofortfest adhesive	2-component epoxy resin	Conrad	CE
Design B-D			
3D-printed EFC	AR-H1 (Keyence)	Rapidobject	EFC top
3D-printed WE holder (20 x 30 mm)	VeroClear RD810 (Stratasys)	AVT-3D-printing (Object Eden260VS)	WE

Item	Material	Ordered from	Application
3D-printed EFC bottom (20 x 30 mm)	VeroClear RD810 (Stratasys)	AVT-3D-printing (Object Eden260VS)	EFC bottom
3D-printed CE-holder	AR-M2 (Keyence)	Rapidobject	CE
Nut (M10, DIN934)	Galvanized steel	Landefeld	CE
M16 3D-printed screw	AR-M2 (Keyence)	Rapidobject	CE
O-Ring, 1.5 x 8.5 mm	EPDM	Landefeld	CE
O-ring 1 x 26 mm	EPDM	Landefeld	Bottom to top

Table S3. Materials used in the flex-E-cell.

Item	Material	Ordered from	Application
3D-printed spacer	High Temp V2 resin (Formlabs)	AVT-3D-printing (Form 2)	Spacer
Ni foil, 0.1 mm	Ni (99.2%)	Metall Jobst	Electrode contacting
PTFE gaskets (0.5, 1 mm thickness)	PTFE	S-Polytec	Sealing
Santoprene gaskets (0.5, 1 mm thickness)	EPDM, PP	AET Lézaud	Sealing
T-connector	n.a.	Landefeld	Tubing
T-connector insulation (tube diameter x isolation: 15 x 25 mm)	n.a.	WekoTrade (Isolierfuchs)	Tubing
Thermocouple type K	PTFE	Therma Thermofühler	Thermocouple
Tubing	C-Flex-Ultra (06434-16)	Cole Parmer	Tubing
Tubing insulation (tube diameter x isolation: 6 x 13 mm)	Kautschuk HiTemp & Solar EPDM	Aeroflec Benelux B.V. (Isolierfuchs)	Tubing
Zirfon 500 UTP Pearl Separator	Polyphenylene sulfide fabric coated with a mixture of a polymer and zirconium oxide	Agfa	Separator

Table S4. Utilized devices for the herein-conducted experiments.

Name	Manufacturer	Specification
3D PolyJet Printer	Stratasys	Object Eden260VS
3D SLA printer	Formlabs	Form 2
Cutting machine	Cricut	Cricut Maker μ07002
flex-E-cell	FXC Engineering	n.a.
Heating plate	VELP Scientifica (vwr)	AREX-6 PRO
Hot press	VOGT Labormaschinen	LaboPress P150H
ICP-OES	Agilent Technologies	5800 VDV
Optical microscope	Keyence	Keyence VHX7000
Oven	LLG Lab-ware	uniOVEN 42
Peristaltic pump	Cole-Parmer Instrument	Masterflex L/S 07551-20 + 12-rolls-4-channel-pump-head (MFLX07623-30) + EasyloadII, model 77202-60
Peristaltic pump	Materflex (vwr)	Ismatec Reglo Digital Pump, 4 channels à 12 rolls (Ismatec 78018-24)
Polishing machine	Struers	LaboPol-20
Potentiostat	Gamry Instrument	1010E, 3000
Potentiostat	Biologic	VSP-300
Potentiostat booster	Gamry Instrument	Reference 30k Booster
Scale	Mettler Toledo	XA105 Dual Range
SEM & EDX	Hitachi	Hitachi Schottky SU5000 FESEM
Torque wrench	PROXXON	MircoClick MC2 (0.4-2 Nm)
Ultrasonicator	EMAG Technologies	Emmi-H30
Water Purification	Diret-Q 5 UV Water Purification System	Merck KGaA
XPS	n.a.	DAISY-FUN ultra-high vacuum cluster

Table S5. Utilized software for data generation and analysis of the herein-conducted experiments.

Name	Manufacturer	Specification
COMSOL Multiphysics	COMSOL	5.6
Echem Analyst	Gamry Instruments	<7.10.0
Microsoft Excel	Microsoft	<2406
Gamry Framework	Gamry Instruments	<7.10.0
ICP Expert	Agilent Technologies	Version 7.5.3.11953
Autodesk Inventor	Autodesk	2019, 2021, 2023
MATLAB	MathWorks	2021b
OriginPro	OriginLab	2020, 2023
Visual Studio Code	Microsoft	1.91.1

Conversion of potentials into RHE and SHE scale

In this work, potentials were measured (meas) against a Hg/HgO RE ($E^{\mathrm{meas}}_{\mathrm{HgHgO}}$) and a K_2SO_4-saturated Hg/$HgSO_4$ RE ($E^{\mathrm{meas}}_{\mathrm{HgHgSO4}}$) and were converted into the RHE ($E^{\mathrm{meas}}_{\mathrm{RHE}}$) or rather SHE scale. The conversion into the RHE scale is done by correcting with the potential of the respective RE potential (Hg/HgO, Hg/$HgSO_4$) *vs*. RHE ($E^{\mathrm{RE}}_{\mathrm{RE,RHE}}$):

$$E^{\mathrm{meas}}_{\mathrm{RHE}} = E^{\mathrm{meas}}_{\mathrm{RE}} + E^{\mathrm{RE}}_{\mathrm{RE,RHE}} = E^{\mathrm{meas}}_{\mathrm{RE}} + (E^{\mathrm{RE}}_{\mathrm{RE,SHE}} - E^{\mathrm{RE}}_{\mathrm{SHE,RHE}}) \quad (9.1)$$

The RE potential *vs*. RHE corresponds to the potential difference between the HER/HOR $E^{\mathrm{RE}}_{\mathrm{SHE,RHE}}$ and the RE reaction $E^{\mathrm{RE}}_{\mathrm{RE,SHE}}$ at the applied pH, electrolyte concentration, and temperature. For Hg/HgO, Hg/$HgSO_4$, and the HER/HOR the Nernst equations are the following:

$$E^{\mathrm{RE}}_{\mathrm{HgHgO}} = E^{0}_{\mathrm{HgHgO}} - \frac{RT}{2F} \cdot \ln \frac{{a_{\mathrm{OH^-}}}^2}{a_{\mathrm{H_2O}}} \quad (9.2)$$

$$E^{\mathrm{RE}}_{\mathrm{HgHgSO4}} = E^{0}_{\mathrm{HgHgSO4}} - \frac{RT}{2F} \cdot \ln a_{\mathrm{SO_4^{2-}}} \quad (9.3)$$

$$E^{\mathrm{RE}}_{\mathrm{SHE,RHE}} = E^{0}_{\mathrm{SHE}} - \frac{RT}{2F} \cdot \ln \frac{a^2_{\mathrm{H^+}}}{a^2_{\mathrm{H_2O}} \cdot a_{\mathrm{H_2}}} = 0\ \mathrm{V} - 0.059 \cdot \mathrm{pH} \quad (9.4)$$

To convert the measured RE potential into the SHE scale, the potential of the RE *vs*. SHE is added:

$$E^{\mathrm{meas}}_{\mathrm{SHE}} = E^{\mathrm{meas}}_{\mathrm{RE}} + E^{\mathrm{RE}}_{\mathrm{RE,SHE}} \quad (9.5)$$

It should be noted that the substitution from activities with concentration must be considered carefully and in concentrated solutions, deviations can occur. In 1 M KOH at 22 °C, $E^{\mathrm{RE}}_{\mathrm{HgHgO}}$ is calculated to be 0.924 V, using the Excel spreadsheet tool by Hausmann *et al*.[136] Practically, the potential of the Hg/HgO redox couple *vs*. RHE, $E^{\mathrm{RE}}_{\mathrm{HgHgO,RHE}}$, was regularly determined in 1 M KOH at RT. It varied between 0.921-0.940 V. The standard potential of the K_2SO_4-saturated Hg/$HgSO_4$ was reported to be 0.64 V.[41] In this work, an empirically determined potential of 0.635 V was taken.

9.2. Design of an Electrochemical Flow Cell

9.2.1. Simulation and Experimental Validation of Mass Transport

Model parameters and mesh independence study for COMSOL Multiphysics simulations

Table S6. Model parameters for COMSOL Multiphysics simulations.

Model parameter	Value	Unit
Temperature	297	K
Reference temperature	293.15	K
Pressure	101325	Pa
Initial fluid pressure	101325	Pa
Fluid density	1000	kg m^{-3}
Dynamic viscosity of fluid	1.002e-03	Pa s
Diffusion coefficient of active species	1.93e-09	m^2 s^{-1}
Inlet concentration of active species	1.26	mol m^3
Exchange current density	1e-06	A m^{-2}
Symmetry factor	0.5	-
Electrons transferred	4	-
Faraday constant	96485	C mol^{-1}
Universal gas constant	8.3145	J mol^{-1} K^{-1}
Maximum triangular element size at electrode area	1.2e-05	m

To exclude the influence of the mesh on the simulation results, a mesh independence study was performed for the final iEFC design. This was done by gradually decreasing the maximum element size of the triangular-shaped elements of the electrode area and evaluating the corresponding limiting current. The parameters of the free tetrahedral mesh were kept constant

and predefined as “normal” in the COMSOL Multiphysics interface. A plot of the limiting current as a function of the maximum element size for a 1 cm^2 electrode can be seen in Figure S1.

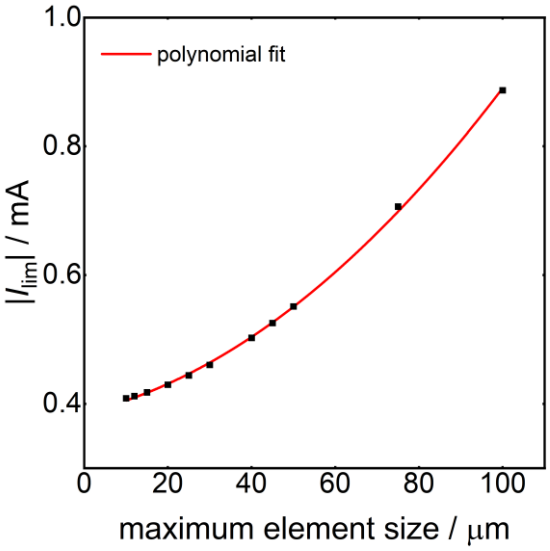

Figure S1. Limiting current depending on the maximum element size of the triangular-shaped meshing elements over the 1 cm^2 electrode area of the final iEFC design. The maximum element size of the triangular elements at the electrode area was continuously decreased until the limiting current reached a limit at a triangular element size of 12 µm.

The absolute value of the limiting current decreases with decreasing maximum element size. For an indefinitely small element size, the polynomial fit intercepts with the y-axis at a limiting current of 0.4 mA. The smaller the size of the elements, the higher the calculation time. Thus, a maximum triangular element size of 12 µm, resulting in a limiting current of 0.412 mA (deviation of 3% from the y-intercept), is used throughout the simulations as a trade-off between calculation time and accuracy.

Concentration distribution at the central x-y plane for the iEFC designs in Figure 5.4

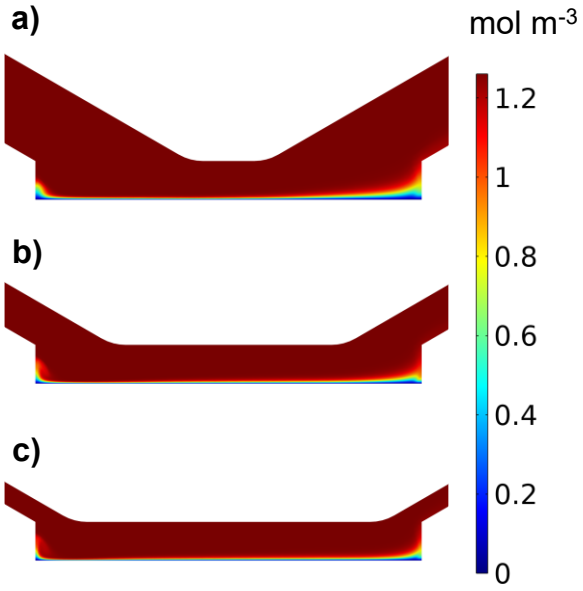

Figure S2. Concentration distribution at the central x-y plane of the herein-developed, preliminary flow geometry with different CWs of a) 2 mm, b) 1 mm, and c) 0.5 mm, complementing Figure 5.4. The inlet volume flow is 1.14 mL min^{-1} (for half of the inlet's cross-section), and the overpotential is 1.5 V. The channel height amounts to 1 mm, and the cell width is 2.5 mm (symmetry plane at 1.25 mm). The scale ranges from 0-1.26 mol m^{-3}.

Flow velocity distribution for the iEFC designs in Figure 5.5

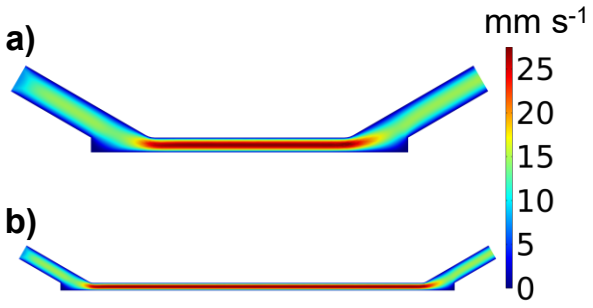

Figure S3. Flow velocity distribution at the central x-y plane of the herein-developed, preliminary flow geometry for an electrode length of a) 1 cm and b) 4 cm, complementing Figure 5.5. The inlet volume flow is 1.14 mL min^{-1} (for half of the inlet's cross-section), and the overpotential is 1.5 V. The channel height amounts to 1 mm, and the cell width to 2.5 mm (symmetry plane at 1.25 mm). The scale ranges from 0-27.5 mm s^{-1}.

Polarization curves for the experimental validation of the Levich analysis for EFCs and the KL relationship

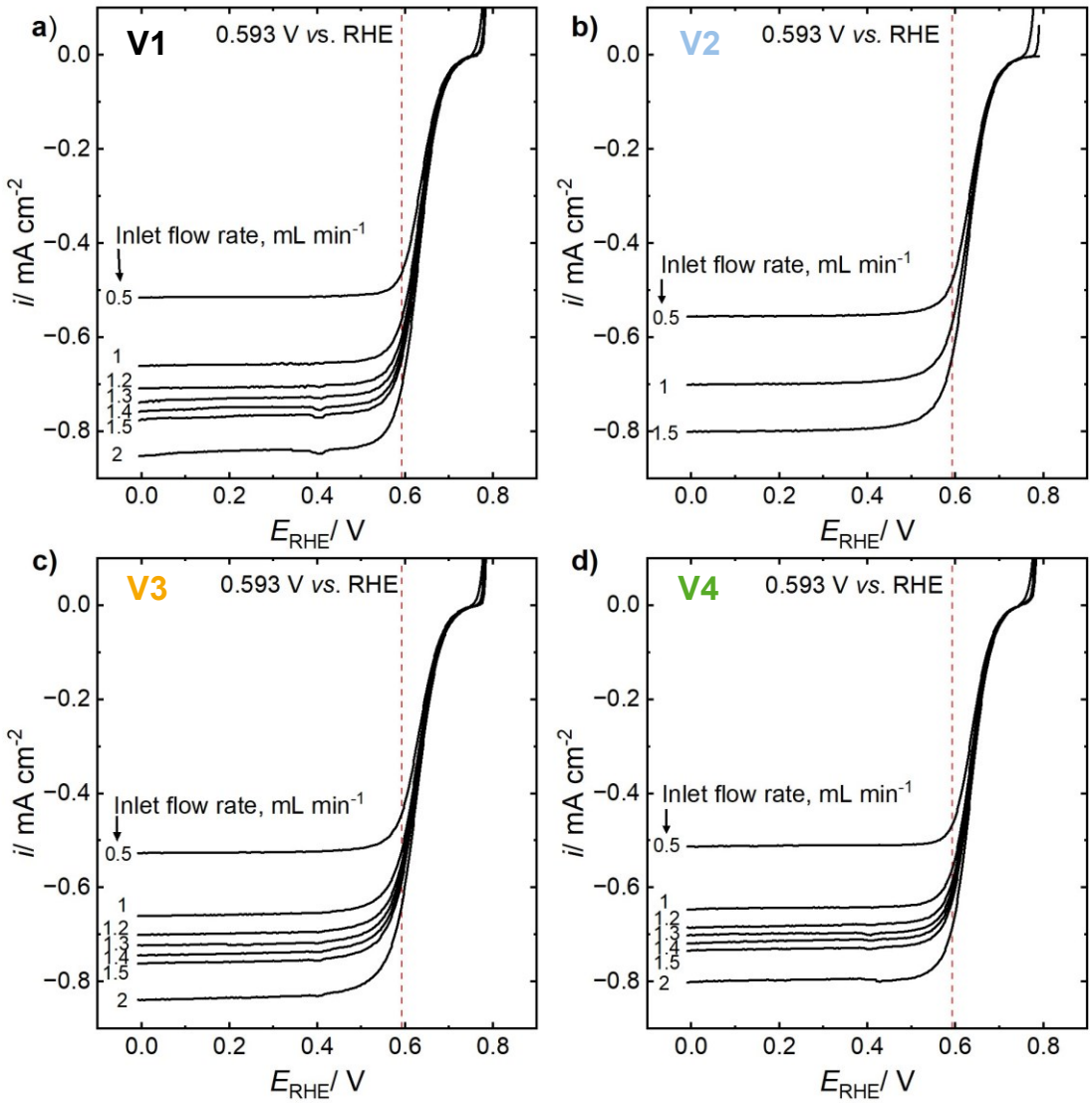

Figure S4. Polarization curves for the experimental validation of the Levich analysis for EFCs and the KL relationship recorded on different days (a-d). As a model reaction, the reduction of ferricyanide was investigated at different flow rates (0.5, 1, 1.2, 1.3, 1.4, 1.5, 2 mL min^{-1}). As electrolyte 10 mM $K_3[Fe(CN)_6]$ in 0.1 M $HClO_4$ was used. For each flow rate, the electrolyte resistance was determined by EIS (10 - 300 000 Hz, 10 mV rms), and three LSV (0.79-0.01 V *vs.* RHE at 2 mV s^{-1}) were recorded. Experiments were conducted at RT.

9.2.2. Adapted Design to Study the Alkaline Water Electrolysis

Table S7. 3D-printing and embedding material screening for the application during CP at 100 mA cm^{-2} at 80°C and 30 wt% KOH in an iEFC, tightened by 0.8 Nm.

Material	Manufacturer	Testing condition	Weight loss /%	Observation
3D-printing				
AR-H1	Keyence	CP at 100 mA cm^{-2} for >10 h (30 wt% KOH, 80 °C)	-	No observable changes
AR-M2	Keyence	>24 h 30 wt% KOH, 80 °C	0.2	No observable changes
		CP at 100 mA cm^{-2} for >10 h (30 wt% KOH, 80 °C)	-	Parts of the iEFC deformed during CP at 80 °C when a tightening force of 0.8 Nm was applied, resulting in a leakage
Clear PP	3D-Printe (printing service)	-	-	Fused Deposition Modeling 3D-print: Too low resolution and deformable
DLP HI TEMP 300-AMB	3D Systems	>24 h 30 wt% KOH, 80 °C	2	An oily film formed (some material probably dissolved)
RGD 525-High Temperature	Stratasys	>24 h 30 wt% KOH, 80 °C	58	Material dissolved
VeroClear	Stratasys	Investigation of electrochemical conditioning in 1 M KOH at RT (see chapter 4.3.2 for conditions)	-	After 3D-printing, the determination of the catalyst's activity in the iEFC was irreproducible during the first experiments. Oily film after experiment observed.
Embedding				
CaldoFix-2	Struers	>24 h 30 wt% KOH, 80 °C	-	Becomes brittle and blurry
EpoHeat CLR	Buehler	>24 h 30 wt% KOH, 80 °C	–0.4	No observable changes

9.3. Electrochemical Conditioning of Ni-(Fe)-based Electrodes at Lab-scale Conditions

9.3.1. Optimization of the Electrochemical Conditioning of $Ni_{70}Fe_{30}$ as Model Electrode

Activation of $Ni_{70}Fe_{30}$ in dependence on the change in oxide charge capacity of the reductive Ni(II)/Ni(III) peak

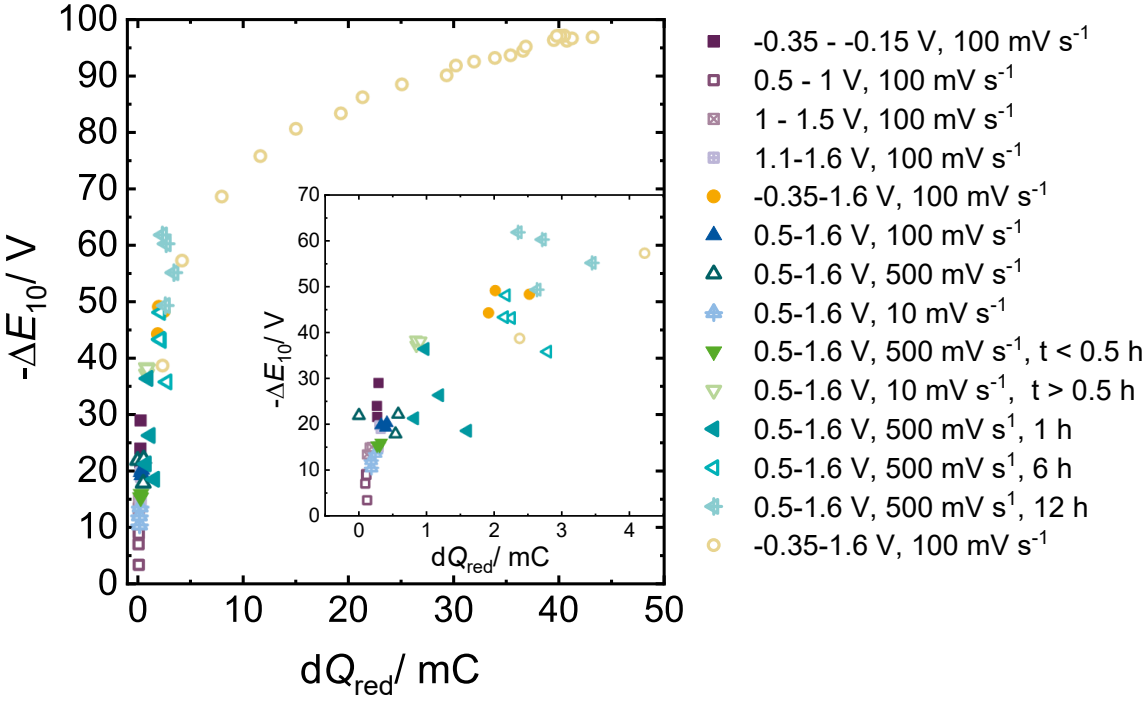

Figure S5. Activation of $Ni_{70}Fe_{30}$, depending on the change in oxide charge capacity of the reductive Ni(II)/Ni(III) peak (1.2-1.5 V *vs.* RHE). The oxide charge capacity was determined by integrating the oxidative Ni(II)/Ni(III) peak for the activity CVs (1-1.6 V, 100 mV s^{-1}) before and after conditioning. For the time-resolved conditioning (–0.35-1.6 V, 100 mV s^{-1}, 0.5-24 h), the conditioning CVs were evaluated. The conditioning sequences correspond to the conditioning sequences from Figure 5.17a, c), d), and Figure 5.19 (100 mV s^{-1}). All experiments were conducted in 1 M KOH at RT.

9.3.2. Influence of the Fe content of the WE and the Electrolyte

Potentials of Ni-(Fe)-based electrodes with varying Fe content

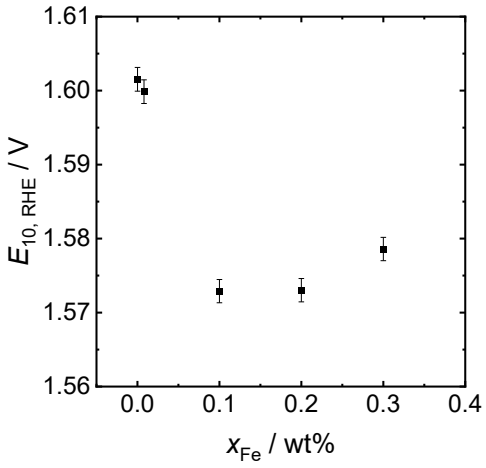

Figure S6. Potential at 10 mA cm^{-2} of Ni-based electrodes with varying Fe content before conditioning. The tested electrode compositions were: $Ni_{99.99}$, $Ni_{99.2}$, $Ni_{90}Fe_{10}$, $Ni_{80}Fe_{20}$, and $Ni_{70}Fe_{30}$. The experiments were conducted in 1 M KOH at RT.

Online ICP-OES spectra during conditioning of $Ni_{70}Fe_{30}$

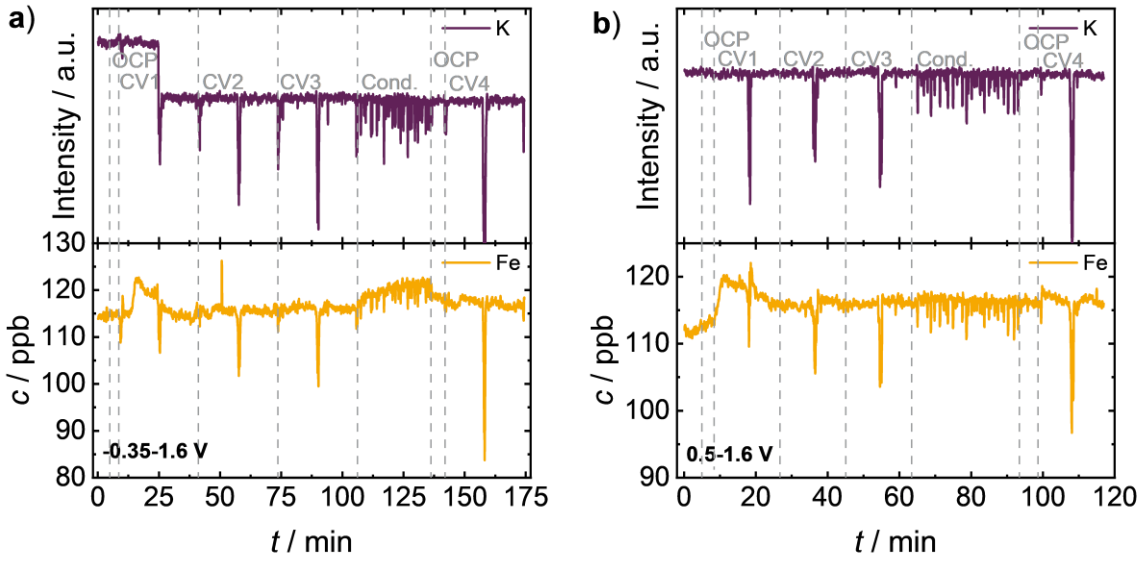

Figure S7. K and Fe concentration, measured by online ICP-OES, while conditioning $Ni_{70}Fe_{30}$ between a) –0.35-1.6 V and b) 0.5-1.6 V. The electrochemical protocol consisted of an OCP, three CVs at 2 mV s^{-1}, CV conditioning at 100 mV s^{-1} for 30 min, OCP, and lastly another CV at 2 mV s^{-1}. In Figure a), a drop of the K baseline from before to after the first gas evolution is visible. Since this baseline drop cannot be seen for Fe, this is considered an artifact. This figure is also displayed in Figure 5.39a,b (Fe) and Figure S20 (K).

Chronopotentiometry for $Ni_{99.99}$ anode at different Fe concentrations

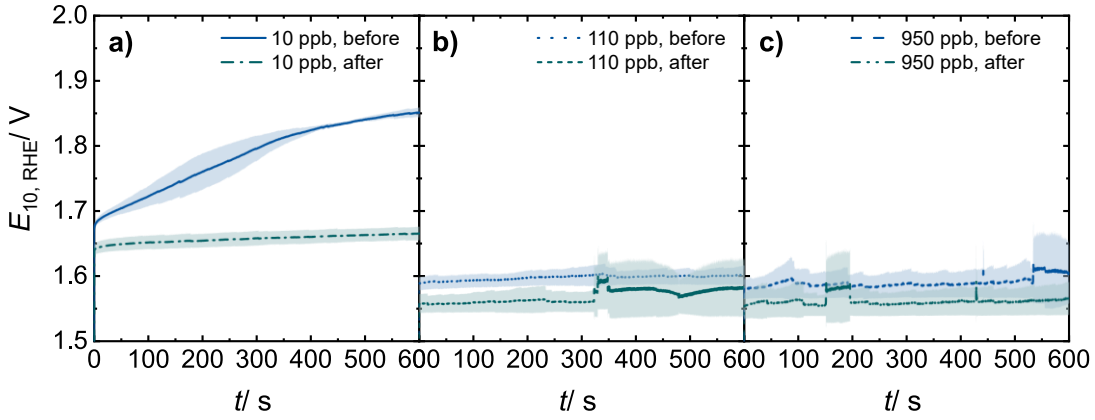

Figure S8. Potential at 10 mA cm^{-2} of $Ni_{99.99}$ before and after conditioning in 1 M KOH electrolyte with approx. a) 10, b) 110, c) 950 ppb Fe. Conditioning was performed between –0.35-1.6 V at 100 mV s^{-1} for 30 min (46 cycles). Only for 10 ppb Fe, electrode degradation is visible before conditioning. Note that jumps in the potential curves are due to gas bubbles and are not associated with degradation.

9.3.3. Understanding the Electrode Material Changes Induced by Electrochemical Conditioning

FTacV: Power spectra for conditioning between 0.5-1.6 V

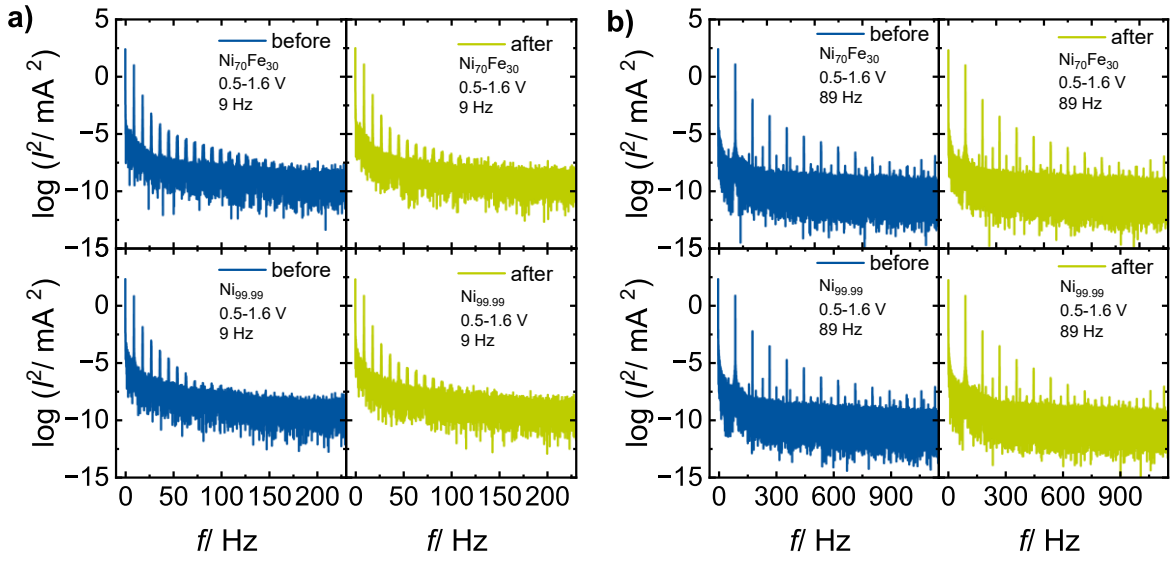

Figure S9. Power spectra from FTacV before and after conditioning $Ni_{70}Fe_{30}$ and $Ni_{99.99}$ between 0.5-1.6 V at 10 mV s^{-1}. FTacV was performed between 1-2 V at 19.073 mV s^{-1} at a) 9 and b) 89 Hz. Experiments were conducted in 1 M KOH at RT.

FTacV: dc and harmonics for conditioning Ni between 0.5-1.6 V

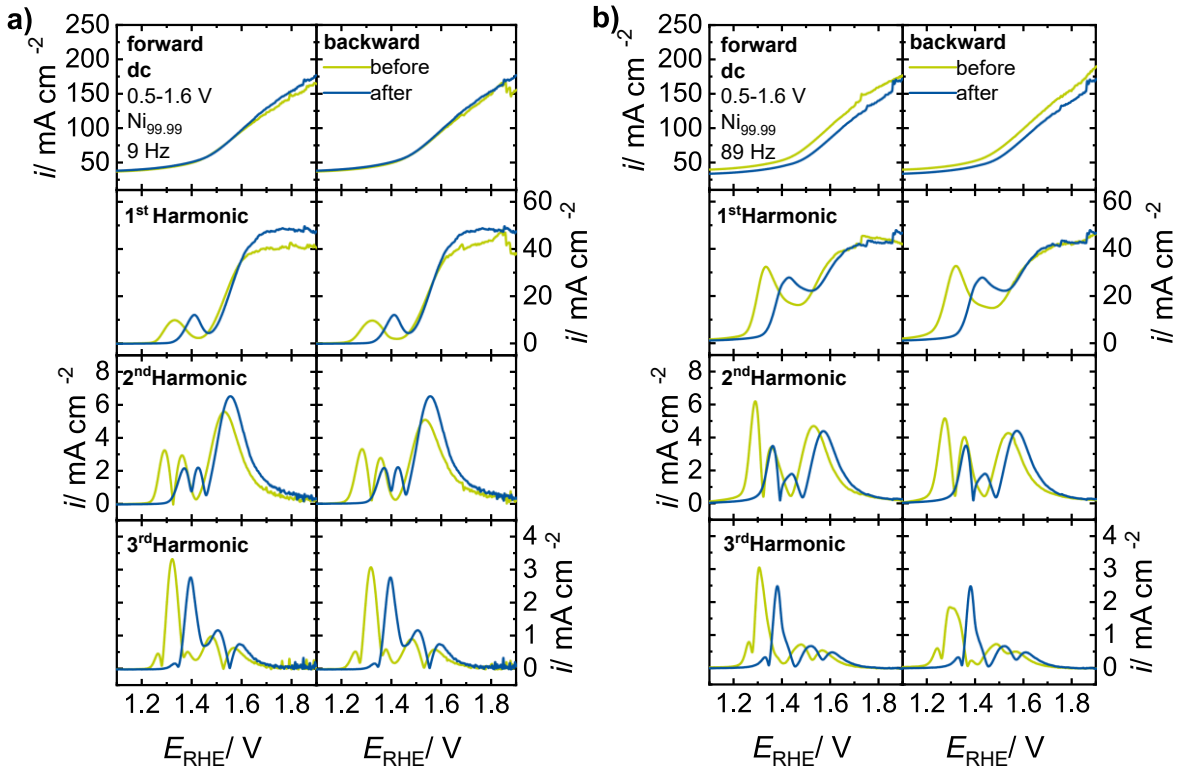

Figure S10. dc, fundamental (1st), 2nd-3rd harmonics from FTacV before and after conditioning $Ni_{99.99}$ between 0.5-1.6 V at 10 mV s^{-1}. FTacV was performed between 1-2 V at 19.073 mV s^{-1} at a) 9 and b) 89 Hz. Experiments were conducted in 1 M KOH at RT.

FTacV: Power spectra for conditioning between –0.35-1.6 V

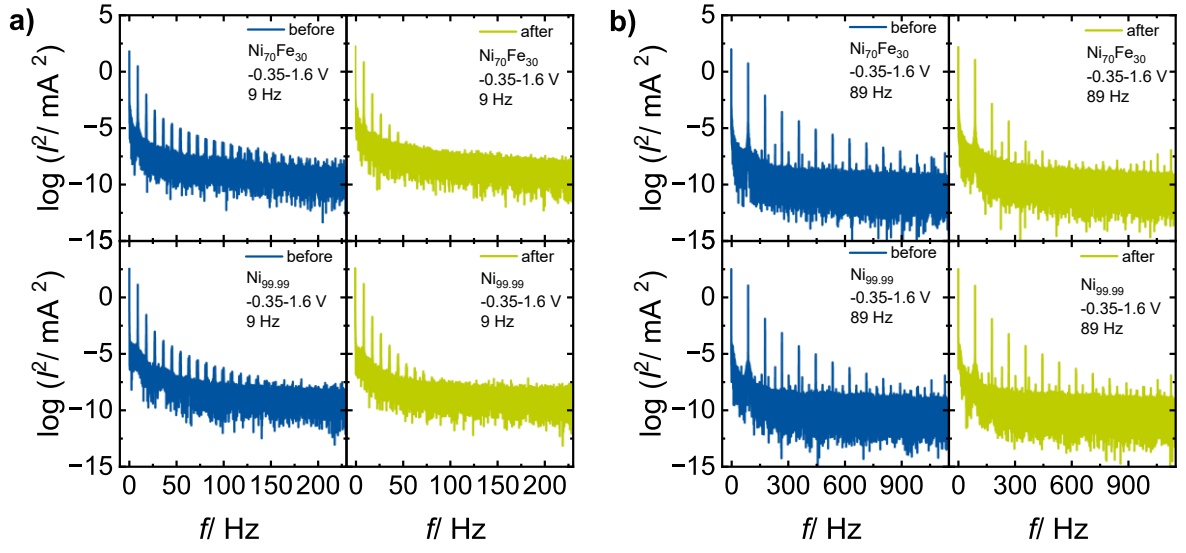

Figure S11. Power spectra from FTacV before and after conditioning $Ni_{70}Fe_{30}$ and $Ni_{99.99}$ between –0.35-1.6 V at 10 mV s^{-1}. FTacV was performed between 1-2 V at 19.073 mV s^{-1} at a) 9 and b) 89 Hz. Experiments were conducted in 1 M KOH at RT.

FTacV: dc and harmonics for conditioning Ni between –0.35-1.6 V

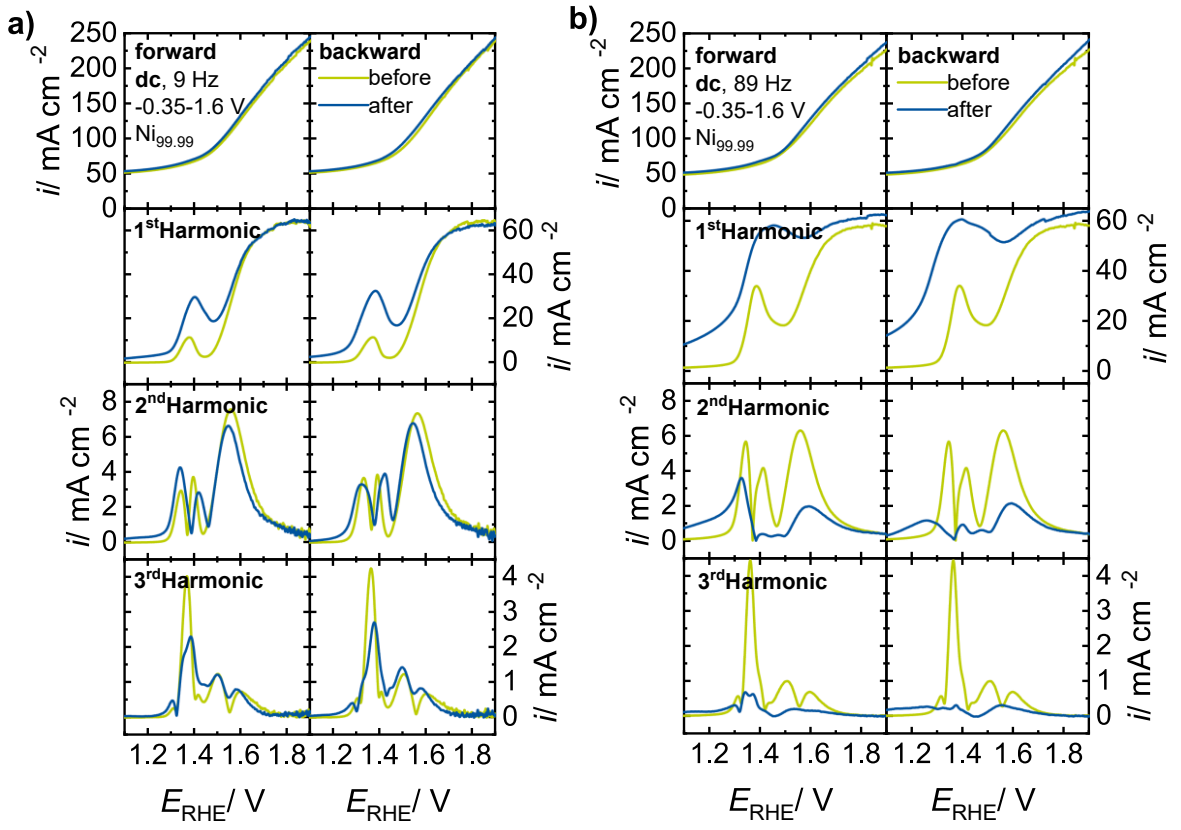

Figure S12. dc, fundamental (1st), 2nd-3rd harmonics from FTacV before and after conditioning $Ni_{99.99}$ between –0.35-1.6 V at 10 mV s^{-1}. FTacV was performed between 1-2 V at 19.073 mV s^{-1} at a) 9 and b) 89 Hz. Experiments were conducted in 1 M KOH at RT.

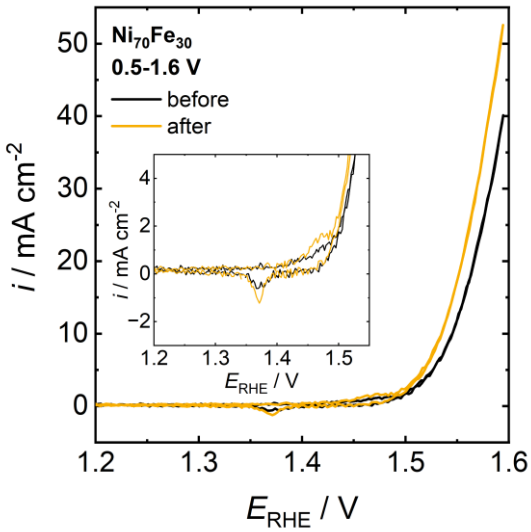

Figure S13. dcCV (1-1.6 V, 10 mV s^{-1}) of the FTacV experiment before and after conditioning of $Ni_{70}Fe_{30}$ between 0.5-1.6 V at 10 mV s^{-1} for 46 cycles. Experiments were conducted in 1 M KOH at RT.

FTIR: Activity CVs before and after conditioning with and without the HER regime

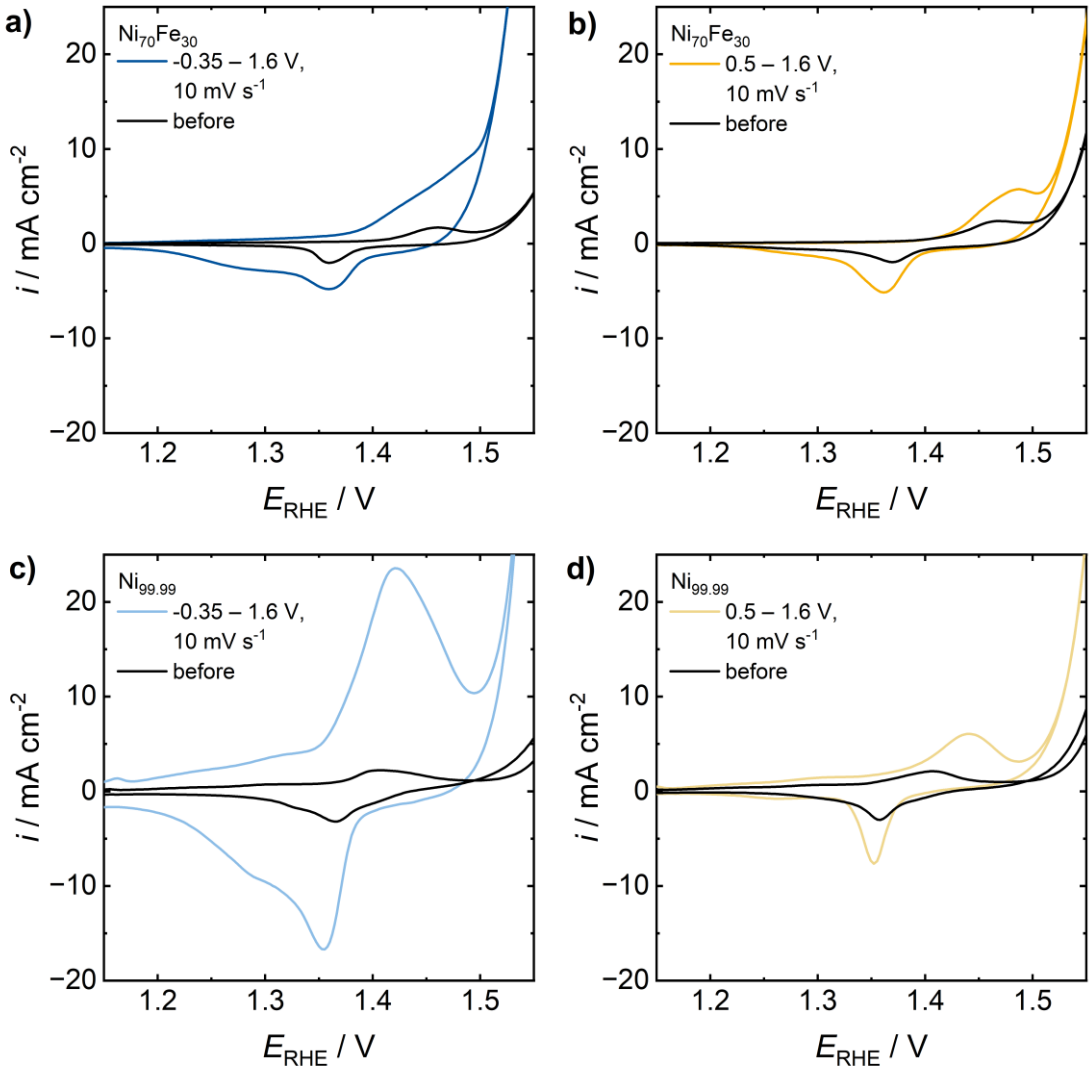

Figure S14. Activity CVs (1-1.6 V, 100 mV s^{-1}) before and after conditioning of a) $Ni_{70}Fe_{30}$ and b) $Ni_{99.99}$, which were characterized afterward by FTIR. Conditioning was performed between –0.35-1.6 V and 0.5-1.6 V at 10 mV s^{-1} for 46 cycles in 1 M KOH at RT. Note that additional peaks might be visible since the 1 cm^2 $Ni_{99.99}$ or rather $Ni_{70}Fe_{30}$ plate electrodes were glued onto embedded WE of the same composition with Ag-containing conductive adhesive and removed after the experiment for characterization.

Microscopy images of electrodes after conditioning with and without the HER regime

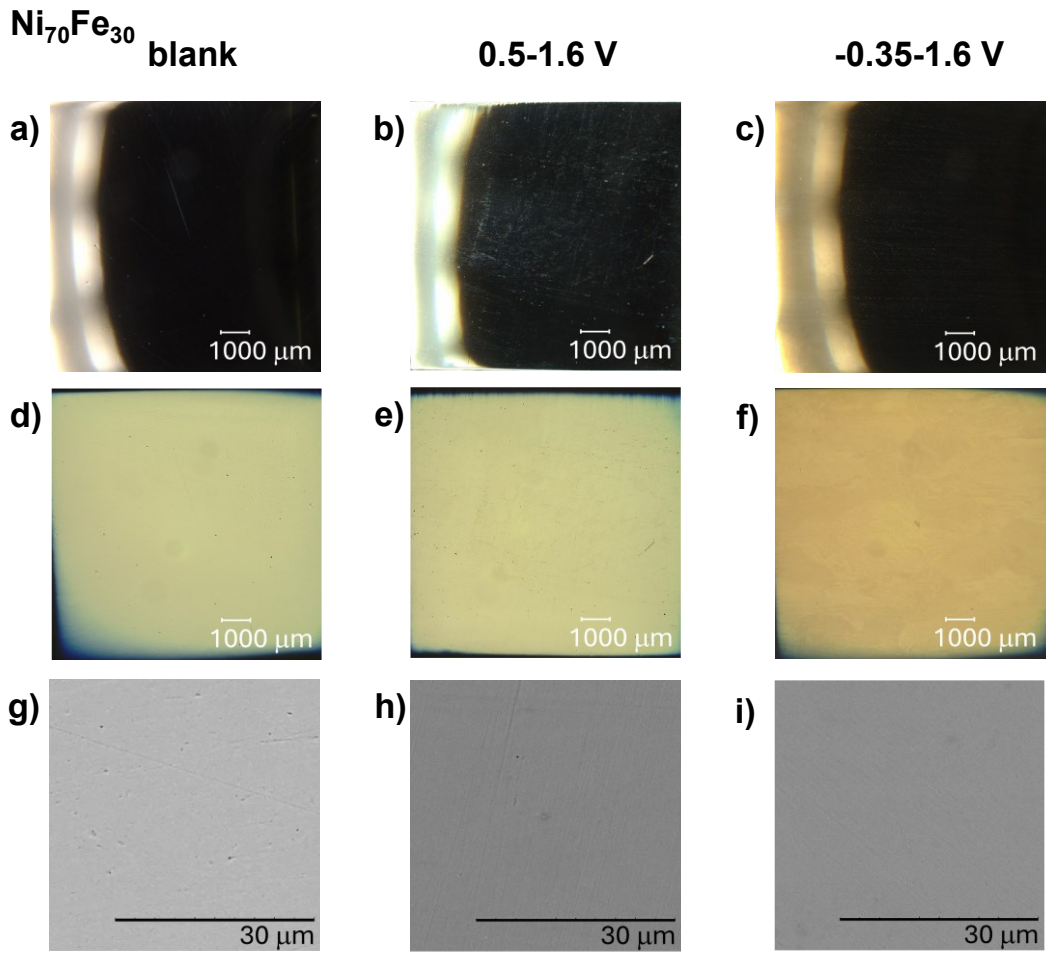

Figure S15. Optical microscopy images (a-f) at 20x magnification and SEM images (g-i) at 3,000x magnification showing the surface structure of $Ni_{70}Fe_{30}$ as blank (a, d, g), after conditioning between 0.5-1.6 V at 10 mV s^{-1} for 46 cycles (b, e, h), and after conditioning between –0.35-1.6 V at 10 mV s^{-1} for 46 cycles (c, f, i). For the optical microscope images, two modes were used: full-ring illumination measured at an angle of 12° (mode 1: a-c) and coaxial illumination measured at a 0° angle (mode 2: d-f). Mode 1 shows the color of the electrode on the left side of the image. This color is only visible due to the light reflection caused by tilting the microscope. Illumination from the top only shows a black color, as seen for the rest of the electrode. Mode 2 indicates the structural change. The color change can, here, not be seen as clearly.

EDX spectra of electrodes after conditioning with and without the HER regime

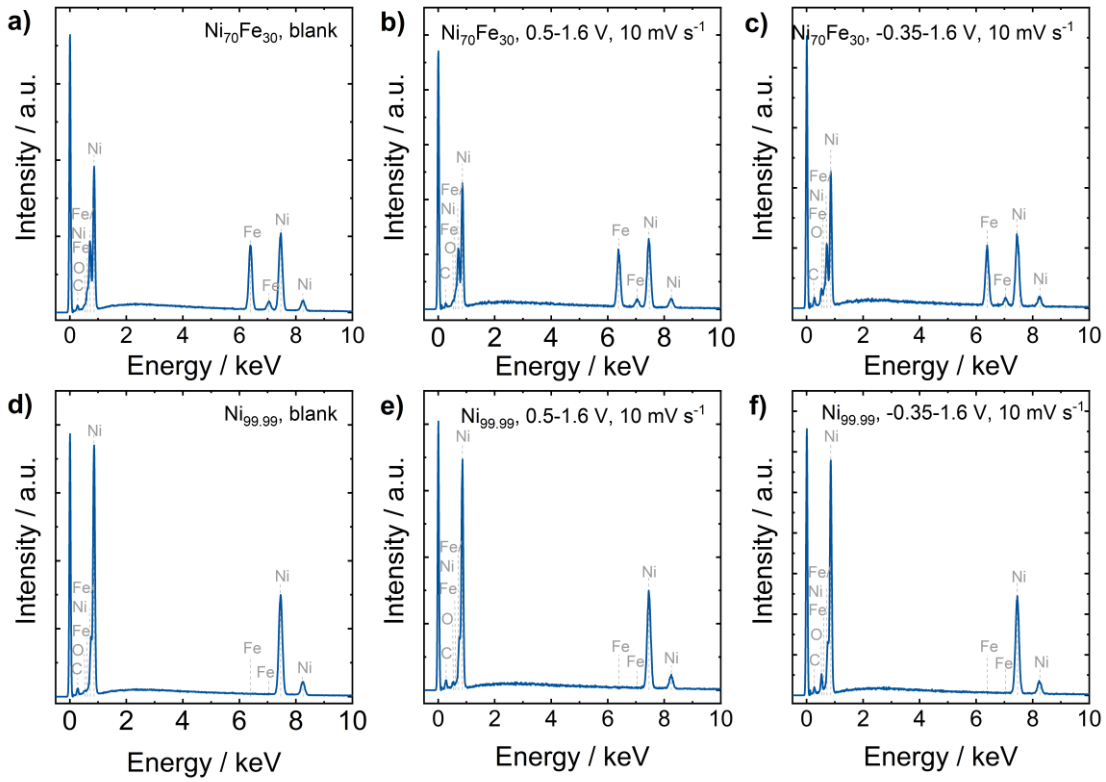

Figure S16. EDX spectra for a-c) $Ni_{70}Fe_{30}$ and d-f) $Ni_{99.99}$ as blank (a, d) and after conditioning. Conditioning was performed between 0.5-1.6 V (b, e) and –0.35-1.6 V (c, f) at 10 mV s^{-1} for 46 cycles.

XPS: Survey and C 1s XPS of electrodes after conditioning with and without the HER regime

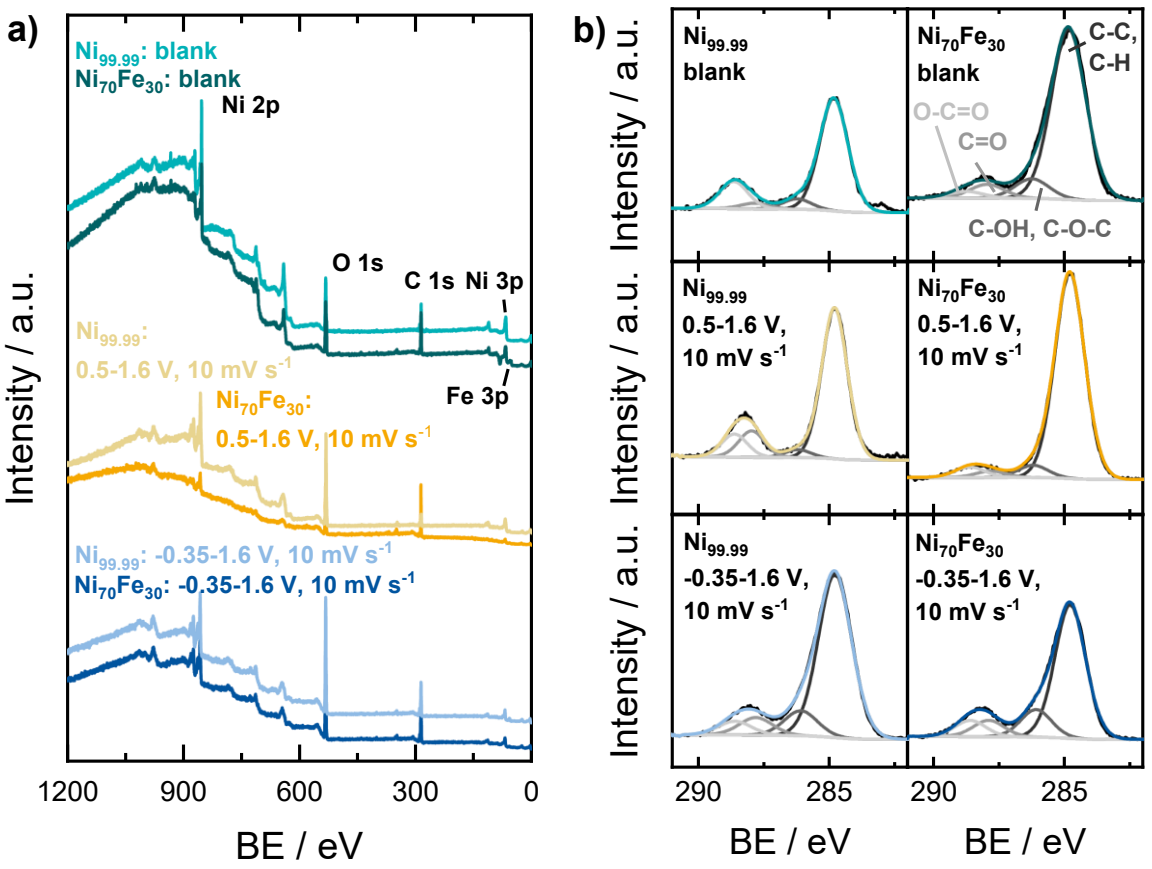

Figure S17. a) Survey and b) C 1s XPS spectra for $Ni_{99.99}$ and $Ni_{70}Fe_{30}$ measured *ex-situ* before and after conditioning. Conditioning was performed between 0.5-1.6 V and –0.35-1.6 V at 10 mV s^{-1} for 46 cycles in 1 M KOH at RT.

XPS: Activity CVs before and after conditioning with and without the HER regime

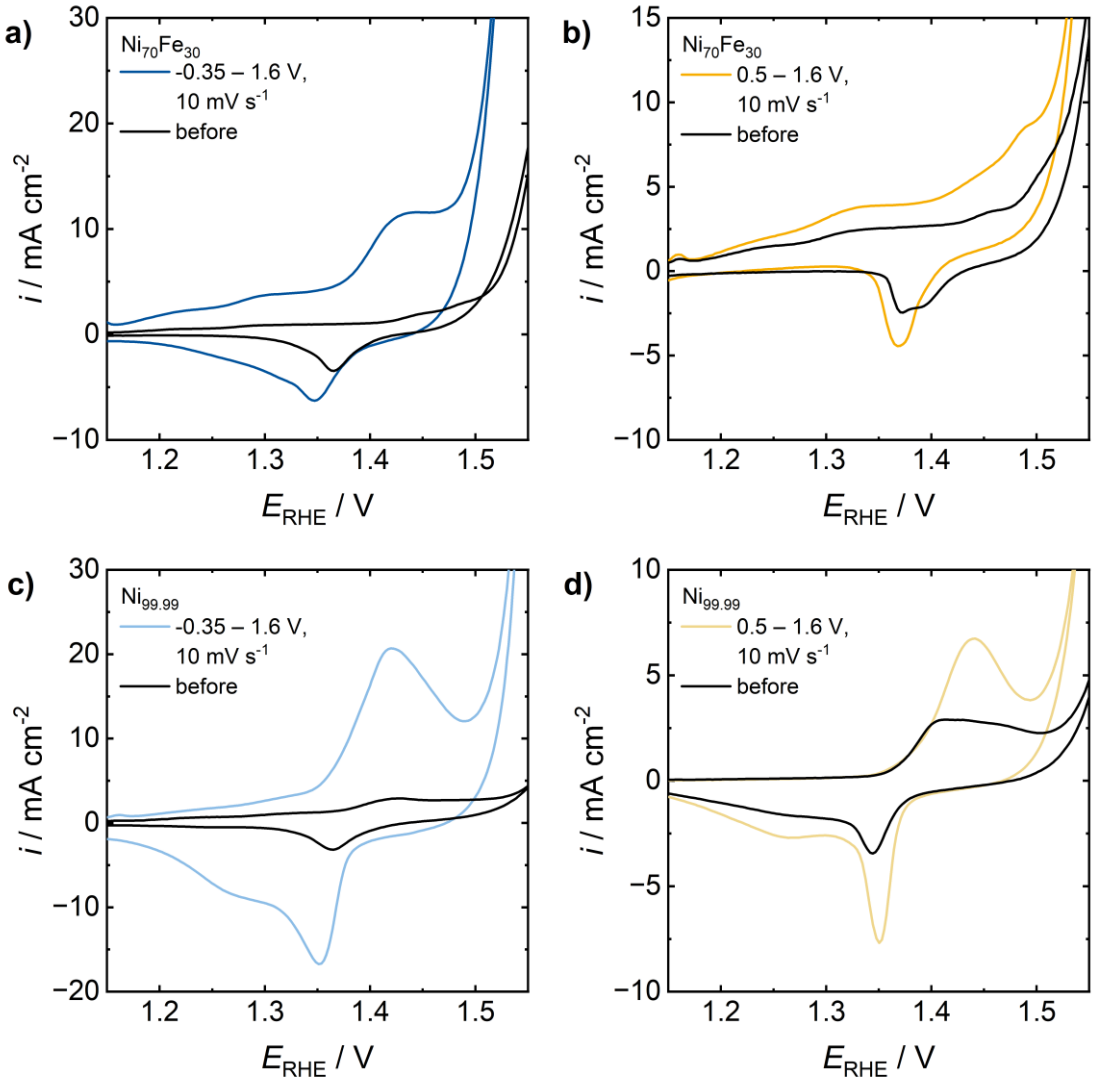

Figure S18. Activity CVs (1-1.6 V, 100 mV s^{-1}) before and after conditioning of a) $Ni_{70}Fe_{30}$ and b) $Ni_{99.99}$ electrodes, which were characterized afterward by XPS. Conditioning was performed between –0.35-1.6 V and 0.5-1.6 V at 10 mV s^{-1} for 46 cycles in 1 M KOH at RT. Note that additional peaks might be visible since the 1 cm^2 $Ni_{99.99}$ or rather $Ni_{70}Fe_{30}$ plate electrodes were glued onto embedded WE of the same composition with Ag-containing conductive adhesive and removed after the experiment for characterization.

ICP-OES: K and Ni concentration during CP

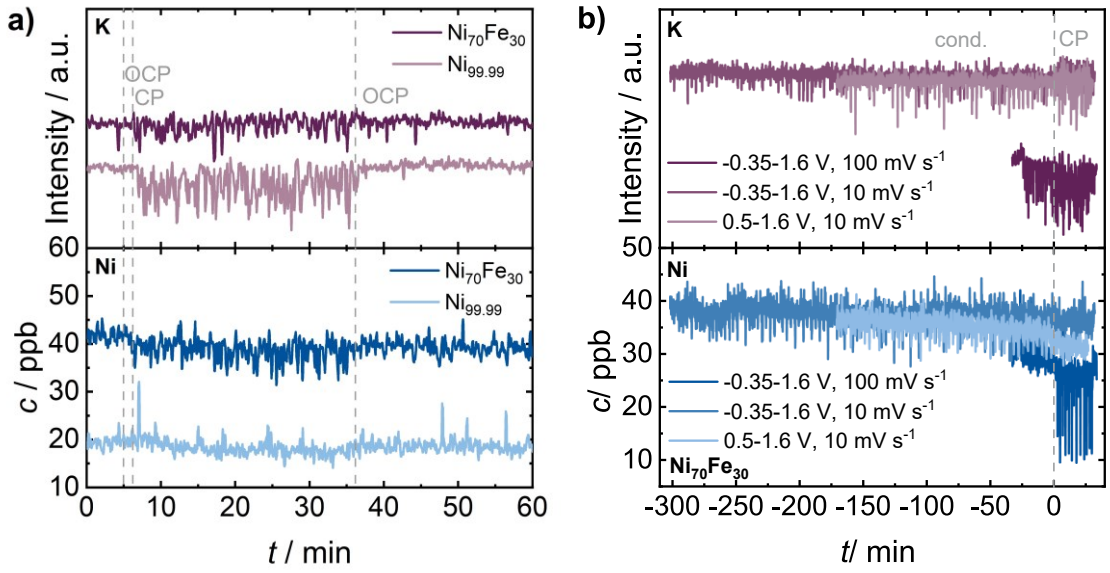

Figure S19. a) K and Ni concentration, measured online by ICP-OES, during a 30 min CP at 10 mA cm^{-2} and a 30 min OCP afterward on $Ni_{70}Fe_{30}$ and $Ni_{99.99}$. b) K and Ni concentration, measured online by ICP-OES, during conditioning of $Ni_{70}Fe_{30}$ between –0.35-1.6 V at 10 and 100 mV s^{-1} and 0.5-1.6 V at 10 mV s^{-1}, followed by a CP at 10 mA cm^{-2} for 30 min.

ICP-OES: K and Ni concentration during CV with and without the HER regime

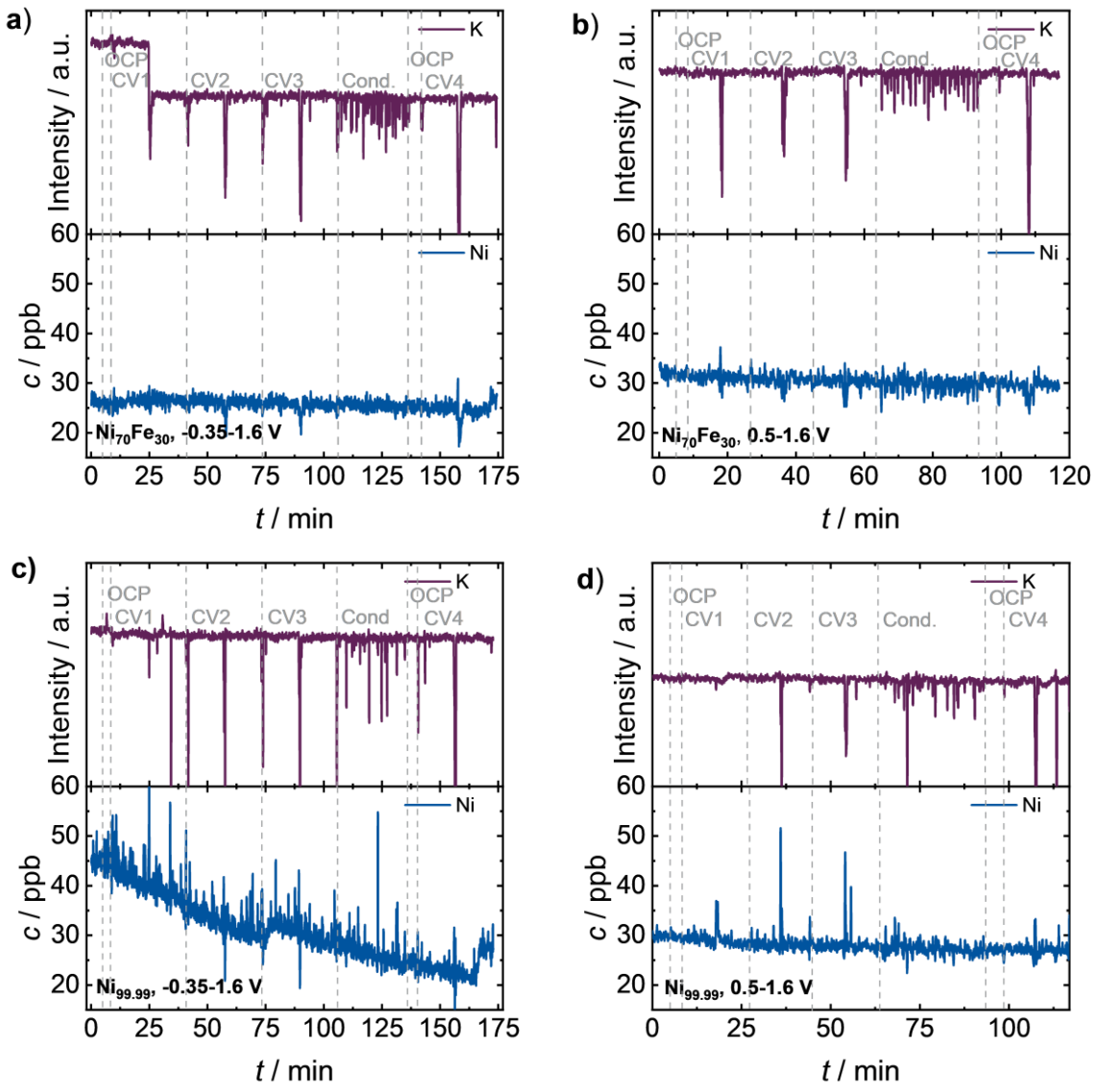

Figure S20. K and Ni concentration, measured online by ICP-OES, while performing on $Ni_{70}Fe_{30}$ (a, b) and $Ni_{99.99}$ (c, d) first three analysis CVs at 2 mV s^{-1}, a 30 min conditioning at 100 mV s^{-1}, and again an analysis CV at 2 mV s^{-1}. CV was performed between –0.35-1.6 V (a c) and 0.5-1.6 V (b, d). Experiments were performed in 1 M KOH at RT.

ICP-OES: Fe concentration during conditioning of $Ni_{70}Fe_{30}$ by CV without the HER regime

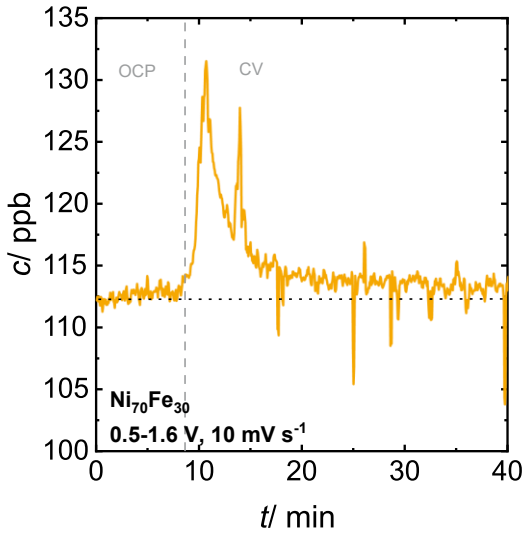

Figure S21. Fe concentration, measured online by ICP-OES, while performing CV conditioning on $Ni_{70}Fe_{30}$ between 0.5-1.6 V at 10 mV s^{-1} in 1 M KOH at RT.